Proceedings of the XXII [illegible] School of [illegible]ics

[illegible]ne, Poland

May 1987

[illegible]art 2 :

condensed matter studies by nuclear methods

INSTITUTE OF NUCLEAR PHYSICS
AND
[illegible]

Report No. 1377/PL

Proceedings of XXII Zakopane School on Physics Zakopane, Poland 1-15 May 1987

part 2 :

condensed matter studies by nuclear methods

INSTITUTE OF
NUCLEAR PHYSICS
AND
JAGIELLONIAN
UNIVERSITY
KRAKÓW 1987

Edited by:

Krzysztof KRÓLAS
Krzysztof TOMALA

WYDANO NAKŁADEM
INSTYTUTU FIZYKI JĄDROWEJ W KRAKOWIE
UL. RADZIKOWSKIEGO 152
NA PRAWACH RĘKOPISU

Kopię kserograficzną, druk i oprawę wykonano w IFJ Kraków

Wydanie I *Zam. 237/87* *Nakład 100 egz.*

SCHOOL SPONSORS

Institute of Nuclear Physics, Kraków
Institute of Physics, Jagiellonian University

SCHOOL ADDRESS

"ZREMB", Zakopane, ul. 15 Grudnia 10a

ORGANIZING COMMITTEE

Chairman: A.Z. Hrynkiewicz

Members: K. Królas /scientific secretary/
M. Cholewa
J. Grębosz
M. Lach
M. Marszałek
M. Rybicka
J. Stanek
K. Tomala
P. Wodniecki

Proceedings of the previous Winter School devoted to the applications of nuclear methods in solid state physics:

- "Nuclear Interactions with Extranuclear Fields" - XI Winter School on Nuclear Interactions, February 4-18, 1973,
- "Hyperfine Interactions" - XVII Winter School, Bielsko-Biała 19 February - 2 March, 1979,
- "Condensed Matter Studies by Nuclear Methods" - XX Winter School on Physics, Zakopane, 20-26 April, 1985.
- "Condensed Matter Studies by Nuclear Methods" - XXI Winter School on Physics, Zakopane, 14-20 April, 1986,

as well as those devoted to selected topics in nuclear structure studies are still available from:

Library,
Institute of Nuclear Physics
ul. Radzikowskiego 152
31-342 Kraków
Poland

EDITORIAL

The present volume includes lectures and seminars presented in the second part of the XXII School on Physics at Zakopane for which the manuscripts were received by Organizers before September 30th, 1987. The proceedings of the first part of School devoted to the nuclear structure studies are published in a separate volume.

The Organizers express their gratitude to the Rector of the Jagiellonian University Prof. dr hab. Józef Gierowski and the Director of the Institute of Nuclear Physics in Kraków Prof. dr hab. Zbigniew Bochnacki for their continuous interest and generous support of the Zakopane meeting.

The help in editorial work by Mrs C. Saklarz and excellent cooperation with Publishing Department of the INP Kraków is greatfully appreciated.

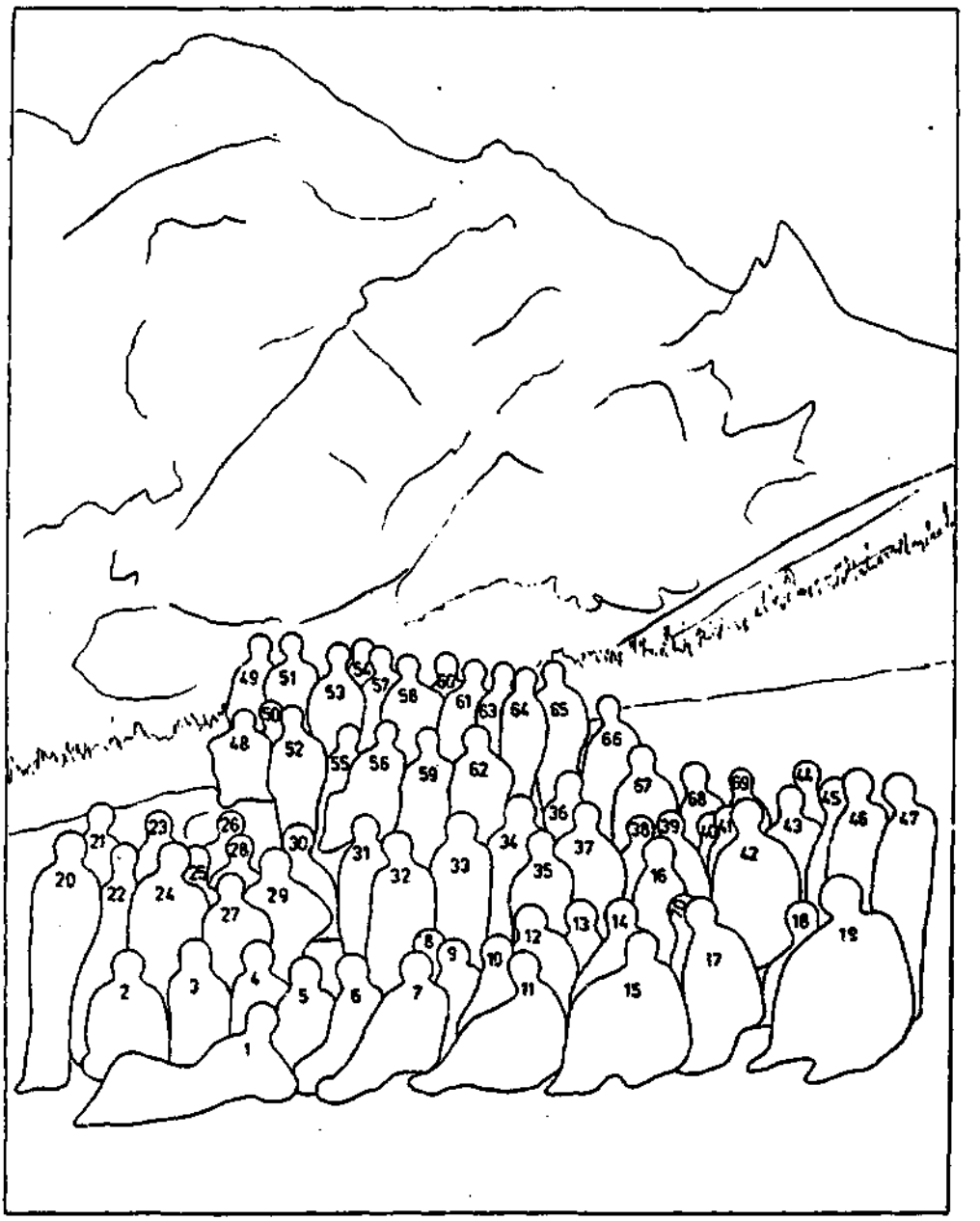
1
2
3
4
5
6
7
8
9
10
11
12
13
14
15
16
17
18
19
20
21
22
23
24
25
26
27
28
29
30
31
32
33
34
35
36
37
38
39
40
41
42
43
44
45
46
47
48
49
50
51
52
53
54
55
56
57
58
59
60
61
62
63
64
65
66
67
68
69

PERSONS AT THE PHOTO

1. J. Grębosz
2. Leszek - guide
3. L. De Doncker
4. M. Lach
5. E. Gędłek
6. E. Dutkiewicz
7. W. Zych
8. M. Rybicka
9. H. Bińczycka
10. E. Danielsen
11. H. Haas
12. D. Dafni
13. W. Tarek
14. S. Nagel
15. K. Królas
16. J. Urban
17. J. Dryzek
18. R. Hajduk
19. R. Vianden
20. N. Subotowicz
21. M. Abd-Elmeguid
22. M. Walki
23. W. Potzel
24. A. Dauminger
25. G. Lieb
26. L. Trache
27. E. Dauminger
28. F. Hardeman
29. D. Kulgawczuk
30. M. Szuszkiewicz
31. J. Stanek
32. M. Rots
33. H. Figiel
34. J. Frąckowiak
35. E. Görlich
36. B. Mikołajczak
37. J. Czerbniak
38. J. Żurawicz
39. J. Hietaniemi
40. A. Gustavsson
41. H. Reuther
42. A. Ozernoi
43. Z. Inglot
44. K. Tomala
45. A. Mayer
46. M. Sudnik
47. V. Rajko
48. A. Hrynkiewicz
49. M. Budzyński
50. G. Marest
51. M. Marszałek
52. M. Finger
53. G. Langouche
54. L. Liszkay
55. J.P. Sanchez
56. H. Mehner
57. K.P. Lieb
58. J. Capala
59. M. Tuszyński
60. K. Szymański
61. E. Japa
62. J. Konraus
63. J. Żukrowski
64. Nguen Hong Chau
65. W. Woch
66. J. Przewoźnik
67. J. Chojcan
68. G. Schatz
69. S. Harris
70. A. Weidinger

C O N T E N T S

LECTURES

IMPURITY- DEFECT INTERACTION IN METALS
H. Vianden 3

HYDROGEN IN METALS: A NEW FIELD FOR PAC
A. Weidinger 20

IMPURITIES AND DEFECTS IN SILICON STUDIED WITH MÖSSBAUER SPECTROSCOPY AND PERTURBED ANGULAR CORRELATION
G.J. Kemerink 44

ION IMPLANTATION OF Te AND I IONS IN Si AND GaAs STUDIED BY MÖSSBAUER SPECTROSCOPY, ION CHANNELING AND NUCLEAR ORIENTATION
G. Langouche 69

IRON IMPLANTATION IN GARNETS STUDIED BY CEMS, X-Ray DIFFRACTION AT GLANCING ANGLES AND TRANSMISSION ELECTRON MICROSCOPY
G. Marest 88

RECENT RESULTS ON IMPLANTED IMPURITY ATOMS IN FERRO-MAGNETIC HOSTS OBTAINED WITH PAC
K.P. Lieb and F. Raether 122

RECENT RESULTS OF PAC APPLIED TO STUDY OF MAGNETIC ALLOYS
M. Rots 137

RECENT DEVELOPMENTS IN PAC SURFACE STUDIES
G. Schatz, T. Klas, R. Platzer, J. Voigt, R. Weache 147

NEW PERMANENT MAGNETS INVESTIGATED BY MÖSSBAUER SPECTROSCOPY
J.P. Sanchez 156

SOME BIOLOGICAL APPLICATIONS OF THE MÖSSBAUER EFFECT
E.R. Bauminger 194

LATTICE DYNAMICAL EFFECTS AND ANHARMONIC CONTRIBUTIONS TO THE MÖSSBAUER ISOMER SHIFT IN ^{67}ZnO

W. Potzel 212

THE USE OF CLUSTER CALCULATIONS FOR THE INTERPRETATION OF HYPERFINE INTERACTION IN SOLIDS

S. Nagel 232

NUCLEAR POLARIZATION INDUCED BY TILTED FOIL FOILS AND APPLICATION TO QUADRUPOLE INTERACTION STUDIES IN SOLIDS

E. Dafni 240

EXPERIMENTS IN ATOMIC AND APPLIED PHYSICS USING SYNCHROTRON RADIATION

E.W. Jones 251

LIST OF GIVEN LECTURES NOT PUBLISHED IN PROCEEDINGS 279

SEMINARS

LIST OF GIVEN SEMINARS AND POSTERS 283

CONCLUDING REMARKS

G. Schatz 315

LIST OF PARTICIPANTS 318

LECTURES

1/2

IMPURITY-DEFECT INTERACTION IN METALS

R. Vianden

Institut für Strahlen- und Kernphysik der Universität Bonn, Bonn, FRG

Abstract:

The interaction of substitutional impurities with interstitially migrating impurities is studied by use of the $\gamma - \gamma$ time differential perturbed angular correlation technique (TDPAC). In aluminium, copper and gold it is observed that the implantation of different rare gases (He, Ne, Ar, Kr, Xe) as well as nitrogen leads to identical quadrupole interaction frequencies at the site of the ^{111}In probe atoms. In view of the very different sizes of the gas atoms the results could only be explained by assuming that the gas implantation initiates the growth of large cavities at the In atoms and the observed EFG is due to In situated at the inner surface of these cavities.
In the bcc metals Nb and Ta the interaction of dilute Hf with interstitially dissolved oxygen is investigated using the ^{181}Hf angular correlation probe. In Nb it is found that the trapping of oxygen at the probe causes a quadrupole interaction frequency of ν_Q = 268(1) MHz with an asymmetry parameter η = 0.68(1). Between 17 K and 293 K the temperature dependence of ν_Q is very weak whereas η varies considerably. In both host metals the orientation of the three principal axes of the EFG tensor is determined to be : V_{zz} parallel to the <110>, V_{yy} to the <100> and V_{xx} to the <110> direction of the bcc host lattice. The results can be explained in the point charge model by assuming that one oxygen atom is trapped on the second nearest neighbor octahedral position next to the substitutional probe atom and the covalent bonds between the probe and the oxygen lead to a localization of charge near the probe atom.

I. Introduction

After the enormous success of the so-called nuclear methods (TDAPC, ME) in the investigation of intrinsic defects in metals (Ple82, Bod85, Sie86) it seems only natural that this method is also applied to the problems of the interaction between interstitial and substitutional defects. Interstitial impurities in metals are known to cause severe changes in their properties

Helium which can be introduced into metals by nuclear transmutation processes or direct implantation of α-particles leads to a loss of ductility, swelling and diminished crack resistance. These phenomena are of great importance for the design and operation of components in the fission/fusion energy technology.

Hydrogen can cause equally unwelcome modifications of materials properties. On the other hand the interstitial solution of hydrogen in metals or alloys is a promising concept for hydrogen storage and therefore attracts considerable interest.

First TDPAC studies in this field have been carried out on He in copper (Ple80, Dei81) and e.g. on C in Pt (Püt82), H in niobium (Rud84, Wei85) and O in silver and gold (Wod82, Pas83, Pas85).

In the following I will report on recent experiments where the effects of implanted He, Ne, Ar, Kr and Xe as well as N on the ^{111}In impurity in copper, aluminium and gold were studied. The results shed new light on the influence of interstitial gases and substitutional impurities on the cavity formation in metals.

In Nb and Ta the trapping of oxygen by ^{181}Hf atoms was observed and a new model for the interpretation of the data will be presented (Wre86).

II. Experimental Details

a) The γ - γ TDPAC technique

The γ - γ TDPAC technique was used to detect the trapping of defects by radioactive probe atoms. This technique is based on the observation of the interaction of a defect induced electric field gradient (EFG) tensor, described by its main component V_{zz} and the asymmetry parameter $\eta = (V_{xx} - V_{yy}) / V_{zz}$ and the nuclear quadrupole moment (Q) of the probe nucleus. The interaction leads to a change in the directional correlation of two γ-rays emitted successively in the decay of the probe nucleus. This correlation is observed by taking time differential coincidence spectra for 90° and 180° with a set-up of four 51 mm x 51 mm CsF detectors, mounted in a plane around the sample. Energy and time information was derived from the anode signals of the photomultipliers by use of window constant fraction discriminators. The time resolution of the set-up was typically 1.2 nsec (FWHM)

for the energies of the cascades involved. From the coincidence counting rates $W_{ik}(\Theta,t)$ (Θ = 90°, 180°, i,k = number of detector) the standard 4 - detector asymmetry ratio (Are80):

$$R(t) = 2 \cdot \frac{W(180^\circ,t) - W(90^\circ,t)}{W(180^\circ,t) + 2 \cdot W(90^\circ,t)} \qquad (1)$$

with $W(180^\circ,t) = (W_{13}(180^\circ,t) \cdot W_{24}(180^\circ,t))^{1/2}$ and $W(90^\circ,t) = (W_{23}(90^\circ,t) \cdot W_{14}(90^\circ,t))^{1/2}$ was evaluated. It is proportional to $A_{22} \cdot G(t)$, where A_{22} is the lowest order directional correlation coefficient of the $\gamma - \gamma$ cascade and G(t) contains the information about the quadrupole interaction. The influence of terms of higher order than A_{22} can be neglected in the case of ^{111}In and is taken into account in G(t) in the case of ^{181}Hf. The data were analyzed assuming a theoretical perturbation function of the form:

$$G(t) = \sum_{n=0}^{3} s_n(\eta) \cdot \cos(c_n(\eta) \cdot \nu_Q \cdot t). \qquad (2)$$

$\nu_Q = e\,Q\,V_{zz}/h$ is the quadrupole interaction (QI) frequency. $c_n(\eta)$ are well known functions of η. For polycrystalline samples with randomly oriented EFG's the $s_n(\eta)$ depend only on η and are independent of the orientation of the detectors relative to the sample. For probe atoms in cubic single crystals the s_n depend additionally on the orientation of the EFG system, represented by its principal axes V_{zz}, V_{yy}, V_{xx} ($|V_{zz}| \geq |V_{yy}| \geq |V_{xx}|$) with respect to the γ - ray detectors. From the changes in the perturbation patterns for different alignments of the detectors along the main crystal axes (e.g. <100>, <110> and <111>) one can thus derive the orientation of the EFG's principal axes relative to the crystallographic axes. A detailed description of the method has been given by Wegener (Weg85). The radioactive isotopes used in the experiments were ^{111}In and ^{181}Hf. ^{111}In decays with a half-life of 2.6d to ^{111}Cd where a 172 - 247 keV γ - γ cascade is emitted. The spin of the intermediate state is 5/2 $^+$, the half-life 84 nsec and the quadrupole moment Q = 0.83(13) b. In ^{181}Hf the intermediate level has the same spin, the half-life is 10.5 nsec, the quadrupole moment 2.53(10)b and the cascade energies are 133 - 482 keV.

b) Sample preparation

Foils of the fcc metals Al, Cu and Au were implanted at the Bonn isotope separator with 80 keV ^{111}In with typical doses of 2 - 4 $\cdot 10^{13}$ at/cm^2. After annealing the samples under vacuum ($p \leq 10^{-7}$ kPa) for 10 min at 523 K the gas implantation

was carried out at room temperature. Here the dose was $2 \cdot 10^{14}$ at/cm^2 and the implantation energy was chosen appropriately to create good overlap between the In probe ions and the post-implanted gas (Fig. 1). For the EFG orientation measurement a Cu single crystal was implanted in a tilted position in order to avoid channeling of the indium or gas ions. The isochronous annealing steps were carried out in vacuum with a holding time of 10 min.

In the case of ^{181}Hf the polycrystalline samples were prepared by electron gun melting neutron activated natural Hf with 99.99% purity Nb under similar vacuum conditions. The Hf-concentration was lower than 0.1 at%. The EFG orientation measurements were carried out with a ^{181}Hf implanted Nb and Ta single crystals which were annealed in an UHV chamber at pressures between $2 \cdot 10^{-10}$ and 10^{-8} kPa. For measurements below room temperature a closed cycle helium refrigeration system was used.

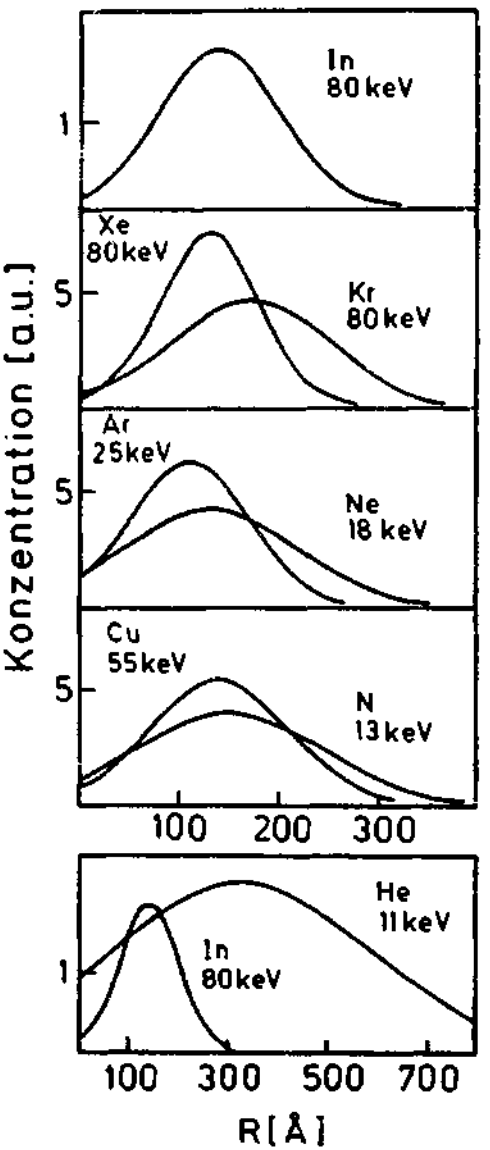

Fig. 1 Implantation energies and estimated range distributions for different implants in copper

III. Experiments and Results

a) Rare Gas – Indium Interaction in fcc Metals

After the preparation of In and rare gas implanted samples as described above TDPAC spectra were recorded after each annealing step with the 4-detector set-up. The experimental asymmetry ratios were formed and a theoretical perturbation function was fitted to the data by the least squares method. The fit function could take into account five different fractions:

$$R(t) = A_{22}\left(f_0 + \sum_{i=1}^{3} f_i \cdot \sum_{n=0}^{3} s_n(\eta_i) \cdot \cos\left(c_n(\eta_i) \cdot \nu_Q^i \cdot t\right) \cdot \exp\left(-c_n(\eta_i) \cdot \nu_Q^i \cdot \delta_i \cdot t\right) + f_4 \cdot \sum_{n=0}^{3} s_n(0) \cdot \exp\left(-n \cdot \delta_4 \cdot t\right)\right)$$

$$\text{with} \sum_{i=0}^{4} f_i = 1 . \qquad (3)$$

Here f_0 is the fraction of probe atoms on unperturbed lattice sites, the f_i are the fractions of probe atoms subjected to quadrupole interactions leading to interaction frequencies ν_Q^i and asymmetry parameter η_i with a possible Lorentzian distribution of half width at half maximum δ_i. f_4 is the fraction of probe atoms on sites with only weak EFG's i.e. $\nu_Q^4 = 0$ MHz and width δ_4.

Before any gas implantation the interaction of vacancies with implanted In probe atoms in pure copper was studied. In this experiment all conditions namely the foil preparation, implantation and annealing parameters were kept equal to those of the following measurements. A fit showed that immediately after the implantation 72% (f_4) of the probe atoms occupied substitutional sites perturbed only by weak EFGs. The remaining fraction (f_3) is subjected to high but nonunique EFG's caused by different defect configurations in the immediate surrounding of the In atoms. Upon annealing at T_{ann} = 373 K a frequency ν_Q^1 = 49.5(7) MHz (η = 0) appears. The corresponding fraction f_1 reaches a maximum of ≈10% around T_{ann}= 473 K before it vanishes at T_{ann}= 723 K.

In a similar experiment where the foil is postimplanted with He (Fig. 2a), a new well defined QI frequency ν_Q^2 = 220(5) MHz (η = 0) appears. Its fraction f_2 reaches a maximum of more than 50% around T_{ann}= 500 K and decreases slowly to 36% at T_{ann}= 703 K. The corresponding asymmetry parameter η_2 varied during this procedure between η_2 = 0.20 after implantation to 0.08 after annealing at 703 K.

A surprising result was found if instead of He another rare gas like Ne, Ar, Kr or Xe was postimplanted with all other parameters kept unchanged. In each case

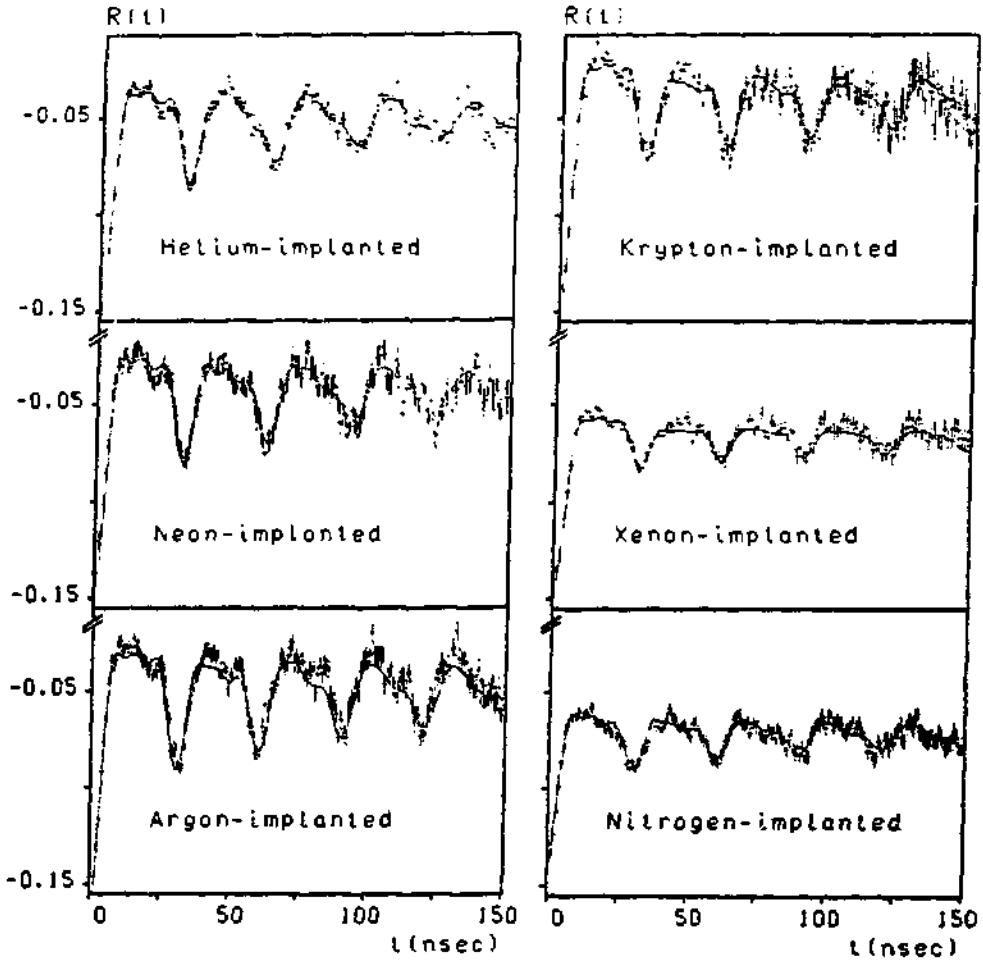

Fig. 2 TDPAC spectra observed for ^{111}In in copper after implantation of different gases and annealing at 523 K.

identical interaction patterns were observed (Fig. 2b ... e) and the least squares fits yielded the QI-frequencies listed in table 1. Isochronous annealing of the samples led to variations of the fractions f_2 as shown in fig. 3.

A further experiment revealed that even the implantation of a non-rare gas like nitrogen led to the same value of the QI frequency (Fig. 2f, Tab. 1).

In order to exclude the possibility that these results are only due to the postimplantation process, e.g. caused by the recoil implantation of some surface contamination on the Cu foil, a control experiment was carried out by postimplanting Cu. However, in this case the same implanted dose of Cu ions produced only the well known frequency $\nu_Q^1 = 49.5(1)$ MHz mentioned above.

An experiment in a Cu single crystal showed that the main component of the EFG tensor V_{zz} was oriented along the ⟨111⟩ crystal axis.

In the previous investigations of He implanted Cu (Ple80, Dei83) the authors explained the QI frequency observed after the He implantation with the formation of small He filled vacancy clusters consisting of 2 - 3 vacancies and He atoms trapped at the substitutional In/Sn probe. However, the explanation of the uniqueness of this observed frequency as well as the small but not negligible asymmetry parameter η and the measured ⟨111⟩ orientation of the main EFG component V_{zz} remained unsatisfactorily.

This model fails completely as an explanation of the present results. The atomic radii of the implanted gases differ considerably (0.71 Å for Ne to 1.31 Å for Xe) and are either smaller or larger than the radius of the host atoms (r_{Cu} = 1.17 Å). Therefore one would have to assume that 2 - 3 strongly undersized (Ne) or oversized (Xe) atoms can be accomodated in some vacancies adjacent to the In probe without changing the local host lattice relaxation. Since due to its $1/r^3$ dependence the EFG at the In site is extremely sensible to small shifts in the surrounding charge distribution this possibility has to be excluded.

Table 1: Quadrupole interaction parameters after implantation of different gases and annealing at T_{ann}. The values were obtained from least squares fits to the data shown in Fig. 2

Implant	ν_Q^2 [MHz]	η_2	δ_2	f_2 [%]	T_{ann} [K]
He	220(5)	0.13(2)	0.074(9)	54(2)	523
Ne	215(5)	0.16(2)	0.070(5)	50(2)	523
Ar	220(5)	0.14(2)	0.054(5)	50(3)	523
Kr	222(5)	0.13(3)	0.068(6)	48(1)	573
Xe	226(6)	0.10(5)	0.082(23)	19(2)	623
N	224(5)	0.13(2)	0.07(1)	23.5(8)	623

The independence of the defect produced EFG on the size of the implanted gas makes it rather probable that the gas atoms only participate catalytically in the formation of a defect complex at the In probe atom without contributing to the EFG. A possible configuration satisfying this conditions would be a larger vacancy cluster (cavity) at the probe atom. For Cu it is known that under irradiation and in the presence of low He concentrations large cavities of octahedral shape bounded by (111) planes are formed (Far80).

The present experiments now seem to indicate that in *pure* Cu migrating vacancies are trapped at In impurities and form faulted dislocation loops. If He or another rare gas is implanted it initiates a threedimensional growth of the vacancy agglomerate with the final result of a cavity. The In atom occupying initially a site in the central region of the dislocation loop will then find itself on the inner (111) surface of the cavity. The gas atom(s) which enabled the cavity growth will finally move freely in the empty volume without influencing the EFG at the In probe.

In this picture one can also immediately understand the ⟨111⟩ direction of V_{zz} since on a (111) surface one expects the gradient of the electric field to be perpen-

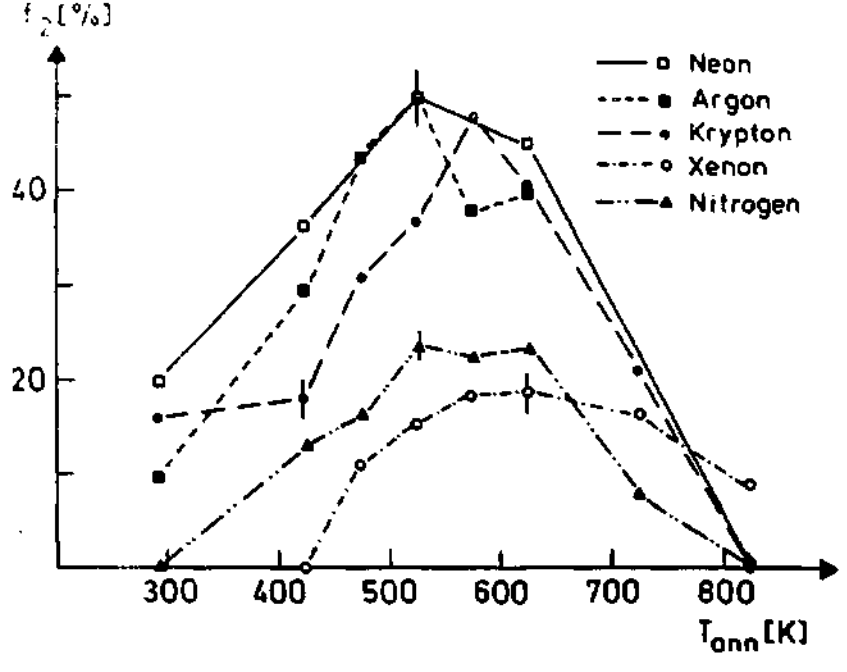

Fig. 3 **Fraction of ^{111}In probe atoms in copper showing the unique quadrupole interaction frequency ν_Q^2 after implantation of different gases (see inset) versus annealing temperature.**

dicular. The gradual reduction of η_2 and the slight increase of ν_Q^2 with increasing annealing temperature is due to th growth of the cavity which moves the edges of the octaeder further away thus reducing the disturbances of the surface EFG. The observed variation of the maximum fraction f_2 (Fig. 3) for different gases has to be attributed most probably to the slightly different overlap of the implantation profiles (Fig. 1) and the correlated vacancy distributions.

Finally the observation of Pleiter (Ple86) who found in a TDPAC experiment in Ni that only a small number (1 - 2) He atoms are needed per In probe to create a similar defect - EFG can be understood.

An independent confirmation of our interpretation comes from a comparison of the present data to the experimental results of Schatz et al. (Sch86). This group studied the EFG experienced by isolated ^{111}In atoms evaporated onto clean (100), (110) and (111) Cu surfaces. All parameters of the EFG measured for In on a (111) surface agree very well with our results. Small variations in the absolute value of ν_Q are attributed to varying strains in the Cu single crystals produced

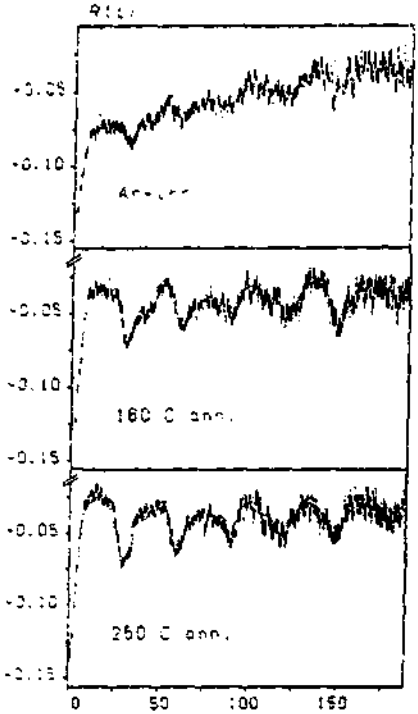

Fig. 4 TDPAC spectra observed for ^{111}In in gold after implantation of argon and annealing at the indicated temperature.

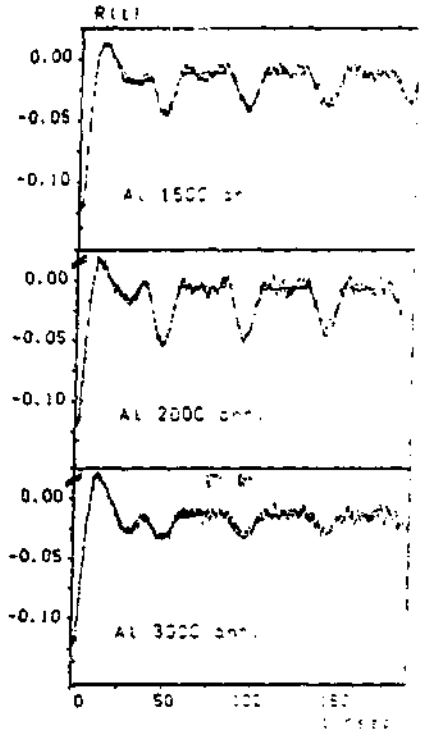

Fig. 5 same as in figure 4 but for argon implanted aluminium

by different methods. Also the temperature dependence of the surface EFG (Sch86) and the He induced EFG have been found to be identical (Ple86).

In view of these results one notes immediately that helium induced cavity growth (Far80) and EFG's attributed to helium decorated defects have also been observed in several other metals (Ple80, Ple84, Dei85). In gold, the only case where a corresponding surface EFG was measured (Sch86), also two identical QI frequencies are present.

This prompted us to carry out similar TDPAC experiments in argon implanted aluminium and gold foils. Preliminary results of these measurements are shown in Fig. 4 and 5. Indeed in both cases the observed frequencies are identical with the values reported after helium implantation. This encouraging result makes it probable that in the future it will be possible to study the early stages of gas assisted cavity growth in various metals.

b) Oxygen - Hafnium Interaction in Niobium and Tantalum

After melting a unique interaction was observed which can be described by $\nu \frac{1}{Q}$ = 268(1) MHz and η = 0.68(1). The fraction f_1 (eq. (3)) of probe nuclei associated with this frequency varied between 5 and 90 % depending on the vacuum in which the melting took place. The amount of probe nuclei on unperturbed or nearly unperturbed lattice sites ($f_0 + f_4$) could be increased by heating the samples in ultra high vacuum ($p \leq 10^{-8}$ kPa) at temperatures $T \geq 2000$ K. This treatment reduced f_1 to values around 5%.

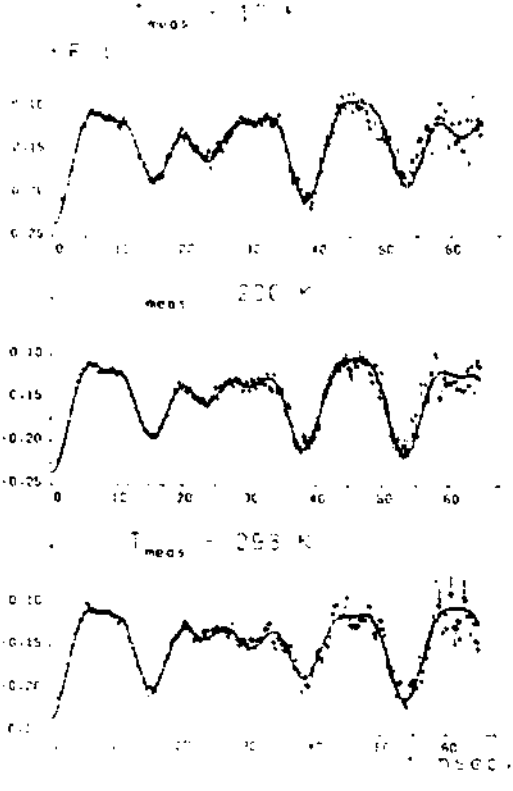

Fig. 6 TDPAC spectra observed for ^{181}Ta in Nb at different temperatures indicated above each spectrum.

The temperature dependence of the quadrupole interaction was measured between 17 K and 293 K. Fig.6 shows three spectra of these measurements. The data could be described by a single frequency showing only a weak temperature dependence, but a strong variation in η (Fig. 7). The orientation of the principal axes of the EFG tensor leading to ν_Q^1 was determined in a measurement in a single crystal. After annealing as decribed above 78% of the probe atoms had trapped the defect leading to ν_Q^1 . TDPAC spectra were recorded at room temperature for different alignments of the crystallographic axes relative to the detectors. The corresponding asymmetry ratios R(t) evaluated as described by Wegner (Weg85) are shown in Fig. 8. For an analysis of the data we calculated the $s_n(\eta)$ for all possible orientations of the EFG system along low indexed crystallographic axes. For the γ - γ cascade used here it is necessary to take into account all $A_{k_1k_2}$- terms of the perturbation function for $k_1k_2 \leq 4$ corrected for the finite solid angle of the detectors. The $s_n(\eta)$ resulting from least squares fits to the data showed a perfect agreement with the theoretical values for a $\langle 110 \rangle$ (V_{zz}), $\langle 100 \rangle$ (V_{yy}) and $\langle 110 \rangle$ (V_{xx}) orientation of the EFG's principal axis system. Calculations for slightly misaligned EFG systems showed that the accuracy of the determination of the V_{zz}- axis was better than 5^0.

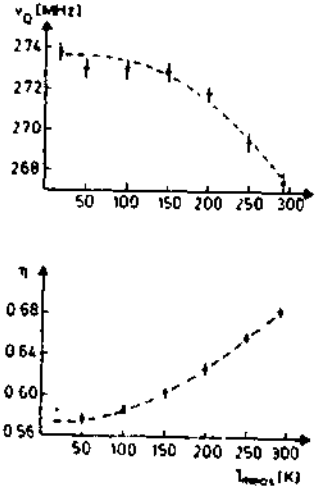

Fig. 7 Temperature dependence of ν_Q^1 and η for ^{181}Ta in Nb

Since Hf is soluble in Nb and the recoil energy transferred to the nucleus by the β-decay to ^{181}Ta is much smaller than the minimum displacement energy of a lattice atom in Nb we can assume that the probe atom Ta occupies a substitutional lattice site. In the present experiments ν_Q^1 could be observed after melting and the cooling rate of the molten samples was low enough ot prevent any quenching effects i.e. we conclude that the frequency cannot be caused by the trapping of a vacancy-like defect. Finally the low Hf concentrations and the virtual immobility of impurities diffusing via a vacancy mechanism at the temperatures where the trapping took place excludes substitutional impurities as causes for the observed frequency.

Only interstitial impurities are known to have the mobility required to explain the high trapping probability at these temperatures. Due to the low impurity content of the Nb used, a sizeable increase of the impurity concentration can only be explained by absorption from the residual gas atmosphere during the sample preparation. An analysis of the residual gas in the unbaked vacuum system showed

that it consisted nearly completely of H_2O and traces of H_2 and N_2. Since these gases also have a high solubility in Nb they will mainly be considered in the following.

For the following discussion it is important to note that the trapping of an interstitial impurity at the probe atom is completely governed by the elemental properties of the ^{181}Hf parent isotope. However due to the extremely fast rearrangement of the electronic surrounding the TDPAC measurement following the decay to ^{181}Ta measures the hyperfine parameters at the site of the nucleus of the Ta atom next to the previously trapped impurity. From the facts that in the temperature range from 20 to 293 K we observe a unique QI frequency and the fraction f_1 remains constant it can be concluded that the trapped impurity does not leave its trapping site within the measuring time of ~ 20 µsec. However slight shifts of the impurity in its interstitial cage cannot be excluded.

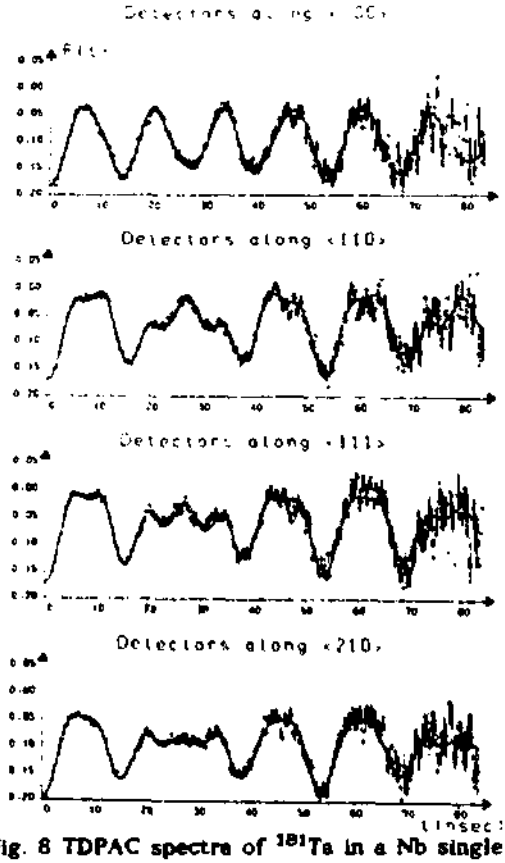

Fig. 8 TDPAC spectra of ^{181}Ta in a Nb single crystal for orientations indicated above.

For the following reasons we exclude H, C and N as impurities responsible for the observed QI:

Hydrogen: In similar experiments a trapping of H at room temperature could not be observed (Men85) due to the high mobility of H. At lower temperatures other QI frequencies were observed possibly due to the formation of Ta - H complexes (Rud84).

Carbon: Annealing of the carefully decarbonized Nb single crystal in a carbonfree vacuum led to a high fraction of probe atoms with a trapped defect.

Nitrogen: Annealing under a nitrogen atmosphere of $p_N \sim 10^{-7}$ kPa did not increase the fraction of decorated probe atoms as compared to samples annealed under $p_N \sim 10^{-10}$ kPa.

Therefore we conclude that ν_Q^1 is due to the trapping of oxygen dissolved in Nb after the decomposition of water vapour at the hot metal surface. This conclusion is supported by the observation of Mendes et al. [Men85] that the same frequency appeared after producing dilute HfNb alloys under a low pressure oxygen atmosphere.

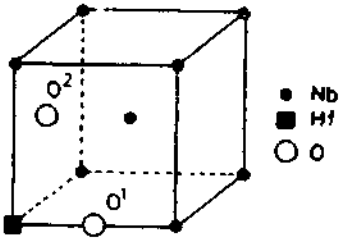

Fig. 9 Possible octahedral sites next to a substitutional Hf atom in a bcc lattice.

Lattice location experiments have shown that oxygen occupies the octahedral interstitial site in Nb [Mat74, Kai78]. Adjacent to the Ta probe atom two sites are possible for the oxygen atom: the nearest octahedral site (O_1) in <100> direction and the second nearest octahedral site (O_2) in <110> direction (Fig. 9). In order to estimate the EFG produced by such trapping configurations we employed a simple point charge model (Z_{Nb}= +5e, Z_O= -2e), which has been reasonably successful in calculating EFG symmetries [see e.g. Kau79].

It can be seen immediately that in this model an oxygen ion on O_1 leads to a <100> orientation of the maximum component of the EFG and to an η equal to zero, so that we can exclude this possible trapping site. An oxygen ion on O_2 produces a <110>, <110>, <100> orientation of the principal EFG axes which is also not in agreement with our results. Furthermore with η = 0.03 the asymmetry parameter is much too small even if one takes into account the displacement of the surrounding Nb atoms caused by the interstitial oxygen [Sch86a].

The simplest configuration which can explain the orientation and the asymmetry of the observed EFG consists of two oxygen ions, one at O_1 and the second near O_2 with a Ta-O distance of 1.98 Å i.e. displaced by 0.33 Å from the ideal position. However it is difficult to understand why only this particular complex should be formed. Further neither a gradual buildup nor disintegration of the complex is observed as one would expect if the configuration would form by the successive trapping of atomically diffusing oxygen. Finally an estimate of the oxygen concentration in the sample from the partial pressures of oxygen and water during melting and annealing excludes this possibility.

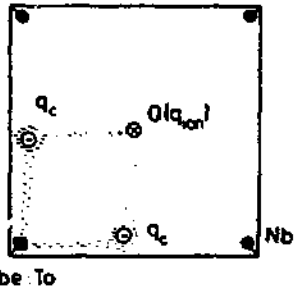

Fig. 10 Position of the assumed covalent charge clouds q_c in the (100) plane for ^{181}Ta in Nb.

Since these attempts to explain the experimental results in a picture where the trapped oxygen is assumed to be a doubly charged negative ion failed we suggest that the covalent contribution to the tantalum - oxygen bond is responsible

for the observed properties of the EFG. From the Pauling electronegativities (Pau40) one estimates the covalency of the bond to be ~ 37%. Therefore if the oxygen is trapped in the O_2 position i.e. in the middle of a (100) plane the bonding p-orbitals of the oxygen localize two more charge clouds in this plane. Each of the clouds has a charge of q_c= -0.37e and q_{ion}= -1.26e, the ionic part, is assumed to be centered on the oxygen ion itself (Fig. 10). This configuration explains well the observed η and orientation of the EFG components. In this model the changes in η at lower temperatures would be due to slight displacements of the additional electron clouds caused by changes in the conduction electron distribution.

It should be mentioned here that due to the fourfold symmetry of the ⟨100⟩ axis similar covalent contributions could not destroy the axial symmetry (η = 0) of an EFG produced by an oxygen ion on the nearest octahedral site O_1.

The oxgen induced EFG at the site of ^{181}Ta in Ta shows very similar properties. A quadrupole interaction frequency of ν_Q= 580(5) MHz and an asymmetry parameter of η = 0.37(1) is observed at room temperature. ν_Q shows a weak and η a strong temperature dependence and the orientation of the EFG's principal axis system was determined to be identical to that observed in Nb.

This similarity and especially the identical orientation of the EFG's principal axis system makes it probable that also here the oxygen is trapped at the second nearest neighbour site. Therefore it is interesting to apply the charge cloud model described above to this system. However in this case one has to consider that after the β-decay of ^{181}Hf to ^{181}Ta the probe atoms is no longer an impurity in the Ta lattice. Therefore the electrons in the Hf–O covalent bond now have to redistribute between the four equivalent Ta atoms surrounding the oxygen in the (100) plane (Fig. 11). This decrease of charge localized near the probe atom leads to a reduction of the asymmetry parameter of the EFG without changing the orientation of its principal axis system. If one takes the value for the covalent charges (q_c = -0.37e and the angle φ = 41.4° , Fig. 10) found in Nb and simply reduces q_c by a factor of four a point charge model calculation taking into account the now four equivalent charge clouds and the known lattice distortions caused by the oxygen atom one obtains an asymmetry parameter η = 0.34 which is very close to the experimental value of 0.37.

Only the change in the absolute magnitude of the EFG i.e. the increase by about 120% from the Nb to the Ta system cannot be explained in this model and has most probably be attributed to changes in the electron distribution around the

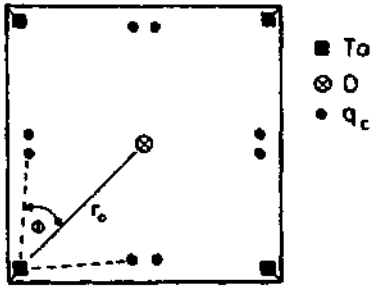

Fig. 11 Position of the charge clouds q_c for ^{181}Ta in Ta.

probe which do not change the symmetry but increase the magnitude of all EFG components by equal amounts.

IV. Summary

TDPAC studies of the cavity growth in copper, gold and aluminium have shown that inert gases play an important role in the early stages of cavity formation in the fcc metals. Additional investigations and complementary measurements as e.g. transmission electron microscopy may yield valuable informations about the kinetics of the cavity growth, their migration as well as their impurity content. Finally these results open new possibilities to study the properties of EFG's on inner surfaces without disturbances of adsorbed gas layers, which usually build up even under the best UHV conditions.
In the bcc metals Nb and Ta QI frequencies induced by the trapping of oxygen at Hf have been observed. The properties of the EFG's (symmetry, orientation) could only be explained in a point charge model by assuming that the substitutional probe atom traps one oxygen atom on the second nearest neighbour octahedral position. However it is necessary to take into account the influence of the covalent contribution to the Ta-O bond which was approximated by assuming two charge clouds off the Ta-O interconnecting line. In this model slight changes in the conduction electron distribution allow also a simple explanation of the observed temperature dependence of η and the differences between the Nb and Ta host.

Acknowledgment

This work has been funded in part by the German Federal Minister for Research and Technology (BMFT) under the contract number 8O1BON1.

V. References

Are80 A.R. Arends, C. Hohenemser, F. Pleiter, H. de Waard, L. Chow and R.M. Suter, Hyp. Int. 8 (1980) 191

Bod85 E. Bodenstedt, Hyp. Int. 24 (1985) 889

Del83 M. Deicher, G. Grübel, W. Reiner and Th. Wichert, Hyp. Int. 15/16 (1983) 467

Far80 K. Farell, Rad. Effects 53 (1980) 175

Kai78 R.E. Kaim, B.W. Palmer, Philos. Mag. A40,2 (1976) 279

Kau79 see e.g. E. Kaufmann, R.J. Vianden, Rev. Mod. Phys. 51 (1979) 161

Mat74 P.P. Matyash, N.A. Shakun, N.P. Dikii, Sov. Phys. JETP Lett. 19 (1974) 18

Men85 P.J. Mendes, J.M. Gil, N. Ayres de Campos, A. Weidinger, R. Pelchel, Proc. of the Int. Symposion Hydrogen in Metals, (1985) Belfast, Phys. Chem. Neue Folge

Pas83 A.F. Pasquevich, F.H. Sanchez, A.G. Bibiloni, J. Desimoni and A. Lopez Garcia, Phys. Rev. B27 (1983) 963

Pas85 A.F. Pasquevich, A. Hoffmann, R. Vianden and U. Wrede J. Appl. Phys. 58 (1985) 3200

Pau40 L. Pauling, The Nature of the Chemical Bond, Oxford, Oxford University Press 1940

Pie80 F. Pleiter, A.R. Arends and H. de Waard, Phys. Lett. 77A (1980) 81

Pie82 F. Pleiter and C. Hohenemser, Phys. Rev. B25 (1982) 106

Pie84 F. Pleiter, K. Post, M. Mohsen and F.S. Wierenga, Phys. Lett. 101A (1984) 363

Pie86 F. Pleiter, priv. communication

Pilt82 U. Piltz, Thesis, Univ. of Bonn, 1982 (unpublished)

Rud84 H.J. Rudolph, Thesis, Univ. of Bonn, 1984 (unpublished)

Sch86 G. Schatz, Int. Conf. on Hyperfine Interactions, Bangalore, India

Sch86a A.v. Schwerin, T.H. Metzger, H. Dosch, J.Peisl, Verh. Dtsch. Phys. Ges. 5 (1986) 1314 and T.H. Metzger priv. communication

Sie87 R. Sielemann, Int. Conf. on Vacancies and Interstitials in Metals and Alloys, Berlin, Mat. Sci. Forum 15-18 (1987) 25

Wei85 A. Weidinger, E. Recknagel, J.M. Gil, P.J. Mendes, N. Ayres de Campos, Hyp. Int. 15/16 (1983) 463

Weg85 D. Wegner, Hyp. Int. 23 (1985) 179

Wod82 P. Wodniecki and B. Wodniecki, Hyp. Int. 12 (1982) 95

Wre86 U. Wrede, Th. Schäfer and R. Vianden, Z. Phys. B64 (1986) 461

HYDROGEN IN METALS: A NEW FIELD FOR PAC*

A. Weidinger

Fakultät für Physik, Universität Konstanz,
D 7750 Konstanz, FRG

1. Introduction

The perturbed angular correlation (PAC) technique uses radioactive nuclei as local probes in the solid. The nuclei interact via the magnetic dipole moment with the local magnetic field and via the electric quadrupole moment with the local electic field gradient (efg) in the solid and therefore provide a means to measure these fields. The information on the interaction is transmitted to the observer by the angular correlation of the emitted γ rays. The method has been applied extensively e.g. for studies of radiation damage /1,2/.

In this paper a short outline of the PAC technique and a review of the application of the method to metal - hydrogen systems is presented. The method is particularly suited for the study of local aspects like defects in hydride structures or hydrogen trapping at impurities. A special but important application is the investigation of hydrogen diffusion at low temperatures.

2. The PAC Method

The essential part of a perturbed angular correlation (PAC) experiment is a γ-γ cascade in a radioactive nucleus with an intermediate state which has a certain, not too short lifetime τ_N. The two γ rays are recorded and the time between their emission is measured (Fig. 1). The detection of the first γ ray (γ_1) in a certain direction leads to an alignment of the nuclear spin in the intermediate state (unequal population of the M-substates) with the consequence that the second γ ray (γ_2) is emitted anisotropically. If during the lifetime of the intermediate state the alignment is changed by an interaction of the nucleus with the local fields in the solid, then the emission characteristics of the second γ ray is changed also. This leads to an oscillating coincidence count rate which reflects the change of the alignment as a function of time. The two detectors are fixed.

The coincidence count rate $N_{12}(\theta,t)$ of detector 1 and 2 as

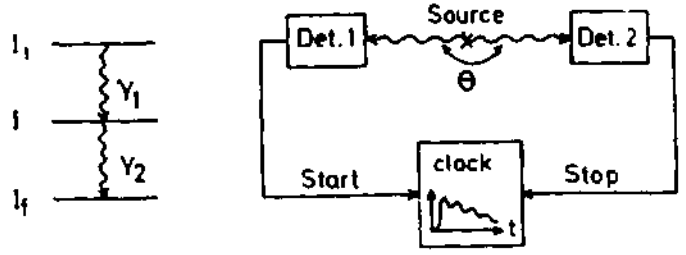

Fig. 1: γ-γ cascade of a nucleus and schematic representation of a perturbed angular correlation (PAC) setup

a function of time t has the following form

$$N_{12}(\theta,t) = N_0 \, e^{-t/\tau_N} \, W(\theta,t) \qquad (1)$$

where τ_N is the mean lifetime of the intermediate state and N_0 a normalizing constant. $W(\theta,t)$ is the time dependent angular correlation and θ is the angle between the two detectors. The general form /3-5/ of $W(\theta,t)$ is rather complicated and shall not be reproduced here. However, in most practical cases, very simple expression for $W(\theta,t)$ can be used; these will be described in the following:

2.1 Quadrupole Interaction in a Polycrystalline Sample

All applications of PAC to hydrogen in metals so far, belong to this category. For a polycrystalline sample (random orientation of the electric field gradients) $W(\theta,t)$ can be written in lowest order as

$$W(\theta,t) = 1 + A_2 G_2(t) \, P_2(\cos\theta) \qquad (2)$$

where A_2 is the anisotropy of the angular correlation and $P_2(\cos\theta)$ is the Legendre polynomial. The higher order terms are usually neglected. Their contributions are partially included in an effective A_2-term. Only in experiments with very high statistics the influence of the higher order terms can be detected. The physically interesting quantity $G_2(t)$ is given by

$$G_2(t) = S_{20} + \sum_{n=1}^{n_{max}} s_{2n} \cos\omega_n t \qquad (3)$$

The ω_n are the transition frequencies in the quadrupole split intermediate state. They are uniquely related to the quadrupole coupling constant

$$\nu_Q = \frac{eQV_{zz}}{h} \qquad (4)$$

and the asymmetry parameter

$$\eta = \frac{V_{xx} - V_{yy}}{V_{zz}} \qquad (5)$$

where Q is the quadrupole moment of the nuclear state and V_{ii} are the components of the electric field gradient tensor in the principal axes frame.The energy splitting of a nuclear level can be calculated by a diagonalization of the quadrupole interaction hamiltonian

$$H_Q = \frac{h\nu_Q}{4I(2I-1)} \left[3I_z^2 - I(I+1) + \frac{\eta}{2}(I_+^2 + I_-^2)\right] \qquad (6)$$

Here $I_\pm = I_x \pm iI_y$ and I_z denote spin operators and I the spin quantum number of the state. For $\eta = 0$ the following simple expression for the energy splitting is obtained

$$E_Q(M) = \frac{h\nu_Q}{4I(2I-1)} \left[3M^2 - I(I+1)\right] \qquad (7)$$

where M is the magnetic quantum number of the spin. The frequencies ω_n in (3) are given by

$$\omega_n = \frac{E_i - E_j}{\hbar} \qquad (8)$$

where E_i and E_j are the eigenvalues of H_Q(see (6)). The s_{2n} values in (3) can be calculated /3-5/. For I = 5/2 and $\eta = 0$, they have the following values:

$$s_{20} = 0.2 \quad s_{21} = 0.37 \quad s_{22} = 0.29 \quad s_{23} = 0.14 \qquad (9)$$

As an example, the PAC spectrum /6/ of ^{181}Ta in tantalum hydride (β-phase) is shown in Fig. 2. Here, only the reduced count rate $A_2G_2(t)$ is displayed. The solid line is a fit to the data with ν_Q = 433 MHz, η = 0.45 from which V_{zz} = 7.64 x 10^{17} V/cm^2 is derived.

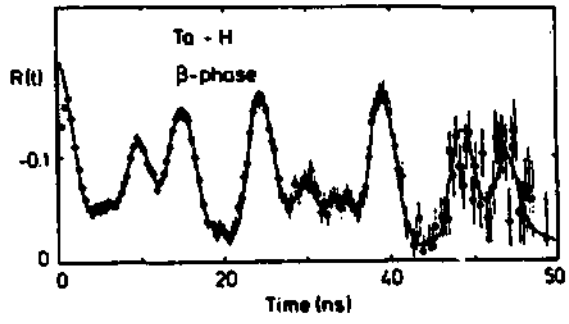

Fig. 2: PAC spectrum of ^{181}Hf - ^{181}Ta in tantalum hydride at 100 K for H/Ta = 0.43 (α + β phase). The solid line is a fit with ν_Q = 433 MHz, η = 0.45 /6/

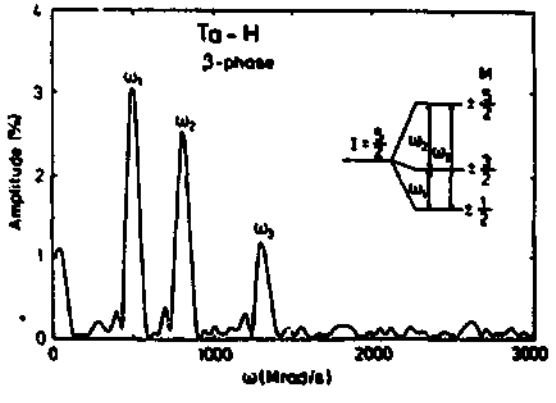

Fig. 3: Fourier transform of the PAC spectrum of Fig. 6.2. In the insert the quadrupole splitting of the I = 5/2 state is shown

The concept of the PAC can be recognized more directly on the Fourier transform of the PAC spectrum (Fig. 3). The three

lines expected for an I = 5/2 intermediate state (see insert of Fig. 3) are clearly seen. The unequal spacings of the lines indicate directly that η must be unequal zero. The intensity ratio of the three lines is given by the s_{2n} values in (3) and is predicted by theory.

3. Experimental Details

3.1 PAC-Sources

^{181}Hf - ^{181}Ta (Fig.4 and Tab.1). ^{181}Hf can be easily produced at a nuclear reactor by the (n,γ) reaction from ^{180}Hf. Unfortunately, no chemical separation of the active from the inactive part is possible. Thus, either mass separation is required or a rather high Hf contamination (minimum ca. 200 ppm, mostly inactive Hf) in the sample must be tolerated. High temperature treatments of the sample must be performed in UHV ($p < 10^{-7}$ Pa) in order to avoid oxygen contamination.

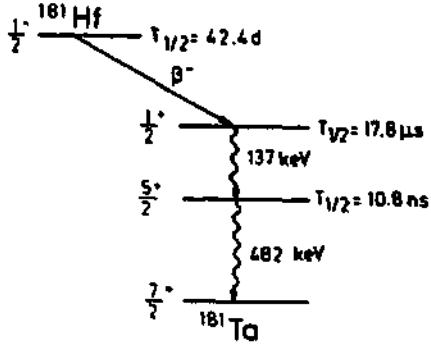

Fig. 4: Partial decay scheme of ^{181}Hf. The nuclear properties which are relevant for the PAC experiment are summarized in Table 1.

^{100}Pd - ^{100}Rh (Tab. 1). ^{100}Pd can be produced by the nuclear reaction ^{103}Rh (d,5n) ^{100}Pd with a deuteron energy of $E_d > 50$ MeV. A chemical separation of ^{100}Pd from Rh is in principal possible /14/ but, because of the inertness of Rh, the separation is rather complicated. Therefore, again, the implantation technique with mass separation has to be applied or the Rh contamination must be accepted.

Table 1: Some properties of nuclear probes which are often used in perturbed angular correlation experiments. $T_{1/2}$ is the halflife of the parent nucleus and intermediate state, respectively. I^{π} designates the spin and parity, μ the magnetic moment in nuclear magnetons and Q the quadrupole moment in barns (1b = 10^{-28} m^2). The γ-γ-cascade is characterized by the energies of the two γ-rays in keV and by the anisotropy coefficients A_2 and A_4. The values of Q are from Ref.6,8,9 and the values of A_2 and A_4 from Ref. 10-13 All other data are taken from the table of isotopes / 7/.

Probe	Parent		Intermediate State				γ-γ-cascade			
	nucleus	$T_{1/2}$	$T_{1/2}$	I^{π}	μ(nm)	Q(b)	$E_{\gamma 1}$	$E_{\gamma 2}$	A_2	A_4
^{181}Ta	^{181}Hf	42.4 d	10.8 ns	$5/2^+$	3.24	2.36	137	482	-0.29	-0.076
^{111}Cd	^{111}In	2.8 d	85 ns	$5/2^+$	-0.77	0.83	171	245	-0.18	0.002
^{100}Rh	^{100}Pd	3.6 d	214 ns	2^+	4.3	0.076	84	75	0.17	0
^{99}Ru	^{99}Rh	15.0 d	20.5 ns	$3/2^+$	-0.28	0.23	353	90	-0.13	-
							528	90	-0.28	-

^{111}In - ^{111}Cd (Tab.1). ^{111}In can be produced by ^{110}Cd(d, n) ^{111}In or ^{109}Ag (, 2 n) ^{111}In and is commercially available. ^{111}In is the most convenient PAC probe provided the metallurgical properties fit to the sample.

^{99}Rh - ^{99}Ru (Tab.1). The source ^{99}Rh can be produced by the nuclear reaction ^{100}Rh (d,3n) ^{99}Rh or ^{99}Ru (d,2n) ^{99}Rh. The separation of the radioactive from the inactive part is again complicated and usually not performed. Because of I = 3/2 for the intermediate state, the asymmetry parameter cannot be determined.

3.2 PAC Set-Up

A conventional PAC set-up consists of four detectors in a configuration as shown in Fig. 5. From each detector a fast and a slow signal are derived, which are used for timing and energy selection purposes, respectively. After the fast-slow coincidence, each detector provides a start as well as a stop signal. By appropriate combinations a maximum of 12 coincidence spectra can be obtained.

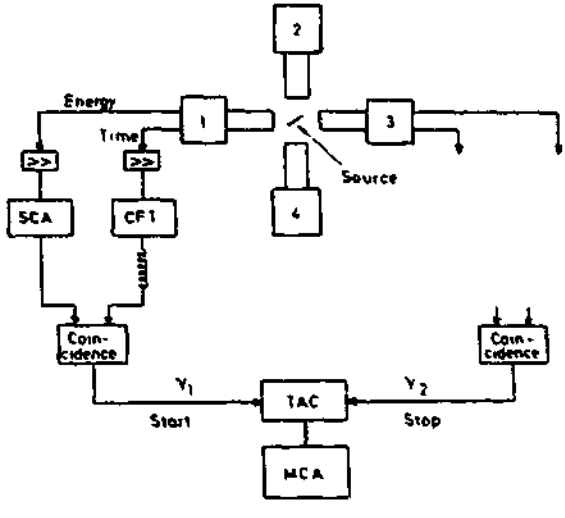

Fig. 5: Four detector PAC set-up and electronics

From the coincidence spectra, $N_{ij}(\theta,t)$ of 4 detectors, where θ is the angle between the detectors i and j, the following ratio is formed (similar expressions for the other combinations):

$$R(t) = \frac{2}{3}\left[\left(\frac{N_{13}(180,t).N_{24}(180,t)}{N_{14}(90,t).N_{23}(90,t)}\right)^{1/2} - 1\right] \qquad (10)$$

This procedure eliminates the exponential decay of the coincidence spectra and even more important the detector efficiency since the efficiency of each detector occurs in the numerator as well as in the denominator. The experimental ratio R(t) gives with the approximation $A_2G_2(t) \ll 1$ the physically interesting quantity $A_2G_2(t)$ (see (2) and (3)), i.e.

$$R(t) \approx A_2G_2(t) \qquad (11)$$

R(t) is usually denoted as experimental PAC spectrum and is fitted with the theoretical function $A_2G_2(t)$. Since the disturbance can be caused by different interactions a more general form of $G_2(t)$ than in (3) has to be used. We set

$$R(t) = \sum_{n=0}^{n_{max}} e^{-\delta\omega_n t} s_{2n} \cos\omega_n t \qquad (12)$$

and

$$G_2(t) = \sum_i f_i e^{-\lambda_i t} R_i(t) \qquad (13)$$

Equation (12) has the same form as (3) (n=0 and $\omega_{n=0}=0$ are included in the summation) but in addition a distribution of the interactions with relative width δ is included. Here a Lorentzian distribution is assumed. Each interaction affects a fraction f_i of probe atoms ($\sum f_i=1$) and may cause a spin lattice relaxation λ_i. The $R_i(t)$ in (13) have the form R(t) as given in (12) but with individual parameters for each interaction. The distribution of interactions causes a dephasing of the precession with a similar effect on the R(t) spectrum as the relaxation rate. In principle these two processes can be distinguished since λ influences the s_{20}-term whereas δ does not. However, in praxis a clear separation is difficult.

4. Applications to Metal Hydrides

Hydride phases can be investigated by the PAC method via the electric field gradient (efg) at the probe site. Changes in the hydride structure are in general connected with large changes in the local efg. However, a direct determination of

the structure is not possible by this method, since the electric field gradient cannot be calculated with sufficient precision in order to be used for structure assignments. Therefore, model calculations can serve only as a rough guide for the discussion.

The data are often compared with predictions of the point charge model in which one assumes, that point charges are located at the hydrogen and lattice atom sites and that the electric field gradient can be calculated by

$$V_{zz} = (1 - \gamma_\infty) \frac{e}{4\pi\varepsilon_0} \sum_{i \neq 0} \frac{z_i}{r_i^3} \left(\frac{3z_i^2}{r_i^2} - 1 \right) \qquad (14)$$

and equivalent expressions for the other componants $V_{\alpha\alpha}$ of the efg tensor. The Sternheimer factor /15/ describes the polarization of the electronic shell of the probe atom by the external efg. The summation in (14) includes all ions around the probe except the probe itself. Sometimes, the screening of the charges by conduction electrons is taken into account by a pseudopotential ansatz. However, since even then no reliable predictions of the efg can be made, the value of these more complicated calculations is questionable.

In the following, a few specific hydride phases will be discussed.

4.1 Palladium Hydride

PAC experiments with the nuclear probes ^{99}Rh-^{99}Ru and ^{100}Pd - ^{100}Rh were performed on polycrystalline Pd-H samples /16/ with hydrogen concentrations between H/Pd = 0.65 and H/Pd = 0.96. The samples were prepared by alloying the irradiated target material with Pd metal to yield sources containing approximately 0.2 at.% Ru or Rh, respectively.

Pure palladium has fcc structure and therefore the electric field gradient at a substitutional site is zero. The same is valid also for the Pd-H system with H/Pd = 1 since in this case all octahedral sites are occupied by hydrogen and the environment of a substitutionel probe atom is again cubic. Experimentally indeed zero or almost zero electric field gradients were observed in these two extreme cases. However, for intermediate concentrations (0 < H/Pd < 1) the cubic environment is disturbed since some of the nearest neighbour octahedral sites are unoccupied and a non-zero efg is expected.

Fig.6 shows two representative PAC spectra for H/Pd = 0.72 and 0.65, respectively. From a statistical point of view

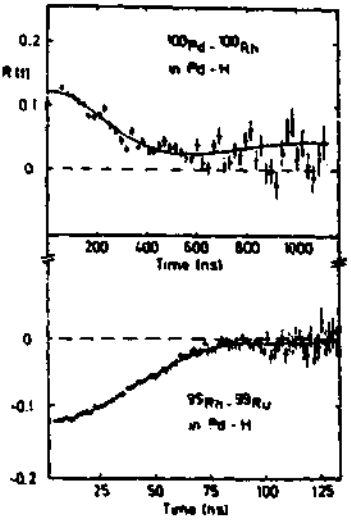

Fig. 6: PAC spectra of ^{100}Pd - ^{100}Rh and ^{99}Rh - ^{99}Ru in Pd-H with H/Pd = 0.72 and 0.65, respectively. The experiment was performed at 77 K /16/

approximately 4 of the 6 nearest neighbour octahedral sites should be occupied, whereas 2 should be vacant on the average. For the source ^{100}Pd, the parent isotope is chemically equivalent to a matrix atom and therefore has the same hydrogen environment as a normal matrix atom. If one assumes, that at 77 K the hydrogen environment does not change after the nuclear conversion from ^{100}Pd to ^{100}Rh, because of the low hydrogen mobility at this temperature, then the PAC probe should see distinct efgs corresponding to hydrogen environments with 1, 2, 3 etc hydrogen vacancies in the first shell (with probabilities according to the statistical distribution of hydrogen for H/Pd = 0.72).

Experimentally (Fig.6) indeed a disturbance of the angular correlation is observed. However, since the efg is very small, the repetition peak of the oszillation cannot be observed in the experimental time window and therefore the resolution is rather poor. The data were fitted with a single efg, but allowing for a distribution around the mean value. According to this fitting procedure, the experiment gives the average value of the different configurations. The experimental efg is $V_{zz} = 1.0 \times 10^{17}$ V/cm^2. This value is more than a factor 10 smaller than the one calculated in the point charge model for a single hydrogen hole in the first shell. This strong reduc-

tion indicates a very effective shielding of the proton charge by the conduction electrons.

The situation is similar for the ^{99}Rh - ^{99}Ru probe (Fig.6). Again, very small efgs were observed. Here, the authors /16/ extracted two different efgs, which they attributed to a single hydrogen hole in the first neighbour shell and to more distant holes, respectively. The corresponding experimental values are: V_{zz} = 2.8 x 10^{17} V/cm^2 and V_{zz} = 1.1 x 10^{17} V/cm^2, respectively. It is intersting to note that V_{zz} produced by a single hole is considerably larger at the probe ^{99}Ru than at the probe ^{100}Rh (if the average value in case of ^{100}Rh is assumed to be representative for a single hole). This difference is not understood at present.

4.2 Tantalum and Niobium Hydrides

The Ta-H system was investigated /17,6/ with the ^{181}Hf - ^{181}Ta probe for several hydrogen concentrations below H/Ta = 0.43. For these concentrations, the Ta-H system is in the $\alpha + \beta$ phase /18/ below approximately 280 K, it then changes to the $\alpha + \zeta$ phase which is stable around room temperature and

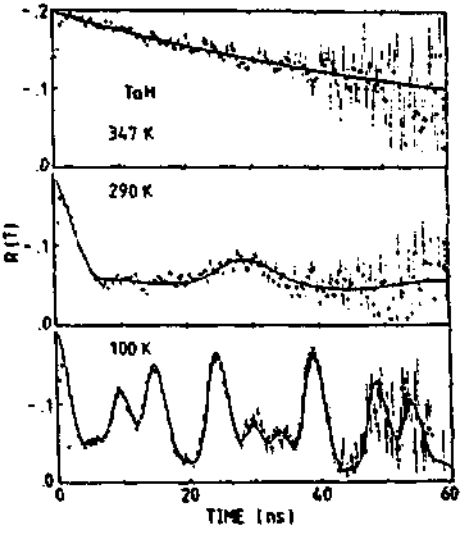

Fig. 7: PAC spectra of ^{181}Hf - ^{181}Ta in Ta - H with H/Ta = 0.43. The structure in the spectrum at 100 K is attributed to the β-phase and that in the spectrum at 290 K to the ζ-phase /6/

finally α phase is reached. The β and ε phase possess ordered hydrogen configurations /18/; the structures were determined by neutron scattering for the deuterides /19,20/.

The PAC spectra (Fig.7) at representative temperatures for the different phases clearly demonstrate the sensitivity of PAC to phase changes. The β-phase quadrupole interaction is experimentally ν_Q = 433 MHz, η = 0.45 whereas theoretically ν_Q = 1157 MHz, η = 0.64 is calculated with V_{zz} from the point charge model and Z = 1 for the hydrogen charges. The rather large experimental quadrupole interaction indicates that in Ta the hydrogen charge is less completely shielded than in Pd. The sign of the hydrogen charge can not be determined in a PAC experiment. The ε -phase has a much smaller (ν_Q = 220 MHz) and almost axially symmetric efg. This result is consistent with the proposed structure in Ref.20. The α phase is cubic, but a small disturbance from diffusing hydrogen atoms is observed (Fig.7).

The phase diagram of Nb-H /18/ shows at low temperatures several ordered hydrogen phases depending on the H-concentration. For H/Nb < 0.75 and T < 200 K, Nb-H is in the $\alpha+\varepsilon$ phase. For the ε - structure three inequivalent Nb environments are expected with two, three and four nearest hydrogen neighbours, respectively. Experimentally /21/ only two different efgs (ν_Q = 546 MHz and ν_Q =481 MHz both with η = 0.65) were found. This deviation is probably caused by the fact that the probe ^{181}Hf - ^{181}Ta is an impurity in Nb and that therefore the local structure around the probe atom is different from the pure Nb-H structure. Above 180 K the PAC data can be fitted with a single efg but with a distribution around the mean value. No difference was found in the PAC spectra between the γ - and β- phase /18/ indicating that the local structure around the probe atom is very similar in these two phases.

4.3 Zirconium and Hafnium Hydride

Pure Zr and Hf have hcp structure and therefore the efg at the substitutional site is a priori non-zero. Hydriding changes these structures: stoichiometric dihydrides are face centered tetragonal, but at somewhat lower hydrogen concentrations they are face centered cubic.

The electric quadrupole interaction at ^{181}Ta in fct $ZrH_{1.97}$ was studied by RASERA et al. /22/ in the temperature range from 20 to 588 K. A static, slightly asymmetric electric quadrupole interaction was found at all temperatures. The static nature of the pattern indicates the absence of significant hydrogen diffusion at these temperatures on a time scale of 100 ns.

DE O. DAMASCENO et. al. /23/ studied $HfH_{1.64}$ with the PAC

probe ^{181}Hf-^{181}Ta. X-ray diffraction showed that the system has fcc structure at room temperature. However, the PAC spectra were by no means undisturbed as expected for the cubic system. The strong disturbance is attributed to hydrogen holes in the non-stoichiometric composition of $HfH_{1.64}$. At room temperature a purely static interaction was found. However, above 373 K a dynamical behaviour was registered which showed motional narrowing at higher temperatures. From the temperature dependance of the relaxation rate an activation energy for hydrogen diffusion is deduced.

4.4 Hydrides of Intermetallic Compounds.

HEIDINGER et al. /24,25/ studied the intermetalic com-

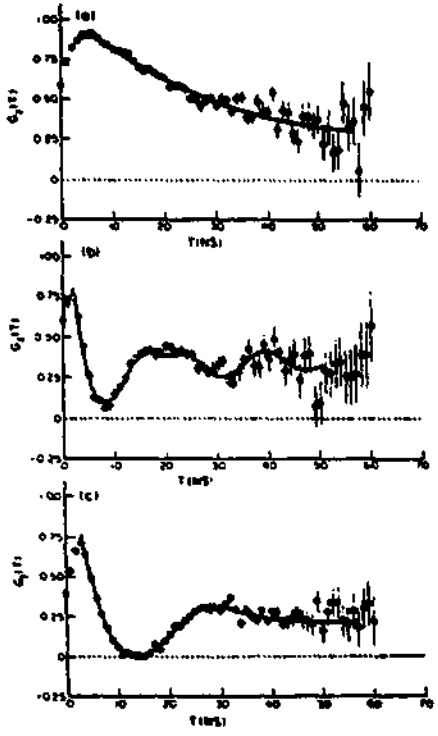

Fig. 8: PAC spectra of ^{181}Hf-^{181}Ta in HfV_2 at different temperatures and different hydrogen concentrations
a) hydrogen free and T = 300 K (cubic AB_2 structure)
b) hydrogen free but at T = 4.3 K (after the martensitic transition) and
c) H/HfV_2 = 3.9 and T = 4.3 K /24/

pounds HfV_2, ZrV_2, TaV_2, and $Hf_{0.5}Zr_{0.5}V_2$ which, without hydrogen, have a cubic Laves phase (C15) structure. These compounds, except TaV_2, undergo a martensitic transition at lower temperatures. In the cubic phase, no electric field gradient is expected if the probe ^{181}Hf-^{181}Ta substitutes an A atom in the AB_2 structure. Experimentally (Fig.8a), a weak disturbance is found which can be attributed to small inhomogeneities of the sample. Hydriding does not change the efg much although the cubic environment should be destroyed for non-stoichiometric hydrogen concentrations. This means that, as in the case of Pd, the proton charge is almost completely screened by the conduction electrons.

After the martensitic transition, a well defined interaction is observed (Fig.8b) in the hydrogen free sample. Hydriding changes the interaction frequency considerably (Fig.8c). It is also found that the martensitic transition is shifted to higher temperatures if hydrogen is added.

VULLIET et al. /26/ studied the system Hf_2Fe for different hydrogen concentrations between 0 and 4.4 H-atoms per unit formula. In the non-hydrided sample, 3/4 of the probe atoms are in a cubic environment and 1/4 in a non-cubic environment as expected for the the structure of Hf_2Fe. Hydriding changes first the 3/4 component and only at higher H - concentrations also the 1/4 component. From this behaviour the authors conclude that at low concentrations hydrogen is localized only near one type of Hf.

5. Hydrogen Trapping at Impurities and Hydrogen Diffusion

In this section, systems with very low hydrogen concentrations will be considered. The purpose of these experiments is to study the behaviour of a single hydrogen atom in a metal and its interaction with impurities. We believe, that the real strength of PAC lies in this field, since the local sensitivity of the probe methods is ideal for these problems. However, in order to reach the high sensitivity it is necessary that hydrogen is trapped at the probe atom.

5.1 Hydrogen Trapping at Interstitial Impurities

The classical case in this field is hydrogen trapping at the interstitial impurities oxygen and nitrogen in V, Nb and Ta (for a recent paper and survey of the literature see Ref.27). As a result of many different experiments the authors /27/ propose that the trapped hydrogen is in a tunneling state between two tetrahedral sites, which are fourth nearest neighbours to the interstitial oxygen or nitrogen atom. N and O are assumed to be at octahedral sites in bcc Nb, Ta and V.

The O-H system in Ta was studied by PEICHL et al. /28/ with the PAC probe ^{181}Hf - ^{181}Ta. Fig.9 shows Fourier transforms of PAC spectra at low temperatures for a $TaO_{0.001}$ and $TaO_{0.001}H_{0.008}$ sample, respectively. In the upper spectrum a single efg (3 lines) with ν_Q = 588 MHz η = 0.35 is observed which is attributed to a single oxygen atom trapped at Hf. In the lower spectrum clearly a different interaction shows up. A fit yields ν_Q = 580 MHz, η = 0.73. The interaction in the lower spectrum is assigned to an O - H pair. The fact that a

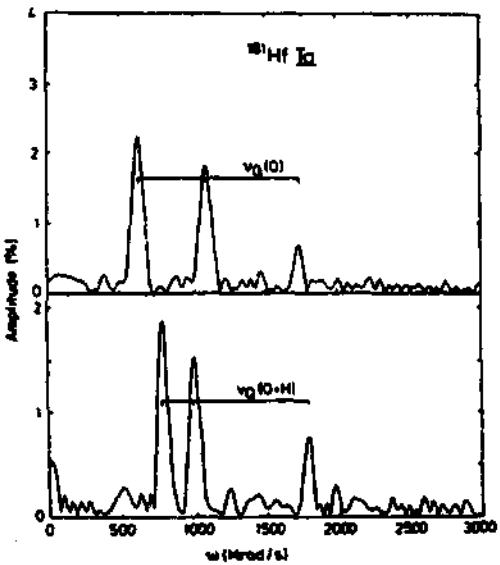

Fig. 9: Fourier spectra of ^{181}Hf-^{181}Ta in Ta. Top: oxygen atom trapped at ^{181}Hf. Bottom: oxygen-hydrogen pair trapped at ^{181}Hf

unique efg is observed clearly demonstrates that only one hydrogen atom can be trapped by one oxygen atom. This result was anticipated by other authors /29/. However, the uniqueness of the efg also requires that the O - H pair has a unique position with respect to the probe atom. Since the parent nucleus ^{181}Hf is attractive for hydrogen (see below) it seems likely that the orientation of the O-H pair is such that hydrogen is nearest neighbour to the probe.

The lower spectrum in Fig.9 was obtained by quenching the sample rapidly to low temperatures. If the sample was cooled slowly, only a fraction of the oxygens (approximately 1/2) captured a hydrogen. This indicates a competition between hydrogen precipitation and hydrogen trapping at oxygen. In the case of deuterium, almost always all oxygen is decorated.

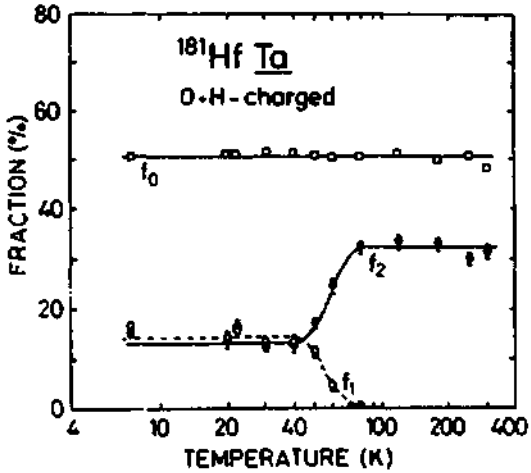

Fig.10: Fraction of probe atoms in different environments. f_0 undisturbed; f_1: efg ν_{Q1} (O - H complex); f_2: efg ν_{Q2} (O - atom). The concentrations are : O/Ta ≈ 0.1 at.%, H/Ta ≈ 1 at.% /28/

Fig.10 shows the fraction of probe atoms seeing an oxygen or O-H pair, respectively. At 55 K, the fraction O-H of the interaction disappears and that of the O interaction increases by approximately the same amount, indicating a conversion of O-H to O at this temperature. Possible explanations are 1) a break-up of the O-H bond or 2) a rearrangement of the pair in such a way, that only the oxygen interaction is seen. However, in this later case, the presence of hydrogen in the neighbourhood of the probe should give rise to at least a small change in the interaction frequency with respect to oxygen alone. Since no change was observed, the explanation 1) seems to be favoured. However, more precise experiments should be performed.

Similar experiments as described here were performed on the O-H and O-D pairs in Nb /30/. The results are comperable with those of Ta . The conversion of O-H(D) to O occurs in Nb around 65 K. An isotope effect as reported in Ref. 28 for Ta was not found for O-H and O-D in Nb.

5.2 Hydrogen Trapping at Substitutional Impurities

Until recently, very little was known on hydrogen trapping at substitutional impurities. However lately, an increa-

sing amount of data became available /31-33/. The PAC method is particularly suited to study this problem if the probe atom is the impurity at which hydrogen is trapped. Since the electric field gradient is drastically changed by the presence of a hydrogen atom close to the probe, trapping and detrapping can easily be recognized. In addition, different configurations can be distinguished via the different electric field gradients. As an example, hydrogen trapping at ^{181}Hf in Ta /34/ will be discussed here.

A Ta sample containing approximately 300 ppm Hf was charged electrolytically with hydrogen (H/Ta = 0.006) and deuterium (D/Ta = 0.06), respectively. If the sample was slowly cooled to 4 K, no disturbance of the PAC spectra was found. However, if the sample was rapidly immersed into liquid helium, a strong modulation appeared. Fig. 11 shows the Fourier spectra of this experiment. The data can be decomposed into two interactions with

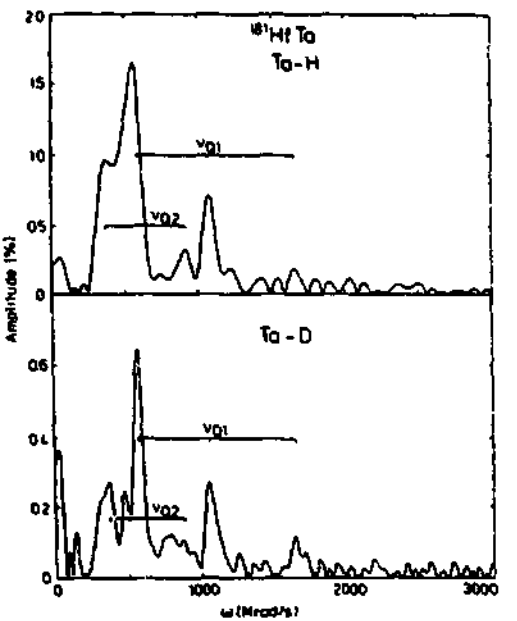

Fig.11: Fourier transforms of PAC spectra for hydrogen and deuterium charged ^{181}HfTa samples which were rapidly immersed from room temperature into liquid helium and measured at 4.2 K. The deuterium charged sample was annealed at 40 K. The concentrations were H/Ta = 0.006 and D/Ta = 0.06, respectively. Thebars connect the three frequencies belonging to a certain interaction.

ν_{Q1} = 580 MHz η = 0.23

and

ν_{Q2} = 300 MHz $\eta \cong 0.8$ and $\delta \cong 10$ %

The first interaction is assigned /34,35/ to a trapped single hydrogen atom and the second to two or more trapped H(D) atoms in different configurations (because of the distribution of ν_{Q2}). The frequencies are very similar for the hydrogen and deuterium charged sample; no significant difference was found (Fig. 11).

The fact, that rapid cooling is required in order to obtain trapping, indicates that the Hf-H binding is rather weak since it cannot prevent precipitation. This behaviour was studied more explicitly in an annealing experiment /34/ in which the sample was rapidely cooled and then warmed up successively to higher temperatures. It was found that the fraction of disturbed probe atoms goes to zero after annealing at around 60 K (with a slight difference for the H- and D-charged sample). The PAC measurements were always performed at 4 K. This experiment shows that the Hf-H and Hf-D pairs are stable up to approximately 60 K and then dissolve whereby the H(D) atoms migrate to precipitates.

The positive binding energy of H(D) to Hf in Ta is consistent with the rule /33/ that elements to the left of the matrix atom in the periodic table are attractive for hydrogen. The HfTa system is similar to TiNb (group IV impurity in group V matrix) for which also a positive binding energy for H-Ti was found /32/.

5.3 Hydrogen Diffusion at Low Temperatures

The low temperature diffusion of hydrogen is particularly interesting since large quantum mechanical effects are predicted. It is expected that the classical over-barrier-hopping mechanism ceases at low temperatures and that tunneling processes take over. At moderately low temperature incoherent tunneling should be dominant, whereas at very low temperatures coherent tunneling or band propagation might show up. (For recent review articles on this subject see Ref. 36-39).

Experimentally, very little is known on this subject. The most direct indication of the onset of quantum diffusion is the bend of the Arrhenius function /40/ for hydrogen diffusion in Nb and Ta. An extension of these experiments to much lower temperatures is not possible since hydrogen precipitates and forms hydride phases in which hydrogen is immobile at low temperatures. However, precipitation can be avoided by trapping hydrogen at impurities. Usually, this prevents also a measurement of hydrogen diffusion in the intrinsic system.

However, if the impurity is radioactive and converts to a matrix atom, then the ideal case of a single hydrogen atom in a pure matrix is realized and the diffusion can be studied.

This idea was applied /35/ to ^{181}Hf in Ta. As can be seen from Fig. 4, ^{181}Hf decays first to an excited state of ^{181}Ta. A hydrogen atom trapped at ^{181}Hf is released after the nuclear conversion and may diffuse away during the 25.7 s lifetime of this state or remain at ^{181}Ta depending on its intrinsic mobility. The subsequent γ-γ cascade will record the presence or absence of hydrogen near the probe atom. Therefore, the fraction of disturbed atoms is a direct measure of the jump frequency of hydrogen in pure Ta. In an experiment at different measuring temperatures (Fig. 12) it was found that up to about 15 K the fraction of disturbed probe atoms is constant but then it drops to zero between 15 and 30 K . These measurements were completely reversible, i.e. the non-converted ^{181}Hf kept their hydrogens whereas the converted ones released them.

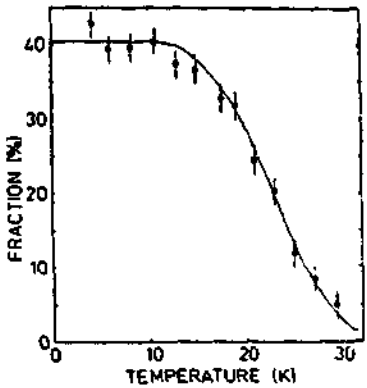

Fig.12: Fraction of probe atoms which are disturbed by a hydrogen atom as a function of temperature. The hydrogen concentration was 0.1 at.%. /35/

In the analysis it was assumed that hydrogen resides at tetrahedral sites /41/ and that the probability of return can be neglected. Then the diffusion coefficient D and the mean residence time can be determined by the following formulas

$$\frac{f}{f_0} = \frac{\tau_C}{\tau_C + \tau_N} \qquad (15)$$

$$\tau_C = 4\bar{\tau} \qquad (16)$$

$$D = \frac{a_0^2}{48\,\bar{\tau}} \qquad (17)$$

where f/f_0 is the relative fraction of the disturbed atoms normalized to the constant value f_0 at low temperatures. The factor 4 in (16) between the correlation time τ_c and the mean residence time $\bar{\tau}$ accounts for the fact that only one out of four jumps leads away from the probe, if tetrahedral sites are considered. Equation (15) gives the relation between D and for tetrahedral-tetrahedral jumps with a_0 as the lattice constant of Ta.

The results of this analysis are shown in Fig. 13. It can be seen that the diffusion coefficients are much larger than expected form an extrapolation of the published data /40/ with an Arrhenius function. On the other hand, the data are well represented by a T^7 temperature dependence as predicted by the small polaron hopping theory /42/ for low temperatures.

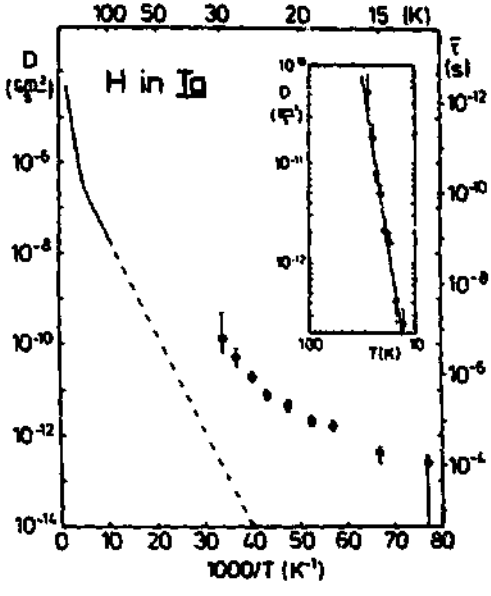

Fig.13: Diffusioncoefficients D and mean residencetime for H in Ta in the α-phase. The thick line represents the data of Ref. 40, the dashed line is an extrapolation assuming an Arrhenius law. In the insert the data are presented on a log-log scale. The solid line shows a T^7 law. /35/

6 Conclusion

The perturbed angular correlation (PAC) method has been used rather little in hydrogen physics so far. This has probably to do with the fact, that the method is still fairly complicated, although simple and standardized set-ups have been developed recently, and that it requires handling of radioactive materials. On the other hand, a rather large number of groups are familiar with the technique. However, they have not applied it to hydrogen problems yet.

Particularly promising are experiments in which the local structure around the probe atom is investigated. For example, hydrogen trapping at substitional impurities (probe atoms), can be investigated with very high precision and many details which are inaccessible by other methods can be studied. The advantage of PAC lies in the fact that different hydrogen configurations can be distiguished and that changes of the structure, e. g. as a function of temperature, can be detected. The diffusion studies described in Sect. 5.3 are probably impracticable at all with classical methods and can be performed only in the way described there. Although the number of systems to which this method can be applied is rather limited, it is nevertheless important that at least on one (or several) systems the principal behaviour of hydrogen diffusion at low temperatures can be studied. Experiments in this connection which are not performed yet, are the investigation of isotope effects and the search for coherent diffusion at very low temperatures. For this later case, the PAC method is well suited, since a localized hydrogen atom finds itself after the nuclear conversion in a pure lattice and the development of the wave function from this initial state can be studied.

Concerning structure studies, PAC as all local probe methods is inferior to diffraction measurements. However, local defects in ordered structures, in particular missing hydrogen atoms in hydrides, can be sensitively investigated. One can also obtain some information on the electronic structure of hydrides via the measured electric field gradient. The method is in principle surface sensitive, if the probe atoms are deposited at the surface, but no such experiments on hydrogen systems were performed yet.

References

* Modified version of an article to be published in " Hydrogen in Intermetallic Compounds ", ed. by L. Schlapbach (Springer Verlag, Heidelberg, Berlin, New York)

1 E. Recknagel, G. Schatz, and Th. Wichert: in Hyperfine Interactions of Radioactive Nuclei, ed. by J. Christiansen, Topics in Current Physics, Vol. 31, (Springer, Berlin, Heidelberg, New York, 1983) p. 133

2 L. Niesen: Hyp. Int. 10, 619 (1981)

3 H. Frauenfelder and R.M. Steffen: In Alpha-, Beta-, and Gamma-Ray Spectroscopy, Vol. 2, ed. by K. Siegbahn (North-Holland, Amsterdam, 1965) p.997

4 K. Alder, H. Albers-Schönberg, E. Heer and T.B. Novey : Helv. Phys. Acta 26, 761 (1953)

5 H.H. Rinneberg: Atomic Energy Review 17, 477 (1979)

6 A. Weidinger: J. Less-Common Met. 103, 285 (1984)

7 C.M. Lederer and V.S. Shirley (eds.): Table of Isotopes, 7th edition, (John Wiley & Sons, Inc., New York, 1978)

8 T. Butz and A.Lerf: Phys. Lett. 97A,217 (1983)

9 R. Vianden: Hyp. Int. 15/16, 1081 (1983)

10 Nuclear Data Sheets 9, 337 (1973)

11 Nuclear Data Sheets 11, 312 (1974)

12 Nuclear Data Sheets 6, 65 (1971)

13 Nuclear Data Sheets 12, 466 (1974)

14 J. S. Evans and R. A. Naumann: Phys. Rev. 136, B1017 (1965)

15 F.D. Feiock and W.R. Johnson: Phys. Rev. 187, 39 (1969)

16 J. Trager, M. Karger, T. Butz and F.E. Wagner: Hyp. Int. 15/16, 795 (1983)

17 P.J. Mendes, J.M. Gil, N. Ayres de Campos, R. Peichl, and A. Weidinger: Hyp. Int. 15/16, 791 (1983)

18 T. Schober and H. Wenzel: in Hydrogen in Metals, Vol.2, ed. G. Alefeld and J. Völkl (Springer Verlag, Berlin, Heidelberg, New York), p.36

19 V.F. Petrunin, V.A. Somenkov, S.Sh. Shil'shtein and A.A. Chertkov: Sov. Phys.-Crystallogr. 15, 137 (1970)

20 H. Kaneko, T. Kajitani, M. Hirabayashi, N. Niimura, A.J. Schultz and P. Leung: J. Less-Common Met. 103, 45 (1984)

21 J. M. Gil, P. J. Mendes, C. Gil, A. P. de Lima, A. Weidinger, and N. Ayres de Campos: J. Less-Common Met. 103, 227 (1984)

22 R.L. Rasera, G.K. Shenoy, B.D. Dunlap, and D.G. Westlake: J. Phys. Chem. Solids 40, 75 (1079)

23 O. de O. Damasceno, A. L. de Oliveira, J. de Oliveira, A. Baudry and P. Boyer: Solid State Commun. 53, 363 (1985)

24 R. Heidinger, P. Peretto and S. Choulet: Solid State Commun. 47, 383 (1983)

25 R. Heidinger, P. Peretto and S. Choulet: Hyp. Int. 15/16, 787 (1983)

26 P. Vulliet, G. Teisseron, J. L. Oddou, C. Jeandey and A. Yaouanc: J. Less-Common Met. 103,

27 A. Magerl, J. J. Rush, J. M. Rowe, D. Richter and H. Wipf: Phys. Rev. B 27, 927 (1983)

28 R. Peichl, A. Weidinger, E. Recknagel, J. M. Gil, P. J. Mendes and Ayres de Campos: Hyp. Int. 15/16, 463 (1983)

29 G. Pfeiffer and H. Wipf: J. Phys. F6, 167 (1976)

30 P.J. Mendes, J.M. Gil, N. Ayres de Campos, R. Peichl and A. Weidinger: Z. Phys. Chem., Neue Folge, to be published

31 H. Kronmüller and P. Varges: Philos. Magn. A51, 59 (1985)

32 G. Cannelli, R. Cantelli, and G. Vertachi:
Appl. Phys. Lett. 39, 832 (1981)

33 A.I. Shirley, C.K. Hall: Acta Metall. 32, 49 (1984)

34 R. Peichl, A. Weidinger, and P. Ziegler:
Z. Phys. Chem., Neue Serie, to be published

35 A. Weidinger and R. Peichl:
Phys. Rev. Lett. 54, 1683 (1985)

36 K.W. Kehr: in Hydrogen in Metals I, Topics in Applied Physics, Vol. 28, ed. G. Alefeld and J. Völkl (Springer, Berlin, 1978), p. 197

37 K.W. Kehr: Hyp. Int. 17 - 19, 63 (1984)

38 D. Richter: in Neutron Scattering and Muon Spin Rotation, Springer Tracts in Modern Physics, vol. 101, ed. G. Höhler (Springer, Berlin, 1983), p. 85

39 A. Seeger: Hyp. Int. 17 - 19, 75 (1984)

40 Zh. Qi, J. Völkl, R.Lässer and H. Wenzel, J. Phys. F.: Met. Phys. 13, 2053 (1983)

41 E. Yagi, T. Kobayashi, S. Nakamura, Y. Fukai, and K. Watanabe: J. Phys. Soc. Japan 52, 3441 (1983)

42 C.P. Flynn and A.M. Stoneham: Phys. Rev. B1, 3966 (1970)

Impurities and defects in silicon studied with Mössbauer spectroscopy and perturbed angular correlation.

G.J. Kemerink
Laboratorium voor Algemene Natuurkunde and Materials Science Centre,
University of Groningen, The Netherlands

Tellurium implanted and laser annealed silicon was studied using ^{119}Sn, ^{121}Sb, ^{125}Te and ^{129}I-Mössbauer spectroscopy. It is concluded that Te is mainly incorporated on substitutional sites and that the various daughters, with the exception of Sn, may occur in more than one charge state. Different charge states are characterized by different isomer shifts and Debye Waller factors. In the case of I one state is observed that shows quadrupole interaction at low temperature that vanishes above 60 K. The disappearance of the splitting is accompanied by a highly anisotropic recoilless fraction.

For ^{111}In implanted and laser annealed silicon two defects with <111> symmetry are observed. These defects, and a third one with the same <111> symmetry, are also produced by 2 MeV proton bombardment. They dissappear around 400 K, corresponding to a dissociation energy of about 1.0 eV. The defects are attributed to the In-vacancy pair that can either occur in different charge states or is decorated with hydrogen.

1. Introduction

Basic to the construction of semiconductor devices is the modification of the electrical properties of the intrinsic material by suitable dopants. The behaviour of the commonly used shallow dopants is well understood. Less well understood are the properties of impurities that introduce levels that do not lie close to the valence or conduction band. This holds a fortior. when the impurities are associated with lattice defects.

In this paper the application of Mössbauer spectroscopy and perturbed angular correlation (PAC) in this field of research is demonstrated for two

systems studied in recent years in Groningen [1-3]. One system is Te implanted Si, using ^{119}Sn, ^{121}Sb, ^{125}Te and ^{129}I-Mössbauer spectroscopy. The other is ^{111}In implanted Si using perturbed angular correlation of the γ-γ cascade in the ^{111}Cd daughter. In both cases the Si is laser annealed after implantation.

It will be shown that Mössbauer spectroscopy can reveal specific properties of deep level states of substitutional impurities. For instance, the effect of a change in charge state affects the electron density at the nucleus and the bonding of the impurity to the lattice and will thus be revealed by a change in isomer shift and recoilless fraction. The presence of quadrupole interaction points to a deviation from cubic symmetry. Using single crystals, detailed information can be obtained about dynamical aspects of relaxation processes as will be shown for I in Si. Since in all cases a parent isotope of the same species, namely Te, was incorporated in the Si, the same impurity site is involved for all Mössbauer probes. After laser annealing this is the substitutional site as was deduced from channeling. Moreover, this site assignment is confirmed by the results to be presented.

In a cubic nonmagnetic host perturbed angular correlation can only show the lowering of the symmetry of the ^{111}Cd probe site. When defects are involved they often can be flagged with a unique quadrupole interaction frequency and, using single crystals, the main axes of the quadrupole interaction tensor can be determined. Together with other information this leads us to the conclusion that the basis defect, after laser annealing, and also after proton irradiation, is the In-vacancy pair.

2. Sample preparation

The starting material in the investigations was n- or p- type floating zone refined single crystalline silicon with a specific sensitivity between 1 and 20 Ωcm. The orientation was mainly <100>, in a few cases <111>. To obtain a wider range of n- or p-type doping levels part of the samples was implanted with P or B prior to use.

The radioactive probe atoms $^{119(m)}$Te, ^{125}Te and ^{129m}Te for Mössbauer spectroscopy and ^{111}In for PAC, were implanted at an energy of about 110 keV using the Groningen isotope separator. ^{121}Te was introduced by implanting the short lived ^{121}Xe, that decays through ^{121}I to ^{121}Te, at 60 keV with the ISOLDE facility [4]. Partial decay schemes relevant to the

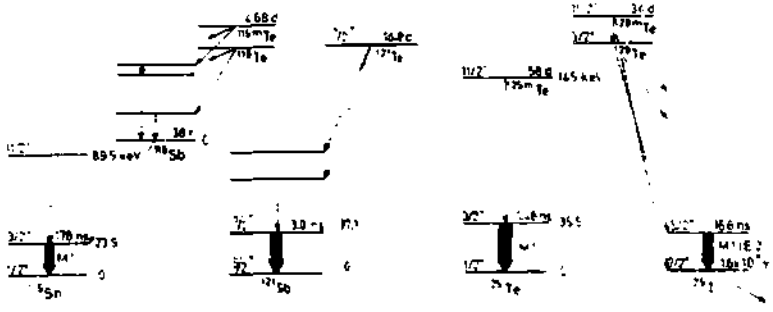

Fig. 1. Partial decay schemes of four radioactive Te isotopes used in this investigation, with an indication of the characteristic properties of the low energy gamma transitions used for Mössbauer spectroscopy.

Mössbauer work are shown in Fig. 1.

The implanted samples were annealed with a pulsed ruby laser with a pulse duration of approximately 30 ns and pulse energy densities of 1.5 - 1.9 J/cm². This results in the melting of a surface layer of about 2500 Å which resolidifies epitaxially, yielding high substitutionality in the case of Te as was first shown by Foti [5]. Some of our own channeling and Rutherford backscattering results that illustrate this behaviour are shown in figures 2 and 3 [6].

In the case of In implanted Si part of the In is incorporated on lattice sites while another part (50-70% under our conditions) segregates at the Si-surface [7-9]. This surface layer was removed using the anodic oxidation technique. Laser annealing also results in the complete electrical activation of co-implanted B- and P-impurities [10].

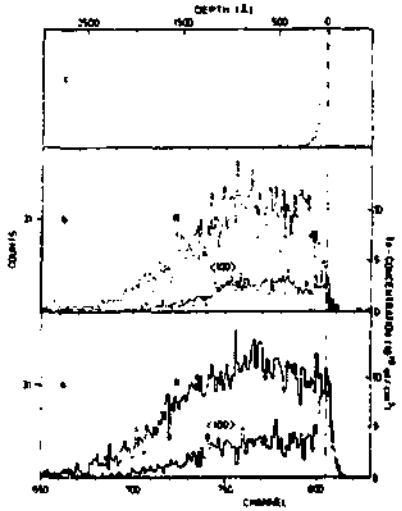

Fig. 2.

Spectra of 2 MeV He^+-ions backscattered from Te-impurities over 105° and emerging under an angle of 15° with the surface (to increase depth resolution).

a: Laser annealed Si-crystal

b: Same after removing of 175 Å Si

c: Layer of about 1 µg Te/cm² evaporated on surface.
<100>: beam along <100> axis,
R: random beam direction

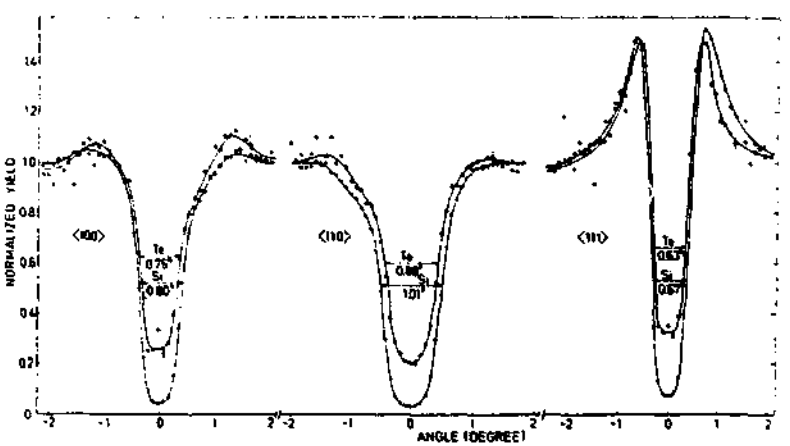

ig. 3. Angular dependence of backscatter yield from Te (Δ) and Si (0) atoms in a laser annealed Si crystal implanted with 1.1 x 10^{15} at.Te/cm². Substitutional fractions derived from minimum yields are 82± 6% for the <100>, 85 ± 6% for the <110> and 92 ± 6% for the <111> string.

3. Results from Mössbauer spectroscopy

3.1. ^{119}Sn impurities in Si

Laser annealed samples, containing 2-4 x 10^{13} at. Te/cm², (including the 4.7 day ^{119m}Te activity that decays to ^{119}Sn through ^{119}Sb) and 2 x 10^{15} at. P/cm², 2 x 10^{15} at. B/cm², or no further doping all yield single line Mössbauer spectra. Isomer shifts (S) and line widths (Γ) derived from these spectra are collected in Table 1.

Table 1.

Te-dose (cm^{-2})	B or P dose (cm^{-2})	Si-type	S[a] (mm/s)	Γ (mm/s)
$2x10^{13}$	$2x10^{15}$P	n^+	1.80(5)	1.12(3)
$4x10^{13}$	-	(n)	1.77(5)	1.12(3)
$2x10^{13}$	$2x10^{15}$B	p^+	1.78(5)	1.11(3)

a) relative to $BaSnO_3$ absorber. T_{meas} = 4.2 K

No differences in S and Γ are observed. The Γ-value is the same as found for a standard single line source of $Ba^{119m}SnO_3$. This observation indicates one unique site of cubic symmetry for the Sn atoms independent of doping. The isomer shift agrees with that observed earlier for substitutional Sn in Si and excludes defect association of the implanted Te-impurities. This conclusion could not be drawn with the same certainty from the channeling experiments alone.

3.2. ^{121}Sb impurities in Si

Samples were implanted at ISOLDE with short lives ^{121}Xe to a dose of $\leq 1*10^{14}$ at/cm² [13]. After the decay of ^{121}Xe (39 min) via ^{121}I (2.1 h) to ^{121}Te (17 d) the Si-crystals were laser annealed. All spectra consisted out of a single line (table 2.) and a quadrupole split component whose

intensity varied between 6 and 20% of the total absorption area (fig. 4). The isomer shift of the split component amounts to - 0.24(4) mm/s with respect to GaSb, the splitting $|e^2qQ/h|$ = 245(60) MHz.

Table 2 shows that there exists a slight difference in isomer shift between n- and p-type samples. The shifts for the heavily doped n-type samples should correspond to neutral Sb, those for the p-type to Sb^+. From the difference in isomer shifts it is estimated that the electron density at the Sb nucleus is 0.7 a_o^{-3} higher for Sb^o than for Sb^+. Feher determined from ENDOR measurements a value of 0.2 a_o^{-3} for the donor electron contact density. These results are not necessarily conflicting since both methods do not probe the same quantity: Mössbauer spectroscopy gives the difference in total contact density between a state with and one without a donor electron, while ENDOR measures the difference in spin-up and spin-down contact density of the state with the donor electron. Electron - electron correlations can affect these quantities in a different way.

Table 2.

B-dose (cm^{-2})	Si-type	S (mm/s)	P-dose (cm^{-2})	Si-type	S (mm/s)
$5x10^{14}$	p^+	0.47(5)	$5x10^{14}$	n^+	0.17(5)
$1x10^{15}$	p^+	0.37(3)	$2x10^{15}$	n^+	0.19(3)
$2x10^{15}$	p^+	0.41(6)	$2x10^{15}$	n^+	0.16(6)

Shift S with respect to GaSb. T_{meas} = 4.2 K. Te-dose $\lesssim 1x10^{14}/cm^2$. Linewidth Γ fixed to 3.2 mm/s.

3.3. ^{125}Te impurities in Si

As in the previous case, the Te activity (60 day ^{125m}Te) was implanted in Si-crystals doped with P or B, yielding n^+, p^+ and compensated type silicon after annealing. A higher Te-dose ($\sim 5x10^{14}/cm^2$) was required because

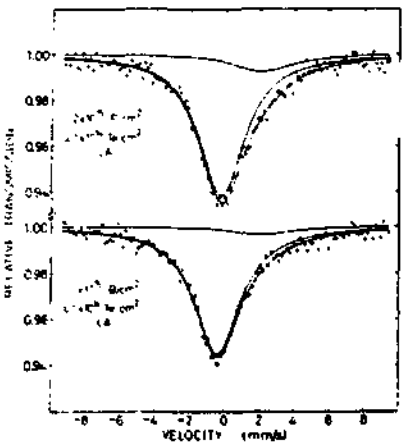

Fig. 4.

Mössbauer spectra of the 37.1 keV gamma line of ^{121}Sb for laser annealed TeSi measured at 4.2 K with GaSb absorber.

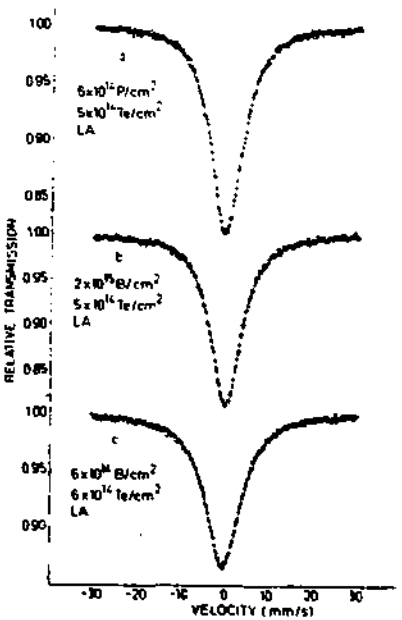

Fig. 5.

Mössbauer spectra of the 35.5 keV gamma line of ^{125}Te for laser annealed TeSi measured at 4.2 K with SnTe absorber:

a. n^+ type Si

b. p^+ type Si

c. compensated Si.

of the low specific activity.

A. Isomer shifts

In Fig. 5., some of the Mössbauer spectra are shown. Each again consists of a single line, but now there are differences in isomer shift. In table 3

parameters derived from least squares fits of Lorentzian lines to these spectra are given. Though the line shifts are only small fractions of the line width, there is a clear difference of the isomer shifts for the n^+ and p^+ samples, from 0.14 to -0.13 mm/s. A crystal with only Te gives essentially the same shift as the P-doped crystal. Both are n^+-type crystals, as follows from our Hall-effect measurements.

Table 3.

Te-dose (cm^{-2})	B or P dose (cm^{-2})	Si-type	S[a] (mm/s)	Γ (mm/s)
$5x10^{14}$	$6x10^{14}$P	n^+	0.14(1)	8.60(4)
$5x10^{14}$	$2x10^{15}$B	p^+	-0.13(1)	8.43(4)
$6x10^{14}$	$6x10^{14}$B	comp	0.06(1)	9.54(4)
$6x10^{14}$		(n^+)	0.16(1)	8.44(4)

a) relative to SnTe absorber. T_{meas} = 4.2 K

The result for p^+ and n^+-type silicon can be understood by realizing that different charge states of the Te configuration are formed for different positions of the Fermi level, determined by the doping of the silicon. This is corroborated by the existence of two levels of Te within the bandgap, at E_c-0.20 eV and E_c-0.41 eV (E_c is the energy of the bottom of the conduction band) as found by Grimmeis et al. [15] and by Lin et al. [16].

In the n^+-type samples (see table 3.), the Fermi level is very close to the conduction band and we expect the level at E_c-0.20 to be filled, making the Te neutral. In the p^+-type sample on the other hand, the Fermi-level is close to the valence band and the Te-atoms should be doubly ionized, in agreement with the findings just mentioned and, in general, with the double donor character of a group VI element. It is to be noted that the Fermi level and

the temperature determine the equilibrium charge state of an impurity. This does not imply, however, that this charge state will be realized during the short lifetime of the Mössbauer level. At low dopant concentrations and at low temperatures the electrons and holes are localized on the donor and acceptor atoms, respectively. Trapping of such a charge carrier by a probe atom can only occur when it is sufficiently close. This implies that high doping levels, where strong delocalization of carriers occurs, are in general required to enable changes in the charge state of levels in the band-gap. Figure 6 shows some characteristics of heavily P-doped Si. As an example let us consider the process $Te^{+} + e \rightarrow Te^{0}$. The time required for trapping a charge carrier can be written as $\tau = \sigma n v$, with σ the trapping cross section, n the carrier concentration and $v = \sqrt{3kT/m^{*}}$ the thermal velocity. When we assume that the electron trapping cross section [17] of 3×10^{-15} cm^2 found for $Se^{+} + e \rightarrow Se^{0}$ is a good estimate for the corresponding process in Te, then $\tau \approx 6$ ps for the P-doped sample. In this case it is seen that τ is indeed short compared to the nuclear lifetime of 1.5 ns.

This discussion also shows that it is probably difficult to measure Te^{+} in our experiments since it requires on the one hand that the Fermi level is between E_c -0.41 eV and E_c -0.20 eV and on the other hand a carrier concentration so high that the formation of Te^{+} occurs fast enough. The Mössbauer line observed for the compensated crystal is therefore probably due to the presence of more than one charge state and possibly transitions between these states [18].

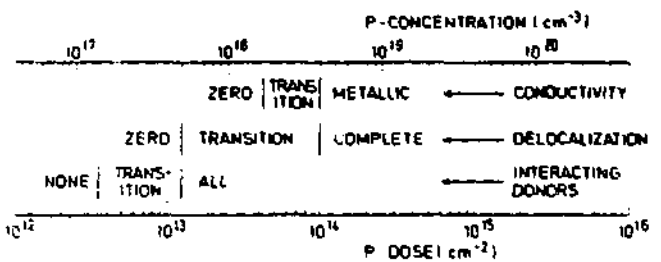

Fig. 6.

Some characteristics of heavily P-doped Si at low temperature (e.g. 4.2 K). The P-dose corresponding to a given P-concentration has been calculated assuming an impurity layer thickness of 2500 Å.

From the difference in isomer shift an increase $\Delta\rho(0) \approx 1..3\ a_o^{-3}$) follows for the contact electron density at Te^o relative to $Te^{+...}$: Thus, each electron contributes about $6a_o^{-3}$, only a small fraction of the density contributed by one s-electron ($\sim 60\ a_o^{-3}$) but of the same order of magnitude as observed for different chemical compounds with Te in the same oxidation state. This suggests a description of the $TeSi_4$ cluster with an M.O.-model, assuming that only the 5s- and 5p-electrons of the Te atom and sp^3 hydridized orbitals on the four tetrahedrally surrounding Si atoms participate in the bonding. A possible M.O.-level scheme is given in Fig. 7. In the neutral configuration two antibonding orbitals are filled. The observed isomer shifts can be explained if a 10-20% admixture of the 5s state is present in the A_1^* orbital. It must be remarked, however, that the simple M.O.-picture does not account for the effective mass-like excited states observed by Grimmeis et al. [15], who derived a contact density of 2.5 a_o^{-3} for one bound donor electron.

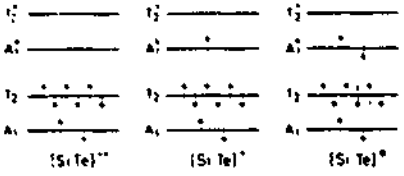

Fig. 7.

Possible M.O. energy level schemes for $TeSi_4$ clusters in different charge states. Orbitals indicated by stars are antibonding.

B. Recoilless fractions

The area of a Mössbauer absorption line is proportional to the recoilless fraction f(T) of the resonant gamma line. Since it is generally difficult to calibrate this area directly in terms of f, the dependence of the absorption area on T is frequently measured. Assuming validity of the Debye model, a Debye temperature can then be determined by fitting the measured area vs T dependence to a Debye model curve. This has been done in Fig. 8. for

Mössbauer spectra of ^{125}Te implanted in p^+ type and n^+-type silicon measured in a range of temperatures from 4-280 K. The decrease for the p^+-type is clearly slower than for the n^+-type, yielding a higher effective Debye temperature $\theta' = 232(3)$ K for the Te^{++}-ion than for the Te° atom ($\theta' = 207(3)$ K). It is interesting to observe such a clear charge dependence of θ'. A plausible explanation of this phenomenon is the following. It is well-known in chemistry that the binding energy (U) between atoms strongly depends on the difference in the number of bonding (n_b) and antibonding orbitals (n_{ab}); in first approximation: $U \propto (n_b - n_{ab})$. The impurity-host force constant $\gamma = -dU/dx$ and the effective Debye temperature $\theta' \propto \gamma^{\frac{1}{2}}$ therefore decreases with increasing n_{ab}.

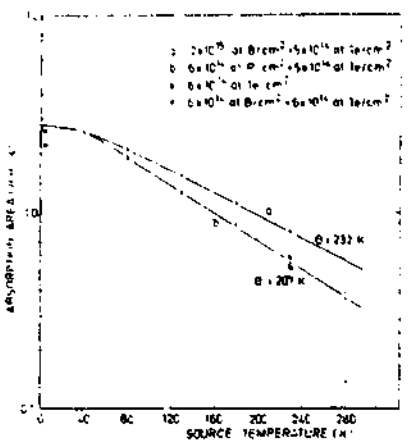

Fig. 8.

Absorbtion areas of ^{125}Te Mössbauer spectra of laser annealed TeSi crystals as a function of source temperature. Plots have been fitted to Debye model curves.

a. p^+-type Si

b. n^+-type Si

3.4. ^{129}I impurities in Si

Samples of n^+, compensated and p^+-type silicon, implanted with the 30 day ^{129m}Te activity and suitable concentrations of B or P dopants and subsequently laser annealed were used as sources for Mössbauer spectroscopy of the 27.8 keV transition in ^{129}I. The results of measurements at 4.2 K are shown in Fig. 9. Large differences in the spectra are found. In all cases there

are at least two components. The isomer shifts of the large components are quite different and a pronounced quadrupole splitting appears for ^{129}I in n^+-type silicon. The values of the parameters derived from the spectra are collected in Table 4. Apparently, the observed isomer shift differences must again be attributed to charge state dependent effects, but the appearance of a strong quadrupole splitting in the P-doped crystal is puzzling at first, since the Te-parent activity is known to be substitutional and therefore has a cubic environment. We shall discuss the isomer shift, quadrupole splitting and recoilless fraction results separately.

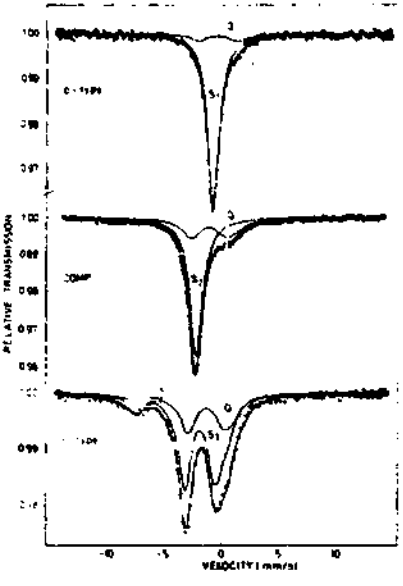

Fig. 9.

^{129m}Te Mössbauer spectra of differently doped Si single crystals implanted with ^{129m}Te and subsequently laser annealed. Absorber Cu^{129}I, temp. 4.2 K.

Top: 2×10^{15} at.B/cm^2, 2.2×10^{14}at.Te/cm^2

Middle: 6×10^{14}at.B/cm^2, 6×10^{14}at.Te/cm^2

Bottom: 2×10^{14}at.P/cm^2, 1.4×10^{14}at.Te/cm^2.

A. Isomer shifts

The isomer shifts of the main spectral components, designated as S_1 for p^+-type, S_2 for compensated and S_3 for n^+-type are given in Table 4. It is seen that, just as in the case of ^{125}Te, the shift increases when going from p^+-type to n^+-type silicon, and to compensated silicon. The difference in isomer shift between S_1 and S_2 corresponds to a contact

Table 4.

Te-dose (cm^{-2})	B or P dose (cm^{-2})	Si-type	compo-nent	S[a] (mm/s)	ΔE_Q (MHz)	θ' (K)
2.2×10^{14}	2×10^{15} B	p^+	S_1	0.94(1)		196(3)
			Q	1.3(1)	550(20)	
6×10^{14}	6×10^{14} B	comp.	S_2	2.34(1)	-	170(3)
			Q	1.7(1)	550(-0)	
1.4×10^{14}	2×10^{14} P	n^+	S_3	2.15(4)	452(8)[b]	155(7)[c]
			Q	1.4(1)	550(20)	

a) relative to $Cu^{129}I$ absorber; b) at 4.2 K; c) see also text.

density increase $\Delta\rho(0) = 6.8(1.0)a_o^{-3}$ that between S_2 and S_3 to a decrease of $-1.1(2)a_o^{-3}$. Such a behaviour can be explained by supposing that the charge state for iodine impurities in p^+-type silicon is I^{++}, for compensated I^+ and for n^+-type I^0. As in the case of ^{125}Te, the shift changes are small compared to the contribution of on e 5s electron in atomic iodine which amounts to $\Delta\rho(0)_{5s} \sim 70a_o^{-3}$. As in that case we assume a M.O. picture with electrons filling the antibonding orbitals, the T_2^* orbital being higher in energy than the A_1^* orbital (Fig. 10.). The addition of an electron to the A_1^* orbital ($I^{++}\rightarrow I^+$) leads to an increase of density because of the partial s character of this orbital. The next electron ($I^+\rightarrow I^0$) fills a T^* orbital which leads to a decrease of the total s density because it screens the nucleus to some extent and has no s character of its own. The influence of this screening on the s density agrees quantitatively with that found for many iodine compounds.

Self consistent Hartree Fock calculations were performed by P. Aerts of the department of chemical physics of our University on ISi_4H_{12} clusters. These yield contact density differences $\Delta\rho(0) = 20a_o^{-3}$ for $I^{++}\rightarrow I^+$ and

$\Delta\sigma(0) = -5a_o^{-3}$ for $I^+ \rightarrow I^o$ (using the level filling scheme of Fig. 10.).

Crystals showing components I^{++} and I^+ were recently measured at 4.2 K in an external field of 2.7 Tesla. In neither case a magnetic hyperfine field expected from a polarized paramagnetic electron was observed. This seems to be conflicting with the interpretation of component I^{++} presented above: either the charge state or the proposed electronic configuration of Fig. 10. must be incorrect.

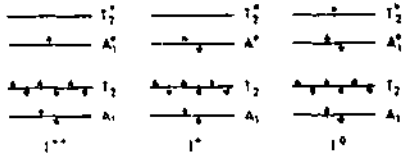

Fig. 10.

Possible M.O.-energy level schemes for different charge states of an ISi_4 cluster consisting of an iodine atom tetrahedrally surrounded by four Si-atoms. Only 5s and 5p I-orbitals and sp^3-hybridized Si-orbitals have been used.

B. Quadrupole split components

In all spectra, a quadrupole split component, designated as Q, is observed, which has a large quadrupole coupling ($\Delta E_Q = eQV_{zz}/h = 550$ MHz). Its relative intensity is less than 25% in most cases. The values of S and ΔE_Q hardly depend on temperature. It is thought that this component is due to strained regions in the crystal where the I-atoms reside in static Jahn Teller distorted states.

The component S_3 is only found in strongly n type silicon, where the iodine is supposedly in the neutral state. There, S_3 is predominant and its quadrupole coupling constant, $eQV_{zz}/h = 452$ MHz at 4.2 K, again indicates a considetable distortion from cubic symmetry, comparable to that of

component Q. Component S_3 has some remarkable properties. In the first place its quadrupole pattern depends strongly on the temperature of the source, as shown in Fig. 11. It experiences a gradual collapse to a single line in the temperature region from 4.2. K to 80 K. Further, the intensity of this single line depends strongly on the angle of emission of the gamma rays relative to the crystal axes. This is also shown in Fig. 11.: the line intensity is much higher for gamma-rays emitted parallel to the <111>-axis than to the <110>-axis. This anisotropy only occurs at source temperatures where the spectrum has collapsed to a single line and it is not seen for component Q. This is demonstrated in Fig. 12, where the intensity of the spectral components S_3 and Q are given for three different gamma directions at some temperatures between 80 K and 200 K.

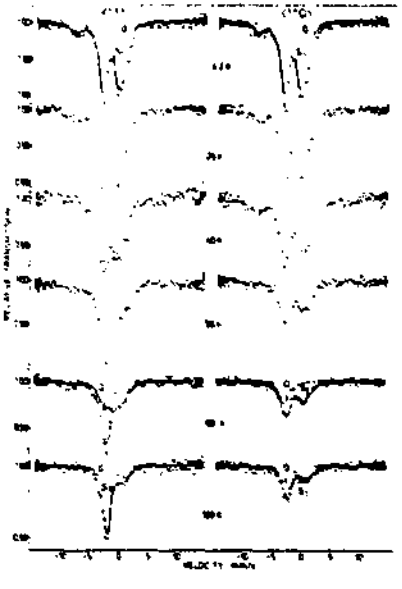

Fig. 11.

^{129}I Mössbauer spectra from a laser annealed Si-crystal of n^+-type for various temperatures. Gamma rays emitted along the <111>-axis (left) or along the <110>-axis (right). $Cu^{129}I$ absorber kept at 4.2 K.

A last feature that is of importance for the interpretation of the observed phenomena is that the e.f.g. deduced from the quadrupole spectra of S_3 is essentially axially symmetric ($\eta \approx 0$) and has a negative sign. This is

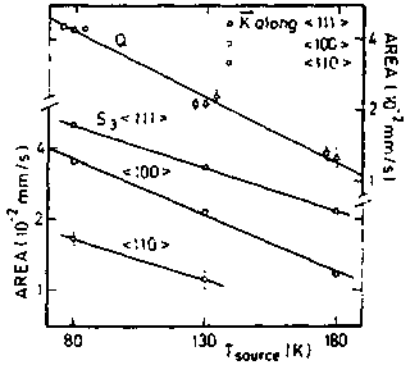

Fig. 12.

Measured absorption area of the relaxing component S_3 and of the non-relaxing split component Q as a function of temperature for directions of observation of the γ-rays along <111>, <100> and <110> crystal axes.

consistent with a trigonal distortion through which the iodine atoms have shifted along a <111>-axis towards three nearest Si-neighbours.

C. Origin of quadrupole relaxation and anisotropic recoilless fraction of component S_3.

In section 3.4.A. we attributed the spectral component S_3 to neutral iodine atoms that have one electron in the T_2^* molecular orbital. In contrast to the A_2^* level this state is orbitally degenerate. Such a state may exhibit a Jahn Teller distortion. The most probable distortion of the tetrahedral complex is trigonal and such a distortion is indeed revealed by the character of the quadrupole interaction found at very low temperatures. The collapse of the spectrum at increasing temperatures indicates a transition of the Jahn-Teller distortion from static to dynamic, with the iodine atoms jumping between four possible equivalent sites on the <111>-axes (see Fig. 13B.). The theory of the spectral shape in the transition region between slow and fast relaxation is very involved, it was not tried therefore to fit the experimental spectra in this region to calculated ones. Thus, only a rough estimate, 20±10 meV, can be given for the activation energy of the jump process.

The anisotropy of the recoilless fraction observed at temperatures where

the relaxation process is fast ($T \geq 80$) can also be attributed to the jumping of iodine atoms between four equivalent sites. A general theory of Mössbauer spectra of atoms that diffuse by jumping through a lattice has first been given bij Singwi and Sjölander [19]. For the special case encountered here, where the atom jumps between a limited number (N) of different positions and in the limit of fast relaxation, their expression for the recoilless fraction reduces to [20]:

$$f = f(T).f_J = f(T) \left| \frac{1}{N} \sum_{n=1}^{N} e^{i\vec{k}.\vec{R}_n} \right|^2 \qquad (1)$$

The "jump Debye-Waller factor" f_J is the squared sum of the amplitudes of coherent emitters on N equivalent positions, with phases given by $\vec{k}.\vec{R}_n$. Here $\vec{k}$ is the wave vector of the gamma rays and $\vec{R}$ the displacement vector of the iodine atoms. $\Delta = |\vec{R}|$ is the absolute displacement from the centre of the tetrahedron. In Fig. 13A. results are shown of calculations of $f_J(\vec{k},\Delta)$ for the jumping process indicated in Fig. 13B., with $\vec{k}$ along the three crystal axes for which measurements were performed.

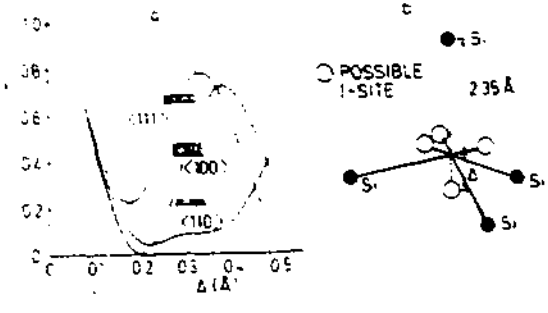

Fig. 13.

a. Jump Debye-Waller factor f_J as a function of I-displacement Δ for directions of observation of γ-rays along the <111>, <100> and <110> crystal axes. Hatched areas indicate experimental values for a source with 2×10^{14} at.P/cm² and 1.4×10^{14} at.Te/cm².

b. Possible I-sites in a trigonally distorted tetrahedron.

Experimental f_J values for one particular source are given by hatched areas. We see that for $\Delta \sim 0.3$Å good agreement is obtained in the <111> and <100> direction but that the experimental f_J value for the <110> direction is too high. It must be remarked, however, that different experimental f_J values

are found for different crystals and temperatures, suggesting that the model represented by Eq. (1) is an oversimplification. The agreement of the model with experiment is better, however, for a trigonal distortion than for a tetragonal one. We can say that the experimental facts can largely be understood on its basis, assuming $\Delta \sim 0.25$–0.35 Å, but that the distortion may be more complicated than assumed for the model.

D. Charge state dependence of the recoilless fraction

In the same way as for the Te implanted samples discussed under 3.3B. the recoilless fractions of substitutional iodine and therefore the characteristic temperatures θ' decrease as the antifonding orbitals are filled (see Table 4.).

4. Results from perturbed angular correlation studies

^{111}Cd in Si

After implantation of ^{111}In, the samples were annealed by irradiation with a Q-switched ruby laser with a pulse width of 25 ns and an energy density of 1.6 J/cm² per pulse. It is known [7-9] that by this procedure indium atoms can be introduced at substitutional lattice positions to concentrations far beyond the solid solubility limit of 2×10^{18} cm^{-3} [21]. It is also known that a significant number of indium atoms segregate at the surface [7-9]. To remove them, a layer of about 60 Å was stripped by means of the anodic oxidation technique, which caused a loss of implanted radioactivity of about 50–70%.

The γ-rays emitted in the decay of ^{111}In were measured with a four-detector coincidence set-up, each detector consisting of a 30 mm x ϕ 44 mm BaF_2 scintillation crystal mounted onto a XP2020Q photomultiplier tube. The achieved time resolution, about 700 ps FWHM, makes it possible to observe QI frequencies up to 3 Grad/s.

The experimental perturbation factor was determined in the standard way [22] by calculating a double-ratio R(t) from the four measured coincidence

time spectra. The QI frequencies were derived either from the Fourier transform of R(t), or by fitting R(t) with a sum of cosine functions. Fig. 14. shows a typical result obtained at room temperature from p-type, <100> silicon (FZ, 2-5 Ωcm) with an estimated indium concentration of $<3\times10^{16}$ cm^{-3}. There are three different defects that give rise to QI frequencies of 328, 418 and 433 Mrad/s (the defects will be labelled accordingly as # 328, # 418 and # 433). The same defects were created by bombarding the sample at 300 K with 2 MeV protons to a dose in the range from 10^{15}-10^{16} cm^{-2}. Under suitable conditions, however, # 418 becomes the dominant defect. The following properties emerge from our PAC measurements.

The defects show equal thermal stability: in a 15 min isochronal annealing sequence they disappear in the temperature range from 100 - 160°C (Fig. 15.)

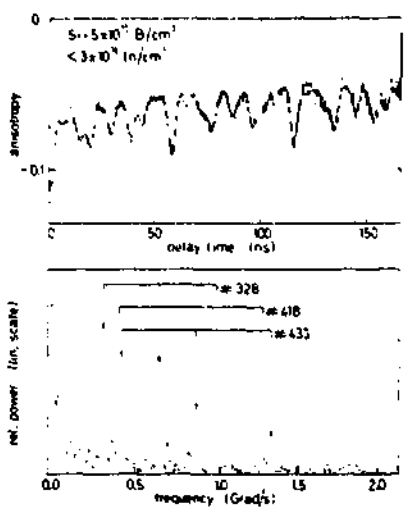

Fig. 14.

a. PAC spectrum R(t) obtained at 300 K from laser-annealed p-type <100> silicon (FZ, 2-5 Ωcm) with an estimated indium concentration of less than 3×10^{16} cm^{-3}.

b. Fourier transform of R(t). The three set of modulation frequencies correspond with the defects # 328, # 418 and # 433, respectively.

Each gives rise to an axially symmetrical EFG tensor with the main principal axis oriented along the <111> crystallographic direction. Therefore, the three defects are closely related. Their symmetry properties suggest that they are due to trapping of a point defect at a nearest neighbour position. To investigate this further, we studied samples with different concentrations

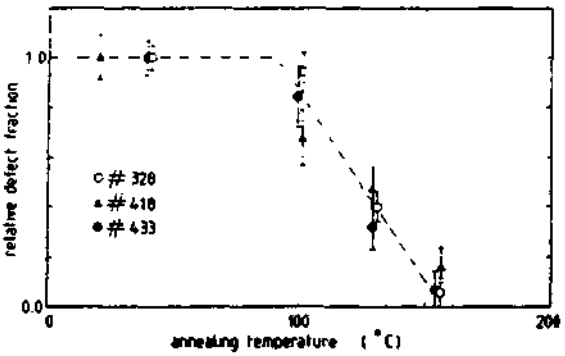

Fig. 15.

Annealing behaviour of # 328, # 418 and # 433.

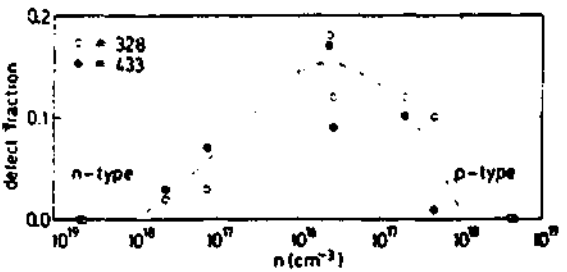

Fig. 16.

Defect fractions for # 328 and # 433 at 300 K as a function of dopant concentration, after laser annealing.

of group III (B, In) or group V (P, As) elements. The following results were obtained.

In laser-annealed p-type silicon, # 328 is the dominant defect (for an indium concentration of about 5×10^{17} cm^{-3} it may even be the only defect present), whereas the formation of # 433 is slightly enhanced in n-type silicon (Fig. 16.). A similar observation was made in the case of proton bombarded p-type silicon, while in compensated or n-type silicon # 418 is dominant instead of # 433. One can observe a reversible transformation of # 433 into # 328 by changing the temperature of the sample, as shown in Fig. 17. These results prove that the same point defect is involved in the formation of # 328, # 418 and # 433.

It should be noted that the defect is trapped by the radioactive atom

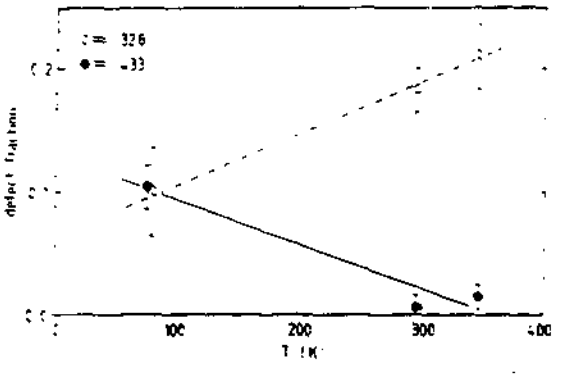

Fig. 17.

Defect fractions for # 328 and # 433 as a function of sample temperature.
Sample: laser-annealed p-type <100> silicon (FZ, 2-5 Ωcm) with an estimated indium concentration of 5×10^{16} cm^{-3}.

^{111}In, whereas the QI is observed on the daughter ^{111}Cd. The electron capture decay of ^{111}In to ^{111}Cd may result in three different charge states of the Cd-defect complex, each correponding with one of the observed QI frequencies. According to this interpretation, the transformation of # 433 into # 328 is due to hole trapping after the nuclear decay.

To check whether the defect is one of the common contaminations of silicon, we co-implanted some samples with either D, C, O or Fe. Deuterium, implanted at 15 keV to a dose of 1×10^{15} at/cm^2 had no influence on the fractions of # 328 and # 433. In the other samples, all implanted to a dose of 3×10^{13} at/cm^2, the above QI frequencies were not observed.

The major intrinsic point defect in laser-annealed silicon is believed to be the lattice vacancy. Therefore, the defect observed in the PAC experiments is most likely a ^{111}In atom that has trapped one of these vacancies. This interpretation is consistent with the symmetry of the defect complex. If the complex dissociates in a single-jump process, we can write the dissociation energy in the form (neglecting entropy factor and the like): $E^d = kT \ln \nu$. By putting the dissociation temperature $T \simeq 400$ K (see Fig. 15.) and the attempt frequency $\nu \simeq 10^{13}$ s^{-1}, we find $E^d \simeq 1.0$ eV, which is similar to the dissociation energy observed for other impurity-vacancy pairs in silicon [23-27]. Defect formation by proton bombardment is possible because the vacancy in each of its charge states is mobile at room temperature.

Wichert and Deicher recently found # 328 and # 433 after exposure of a sample to a H-plasma discharge or to boiling water. This might indicate

that H is involved in these defects, e.g. that the In-vacancy pair is decorated with H.

Impurity-vacancy interactions in silicon are controlled by Coulomb forces and, eventually, by the strain field around the impurity. The latter will lead to trapping of vacancies that are within a certain trapping radius. Vacancies migrate as V^{2+} in p-type silicon and as V^{2-} in n-type silicon [29], whereas the acceptor indium will be negatively charged in either type. Therefore, Coulomb attraction will enhance the formation of In-V in p-type silicon but not in n-type silicon, in accordance with the results of the PAC experiments (Fig. 16.). The fact that no In-V complexes are formed if the dopant concentration exceeds 10^{18} cm^{-3} implies that both P and B impurities act as competitive trapping centres for vacancies at room temperature.

From the observed defect fractions (see Fig. 16.) and the known dose of implanted indium atoms, the absolute number of In-V pairs can be deduced. Numbers as large as $1x10^{12}$ cm^{-2} are obtained in this way. Assuming that all vacancies in the melted silicon layer were trapped at the indium atoms and taking the width of this layer to be $2x10^{3}$ Å for the present laser condition conditions [6], we find a lower limit of about $5x10^{16}$ cm^{-3} for the vacancy concentration in laser-annealed silicon.

Conclusions

It was shown that in favourable cases Mössbauer spectroscopy can yield a great deal of information on the electronic and lattice dynamical properties of impurities in silicon. Different charge states, with different bond strength to the host, have been identified. For I an interesting deformation, static at low and dynamic at higher temperatures, could be studied in considerable detail.

With perturbed angular correlation the In-V defect was identified. This defect manifests itself in three different configurations. The difference is either due to a difference in charge state and/or decoration with hydrogen.

This work was performed as part of the research program of the "Stichting voor Fundamenteel Onderzoek der Materie" (FOM) with financial support from the "Nederlandse Organisatie voor Zuiver Wetenschappelijk Onderzoek" (ZWO)

References

1. G.J. Kemerink, H. de Waard, L. Niesen and D.O. Boerma, Hyperfine Interactions 14 (1983) 37.
2. G.J. Kemerink, H. de Waard, L. Niesen and D.O. Boerma, Hyperfine Interactions 14 (1983) 53.
3. G.J. Kemerink and F. Pleiter, accepted for publication in Phys.Lett. A.
4. H. Ravn, L.C. Carraz, J. Denimal, E. Kugler, M. Skarestad, S. Sundell and L. Westgaard, Nucl. Inst. Meth. 139 (1976) 267.
5. G. Foti, S.U. Campisano, E. Rimini and G. Vitaly, J. Appl. Phys. 49 (1978) 2569.
6. G.J. Kemerink, D.O. Boerma, H. de Waard and L. Niesen, Rad. Eff. 69 (1983) 83.
7. S. Kurnaev and E. Uggerhøj, Rad. Eff. 40 (1979) 91.
8. C.W. White, S.R. Wilson, B.R. Appleton and F.W. Young jr., J. Appl. Phys. 51 (1980) 738.
9. S.U. Campisano and J.M. Poate, Appl. Phys. Lett. 47 (1985) 485.
10. N. Natsuaki, M. Tamura and T. Tokuyama, J. Appl. Phys. 51 (1980) 3373.
11. A. Baldereschi and J.J. Hopfield, Phys. Rev. Lett. 28 (1972) 171.
12. H.P. Hjalmarson, P. Vogl, D.J. Wolford and J.D. Dow, Phys. Rev. Lett. 44 (1980) 810.
13. H. Andreasen, G.J. Kemerink, H. de Waard and G. Weyer, to be published.
14. G. Feher, Phys. Rev. 114 (1959) 1219.
15. H.G. Grimmeis, E. Janzén, H. Ennen, O. Schirmer, J. Schneider, R. Wörner, C. Holm, E. Sirtl and P. Wagner, Phys. Rev. B24 (1981) 4571.
16. A.L. Lin, A.G. Crouse, J. Wendt, A.G. Campbell and R. Newman, Appl. Phys. Lett. 38 (1981) 683.
17. H.G. Grimmeis, E. Janzén and B. Skarstam, J. Appl. Phys. 51 (1980) 3740.
18. E. Kankeleit and A. Körding, J. Phys. 37 (1976) C6-65.
19. K.S. Singwi and A. Sjölander, Phys. Rev. 119 (1960) 863.
20. G. Vogl, W. Mansel and P.H. Dederichs, Phys. Rev. Lett. 36 (1976) 1497.
21. S. Fischler, J. Appl. Phys. 33 (1962) 1615.
22. A.R. Arends, C. Hohenemser, F. Pleiter, H. de Waard, L. Chow and R.M. Suter, Hyperfine Interactions 8 (1980) 191.

23. G.D. Watkins, Phys. Rev. 155 (1967) 802.
24. E.L. Elkin and G.D. Watkins, Phys. Rev. 174 (1968) 881
25 G.D. Watkins, Phys. Rev. B12 (1975) 4383.
26 G.D. Watkins, Phys. Rev. B13 (1976) 2511.
27. A. Chantre, Phys. Rev. B32 (1985) 3687.
28. Th. Wichert and M. Deicher, private communication.
29. G.D. Watkins, A.P. Chatterjee and R.D. Harris, Defects and Radiation Effects in Semiconductors 1980, ed. R. Hasiguti (The Institute of Physics, London, 1981) p. 199.

ION IMPLANTATION OF Te AND I IONS IN Si AND GaAs STUDIED BY MÖSSBAUER SPECTROSCOPY, ION CHANNELING AND NUCLEAR ORIENTATION

G. Langouche
Instituut voor Kern- en Stralingsfysika, University of Leuven,
Celestijnenlaan 200 D, B-3030 Leuven, Belgium

1. INTRODUCTION

Hyperfine interaction studies of implanted radioactive atoms in semiconductors offer the possibility to study the microscopic neighbourhood of these atoms. Studies of this kind are of fundamental interest, as the different mechanisms that determine the final site of an impurity atom [1] are still not fully understood. The question whether there is really impact amorphization upon implantation, for example, is still a matter of discussion. The technological interest, on the other hand, in understanding the microscopic configuration of impurity atoms in semiconductors, is of course evident. This configuration will determine the macroscopic electrical transport behaviour and optical properties of the implanted material.

This paper deals mainly with results obtained with Mössbauer Spectroscopy and Ion Channeling on the behaviour of Te and I atoms in semiconductors. The newest results deal with implantations in GaAs, but a review of the data on implantations in Si will provide the necessary background.

In recent years the interest in GaAs as a technologically important semiconductor material has been increasing steadily because of its superior properties in terms of electron mobility, intrinsic resistivity and, e.g. radiation hardness. Moreover, its wider bandgap than Si makes it especially useful both for optical devices and elevated temperature operation.

Chalcogen impurity atoms (S, Se, Te) in GaAs are expected to behave as donor atoms when they occupy substitutional As sites. However, the lack of sufficiant electrical activation at higher doping levels is a puzzling experimental result. It has stimulated intensive research especially with techniques revealing information on the nature of the microscopic neighbourhood around the impurity atom such as Extended X-ray Absorption Fine Structure (EXAFS) spectroscopy [2-3], Ion Channeling and also Mössbauer Spectroscopy [4-6].

Tellurium is indeed an element that is very well suited for high resolution hyperfine interaction studies: while ^{125}Te itself is a Mössbauer isotope (3/2 → 1/2 transition of 35 keV) that can be studied directly in the decay of ^{125m}Te, two other Mössbauer isotopes can provide indirect information on the Te lattice configuration. ^{129m}Te decays to the ^{129}I Mössbauer transition (5/2 → 7/2 transition of 28 keV) which is superior in resolution to ^{125}Te. The shortlived ^{119}Te isotope decays via ^{119}Sb to the ^{119}Sn Mössbauer transition (3/2 → 1/2 transition of 24 keV), but because of the possible influence of this intermediate state, experiments with this isotope will not be discussed in this paper. We will also mention a few experiments where the ^{125}Te Mössbauer transition was populated via the ^{125}I parent, rather than via ^{125m}Te.

2. Te IN Si AFTER LASER ANNEALING.

The data on the lattice configuration around Te atoms implanted in semiconductors remained for a long time ambiguous, until it was shown by channeling experiments [7] that pulsed laser irradiation of the implanted layer drives almost all the Te atoms into substitutional sites. This allowed De bruyn et al. [8 - 10] to make a consistent interpretation of the measured Mössbauer spectra of Te implanted in Si, which was subsequently laser annealed.

Kemerink et al. [11] made a detailed study of the Mössbauer spectra of laser annealed Te-implanted Si as a function of the doping of the host. They studied ^{125}Te in the decay of implanted ^{125m}Te and ^{129}I in the decay of implanted ^{129m}Te. In both cases the substitutional atom was found in a different charge state, reflected by a difference in isomer shift, depending on the doping of the Si host. Te^0 and Te^+ were detected, while for I three charge states were observed: I^{++}, I^+ and I^0, and the latter one was found to be Jahn-Teller distorted.

3. Te IN Si AFTER OVEN ANNEALING

The substitutional site, occupied by Te atoms implanted in Si, followed by laser annealing, was found to be metastable. Subsequent thermal annealing of a laser annealed sample results [10, 12, 13] in a site symmetry change: the Mössbauer spectrum changes back to the original spectrum which is observed in as-implanted samples. Oven annealing (in inert gas atmosphere) of Te-implanted Si does not result in any drastic change from the as-implanted spectrum shape. This can be judged from Figure 1 for the ^{125}Te resonance in the decay of ^{125m}Te, measured versus a ZnTe-absorber containing 2 mg/cm^2 ^{125}Te, and for the ^{129}I resonance in the decay of ^{129m}Te, measured versus a CuI absorber, containing 8 mg/cm^2 ^{129}I. The implantation dose was 5 x 10^{14} atoms/cm^2 for both samples.

This is a fairly surprising result as it is well known that the implanted layer is completely amorphized during the ion implantation procedure, at least for implantation doses above 10^{14} atoms/cm^2. We thus conclude that the local symmetry around the Te atom, reflected in the hyperfine interaction parameters, is the same in amorphized Si, and in monocrystalline Si layers obtained by the solid phase epitaxial regrowth due to oven annealing.

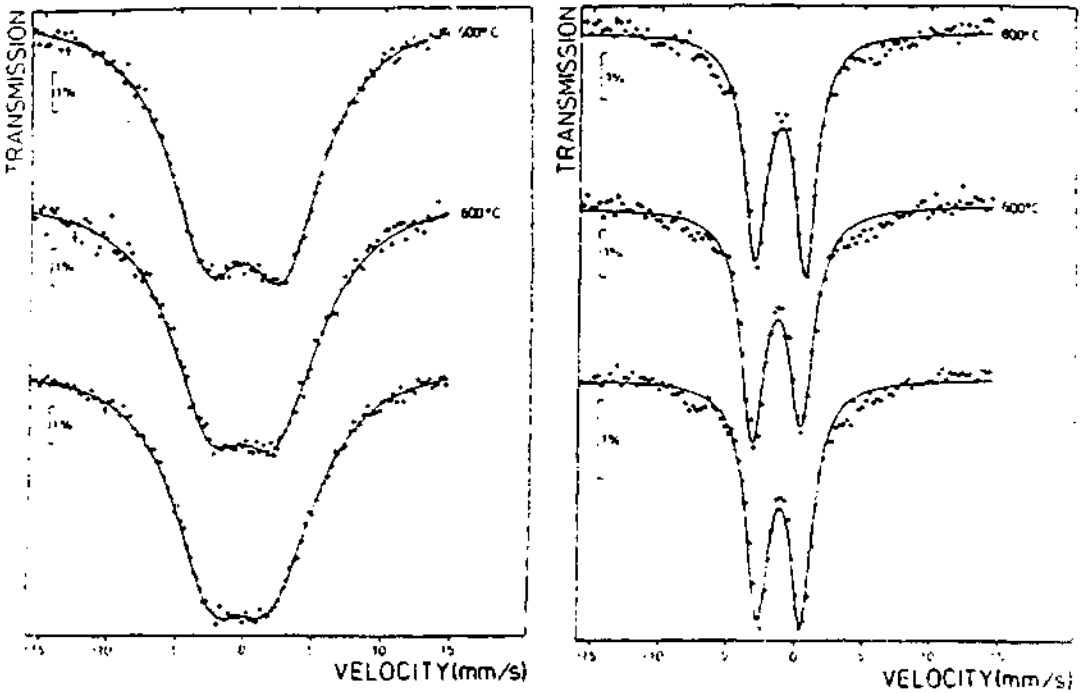

Figure 1 Mössbauer spectra from sources of ^{125m}Te and ^{129m}Te implanted in Si, right after implantation and after oven annealing.

	^{125}Te	^{129}I
quadrupole splitting	(mm/s)	(MHz)
as implanted	+ 4.55(7)	+ 483(8)
600°C annealed	+ 4.94(7)	+ 536(8)
800°C annealed	+ 5.60(7)	+ 560(9)
linewidth (mm/s)	7.1(1)	1.6(1)
isomer shift (mm/s) versus absorber	- 0.27(5) ZnTe	- 1.42(7) CuI

Table 1: Mössbauer parameters of the spectra shown in Figure 1. The signs of the ^{125}Te quadrupole interactions are derived from the nuclear orientation experiments, discussed further. In the ^{129}I analysis, the asymmetry parameter η was taken = 0.

Except for low implantation doses, the Mössbauer spectra of as-implanted and oven-annealed Te-implanted Si, shown in Figure 1, do not contain the single line resonance due to substitutional Te or I, observed after laser annealing. Although an analysis of the spectra with two roughly equal intensity single lines gives even a somewhat better quality fit, the spectra have been analysed with a single electric quadrupole interaction, the parameters of which are given in Table 1.

Indirect arguments [9, 10, 13] for a quadrupole interaction analysis were based on the systematically correlated behaviour of the two resonances, the difficulty to interpret the isomer shifts of the separate ^{125}Te resonances, the linewidth of the ^{129}I resonances and the derived ratio between the quadrupole interactions strengths for both isotopes, and between the two measured isomer shifts.

Kemerink [14] obtained similar Mössbauer spectra, and made also a quadrupole interaction analysis. A somewhat better fit was obtained by assuming a (Lorentzian) distribution with a width of about 40 % around an average quadrupole splitting value of 570 MHz, and a asymmetry parameter η = 0.8 was obtained as best fit value. A still better fit could be obtained by adding weak extra components in the spectrum, especially at low implantation doses: at implantation doses of 10^{12} and 10^{13} atoms/cm^2 about 15 % of the spectrum area could be assigned to a single line, with the same parameters as the substitu-tional line from the the laser-annealed samples.

A more direct argument for a quadrupole interaction was obtained from a time-differential perturbed angular correlation (TDPAC) measurement on an unannealed ^{129m}Te implanted Si sample by Kemerink et al. [15]. An analysis, using the above mentionned values for the quadrupole splitting and its spread, was found to be consistent with the data, although the statistics of the difficult measurement was rather poor.

Maybe the most direct argument for a single quadrupole interaction hypothesis, which also allows for the sign determination of the ^{125}Te quadrupole interaction, is discussed in section 5 of this review, where it is shown that the ratio between the two Mössbauer resonances in the ^{125}Te spectrum changes at extremely low temperature, due to nuclear orientation effects.

So far we have not discussed the possible origin of this large electric field gradient. A model has been proposed [10, 12] in which the Te atom relaxes towards an associated vacancy in the <111> direction, as shown in Figure 2.

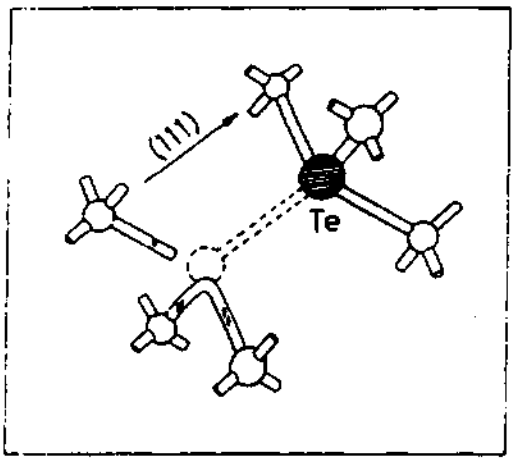

Figure 2
Impurity plus nearest neighbour vacancy model for Te and I in Si.

Using this model, Van Rossum et al. [16] have calculated (Table 2) displacements towards a vacancy in the <111> direction that would introduce an EFG of the observed order of magnitude. It was comforting to observe that the calculated displacements (z) result in impurity-host bond lengths (R), which are consistent with Pauling covalent radii (R_{cov}).

	V_{zz} (10^{18} V/cm^2)	z (A)	R (A)	R_{cov} (A)
Te(Si)	- 3.47	0.34	2.49	2.49
I(Si)	- 3.83	0.16	2.41	2.45

Table 2 Experimental field gradient V_{zz}, calculated displacement z and bond length R for Te and I implanted in Si, and Pauling covalent radius R_{cov}.

A more direct test for the lattice configuration around the implanted Te atoms should in principle be possible from channeling studies on oven-annealed samples. Unfortunately, the reported results are not conclusive, and even seem inconsistent. Several channeling studies on Te in Si have been published, but we will only mention two recent ones, which were undertaken in combination with Mössbauer experiments.

Kemerink et al. [14, 17] report channeling spectra for 900°C annealed samples where the Te channeling dips are appreciably narrower and less deep than the host strings. However, no significant differences are noticed between the different strings, so that the Te site cannot be uniquely determined. A laser annealed sample, subsequently thermally annealed at 900°C, showed an increase in the χ_{min} of Te from 23 to 39 %, clearly indicating a site change.

Dezsi et al. [18], on the other hand, report similar experiments. A drastic reduction in the width of the angular scan in the <100> direction is observed upon thermal annealing of the laser annealed sample, from 96 % to 77 % of the Si scan width. But χ_{min} only rises from 13 % to 15 %, as can be seen in Figure 3.

These channeling data therefore clearly demonstrate a site location change for the Te atom, but clear evidence for the size and the direction of this change has not been obtained yet.

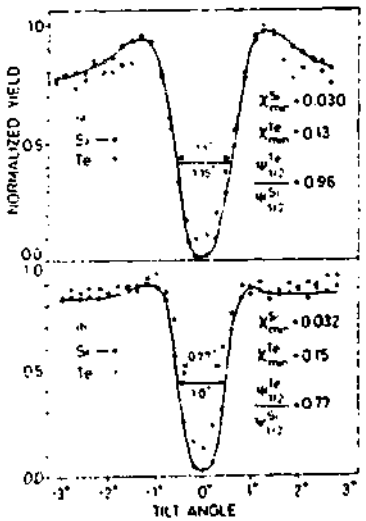

Figure 3
<100> angular scans for (a) laser annealed and (b) subsequently 700° C thermally annealed Te in Si.

4. IMPLANTATION OF I IN Si

The implantation site of I directly implanted in Si, in contrast to the I site in the decay of implanted Te, discussed previously, was also investigated by Mössbauer spectroscopy as well as by ion channeling.

Mössbauer spectroscopy on ^{125}Te in the decay of ^{125}I implanted into Si shows essentially the same spectra as after ^{125m}Te implantation [10, 19], as well for as-implanted as for thermally and laser annealed samples. It is therefore concluded that also the implanted I atom after implantation and annealing, resides in a very similar lattice configuration as the Te atom.

Detailed channeling studies by Boerma et al. [20-22], on thermally annealed I-implanted Si showed that the major part of the I atoms occupies a lattice site which is shifted about 0.15 Å into the <111> direction, and is therefore probably vacancy-associated in that direction, in agreement with the model shown in Figure 2. It is comforting to see that the measured shift is almost exactly equal to the value calculated from the Mössbauer data given in Table 2.

5. NUCLEAR ORIENTATION USING DEFECT INDUCED ELECTRIC FIELD GRADIENTS

In order to study nuclear quadrupole interactions with the technique of nuclear orientation (NO) at low temperatures, one normally has to use single crystal hosts, in which the principal axis system (PAS) of the EFG has a unique direction with respect to the macroscopic orientation of the sample. In this way, when cooled down to sufficiently low temperatures in the millidegree Kelvin region, one obtains a non isotropic angular distribution of the emitted radiation. This is a consequence of the fact that lower lying nuclear hyperfine sublevels of the parent state obtain preferential Boltzmann populations, and the emitted radiation is not added up to an isotropic sum any more. If, however, one does not detect the sum of these radiation components, but one resolves these components energetically, by using Mössbauer spectroscopy, the condition for a macroscopic orientation of the PAS is not necessary any more. In this case, one measures directly the unequal populations of the hyperfine sublevels, and from this the hyperfine interaction of the parent state, responsible for the nuclear orientation, can be derived, without the use of single crystals.

Especially electric quadrupole interaction studies by "classical" low temperature nuclear orientation experiments are hampered by the fact that sufficiently large single crystals, containing radioactive atoms, are not easily available, and are often very difficult to handle in NO equipment. Mössbauer spectroscopy on oriented nuclei allows the use of polycrystalline samples. A general discussion on the use of Mössbauer spectroscopy to detect NO effects, can be found in Ref. 23.

Defect-induced EFG in cubic lattices, as the ones discussed in the previous section, are normally directed in several equivalent directions. They therefore do not result in an anisotropic radiation pattern in classical low temperature nuclear orientation experiments. Detection of the radiation by Mössbauer spectroscopy therefore allows even the use of cubic lattices in nuclear quadrupole orientation experiments.

We have demonstrated this [24] in a NO-Mössbauer experiment, in collaboration with the hyperfine interaction group of the university of Lyon, using the EFG of Te in Si.

The Si lattice is certainly not the best candidate, in terms of thermal conductivity, to obtain a low temperature. We have used this lattice because the EFG is large, unique and well known. As a parent state we used ^{125}I, implanted into Si with 1×10^{15} atoms/cm^2, and we oven annealed this sample to 800° C. A good thermal contact with the Cu cold finger of the ^3He-^4He-refrigerator was obtained by evaporation of 50 nm Co onto the implanted and annealed surface, on which Sn solder could easily be applied. The temperature of the substrate was monitored by a $^{60}Co(Fe)$ thermometer. A fairly thick absorber of 10 mg/cm^2 ^{125}Te in Mg_3TeO_6 was used to maximize the experimental effect, at the expense of some extra line broadening, as can be seen in Fig. 4.

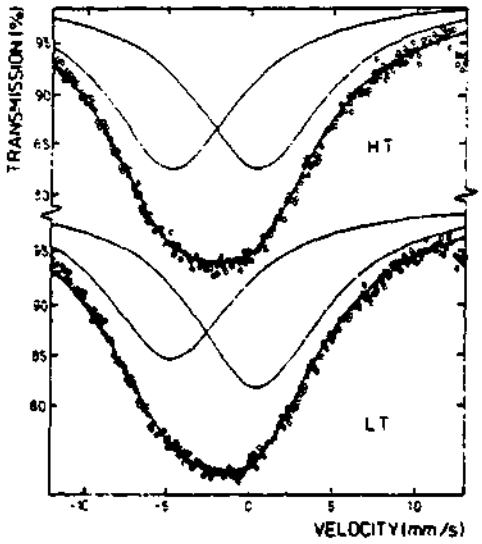

Figure 4
^{125}Te Mössbauer spectra of $^{125}I(Si)$ source at 4.2 K (HT) and 50 mK (LT)

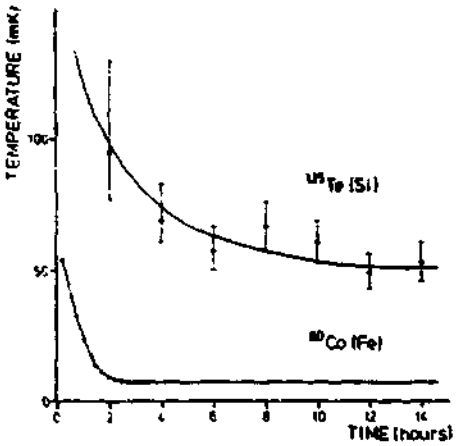

Figure 5
Evolution in time of the temperature at the $^{60}Co(Fe)$ thermometer and the $^{125}Te(Si)$ source

The nuclear orientation effects in the source can clearly be seen in Figure 4. The cooling behaviour is shown in Figure 5. Although the substrate descends to 7 mK, the Si host only reached 50(5) mK. The shape of the cooling curve is typical for a steeply increasing relaxation time with decreasing temperature, until an equilibrium is reached between the low-temperature thermal conductivity of the semiconducting host, and the radioactive heating from the source nuclei. The loss of heat conduction at low temperatures is due to the lack of conduction electrons in the host.

The observed asymmetry in the Mössbauer spectrum is directly proportional to QV_{zz}/kT of the parent state. As the positive velocity line (Figure 4) gains in intensity at low temperatures, and as both quadrupole moments have the same sign, this means that V_{zz} must have the same sign at the parent (I) state as at the excited Mössbauer (Te) state. As the sign of V_{zz} at the I atom is known from ^{129}I Mössbauer data, we derive a negative sign for the EFG at the Te site.

6. CONCLUSIONS ON THE LATTICE SITE OF Te AND I IN Si.

A remarkebly stable defect configuration appears to exist around Te and I atoms in as-implanted and oven-annealed Si, wich is hardly changing, even when the Si matrix is turning from amorphous to crystalline during epitaxial solid phase regrowth. This defect site is characterized by a large electric field gradient of almost - 4 x 10^{18} V/cm^2, both at the Te and the I nucleus. The increase in the EFG at higher annealing temperatures is thought to be due to the increased defect-free quality of the surrounding Si crystal.

There is less certainty about a microscopic model for this defect configuration, but theoretical calculations of the EFG, as well a channeling results on I, indicate a shift towards a near neighbour vancancy in the <111> direction.

At lower implantation doses a small part of the implanted atoms lands up in the substitutional site. Even at the lowest doses studied (10^{12} atoms/cm^2) not more then 15 % of the atoms are found in this site

7. MOSSBAUER AND CHANNELING DATA ON Te IN GaAs

The first Mössbauer experiments on Te in GaAs indicated a very similar behaviour for the GaAs host as for Si [25]. As-implanted and oven annealed samples of ^{129}I in the decay of ^{129m}Te showed an isomer shift of - 0.92(1) mm/s with respect to an CuI absorber, and a quadrupole interaction of + 290(10) Mhz, roughly half the interaction strength of the Si matrix. Laser annealed samples showed a single line with isomer shift δ = - 0.67(1) mm/s with respect to CuI, and a linewidth of 1.84(4) mm/s.

A calculation [26] of the EFG in GaAs and other III-V semiconductors using vacancy association in the first neighbour shell (Figure 2) as lattice configuration model, with a tendency of the I atom to approach covalent bond distances, resulted in complete agreement with the experimental data. This confirmed the conclusions about type IV semiconductors: the impurity atom has a strong tendency to relax into a position which makes its distance to the nearest neighbour host atom consistent with the normal covalent bond distance.

While the first reported Mössbauer data on ^{129}I in GaAs indicated a strong similarity between type IV and type III-V semiconductors, a number of surprising differences became apparent when a series of more detailed measurements was performed as a function of annealing temperature [4, 5] and implantation dose [27].

For an implantation dose of 10^{15} atoms/cm^2 of ^{129m}Te into n-type GaAs (Figure 6) the quadrupole split spectrum collapses into a somewhat broadened single line, with the same parameters as the laser-annealed samples (Table 3), in an annealing temperature range between 200° C and 500° C.

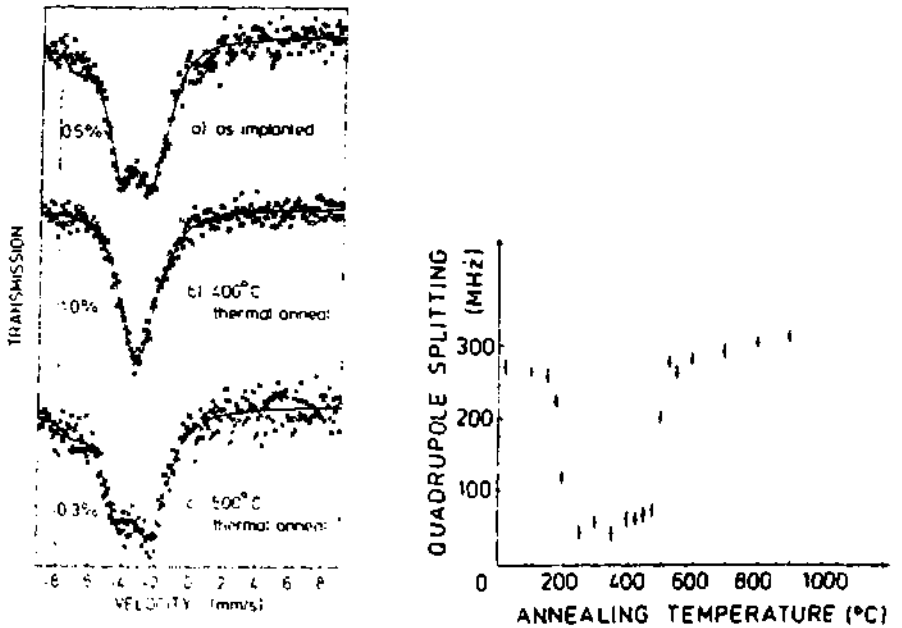

Figure 6 Mössbauer spectra of ^{129m}Te in GaAs versus a Na_5IO_6-absorber and experimental quadrupole splittings as a function of annealing temperature.

annealing region	annealing temperature (°C)	eQV_{zz} (MHz)	δ (mm/s)	Γ (mm/s)
1	20 - 200	+ 266(6)	- 0.90(3)	1.9(1)
2	200 - 500	+ 59(5)	- 0.60(3)	2.5(1)
3	500 - 900	+ 289(9)	- 0.77(3)	2.0(1)

Table 3 Average values for the Mössbauer quadrupole plitting (eQV_{zz}), isomer shift (δ) and linewidth (Γ) in the three annealing regions.

We have performed also channeling studies (Figure 7) in different directions inside and outside this annealing region [28], and observed a Te atom in the shadow of the lattice atoms at an annealing temperature of 450°C, while a distinct displacement was observed at 550°C. An analysis of the angular scans in different directions is consistent with a displacement of about 0.135 Å in the <111> direction for the majority of the implanted Te atoms.

More recent data [27] show that this thermal behaviour is strongly dose dependent. A sample implanted at 2×10^{13} atoms/cm^2 shows the single line throughout the whole annealing region (up to 900°C in steps of 100°C) while a sample implanted at an intermediate dose (10^{14} atoms/cm^2) shows an intermediate behaviour: a single line fraction is present in all spectra, and varies in population from about 30 % below 200° C annealing, to more than 90 % between 200°C and 500°C, and about 60 % at annealing temperature above 600°C.

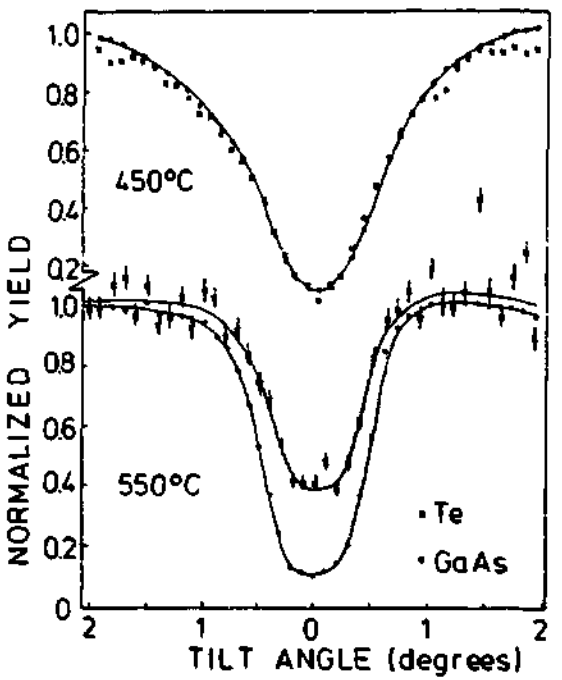

Figure 7 Channeling angular scans in the <100> direction for Te in GaAs at different annealing temperatures.

The Mössbauer and channeling data of Te-implanted GaAs show three major points of difference with implantations in Si and Ge:

(1) Apart from the vacancy-associated site a new site is populated during thermal annealing. Its single line spectrum suggests an unperturbed first neighbour shell. A slight line broadening might be due to defect association in more distant neighbour shells.

(2) At doses of 2×10^{13} atoms/cm^2 no sign of vacancy association is seen, not even when the lattice is amorphous

(3) While the 200°C annealing temperature transition towards a more regular lattice site can be associated with the onset of recrystallization of the amorphized GaAs, it is not clear what mechanism is be responsible for the vacancy association at high annealing temperatures and high implantation doses.

8. EXAFS ON Te IN GaAs

Extended X-ray absorption fine structure (EXAFS) were recently reported on S implanted in GaAs, with doses of $10^{15}$and 10^{16} atoms/cm^2 and annealed to 900°C [2], and for Te grown into GaAs [3], with a carrier concentration of 8×10^{18} cm^{-3}. Figure 8 shows the S-data. According to the authors, the behaviour of S in GaAs is typical also for other chalcogens, including Te.

The authors claim that their data can only be fitted well with a model in which two S-sites are almost equally populated:

(a) unperturbed substitutional S on an As site, with normal bond lengths of 2.45 Å.

(b) S on an As site, with an unperturbed first neighbour shell with four S neighbours at equal distances, which are 0.14(4) Å shorter than the normal bond lengths in GaAs, but with an associated vacancy in the second neighbour shell.

According to Greaves et al. [3], the Te EXAFS data are consistent with an 100 % population of a defect site, where the Te atom has an intact first neighour shell, with bond lengths 0.13 Å longer than the normal bond lengths in GaAs, and with an associated vacancy in the second neighbour shell. This site is thus very similar to the (b)-site of S except for the expansion of the first neighbour shell instead of the relaxation towards the central chalcogen.

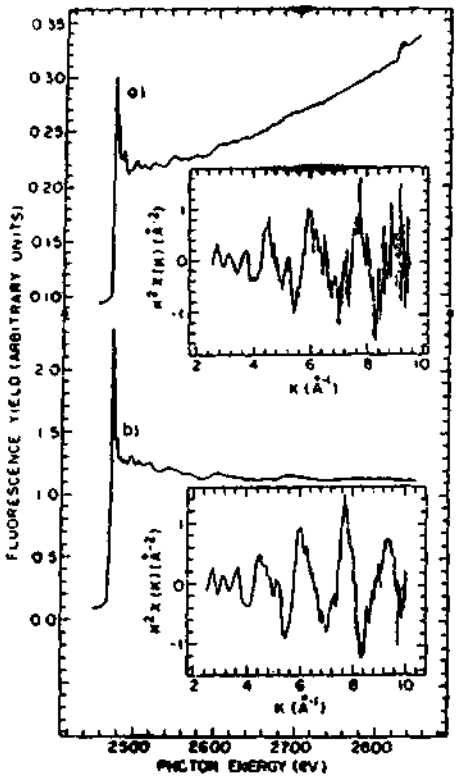

Figure 8
EXAFS spectrum for S implanted in GaAs and annealed at 900°C (a) 10^{15} (b) 10^{16} atoms/cm^2 [from Ref 2]

The two interpretations are consistent in that they both assume a defect-associated lattice site with a defect in the second neighbour shell. However, there is no agreement with the first-neighbour vacancy association model discussed in the previous section.

The channeling data are maybe not conclusive in this respect, as they measure displacements with respect to lattice rows, wich might also be present if defect association occurs in more distant neighbour shells. We do not see, however, how the very large EFG measured in Mössbauer spectroscopy, can be associated with an intact first neighbour shell. The hyperfine interaction data are especially sensitive to defects in the first neighbour shell, while radial distribution functions, derived from EXAFS data, measure the average distance of this global shell.

However, a more probable origin for this difference in results might be found in a difference between the samples studied, especially in view of the strong dose dependence observed in the Mössbauer data, discussed in the previous sections. Comparative measurements, using identical samples in both techniques, are urgently needed.

9. CONCLUSIONS

We have demonstrated how hyperfine interaction studies can lead to a first-neigbour-vacancy-associated model for the lattice configuration of implanted Te and I atoms in type IV and type III-V semiconductors. Ion channeling results support this model, but EXAFS-data, at least for Te in GaAs, are interpreted with a second-neigbour-vacancy-associated model, with a intact first neighbour shell. The most likely reason for this discrepancy is a difference in sample preparation.

REFERENCES

[1] G. Langouche, Proceedings of the International Conference on the Applications of the Mössbauer Effect (Alma Ata, 1983) Edited by Kagan and Lyubutin, (Gordon and Breach 1985) Volume 1, 395.

[2] F. Sette, S.J. Pearton, J.M. Poate, J.E. Rowe and J. Stöhr, Phys. Rev. Lett. 56 (1986) 2637.

[3] G.N. Greaves, P.J. Halfpenny, G.M. Lamble and K.J. Roberts, Proceedings of the EXAFS-conference (Fontevraud 1986) to be published in J. de Physique.

[4] D. Schroyen, I. Dezsi and G. Langouche, Nucl. Instr. Meth. B15 (1986) 410.

[5] D. Schroyen, P. Hendrickx and G. Langouche, Materials Science Forum, 10-12 (1986) 1177.

[6] L. Niesen, D.O. Boerma and Z.Y. Qun, to be published in Hyp. Int.

[7] G. Foti, S.U. Campisano, E. Rimini and G. Vitali, J. Appl. Phys. 49 (1978) 2569.

[8] J. De Bruyn, G. Langouche, M. Van Rossum, M. de Potter and R. Coussement, Phys. Lett. 73A (1979) 356.

[9] J. De Bruyn, R. Coussement, I. Dezsi, G. Langouche, M. Van Rossum and M. de Potter, Proceedings of the International Conference on Nuclear Methods in Materials Research (Darmstadt 1980) Edited by Vieweg (Braunschweig 1980) 451.

[10] J. de Bruyn, Ph. D. Thesis, Leuven University 1982 (unpublished).

[11] G.J. Kemerink, H. de Waard, L. Niesen and D.O. Boerma, Hyp. Int. 14 (1983) 37, and ibid. 14 (1983) 51.

[12] I. Dézsi, M. Van Rossum, J. De Bruyn, R. Coussement and G. Langouche, Phys. Lett. 87A (1982) 193.

[13] J. De bruyn, R. Coussement, I. Dezsi, G. Langouche and M. Van Rossum, Hyp. Int. 10 (1981) 973.

[14] G.J. Kemerink, Ph. D. Thesis (Groningen 1981).

[15] G.J. Kemerink, F. Pleiter and A.R. Arends, Hyp. Int. 10 (1981) 983

[16] M. Van Rossum, I. Dezsi, K.C. Mishra, T.P. Das and A. Coker, Phys. Rev. B 26 (1982) 4442.

[17] H. de Waard and G.J. Kemerink, Physica 116B (1983) 210.

[18] I. Dezsi, M. Van Rossum, G. Langouche, R. Coussement, D. Schroyen and M.F. Wu, Appl. Phys. Lett. 44 (1984) 505.

[19] I. Dezsi, R. Coussement, G. Langouche and M. Van Rossum, Rad. Eff. Lett. 76 (1983) 221.

[20] D.O. Boerma, P.J.M. Smulders and T.S. Wieringa, Mat. Res. Soc. Symp. Proc. 27 (1984) 259.

[21] G.J. Kermerink, D.O. Boerma, H. de Waard and L. Niesen, Rad. Eff. 70 (1983) 183.

[22] H. Bemelmans & G. Langouche (to be published)

[23] G. Langouche, M. Van der heyden, M. Tong, I. Berkes, M. Fahad, O.E. Hajjaji and G. Marest, Hyp. Int. 1987 (to be published)

[24] I. Berkes, O.E. Hajjaji, B. Hlimi, G. Marest, E.H. Sayouty, G. Langouche, M. Van der heyden and M. Tong, Hyp. Int. 1987 (to be published)

[25] M. Van Rossum, I. Dezsi, G. Langouche, J. De bruyn and R. Coussement, Mat. Res. Soc. Symp. Proc. (1981) 359.

[26] M. Van Rossum, G. Langouche, K.C. Mishra and T.P. Das, Phys. Rev. B 28 (1983) 6086.

IRON IMPLANTATION IN GARNETS STUDIED BY CEMS, X-RAY DIFFRACTION AT GLANCING ANGLES AND TRANSMISSION ELECTRON MICROSCOPY

G. MAREST

Institut de Physique Nucléaire (and IN2P3), Université Claude Bernard Lyon-I
43, Bd du 11 Novembre 1918 - 69622 Villeurbanne Cedex (France)

ABSTRACT

Due to their numerous physical properties, garnets are often used in new technologies. Recently it has been shown that high doses implanted ions, chemically reacting with the matrix could give interesting results. If the bulk is completely amorphized after implantation, further annealings can recrystallize it. In this study $Y_3Fe_5O_{12}$, $Y_3Al_5O_{12}$ and $Gd_3Ga_5O_{12}$ single crystals were 100 keV implanted with ^{57}Fe ions at doses ranging between 10^{16} and 10^{17} ions.cm^{-2}. The iron chemical states were determined thanks to Conversion Electron Mössbauer Spectroscopy (CEMS) and it was shown that the alloying elements of the matrix could influence the nature of the created phases. After thermal treatments the sample superficial layers were characterized using CEMS, glancing angle X-Ray Diffraction (GXRD), Transmission Electron Microscopy (TEM) and Rutherford Backscattering Spectroscopy (RBS). Different annealing stages were put forward : the oxidation of the implanted iron below 650°C and the garnet recrystallization around 850°C with some iron substitution in the garnet octahedral and tetrahedral sites. The over-stoichiometric iron forms particles of mixed oxides $(FeAl)_2O_3$, $(FeGa)_2O_3$ or particles of pure Fe_2O_3 oxide depending on the garnet. For the first time it is proved that after annealing around 1200-1300°C a complete rebuilding of the garnet matrix can induce for these oxide particles at room temperature a Morin transition.

I. INTRODUCTION

Magnetic single crystal films of garnets are the subject of great interest due to the large potential for applications. Yttrium iron garnet $Y_3Fe_5O_{12}$(YIG) is the basic material in which any metal of the periodic table can be substituted in the crystalline lattice to create new physical properties. Ion implantation, a non-equilibrium doping technique, is interesting to introduce into a garnet a wide variety of atomic species properly chosen so as to obtain a specific dopant effect for new applications or to synthetize new materials.

Previously, in the particular case of bubble garnets, this technique has been extensively used with rare gas ions at low doses in order to produce a small damage for suppressing hard bubble formation and for making propagation patterns for memory displays [1]. More recently other ions (H, Fe, Ga, As, ...) which chemically react with the matrix elements have been implanted in order to produce some peculiar effects on the magnetic properties [2-4]. In the latter case high implantation doses are generally used leading to the amorphization of the matrix [5]. The formation of an amorphous layer in heavily implanted garnets has been shown directly by transmission electron microscopy [5,6] and indirectly using conversion electron Mössbauer spectroscopy [7-14], RBS and channelling [8, 12-18], X-ray double crystal diffraction and ferromagnetic resonance [2, 19, 20] and a susceptibility method [21]. This highly damaged layer can be recrystallized by means of high temperature annealings. The crystalline regrowth mechanism starts from the bottom of the damaged layer by an epitaxial regrowth process [2].

Some measurements have been undertaken on iron implanted $Y_3Fe_5O_{12}$ (YIG), $Y_3Al_5O_{12}$ (YAG) and $Gd_3Ga_5O_{12}$ (GGG) garnets. In the case of YIG it is of underlying interest to know how will be the behavior of overstoichiometric iron introduced by implantation at different stages of the annealing process. For YAG and GGG the practical aim is to try making ferromagnetic out of non magnetic garnets by substitution of Al or Ga by Fe during thermal treatments. The study of the evolution of the implanted iron (depth, charge states, precipitated phases) as a function of thermal annealings is the purpose of this study. Rutherford backscattering (RBS), conversion electron Mössbauer spectroscopy (CEMS), transmission electron microscopy (TEM) and X-ray diffraction at glancing angles (GXRD) techniques have been used to characterize the damage and the implanted ions.

II. EXPERIMENTAL

A pure YIG single crystal enriched with 25% of ^{57}Fe isotope has been used for $^{56}Fe^{+}$ implantation whereas a non-enriched YIG single crystal has been used for implantation of ^{57}Fe ions. Implantations in garnet single crystals of YIG, YAG and GGG were carried out at room temperature with 100 keV energy using the isotope separator of the Institut de Physique Nucléaire de Lyon. During implantation the current density was maintained rather low (~ 3 $\mu A.cm^{-2}$) to prevent thermal effects.

Ion depth profiles have been measured using the Rutherford backscattering spectroscopy technique of 2 MeV alpha particles produced in the 2.5 MeV Van de Graaff of the Département de Physique des Matériaux de l'Université Lyon-1.

CEMS spectra were recorded at room temperature RT and liquid nitrogen temperature (LNT) using a helium flow proportional counter in which the sample was placed in backscattering geometry. For measurements a liquid helium temperature (HeT) the 7.3 keV conversion electrons were selected and focused by means of magnetic coils on a channeltron detector. This Mössbauer device has been described by Massenet [22]. The source was 50-100 mCi ^{57}Co in a rhodium host. The velocity scale and all the data are referred to metallic iron absorber at RT. The spectra were fitted with a computer least-squares procedure with the assumption of Lorentzian shapes of Mössbauer lines or of a distribution in the hyperfine field values [23] due to the existence of non homogeneous phases. The CEMS technique is very sensitive and convenient for the study of implanted layers since it probes mainly a depth comparable to the one which contains impurities and induced defects, taking into account the above mentioned implantation energy. This depth resolution is very useful when the sample contains itself iron (case of YIG) or when the iron content is very low (~ 10^{16} iron atoms.cm^{-2}).

Some samples have been studied with TEM using the JEOL 200CX apparatus of the Centre d'Etudes Nucléaires de Grenoble. To obtain a real "tridimensional" characterization of the implantation defects, two series of observations have been performed ; the first series is classical with a bevelled thinning of the implanted zone whereas the second series is more difficult to use with a thinning in a parallel direction to the surface of the sample [24].

Grazing incidence X-ray diffraction spectroscopy [25] has been used as a complementary technique to identify precipitated phases, to determine sizes of precipitates and to follow the crystallization of garnets. When the X-ray beam makes an incidence angle of 1° with the surface the penetration depth of

CuKα (λ = 0.154 nm) radiation is small (some tenths of nanometers) allowing to probe only the implanted zone without perturbation of the background due to the substrate. The detection of the diffracted X-ray beam is performed in the equatorial plane defined by the incident beam and the normal to the surface. By this way the Bragg peaks due to the single crystalline part of the sample are not observed.

Unless otherwise states most of the thermal treatments were performed in air for 1h.

III. RESULTS

A/ As-implanted Garnets

Garnets have been implanted at medium and high doses in the range 10^{16} - 10^{17} ions.cm^{-2}. A part of the obtained data has been published recently [26].

1/ RBS data

After each implantation RBS measurements have been performed to control depth and concentration of implanted iron. **Figures 1** and **2** show spectra obtained with implanted YIG and YAG.

In **table 1** are reported experimental and calculated values of the mean penetration depth R_p and of the straggling range 2 ΔR_p in the different garnets. Systematic differences between experimental and calculated values can be explained by the fact that for such high doses the sputtering effect plays an important role.

	R_p (nm)		2 ΔR_p (nm)	
	Exp.	Calc.	Exp.	Calc.
YAG	32	41	40	38
YIG	31	39	50	38
GGG	32	34	45	38

Table 1

The iron profiles have a gaussian shape and the implanted layer concerns approximatively the first 100 nm outermost layers.

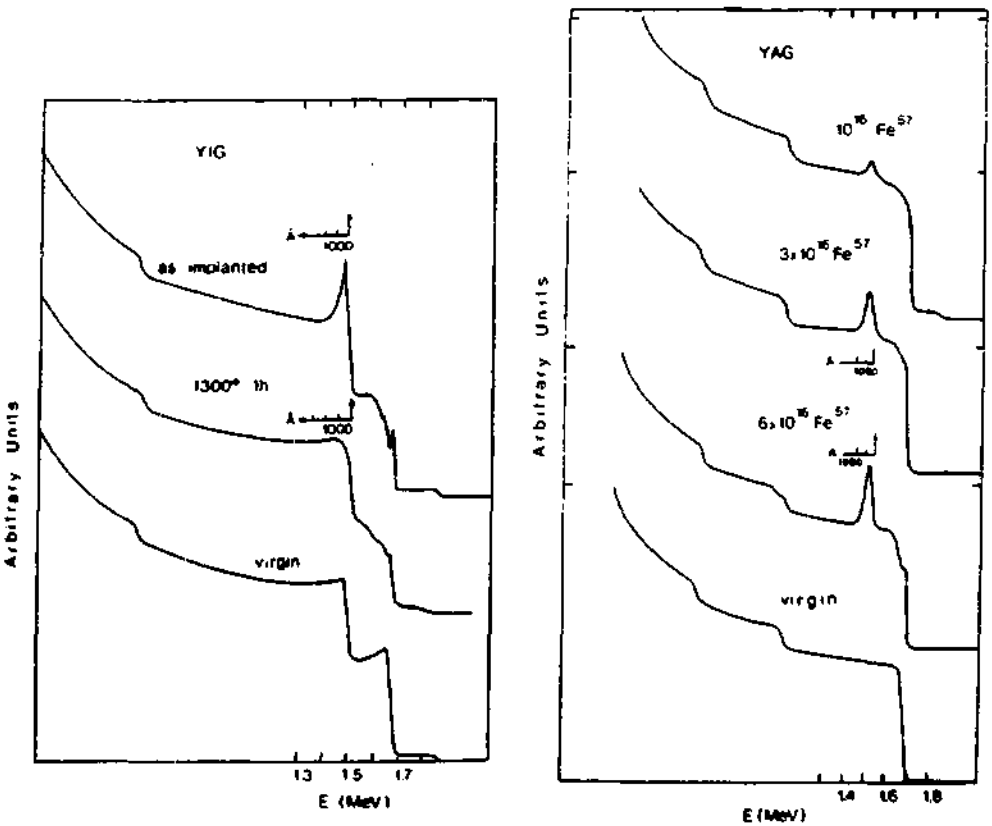

Figures 1 and 2 - *Rutherford backscattering at 160° of 2 MeV alpha-particles on iron implanted YIG and YAG garnets.*

2/ Mössbauer results.

a) Yttrium iron garnet

Figure 3 displays the as-grown YIG spectrum. Its good resolution, due to the enriching of ^{57}Fe, allows to consider 4 subspectra corresponding to 2 octahedral (a) sites and 2 tetrahedral (d) sites with different hyperfine parameters (isomer shifts (IS), quadrupole splittings (QS) and hyperfine fields (HF) [4].

Mössbauer spectra obtained with the two types of $Y_3Fe_5O_{12}$ samples are similar (figure 4). So it can be stated, from such a comparison that whether implanted or originally present in the matrix, iron cannot be discriminated from one another. Mössbauer spectra are made up 3 components : 1) a sextet [IS = 0.02(2) $mm.s^{-1}$ and HF = 333(3) kOe] is due to implanted iron precipitates, 2) an assymmetric doublet [IS = 0.46(2) $mm.s^{-1}$, QS = 0.95(3) $mm.s^{-1}$] is Fe^{3+} in a not

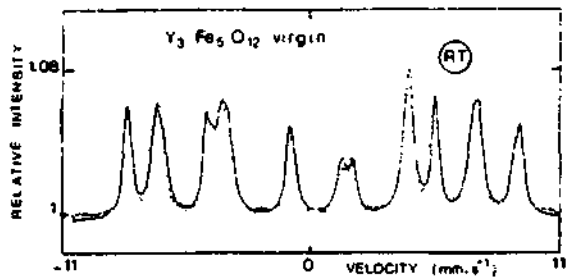

Figure 3 - Mössbauer spectrum of a $Y_3Fe_5O_{12}$ single crystal at RT. The line is the fitted theoretical curve.

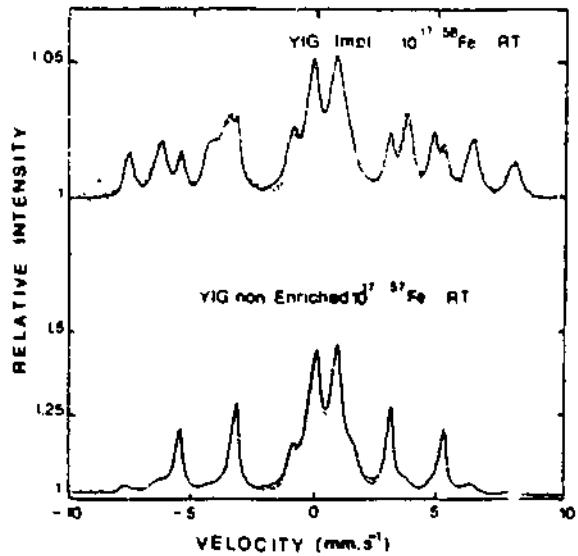

Figure 4 - RT Mössbauer spectra of enriched and non-enriched garnets implanted with 10^{17} $^{56}Fe^+.cm^{-2}$ and $^{57}Fe^+.cm^{-2}$ respectively.

well defined environment and 3) 4 sextets a, a', d and d' due to the crystalline underlying part of the implanted layer. The parameters of Fe^{3+} are comparable to the parameters measured by Eibschütz et al. [27] (IS = 0.49 $mm.s^{-1}$, QS = 1.12 $mm.s^{-1}$) for a vitreous YIG. Thus we are tempted to assign this component to the amorphized garnet.

b) Yttrium aluminium garnet

YAG single crystals have been implanted with 10^{16}, $3x10^{16}$, $6x10^{16}$ and 10^{17} $^{57}Fe^+$.ions.cm^{-2} [13]. The analysis of the spectra displayed in **figure 5** shows that iron is distributed into 3 different charge states : Fe^{2+} (wide doublet), Fe^{3+} (narrow doublet) and Fe^0 (single line) due to small metallic precipitates which behave superparamagnetically at RT. For the dose of 10^{17} ions.cm^{-2} the size of the iron

precipitates is sufficiently large to exhibit a magnetic pattern whose lines have a non-Lorentzian shape thus reflecting a distribution in the hyperfine fields due to different sizes of iron precipitates. A mean size lower than 10 nm can explain the measured 313(5) kOe effective field less than the value 330kOe of bulk iron. The Fe^{3+} valence state defined by the doublet with IS = 0.43(5) $mm.s^{-1}$ and QS = 1.2(4) $mm.s^{-1}$ is interpretated as due to the formation of an amorphous garnet. The Fe^{2+} valence state can be explained by the formation of a $FeAl_2O_4$ compound. Its hyperfine parameters IS = 0.97(5) $mm.s^{-1}$ and QS = 1.64(8) $mm.s^{-1}$ are in good agreement with those given by Coey et al. [28].

c) Gadolinium Gallium Garnet

Figure 6 shows Mössbauer spectra registered at RT after implantations at 10^{16}, 3×10^{16}, 6×10^{16} and 10^{17} $^{57}Fe^+.cm^{-2}$. Fitted parameters are summarized in **Table II** [29].

Dose		10^{16}	3×10^{16}	6×10^{16}	10^{17}
SL Fe^0	DI ($mm.s^{-1}$)	0.01 ± 0.03	0.01 ± 0.03		
	Relative Area (%)	20 ± 2	21 ± 4		
D Fe^{3+}	DI ($mm.s^{-1}$)	0.43 ± 0.02	0.38 ± 0.03	0.49 ± 0.02	0.47 ± 0.02
	EQ ($mm.s^{-1}$)	1.28 ± 0.03	0.82 ± 0.03	0.86 ± 0.05	0.90 ± 0.06
	RA (%)	13 ± 2	17 ± 5	9 ± 4	6 ± 3
D Fe^{2+}	DI ($mm.s^{-1}$)	1.00 ± 0.02	1.01 ± 0.01	0.85 ± 0.03	0.85 ± 0.03
	EQ ($mm.s^{-1}$)	1.54 ± 0.03	1.54 ± 0.03	1.7 ± 0.07	1.70 ± 0.05
	RA (%)	67 ± 2	55 ± 5	46 ± 5	25 ± 5
SX FeGa	DI ($mm.s^{-1}$)		0.20 ± 0.03	0.18 ± 0.03	0.12 ± 0.02
	H (kOe)		247 ± 8	267 ± 7	287 ± 7
	RA (%)		7 ± 2	45 ± 6	69 ± 6

Table II *- Hyperfine parameters at RT of compounds formed in* $Gd_3Ga_5O_{12}$ *after implantations of* ^{57}Fe *at different doses. SL : single line, D : doublet, SX : sextuplet, RA : relative area.*

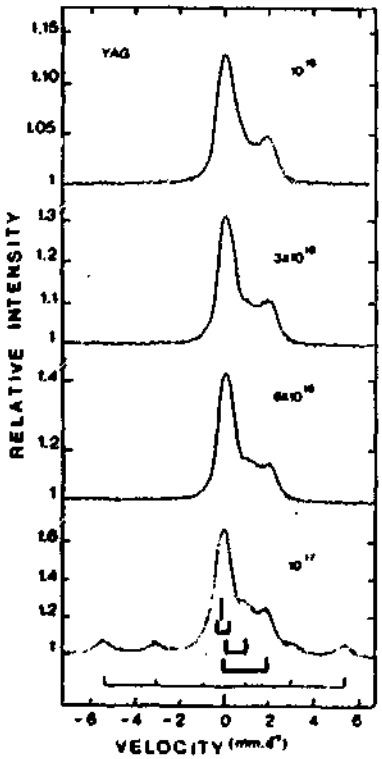

Figure 5 - CEMS spectra for $Y_3Al_5O_{12}$ garnets implanted with four ^{57}Fe doses.

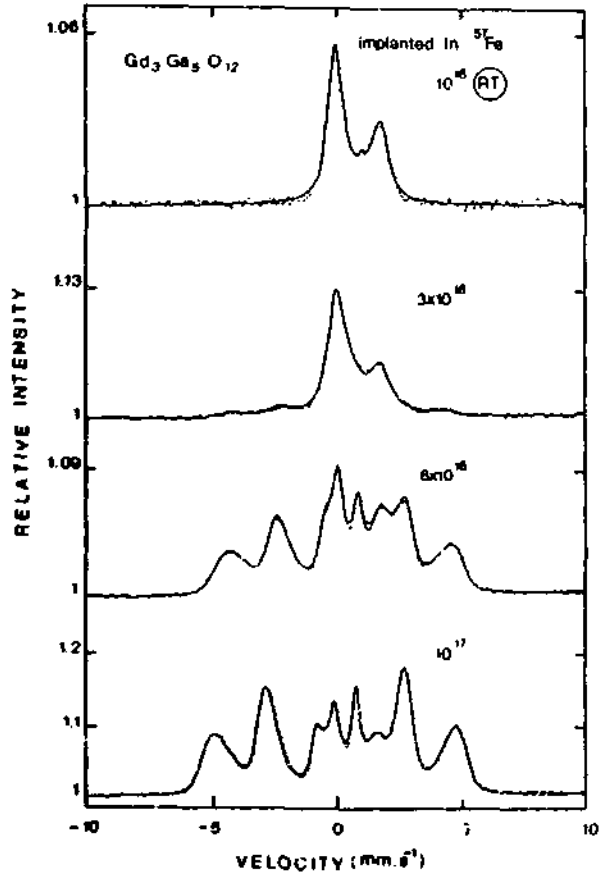

Figure 6 - CEMS spectra of $Gd_3Ga_5O_{12}$ garnets implanted with 1, 3, 6 and 10.10^{16} $^{57}Fe^+.cm^{-2}$.

For medium doses 10^{16} and 3.10^{16} iron precipitates under small particles Fe^{0} : IS = 0 $mm.s^{-1}$. The two other Fe^{3+}, Fe^{2+} valence states are present in each sample as it was the case for $Y_3Al_5O_{12}$. The Fe^{3+} state can be attributed to the existence of an amorphous garnet layer as for YIG and YAG. The Fe^{2+} valence state could be explained by the formation of a $FeGa_2O_4$ compound whose hyperfine parameters IS = 1.00 2 $mm.s^{-1}$ and QS = 1.54 3 $mm.s^{-1}$ are in agreement with those of Coey et al. [28].

The magnetic phase created after implantation at high dose displays a sextuplet whose wide and assymmetrical lines are sign of a large number of various surroundings around Mössbauer nuclei. The analysis of this hyperfine distribution has been performed using a computer programme edited by Le Caër et al. [30]. This programme allows to substract the non-magnetic part of the spectrum previously determined at low doses and then to obtain the hyperfine parameter distribution as shown in **figure 7**. The hyperfine field distribution has been fitted assuming a linear dependence between the isomer shift and the hyperfine field : IS = aH + b. The fitted parameters are similar with the parameters obtained by Newkirk et al. [31] for $Fe_{1-x}Ga_x$ compounds. We have followed the variation of the hyperfine field of this $Fe_{1-x}Ga_x$ compound as a function of the dose. From this dependence and the results reported by Newkirk et al. a mean value for x can be deduced for each dose. For 10^{17} ions.cm^{-2} we have calculated $\bar{x}$ = 0.19.

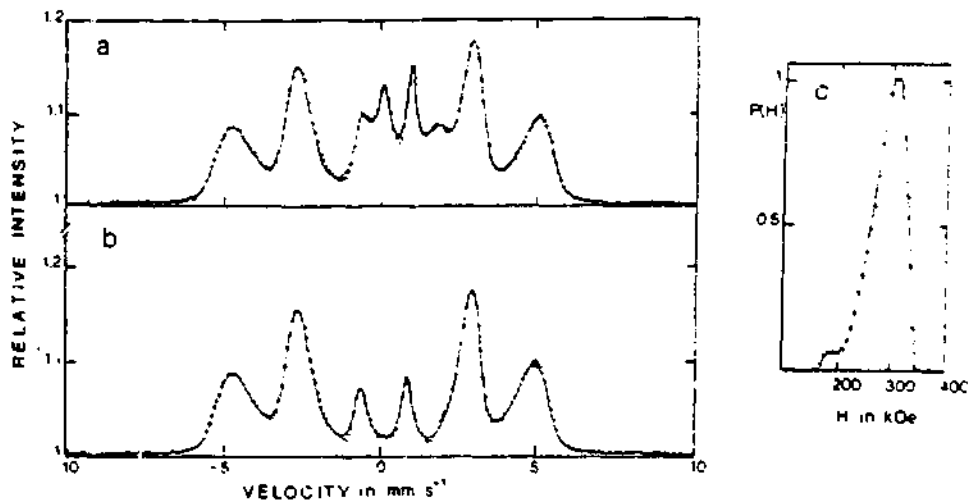

Figure 7 *- a) Total CEMS spectrum of a 10^{17} $^{57}Fe^{+}.cm^{-2}$ implanted $Gd_3Ga_5O_{12}$ garnet ; b) Extracted magnetic part of the spectrum ; c) Hyperfine magnetic distribution.*

3/ Complementary results

The amorphization of the implanted layer and the precipitation of large iron aggregates are demonstrated by glancing angle (0.8°) X-ray diffraction spectra obtained for a YAG sample implanted with 3×10^{16} and 10^{17} ions.cm^{-2} (**figure 8**). In the first case two bumps are observed around 16° and 22° Bragg angles characteristic of amorphized phases. For 10^{17} ions.cm^{-2} the same degree of amorphization is obtained but the [110] line of α-Fe appears at 22.5° (2.04 Å) on the second bump. From the large width of the [110] line it can be deduced a mean size of about 10 nm for the grains [32]. The (211) peak of α-Fe appears around 41.3°. It is weak and spread out due to the small quantity and size of the precipitates.

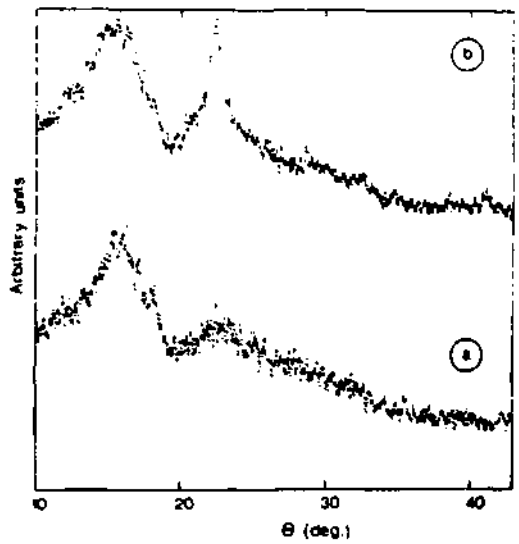

Figure 8 - X-ray diffraction spectra of YAG implanted with a) $3x10^{16}$ Fe^+.cm^{-2} and b) 10^{17} Fe^+.cm^{-2}

A further evidence for the precipitation of iron is given by the cross-section micrograph (**figure 9**) obtained by TEM for a YAG sample implanted with 10^{17} Fe^+.cm^{-2}. The iron precipitates are dispersed inside the implanted layer between 25 and 65 nm and the grain size is estimated to vary from 3 to 7 nm [24]. These results are in a very good agreement with the RBS and X-ray diffraction measurements. The distribution in sizes of the iron precipitates is also clearly demonstrated by the simultaneous presence in the CEMS spectrum of a single line and of a sextuplet with deformed shapes. A measurement performed at liquid nitrogen temperature shows a decrease of the single line contribution (16% to 5%)

and an increase of the sextet contribution (22% to 38%) indicating a mean size for the precipitates of the order of 6 to 10 nm. These CEMS measurements indicate also that the magnetization of these precipitates is randomly oriented [$A_{2,5}/A_{1,6}$ = 0.72.3].

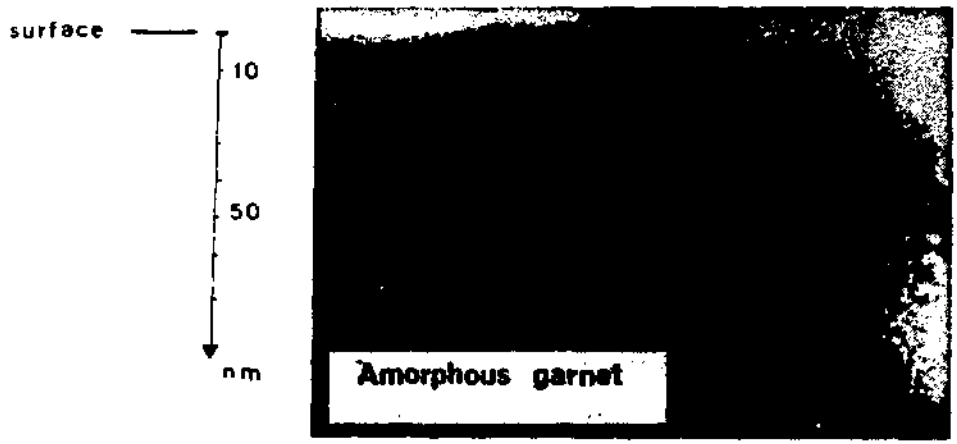

Figure 9 - *Cross-section micrograph of 10^{17} $Fe^{+}.cm^{-2}$ implanted $Y_3Al_5O_{12}$.*

In figure 10 the X-ray diffraction spectrum corresponding to a $Gd_3Ga_5O_{12}$ garnet implanted with 10^{17} $Fe^{+}.cm^{-2}$ is presented. The bump located at 15.6° is representative of an amorphized garnet and/or of an amorphous oxide ($FeGa_2O_4$ for

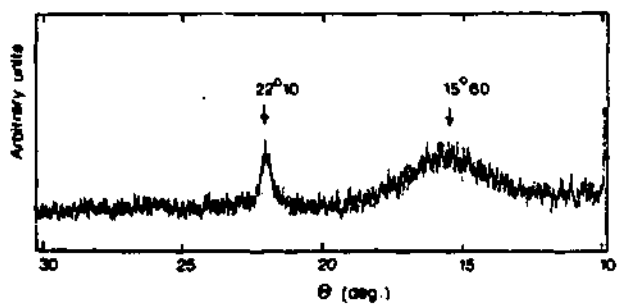

Figure 10 - *X-ray diffraction spectrum of $Gd_3Ga_5O_{12}$ implanted with 10^{17} $Fe^{+}.cm^{-2}$*

example . The wide reflexion located at 22.10° can be explained by the presence of a crystallized $Fe_{1-x}Ga_x$ alloy with a bcc structure [33]. From the precise measurement 2.894 Å of the a parameter it is possible to deduce x = 0.15 from the variation of a as a function of x [33].

B/ Annealing behaviours up to 850°C

1/ Case of implanted YIG garnets

As soon as the samples are annealed at 450°C the iron precipitates disappear and apart the four sextets of the underlying garnet a well defined doublet with IS = 0.33 $mm.s^{-1}$ and QS = 1.10 $mm.s^{-1}$ is present in the spectrum (**figure 11**). After annealing at 650°C the relative intensity of the assymmetrical doublet due to the amorphous layer decreases indicating an appreciable rearrangement at the back of the implanted layer. This regrowth epitaxy is now well spread out after the 850°C treatment as seen by the important increase of the garnet sextets. Now the doublet has vanished to give a new sextuplet with hyperfine parameters (δ = 0.39(2) $mm.s^{-1}$, QS = 0.37(3) $mm.s^{-1}$ and H = 518(3) kOe) typical of large (> 20 nm) α-Fe_2O_3 particles [34].

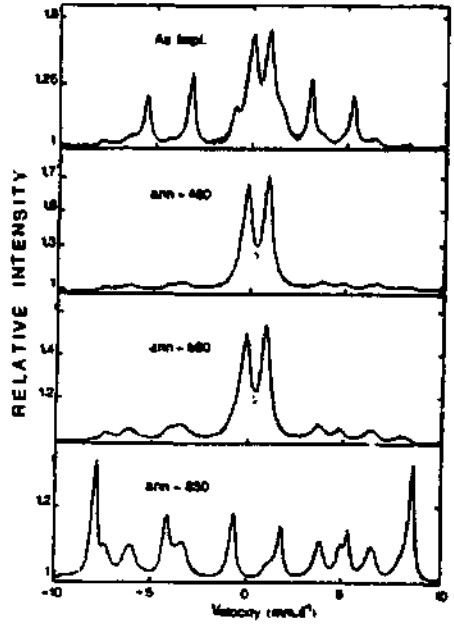

Figure 11 - CEMS Spectra of annealed implanted YIG.

2/ Case of implanted YAG garnets

For the four different implantation doses after annealing at 450°C Mössbauer spectra are converted in an assymmetric doublet which persists even when the temperature is 650°C. In the case of the highest dose a measurement at liquid

helium temperature shows that a part of the amorphous phase is magnetic (**figure 12**).

After annealing at 850°C the recrystallization of implanted $Y_3Al_5O_{12}$ is almost complete. Iron is located in tetrahedral (d) and octahedral (a) sites as shown in **figure 13.** Hyperfine parameters [IS_d = 0.14(2) $mm.s^{-1}$, QS_d = 1.02(4) $mm.s^{-1}$, IS_a = 0.40(4) $mm.s^{-1}$, QS_a = 0.45(2) $mm.s^{-1}$] correspond to the two quadrupole doublets D_d and D_a of a mixed $Y_3Fe_{5-t}Al_tO_{12}$ garnet ($0 < t < 4$) studied by Czerlinsky et al. [35] [IS_d = 0.12 $mm.s^{-1}$, QS = 0.96 $mm.s^{-1}$, IS_a = 0.41 $mm.s^{-1}$, QS_a = 0.46 $mm.s^{-1}$]. To confirm our interpretation 1.1 x 10^{17} $Al^+.cm^{-2}$ have been implanted at 50 keV in a $Y_3Fe_5O_{12}$ single crystal garnet enriched with 25% of ^{57}Fe isotope [14]. In these conditions the local concentration Al/Fe in the implanted layer is comparable to the Fe/Al concentration in YAG. During thermal treatments the recrystallization stages have been found identical in the two cases and seen to be governed by the same thermodynamical and chemical rules (**figures 14 and 15**).

YAG implanted with 10^{17} $Fe^+.cm^{-2}$ and annealed at 850°C has been analysed by XRD. **Figure 16** displays well defined lines corresponding to a $Y_3(Al,Fe)_5D_{12}$ garnet with a Fe/Al = 0.36 ratio. This ratio has been determined from an extrapolation between YAG and YIG lattice parameters. A diffraction spectrum of the first 100 nm outermost layers corresponds to a polycrystalline sample with randomly oriented grains. From the ratio Fe/Al = 0.36 and the area ratio of the two D_d and D_a doublets a mean composition for the substituted garnet has been estimated to be $Y_3[Al_{1.43}Fe_{0.57}](Al_{2.25}Fe_{0.75})D_{12}$.

A measurement at LNT shows that the garnet is magnetic. The average hyperfine field $\langle H \rangle$ = 460 kOe is reduced compared to H_a = 545 kOe and H_d = 474 kOe measured for virgin $Y_3Fe_5D_{12}$ at the same temperature [4]. The two sextuplets relative to a and d-sites are not resolved and broad lines of the sextet are due to a wide inhomogeneity in the iron environments. For the weaker doses the garnet built after annealing at 850°C is not magnetic. This can be explained by a lower iron substitution in the garnet.

3/ Case of implanted GGG garnets

For the sample implanted with 10^{16} $Fe^+.cm^{-2}$ (**figure 17**) and annealed at 400°C or 600°C the Mössbauer spectrum is reduced to a single assymmetric doublet characteristic of an amorphous phase as in the case of YIG and YAG annealed samples.

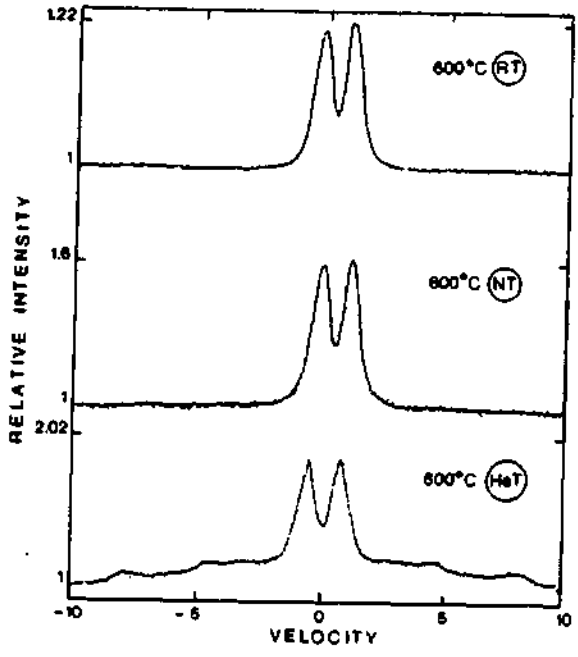

Figure 12 - CEMS spectra of an amorphous garnet created after annealing at 600°C in a 10^{17} ions. cm^{-2} implanted YAG.

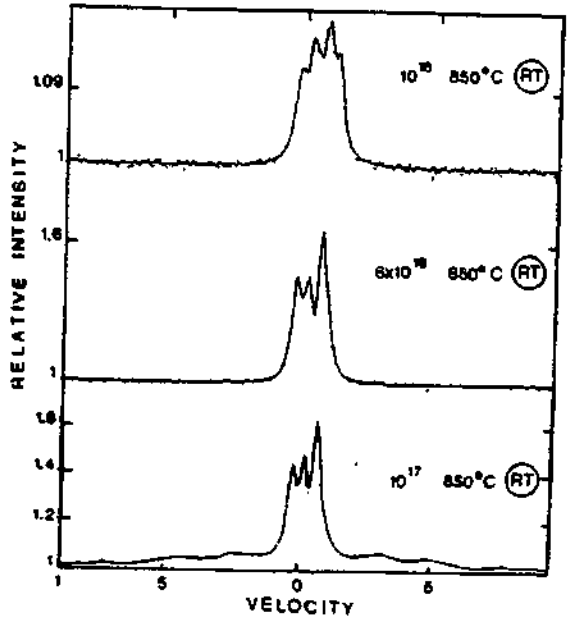

Figure 13 - CEMS spectra exhibiting the recrystallization of the garnet with iron in a and d sites of $Y_3Al_5O_{12}$ after annealing at 850°C.

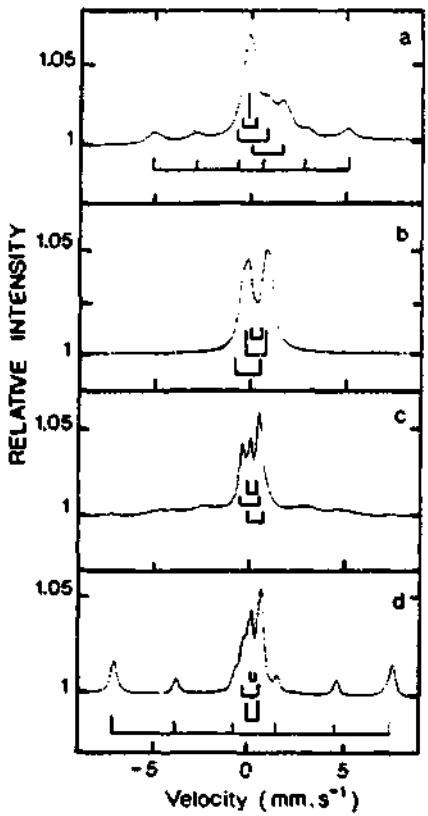

Figure 14 - *CEMS spectra obtained at room temperature for YAG crystal implanted with 100 keV $^{57}Fe^{+}$ ions (1.10^{17} ions.cm^{-2}) (a) and subsequently annealed in air at temperatures of 400°C (b), 850°C (c) and 1100°C (d).*

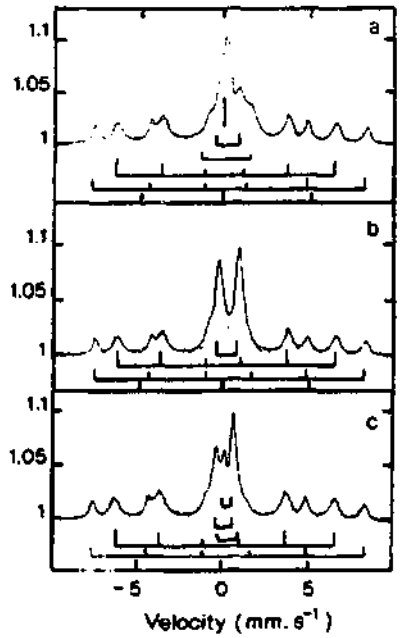

Figure 15 - *CEMS spectra obtained at room temperature for a YIG crystal implanted with 50keV Al^{+} (1.1×10^{17} ions.cm^{-2}) (a) and subsequently annealed in air at 400°C (b) and 850°C (c).*

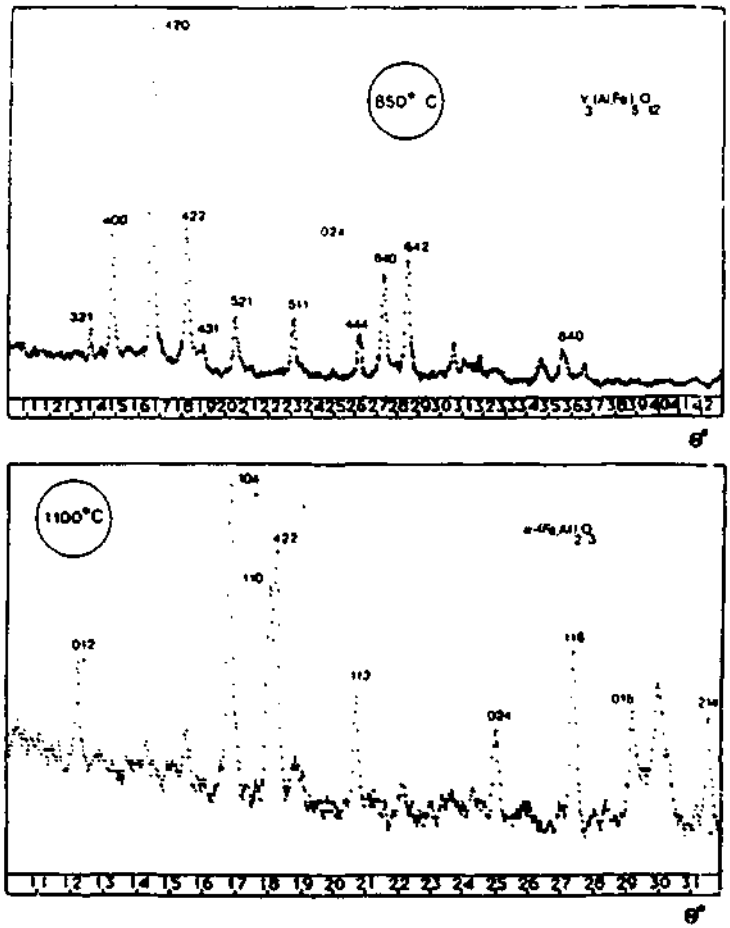

Figure 16 - *Lines of a polycrystalline $Y_3Al_{3.7}Fe_{1.7}O_{12}$ garnet are observed after annealing at 850°C of 10^{17} $Fe^+.cm^{-2}$ implanted YAG. After annealing at 1100°C garnets grains are oriented and observed diffraction lines are due to $\alpha(Fe_{0.87}Al_{0.13})_2O_3$ only.*

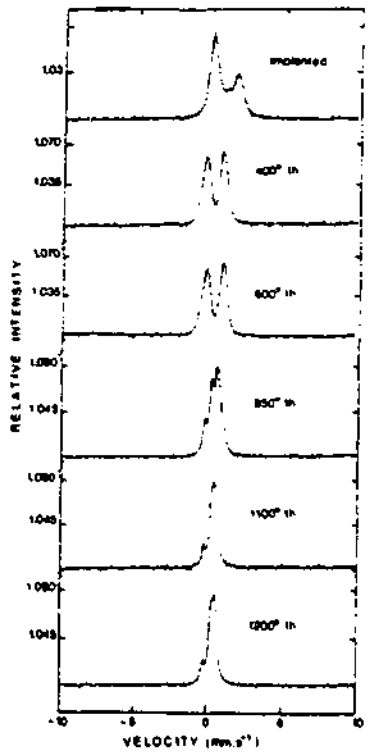

The thermal evolution of the Mössbauer spectrum for the sample implanted with 10^{17} Fe.cm^{-2} and annealed at 200, 400, 650°C is presented in **figure 18.** The $Fe_{1-x}Ga_x$ is stable at 200°C but vanishes at 400°C. Part of iron shares in the formation of an amorphous garnet, the remaining precipitates under mixed $(Fe_{1-x}Ga_x)_2O_3$ characterized by a reduced hyperfine field (HF = 511 kOe) compared to the hyperfine field of a pure α-Fe_2O_3 compound (HF = 518 kOe). The middle part of the spectrum represents the amorphous garnet.

Figure 17 - *CEMS spectra of annealed* 10^{16} Fe^+.cm^{-2} *implanted* $Gd_3Ga_5O_{12}$.

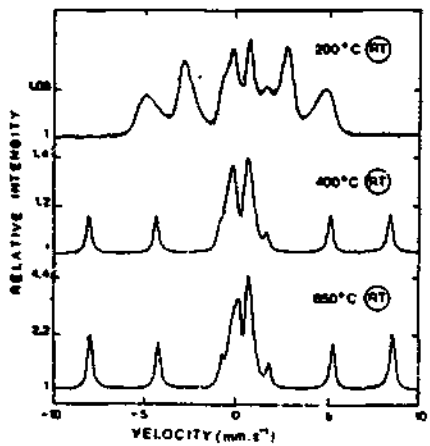

Figure 18 - *CEMS spectra of annealed* 10^{17} Fe^+.cm^{-2} *implanted* $Gd_3Ga_5O_{12}$.

C/ Annealing behaviours above 850°C

This thermal stage is the most interesting because the implanted layers are almost completely recrystallized. Depending on the acceptance of iron by the host different behaviours can be predicted.

1/ Morin transition in YIG

The CEMS spectra obtained at RT and corresponding to implanted YIG subsequently annealed at 850°C, 1100°C, 1200°C and 1300°C are presented in **figure 19.** The vertical broken lines locate the positions of 1, 2, 5 and 6 lines of the sextuplet characteristic of α-Fe_2O_3 ; its hyperfine parameter values are given in **Table III** with those obtained in annealed YAG and GGG samples [36].

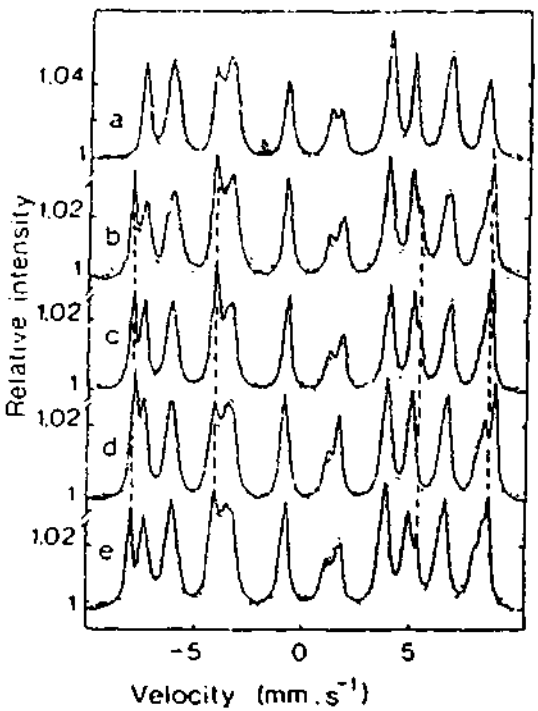

Figure 19 - *CEMS spectra for an enriched YIG : as-grown* **(a)**, *implanted with* 10^{17} $Fe^+.cm^{-2}$ *and annealed at 850* **(b)**, *1100* **(c)**, *1200* **(d)** *and 1300°C* **(e)**.

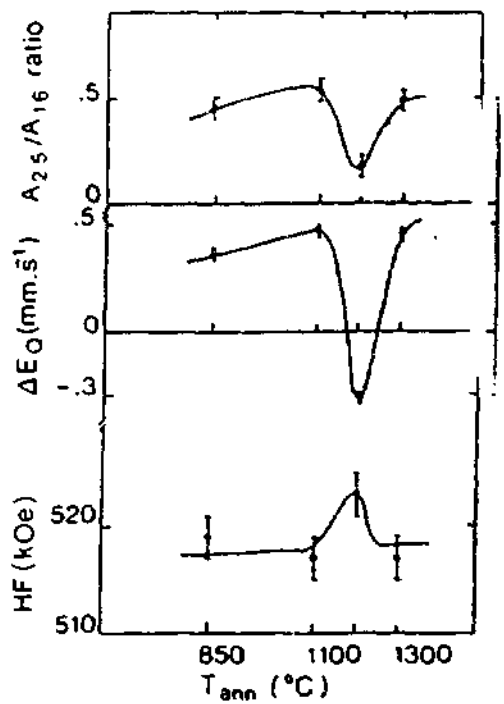

Figure 20 - *Variations of* α-Fe_2O_3 *hyperfine parameters as a function of annealing temperature.*

T_{ann} (°C)		850		1100		1200		1300(1h)		1300(3h)	
		RT	LNT	RT	LNT	RT	LNT	RT	LNT	RT	LNT
YIG	IS	0.38		0.37		0.38	0.55			0.37	0.51
	HF	519		517		523	541			517	544
	ΔE_Q	0.45		0.53		-0.32	-0.84			0.45	-0.82
YAG	IS	0.31	0.49	0.37	0.48			0.39	0.47		
	HF	p(H)	p(H)	503	p(H)			p(H)	p(H)		
	ΔE_Q	0.4	0.45	0.45	0.45			0.12	-0.64		
GGG	IS	0.37	0.48			0.37					
	HF	501	528			p(H)					
	ΔE_Q	0.45	0.39			0.40					

Table III - *Isomer shifts IS and quadrupole splittings ΔE_Q are given in $mm.s^{-1}$ and hyperfine fields HF are in kOe. p(H) means a distribution on HF values.*

There is no change between 850°C and 1100°C but when the annealing temperature rises up 1200°C the line positions of α-Fe_2O_3 are shifted at RT and the quadrupole splitting ΔE_Q defined by $\Delta E_Q = P_{12} - P_{56}$ where P_{12} and P_{56} are the distances between lines 1-2 and 5-6 respectively becomes negative. Such a sign change of ΔE_Q is characteristic of the so-called Morin transition [37, 38] which has been found in certain transition metal ion sexquioxides isomorphous to α-Al_2O_3.

Rhombohedral α-Fe_2O_3 oxide is characterized by an anisotropy transition for a Morin temperature (T_M = 263 K) at which Fe^{3+} spins go from being in the (111) plane with a slight canting out of the plane (weak ferromagnetism for $T > T_M$) to being aligned in the [111] direction which is the symmetry axis of the crystal and the principal axis of the electric field gradient V_{zz} as well. From the Mössbauer spectroscopy point of view this Morin transition will appear by a change in the quadrupole value ΔE_Q as it depends on the angle θ between the direction of V_{zz} and of the hyperfine magnetic field HF acting on the iron nuclei :

$$\Delta E_Q = - eQV_{zz} \quad \frac{3\cos^2\theta - 1}{2}$$

For $T > T_M$, HF is perpendicular to [111], $\theta = \pi/2$, $\Delta E_Q = +1/2\ eQV_{zz}$.
For $T < T_M$, HF is parallel to [111], $\theta = 0$, $\Delta E_Q = - eQV_{zz}$

From Table III it can be inferred that the large α-Fe_2O_3 particles developed in the course of high temperature annealing of Fe-implanted YIG behave as pure

bulk ferric oxide. Moreover this pure α-Fe_2O_3 made after a 1200°C anneal is found to be, at RT, as if it was in the low temperature regime below T_M. We have to point out that for 1200°C there is a simultaneous change in the HF, ΔE_Q and the areal ratio $A_{2,5}/A_{1,6}$ of the second or fifth to the first or sixth line values (**figure 20**). $A_{2,5}/A_{1,6}$ = 0.17(5) indicates an orientation of HF preferentially oriented perpendicular to the surface. After an annealing for 3h at 1300°C α-Fe_2O_3 precipitates recover their "normal" hyperfine parameters indicating a stress release.

A RBS measurement performed after the annealing at 1200°C has shown a strong diffusion of iron inside the lattice. In XRD spectra taken after annealings at 1100°C and 1200°C weak but well defined lines typical of Fe_2O_3 particles are observed (**figure 21**). The intensity ratio of the Bragg rays after 1100°C annealing agrees with a random orientation for Fe_2O_3 precipitates but the large increase in the (104) line intensity is an indication that some Fe_2O_3 grains are preferentially oriented with the c-axis normal to the sample surface after annealing at 1200°C.

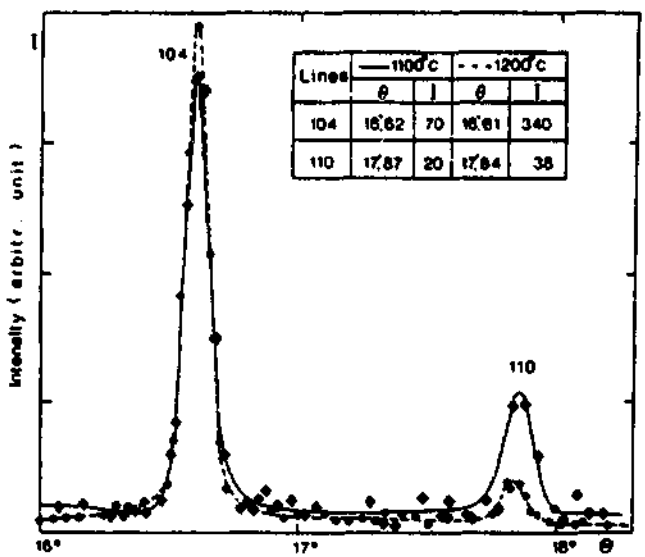

Lines	—1100°C		- - -1200°C	
	θ	I	θ	I
104	16,62	70	16,61	340
110	17,87	20	17,84	38

Figure 21 - *XR Dspectra at glancing angle of α-Fe_2O_3 particles after annealing at 1100 and 1200°C. The intensity variation shows a [111] orientation normal to the surface for these particles after 1200°C annealing.*

In TEM big precipitates of Fe_2O_3 (mean diameter $d \approx 200$ nm) are obvious after annealing at 1100°C (**figure 22**). The subsequent annealing at 1200°C increases the particle size ($d \sim 300$ nm) and the bigger precipitates exhibit facets with an hexagonal geometry (angles between faces = 120°). Cross-section micrographs display large α-Fe_2O_3 precipitates (300 nm length and 100 nm thick), oriented along the [111] direction and half sunk in YIG (**figures 23 and 24**). In these micrographs we observe that precipitates are completely located near the surface, their shape is not at all spherical and their thickness is on average less than 100 nm.

Figure 22 - *A TEM spectrum of a 10^{17} Fe.cm^{-2} implanted $Y_3Fe_5O_{12}$ and annealed at 1100°C (perpendicular view of the surface).*

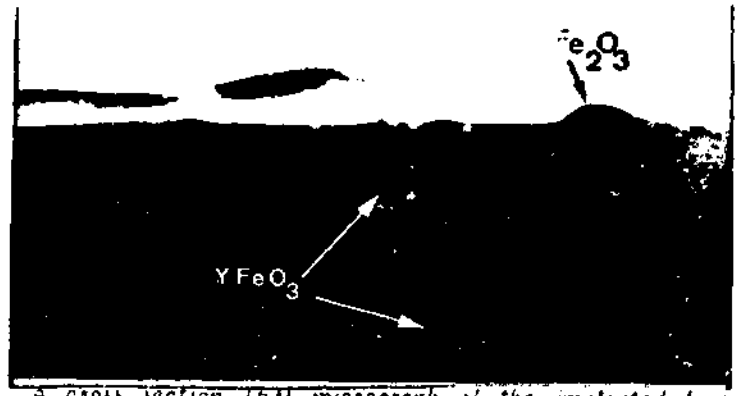

Figure 23 - A cross section TEM micrograph of the implanted layer after annealing at 1200°C.

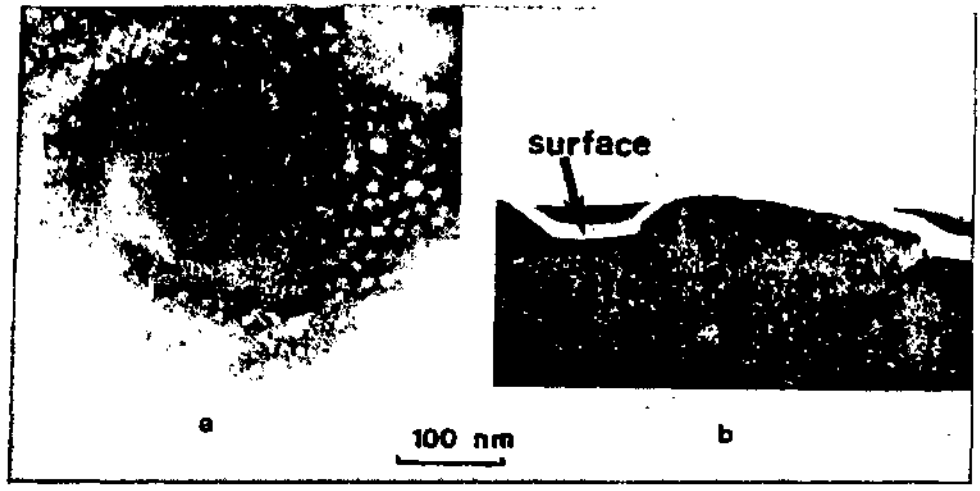

Figure 24 - TEM spectra of an α-Fe_2O_3 particle. (a) perpendicular view of the surface, (b) cross section view.

2/ Mixed α-$(Fe_{1-x}Al_x)_2O_3$ oxide

Mössbauer spectra of 10^{17} $Fe^+.cm^{-2}$ implanted YAG have been registered at RT and LNT after annealing at 1100°C for 1h (**figure 25 a-b**). These is a coexistence of a garnet structure (magnetic at LNT) with an oxide whose parameters are compiled in **Table III.** The line shapes are not lorentzian and we have to assume a distribution in hyperfine fields. It is noteworthy that the quadrupole splitting ΔE_Q remains positive. A XRD measurement (**figure 16**)

proves that these precipitates are substituted $(Fe_{1-x}Al_x)_2O_3$ oxides with $\bar{x} = 0.1$; $\bar{x}$ is determined from an extrapolation between the lattice parameters of isomorphous α-Al_2O_3 and α-Fe_2O_3. A line located at 18.2° is attributed to the (422) reflexion of $Y_3Al_5O_{12}$ and its relative large width confirms that defects still exist into the matrix.However, as only one line is detected and not a powder spectrum as after annealing at 850°C, it is possible to assume that the garnet has removed its crystalline state. From the dependence of HF as a function of the mean concentration $\bar{x}$ measured by Janot et al. [39] we deduce $\bar{x} = 0.1$ in accordance with the XRD measurement. These oxide precipitates have also been observed by TEM measurements [24] for 10^{17} Fe.cm^{-2} but not for 1 and 3×10^{16} ions.cm^{-2}. Their shape is oblate and they are randomly oriented.

When an annealing is performed at 1300°C for 1h (**figure 25 c-d**) the amount of iron substituted in the garnet structure diminishes whereas the oxide quantity increases.

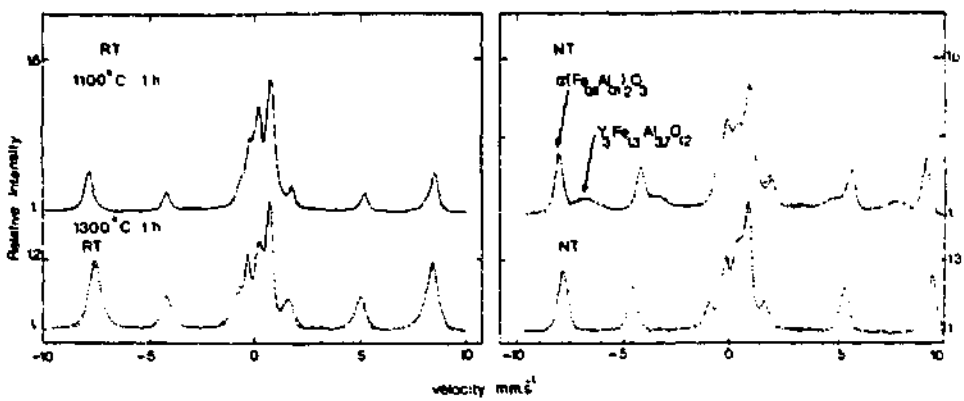

Figure 25 *- CEMS spectra registered at RT and LNT for a 10^{17} $^{57}Fe^{+}$.cm^{-2} implanted YAG (a-b) after annealing at 1100°C ; (c -d) after annealing at 1300°C.*

The iron diffusion observed by a RBS measurement [29] explains the larger Al concentration in α-$(Fe_{1-x}Al_x)_2O_3$ which is confirmed by the decrease of HF (496(3) kOe) at RT. From this value it is possible to estimate $\bar{x} = 0.23$. The abnormal value $\Delta E_Q = 0.12(3)$ mm.s^{-1} (**Table III**) shows a change in the orientation of the Fe^{3+} spins versus [111] direction as in the case of iron implanted YIG.

A longer annealing (3h) at 1300°C completely eliminates the oxide contribution in the CEMS spectrum. By RBS iron is no more visible. Iron has diffused into

the matrix and the garnet which was formed during the annealing at 850°C is now poorer in iron and then it remains paramagnetic even at low temperature. A TEM measurement has shown that very big precipitates ($\bar{d}$ = 235 nm) are found at the surface level after the first annealing at 1300°C.

3/ Mixed α-$(Fe_{1-x}Ga_x)_2O_3$.

We have shown that 800°C is the recrystallization temperature for garnets and during its diffusion iron is able to substitute to gallium to share in the formation of a $Gd_3(Ga,Fe)_5O_{12}$ garnet during the reepitaxial regrowth of the damaged layer. Evolution of CEMS spectra for 10^{16} $Fe^+.cm^{-2}$ is presented in figure 17. The sample remains paramagnetic after 1100 and 1200°C annealings and spectra can be fitted with the two doublets characteristic of d and a-sites of a garnet and with a doublet due to the presence of a mixed $\alpha(Fe,Ga)_2O_3$ oxide as in the case of YAG.

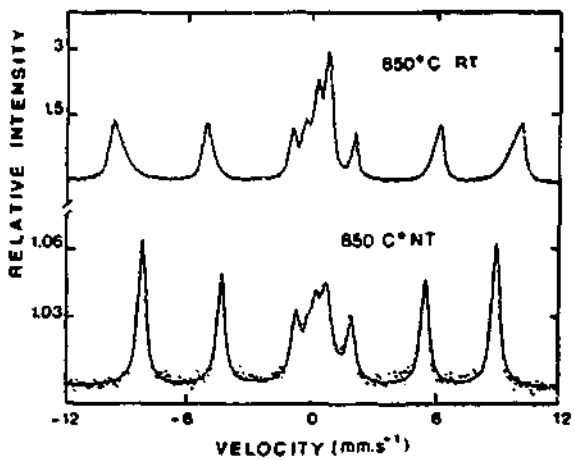

Figure 26 - CEMS spectra at RT and LNT of 10^{17} $Fe^+.cm^{-2}$ implanted $Gd_3Ga_5O_{12}$ garnet after a 850°C annealing.

For 10^{17} $Fe^+.cm^{-2}$ the phases are the same but now a large magnetic component due to $\alpha(Fe,Ga)_2O_3$ appears (figure 26). Its hyperfine magnetic field value decreases when the annealing temperature increases (511 kOe at 650°C, 501 kOe at 850°C and <430> kOe at 1200°C). This decrease can be escribed to the diffusion of iron inside or outside the matrix and subsequently to the formation of a mixed oxide becoming richer in gallium. The p(H) distribution is due to various x values for $(Fe_{1-x}Ga_x)_2O_3$. No Morin transition has been detected even after annealing at 1200°C.

By TEM (figures 27 and 28) it is possible to observe Fe_2O_3 precipitates after annealings at 1100 and 1200°C. The density is about 10^{8} particles.cm^{-2}. A short annealing at 1300°C is enough to remove the precipitates.

Figure 27 - A cross-section TEM micrograph of GGG annealed at 1100

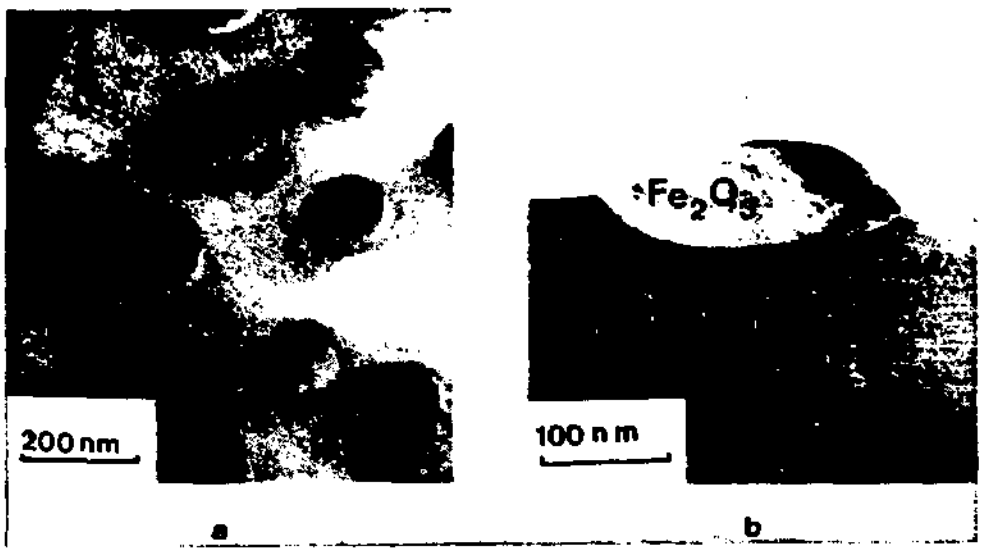

Figure 28 - TEM Spectra of 1200°C annealed GGG
(a) perpendicular view of the surface
(b) cross-section

IV. DISCUSSION

It has been seen that for the different garnets three annealing stages have to be considered : just after implantation, annealings below 650°C and then above 800°C. When in the first stage phases due to iron implantation depends on the garnet and on the dose, in the two other stages the evolution of the implanted layer is rather similar with at the beginning a transformation of metastable phases in an amorphous garnet and after a complete recrystallization of the perturbed zone with creation of a new garnet and of an oxide with participation of the implanted iron.

A/ Characterization of implanted iron in garnets

In figure 29 are presented CEM spectra [26] obtained with 10^{16} and 10^{17} ions.cm^{-2} implanted garnets : YIG, YAG, GGG and a ferrimagnetic bubble garnet $(Y\ Sm\ Lu\ Ca)_3(Fe\ Ge)_5O_{12}$.

Iron implantation with 10^{16} ions.cm^{-2} dose leads mainly to the amorphization of the outermost layers of garnets. Iron is dispersed in the implanted layers and locally it can precipitate into small superparamagnetic iron aggregates or oxide compounds. At higher doses the local iron concentration is enough to give rise to precipitation of larger iron aggregates. In YIG iron is overstoichiometric and only big ferromagnetic α-Fe aggregates exist. In the other garnets a distribution in size appears : dispersion of small precipitates visible on the TEM micrograph, broad lines in X-ray diffraction spectra, non-Lorentzian lines for YAG and bubble garnet, single line for YAG in CEMS spectra.

The chemical affinity of garnet elements with iron plays a role formation of other phases. Even for 10^{16} ions.cm^{-2} iron is associated with y to form YFe compound in YAG. In GGG the affinity between iron and gallium hinders formation of iron precipitates and favours the creation of a magnetic $Fe_{1-x}Ga_x$ compound with x depending on the dose. In any garnet iron substitutes easily after implantation.

In YAG, GGG and the bubble garnet exists a Fe^{2+} state (doublet with IS = 1.0 mm.s^{-1} and QS = 1.65(10)mm.s^{-1}) whatever the dose is. Coey et al. [28] have measured IS = 0.95 mm.s^{-1} and QS = 1.75 mm.s^{-1} for $FeGa_2O_4$ and Ogale et al. [40] have determined for Fe Al_2O_4 IS = 1.00 mm.s^{-1} and QS = 1.65 mm.s^{-1}. Just after implantation we propose to assume that iron is embedded into ferrite compounds.

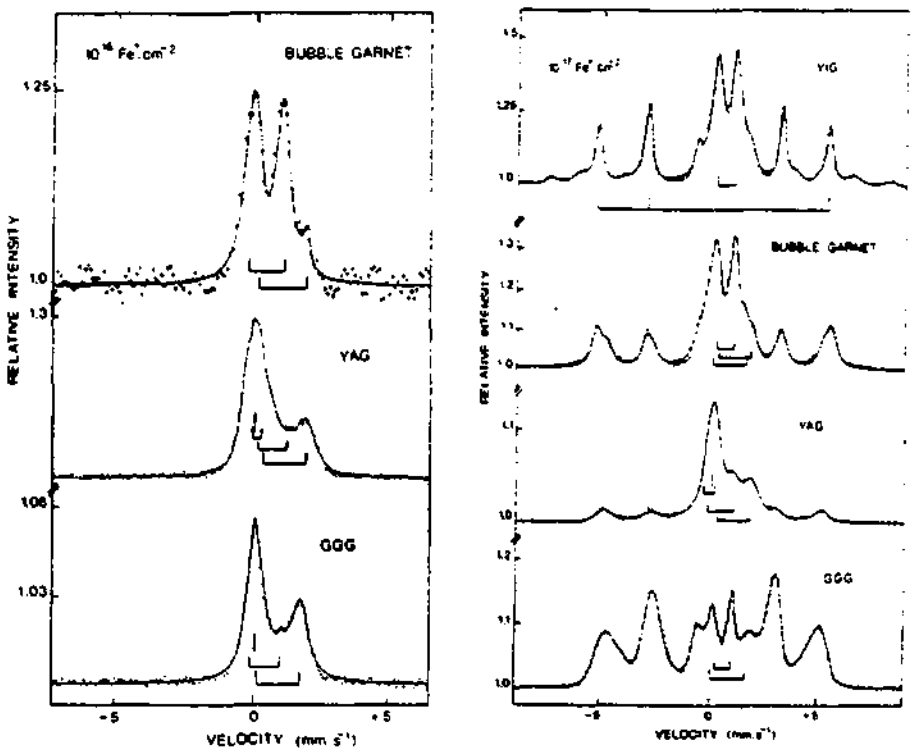

Figure 29 - CEMS spectra for YIG, YAG, GGG and ferrimagnetic bubble garnets implanted with (a) 10^{16} $^{57}Fe^{+}.cm^{-2}$, (b) 10^{17} $^{57}Fe.cm^{-2}$.

B/ Annealings at low temperatures (T_{ann} < 650°C)

Thermal treatments allow the recrystallization of damaged matrix by internal processes such as defects annealings or impurity diffusion. For T_{ann} < 650°C the behaviour of the various garnets is identical.

Fe^{2+} and Fe^{0} valence states disappear at 200°C and iron is completely oxidized. It is only for GGG that 400°C is needed to vanish the metallic Fe-Ga phase. The hyperfine parameters IS = 0.31(2) $mm.s^{-1}$, QS = 1.18(8) $mm.s^{-1}$ of the

assymmetric doublet correspond to the values IS = 0.31 $mm.s^{-1}$, QS = 1.12 $mm.s^{-1}$ obtained by Gyorgy et al. [41] for an amorphous $Y_3Fe_5O_{12}$ garnet. In fact we propose in this study that the doublet can be due to the coexistence of an amorphous garnet ($Y_3Fe_5O_{12}$, $Y_3Al_{5-x}Fe_xO_{12}$, $Gd_3Ga_{5-x}Fe_xO_{12}$) and a mixed $\alpha(Fe_{1-x}M_x)_2O_3$ oxide with M = Ga or Al ($0 \leq x \leq 1$).

C/ **Recrystallization of implanted garnets**

After annealing at 850°C Mössbauer spectra show a recrystallization of garnets. XRD and TEM measurements on $Y_3Al_5O_{12}$ and $Y_3Fe_5O_{12}$ display a polycrystalline outermost layer (~ 100 nm). It is possible that recrystallization starts from dispersed points of nucleation and then garnet grains growth without preferential orientation. After thermal treatment at 1100°C samples become single crystals due to a correlation between the reepitaxial front coming from the bottom of the damaged layer and the grains of the polycrystalline garnet located near the surface. Then other compounds different from the garnet can be observed by TEM as they are crystallographically uncorrelated with the matrix (**figure 16**).

The substitution of iron about 850°C in the garnet structure is not identical for YAG and GGG. For YAG the almost totality of implanted iron is embedded into a polycrystalline garnet which is magnetic at LNT. For GGG only a third of implanted iron is included in the formation of a mixed garnet, the other part remaining oxidized in $\alpha(Fe,Ga)_2O_3$ precipitates. This different behaviour can be due to the fast diffusion of iron as shown by RBS measurements.

A limited amount of iron is accepted to form during the reepitaxial regrowth a $RE_3M_{5-x}Fe_xO_{12}$ garnet (RE is a rare earth, M a diamagnetic ion). An explanation of this restricted acceptance can lie in the differences between the lattice parameters of the host $Y_3Al_5O_{12}$ (a = 12.00 Å) or $Gd_3Ga_5O_{12}$ (a = 12.376 Å) and the garnet we want built : $Y_3Fe_5O_{12}$ (a = 12.376 Å) or $Gd_3Fe_5O_{12}$ (a = 12.479 Å). At 1100°C, due to the co-ordination between the polycrystalline garnet and the substrate, only a limited quantity of iron can be accepted to limit the lattice differences. Then the refused overstoichiometric iron can only form mixed $(Fe_{1-x}M_x)_2O_3$ oxides with trivalent ion M = Al or Ga.

D/ Substituted $\alpha(Fe,M)_2O_3$ oxides

These oxides are very well characterized with Mössbauer spectroscopy. The reduction in the hyperfine field value with respect to the value for pure αFe_2O_3 hematite is proportional to the number of introduced (Ga^{3+} or Al^{3+}) impurities. For $Y_3Fe_5O_{12}$ the iron oxide is pure hematite and its microscrystals located near the surface increase as the temperature arises. With a mean range of 40 nm for implanted iron we can imagine that iron oxide particles are closed in the first 50 nm and that finally during the recrystallization process they can expand toward the free surface only.

For highest annealing temperatures (1200 and 1300°C) an orientation of Fe^{3+} spin along the [111] direction of rhombohedral oxide has been observed. This Morin transition (EQ = -0.81 $mm.s^{-1}$) occurs at RT and this very astonishing behaviour could be explained by pressure effects due to lateral strains existing in the recrystallized zone. This phenomenon disappears after a further annealing for 3h when oxide particles break the surface as it has been displayed by TEM measurements (**figure 23**). Very recently Bruzzone et al. [42] have studied the variation of the Morin transition of αFe_2O_3 as a function of applied hydrostatic pressures. They have shown that a pressure of about 15 kbar can induce a Morin transition at RT.

For $Y_3Al_5O_{12}$ and $Gd_3Ga_5O_{12}$ garnets the Morin transition of mixed oxide is influenced by the presence of diamagnetic impurities. These impurities can lower the Morin temperature [43]. De Grave et al. [44] have shown that the transition was lowered below 77 K (instead 263 K for pure αFe_2O_3) for an $\alpha(Fe_{1-x}Al_x)_2O_3$. When $x > 0.077$ no Morin transition occurs even at 77 K. In our implanted $Y_5Al_5O_{12}$ garnet implanted with $10^{17} Fe^+.cm^{-2}$ we have estimated from the GXRD measurement that after annealing at 1100°C $x = 0.13$.

Quadrupole splittings deduced from Mössbauer spectra indicate no Morin transition : EQ = 0.45(3) $mm.s^{-1}$ at RT and EQ = 0.41(3) $mm.s^{-1}$ at LNT. After a further annealing at 1300°C for 1h lateral strains can exert on oxide precipitates orientating magnetic moments of iron because lattice deformations. The measured effective field H_{eff} = 496(4) kOe, lower than 503(4) kOe obtained after 1100°C annealing, shows that Al concentration has increased. Consequently, in absence of

strains, the Morin transition must be lower. In fact, fits of CEMS spectra give EQ = 0.11(3) $mm.s^{-1}$ and - 0.64(3) $mm.s^{-1}$ at RT and LNT respectively. The quadrupole splitting is small at RT but not negative. We can assume that strains are too weak to induce a Morin transition at RT because diamagnetic ions play an antagonistic role. A subsequent annealing at 1300°C for 1h removes this phenomenon.

In the case of the paramagnetic $Gd_3Ga_5O_{12}$ garnet implanted with 10^{17} $Fe^+.cm^{-2}$, mixed $\alpha(Fe_{1-x}Ga_x)_2O_3$ oxides have no Morin transition due to the high concentration in gallium ($x \simeq 0.2$). The Morin transition must be below 77 K and no strains on oxide particles could be detected because during the last annealing at 1300°C for 1h the magnetic phase of oxides was completely vanished.

V. CONCLUSION

In this paper a contribution to the study of various garnets implanted with iron and their evolution during thermal treatments have been presented. The association of complementary techniques well adapted to the study of implanted layers has allowed to draw some conclusions :

.. Ion implantation of iron in garnets can produce segregation phenomena or create new phases with matrix elements. These effects are complex and depend on dose and garnet.

.. Annealings under air show the metastability of produced phases and the participation of iron to the formation of new garnets and of α-Fe_2O_3 or $\alpha(Fe,M)_2O_3$ oxides with M = Al, Ga. Annealing temperatures above 800°C are necessary to completely recrystallize the implanted layer.

.. Alterations of the Morin temperature can be explained by the occurence of lateral strains produced during the total rebuilding of the implanted layer about 1200°C. For the first time a Morin transition has been detected above RT in pure α-Fe_2O_3 without the use of external mechanical means. More accurate measurements of the lattice parameters are now being made in order to examine the high pressure assumption.

ACKNOWLEDGMENTS

The author is very indebted to his co-workers Dr. N. KORNILIOS (I.P.N. Lyon) for CEMS measurements, Drs. F. RAVEL and Ph. GERARD (LETI-C.E.N. Grenoble) for TEM study, Drs. B. GILLES and M. BRUNEL (C.N.R.S. Grenoble) for GXRD spectra, Dr. A. PEREZ (D.P.M. - U.C.B. Lyon-1) for RBS measurements, Dr. A. PLANTIER (I.P.N. Lyon) who carried out the implantations.

REFERENCES

[1] P. GERARD
Thin Solid Films, **114 (1984)** 3

[2] P. GERARD, M. MADORE, G. SURAN
IEEE Trans. Magn. Mag., **18** (1982) 1274

[3] G. MAREST, A. PEREZ, J.L. PONTHENIER, P. GERARD, J.M. ROBERTSON,
J. Appl. Phys., 55 (1984) 2560

[4] G. MAREST, A. PEREZ, P. GERARD, J.M. MACKOWSKI
Phys. Rev., B-34 (1986) 4831

[5] P. GERARD, F. RAVEL, J.L. PONTHENIER, M. DUPUY, B. BLANCHARD
J. Appl. Phys., 55 (1984) 2563

[6] T. OMI, C.L. BAUER, M.H. KRYDER
J. Appl. Phys., 53 (1982) 2528

[7] P.J. PICONE, A.H. MORRISH
J. Appl. Phys., 53 (1982) 2471

[8] C.P. SKRIMSHIRE, G. LONGWORTH, G. OEARNALEY
J. Phys., D-12 (1979) 1951

[9] P.J. PICONE, A.H. MORROSH
Solid State Comm., 34 (1980) 743

[10] P.H. SMIT, H.A. ALGRA, J.M. ROBERTSON
Appl. Phys., 22 (1980) 299

[11] P.H. SMIT, H.A. ALGRA, J.M. ROBERTSON
J. Appl. Phys., 52 (1981) 2364

[12] A. PEREZ, G. MAREST, P. GERARD, M. MADORE, P. MARTIN
Nucl. Instr. Meth., **209/210** (1983) 1175

[13] G. MAREST, P. GERARD, A. PEREZ
Mater. Res. Soc. (Europe) Proceedings, (June 1984) p. 227

[14] G. MAREST, K. KORNILIDS, A. PEREZ, P. GERARD
Hyperfine Inter., 29 (1986) 1249

[15] B.M. PAINE, V.S. SPERIOSU, L.S. WIELUNSKI, H.L. GLASS, M.A. NICOLET,
Nucl. Instr. Meth., 151 (1981) 80

[16] P. GERARD, M.T. DELAYE, R. DIANELOU
Thin Solid Films, 88 (1982) 75

[17] P. GERARD, M. MARTIN, R. DIANELOU
J. Magn. Magn. Mater., 35 (1983) 303

[18] D. KELLOWE, L.S. WIELUNSKI, H.S. JUN, R.E. BENENSON
Nucl. Instr. Meth. in Phys. Res., B-2 (1984) 729

[19] W.H. de ROODE, H.A. ALGRA
J. Appl. Phys., 53 (1982) 2471

[20] H.AWANO, V.S. SPERIOSU, C.H. WILTS
J. Appl. Phys., 55 (1984) 3043

[21] J. MARTENSEE, C.W. SEARLE, H.A. WASHBURN
J. Appl. Phys., 52 (1981) 2361

[22] O. MASSENET
Nucl. Instr. Meth., 153 (1978) 419

[23] G. LE CAER, J.M. DUBOIS
J. Phys., E-12 (1979) 1083

[24] F. RAVEL
Thesis, I.E.T.I.-C.E.N.G, Univ. Grenoble, (1986)

[25] M. BRUNEL, F. de BERGEVIN
Acta Cryst., A-42 (1986) 299

[26] N. KORNILIOS, G. MAREST, A. PEREZ, M. BRUNEL, B. GILLES, P. GERARD, F. RAVEL
Nucl. Instr. Meth. in Phys. Res., B-19/20 (1987) 860

[27] M. EIBSCHUTZ, M.E. LINES, K. NASSAU
Phys. Rev., B-21 (1980) 3767

[28] J.M.D. COEY, E. DELVIN, R.J. GAMBINO
J. Appl. Phys., 53 (1982) 7810

[29] N. KORNILIOS
Thesis. Univ. Lyon, (November 1986)

[30] G. LE CAER, J.M. DUBOIS, H. FISHER, V. GONSER, H.G. WAGNER
Nucl. Instr. Meth. in Phys. Res., B-5 (1984) 25

[31] L.R. NEWKIRK, C.C. TSUEI
Phys. Rev., B-4 (1971) 4046

[32] B. GILLES
Thesis, Univ. Grenoble, (December 1986)

[33] H.L. LUO
Trans. AIME, 239 (1967) 119

[34] W. KUNDIG, H. BOMMEL, G. CONSTABARIS, R.H. LINDQUIST
Phys. Rev., 142 (1966) 327

[35] E.R. CZERLINSKY, R.A. MAC MILLAN
Phys. Stat. Sol., **41** (1970) 333

[36] G. MAREST, N. KORNILIOS, A. PEREZ, F. RAVEL, P. GERARD, B. GILLES, M. BRUNEL
Proc. "Hyperfine Interactions", Conference Bangalore (India) (1986) (to be published)

[37] O. KISTNER, A. SUNYAR
Phys.Rev. Lett., **4** (1960) 412

[38] J.O. ARTMAN, J.C. MURPHY, S. FONER
Phys. Rev., **A-138** (1965) 912

[39] C. JANOT, H. GIBERT
Bull. Soc. Franç. Minéral. Cristall., **93** (1970) 213

[40] S.B. OGALE, D.M. PHASE, P.P. PATIL, S.M. KANETKAR, S.V. GHAISAS, V.G. BHIDE, S.K. DATA
Hyperfine Inter., **29** (1986) 1193

[41] E.M. GYORGY, K. NASSAU, E. EIBSCHUTZ, J.R. WASZCZAK, C. WANG, J.C. SHELTON
J. Appl. Phys., **50** (1979), 2883

[42] C. BRUZZONE, R. INGALLS
Phys. Rev., **B-28** (1983) 2430

[43] P. BESSER, A. MORRISH, C. SEARLE
Phys. Rev., **153** (1967) 2632

[44] E. DE GRAVE, L.H. BOWEN, S.B. WEED
J. Magn. Magn. Mat., **27** (1982) 2471

RECENT RESULTS ON IMPLANTED IMPURITY ATOMS IN FERROMAGNETIC HOSTS OBTAINED WITH PAC

Klaus-Peter Lieb and Friedrich Raether
II. Physikalisches Institut, Universität Göttingen, and
Sonderforschungsbereich 126, Göttingen/Clausthal,
D-3400 Göttingen, Fed. Rep. Germany

I. Introduction

Probing the hyperfine interaction of impurity atoms in ferromagnetic hosts has been a longstanding task in which many nuclear and solid state physicists have been involved. Progress in this area has come in "waves" whenever new implantation facilities (for instance ISOLDE at CERN, heavy ion accelerators,..), measuring techniques (μ-spin resonance, NMR on oriented nuclei in sub-Kelvin cryostats,...) or new theoretical approaches became available. We have seen some fine examples for new results in several contributions to this Conference.

In this talk, we shall give a brief survey over a number of studies which the Göttingen group has recently performed or in which we have been involved. In all experiments, the IMPAD or TDPAC technique after in-beam recoil implantation with heavy-ion reactions or implantation of the radioactive nuclei with an ion implanter (ISOLDE at CERN, IONAS at Göttingen) have been employed. Several of these studies are devoted to characterize the implantation site(s) in the ferromagnetic lattice in order to calibrate the magnetic hyperfine field(s) and ultimately to deduce nuclear magnetic moments. Others were explicitly undertaken to investigate defect configurations (e.g. in the case of ^{111}In in fcc-Co), phase transitions and/or chemical reactions (^{111}In in NiO [BOL87]). It is these two faces which makes this type of research exciting most of the time, but occasionally frustrating.

II. Substitutional implantation - the systems Cr and Br in Fe

In light nuclei, very often the IMPAD technique is the only way to find out the distribution of impurity fields caused by different micro-environments, as there are essentially no Mössbauer probes and few isomeric states populated in cascades following sufficiently long-lived β-emitters. In continuation of our previous heavy-ion IMPAD experiments on ^{41,42}Ca and ^{40,41,43}K in Fe [UHR75,BRA78,BER83,RAE84], we have recently studied the system ^{48}V/Fe in order to complete the systematics of impurity atoms near the Z=18 electronic shell closure [RAE87a].

The ^{48}Cr activity was produced via the reaction ^{46}Ti(α,2n) with the 43 MeV α-beam of our synchrocyclotron. A multi-layer target consisting of twelve 11 μm thick ^{nat}Ti foils and twelve 3 μm thin annealed Fe foils was chosen so that the recoil implanted ^{48}Cr nuclei came to rest in the Fe foils. When the irradiated Ti foils were separated from the foil stack and since the activation of the Fe backings by the α-beam did not interfere with the 113-308 keV cascade in ^{48}V populated in the EC decay of ^{48}Cr ($T_{1/2}$=21.56 h), the Larmor precession in the 308 keV isomeric state (τ=10.3 ns) could be measured via the PAC technique with a set-up of four BaF_2 detectors. The detectors, each 45 mm in diameter and 38 mm in length, were arranged in 90° geometry; they were coupled to XP2020Q photomultipliers and a conventional fast-fast coincidence circuit with window constant fraction discriminators. The 12 time spectra of all possible coincidence combinations were stored in a CAMAC histogramming memory. The circuit is displayed in Fig. 1; the prompt time spectrum of the 113-308 keV coinicidence had a resolution of 1.0 ns FWHM. The measured perturbation spectra

$$R(t) = [W(180,t)-W(90,t)]/W(180,t)+W(90,t)]$$

of which one is displayed in Fig. 2 can be fitted with a single Larmor frequency ω_L=93.0(3) MHz; the fraction at this site exceeds 80% and is attributed to substitutional implantation. Adopting the magnetic hyperfine field obtained from NMR, B=8.73(3) T [ROI64], we find the g-factor of the 308 keV atate as g=0.222(8), in fair agreement with the result of a previous time integral measurement in an external field, g=0.188(17) [AUE67]. No other fraction with a well defined Larmor frequency was observed.

A similar experiment [RAE87b] has been performed for the 755-250 keV cascade in ^{77}Se involving the 250 keV isomeric state (τ=13.4 ns, g=0.42(4)) and fed in the β-decay of ^{77}Br ($T_{1/2}$=57 h). The ^{77}Br activity was produced at ISOLDE and implanted at room temperature into a polycristalline Fe foil which had been annealed for 10 h at 1230 K; the implantation dose was 6 10^{13} cm^{-2} and the implantation energy was 60 keV. The PAC spectra were again taken

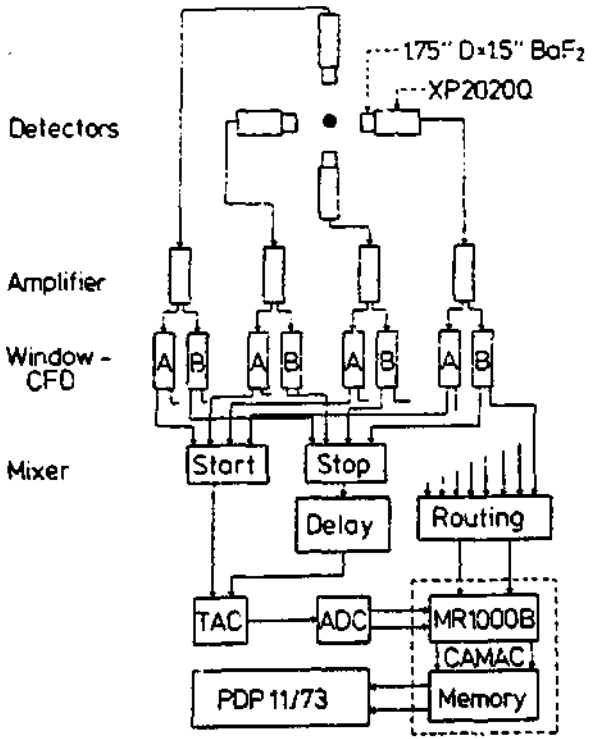

Fig. 1: PAC fast-fast coincidence circuit with BaF_2 detectors

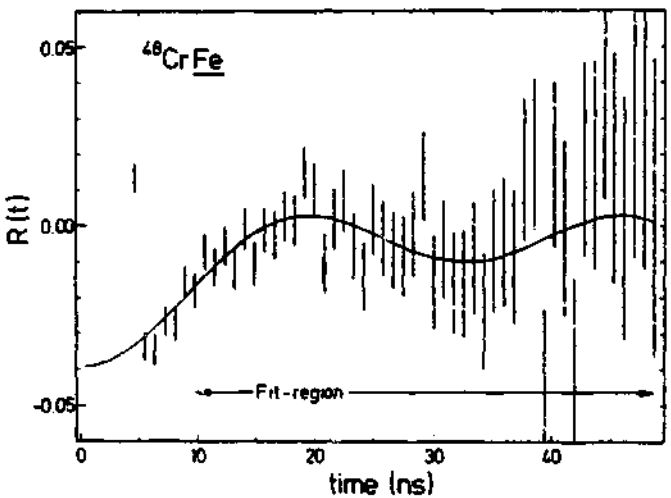

Fig. 2: Perturbation function of the 113-308 keV cascade in 48V after recoil implantation of ^{48}Cr in Fe

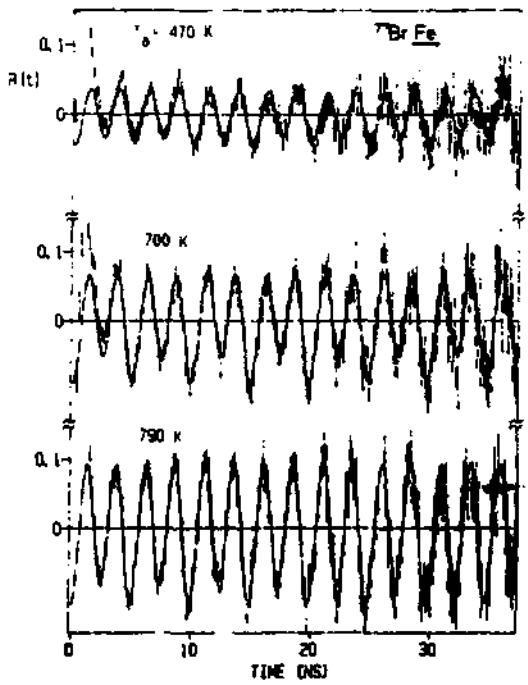

Fig. 3: PAC spectra of the 755-250 keV cascade in ^{77}Se after implantation of ^{77}Br in Fe and annealings at 470, 700 and 790 K.

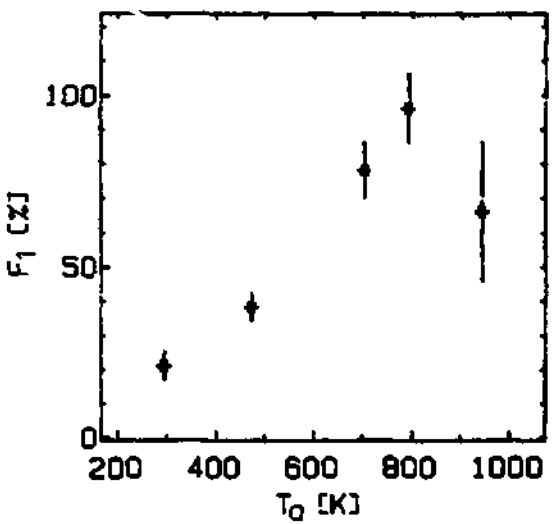

Fig. 4: Substitutional fraction f_1 as function of the annealing temperature T_a.

with the BaF_2 apparatus at Göttingen, in the course of an annealing program of successive vacuum heatings at 470, 700, 790 and 940 K, for 15 min each. The perturbation functions displayed in Fig. 3 clearly show a single Larmor frequency of $\omega_L(RT)$ = 1272(2) MHz, attributed to substitutional, defect-free implantation. Its fraction rises from 21(4) % after implantation to nearly 100 % at 793 K, but then the total activity drops due to outdiffusion of the ^{77}Br activity (see Fig. 4). This diffusion process was confirmed in a Rutherford backscattering experiment with 1.0 MeV α-particles impinging onto an iron foil into which we had implanted $4*10^{15}/cm^2$ $^{81}Br^+$ ions at 80 keV.- We also performed a PAC control experiment in which we implanted $5*10^{10}/cm^2$ ^{77}Br ions ($+2*10^{14}/cm^2$ ^{79}Br ions) at 270 keV into an annealed Fe foil. The ^{77}Br activity was produced in the synchrocyclotron via the reaction $^{77}Se(d,2n)$ at 15 MeV, chemically separated from the target material and transferred to $K^{77}Br$ and finally placed into the ion source of IONAS. The Larmor frequency found at the higher implantation energy and lower dose, ω_L=1260(70) MHz, is in good agreement with the previous figure.

Using the rather badly known g-factor of the isomeric state [AUE67], one arrives at a substitutional hyperfine field of B(SeFe)=62(6) T which is in agreement with the previous figure B=69(6) T obtained in an NMR/ON experiment for ^{82}Br [CAL74]. Clearly, a remeasurement of the g-factor with higher accuracy would make this probe very useful for further studies, in connection with BaF_2 detectors. It is norteworthy that no other sharp Larmor frequency was observed in the Fourier spectrum. Since the Oxford group, in a channeling experiment, had found evidence for a large fraction of non-substitutional Br atoms with a well defined position in the lattice [ALE74], we had hoped to identify the corresponding complex as component in the hyperfine spectrum. The present experiment excludes such component of more than 30%, if the quadrupole frequency of this complex does not exceed $\omega_Q \approx 200$ MHz. For higher ω_Q values the quadrupole splitting would give rise to a complex hyperfine spectrum which would be difficult to disentangle. On the other hand, such large quadrupole interaction seems rather unlikely.

Fig. 5 summarizes the substitutional hyperfine fields of light impurities in iron and their fractions at room temperature implantation. Also given are the fields calculated by Kanamori and coworkers [KAN84, AKA83]. It is evident that the implantation of "oversize" impurities near the Z=18 and Z=36 shell closures into substitutional, defect-free sites is hindered, an effect previously observed via Mössbauer spectroscopy near the Z=54 atomic shell closure [WAA75].

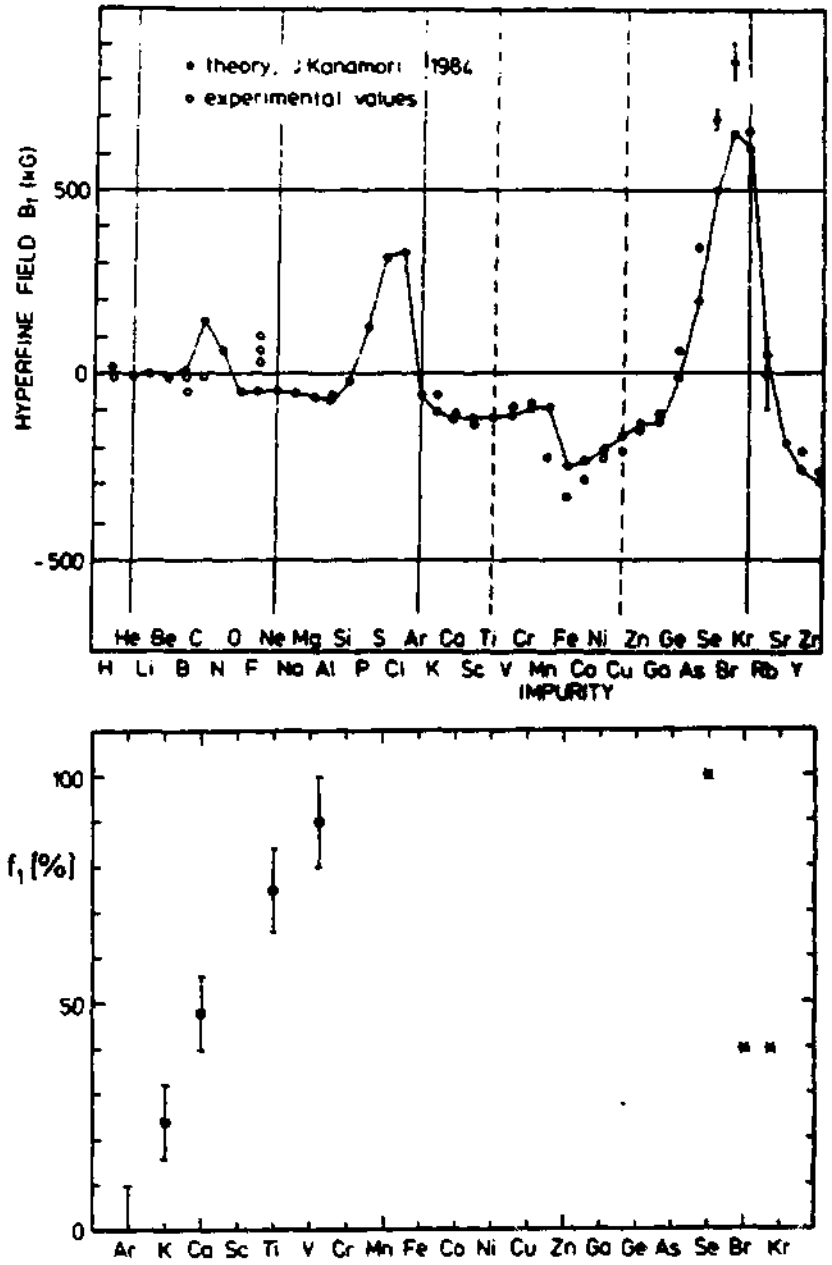

Fig. 5: Compilation of substitutional hyperfine fileds of light and medium impurities in Fe (exp. and theoretical predictions (KAN84)).
Fraction f_1 of substitutional implantation at room temperature for impurities near the Z=18 and Z=36 atomic shell closures

III. Observation of the In-V complex in fcc-Co

The systematics of hyperfine fields of Z=50 substitutional impurity atoms obtained from Mössbauer spectroscopy [WEY66] and previous high temperature PAC experiments on ^{111}In in fcc-Co [LIN78] point to a large negative hyperfine field of B(CdCo)=-28.74 T at room temperature. It is therefore to be expected that radiation induced ^{111}In-defect complexes which usually feature reduced hyperfine field strengths [WAA75] should be well observable in this system. In collaboration with G. Weyer and J. Chevallier from the University of Aarhus, we have therefore performed a detailed study.

The typically 70-180 nm thin Co single crystals were epitaxially grown on NaCl crystals with an intermediate layer of LiF. Rutherford backscattering spectra with 900 keV α-particles shown in Fig. 6 reveal the composition and orientation of the probe: the curve (a) represents the backscattering yield at random incidence, while the curve (b) is the one at incidence along the [100] channel and observation of the backscattered α-particles in the (100) plane. The lattice constant a=0.356 nm was obtained by TEM. Some $2*10^{13}$ ^{111}In$^+$ ions/cm^2 were implanted at 250 keV with IONAS and the perturbation functions R(t) of the 171-245 keV cascade in ^{111}Cd were measured with the BaF_2 detector set-up described above. By variation of the implantation, annealing and measuring temperatures, the production and desintegration of ^{111}In-defect complexes and the temperature dependence of their hyperfine fields were measured.

Fig. 7 shows some R(t) functions taken at room temperature during a cumulative annealing cycle at 300-873 K, for 15 min at each step. The frequency spectrum deduced after the 453 K annealing shown in Fig. 8 clearly exhibits four fractions with the Larmor frequencies ω_1=346.9(1) MHz, ω_2=255.6(7) MHz, ω_3=415.3(3) MHz and ω_4=381.9(5) MHz at room temperature. Using the known g-factor of the isomeric state in ^{111}Cd and correcting the measured local fields for the strength of the polarizing external field, B_{ext} = 0.16 T, we arrive at the following hyperfine fields: B_1=-23.82(8) T, B_2=-17.59(7) T, B_3=-28.55(10) T, and B_4=-26.21(9) T. By taking PAC spectra with different crystal orientstions relative to the external field direction, we proved that none of the fractions had a large quadrupole interaction component.

The fraction 1 must be assigned to substitutional implantation into a defect free environment [LIN78]. The second fraction is formed at room temperature, but not at liquid nitrogen implantation and disappears at some 650 K. In analogy to a similar complex

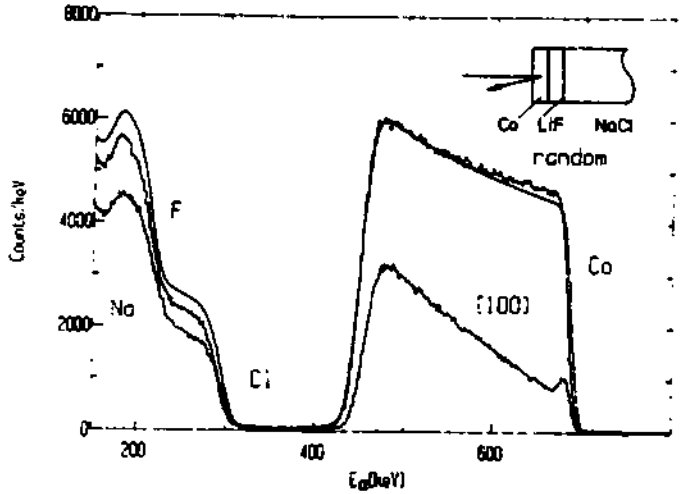

Fig. 6: Rutherford backscattering spectrum of the Co-LiF-NaCl sample, taken in random and 100 channeling geometry.

^{111}InCo

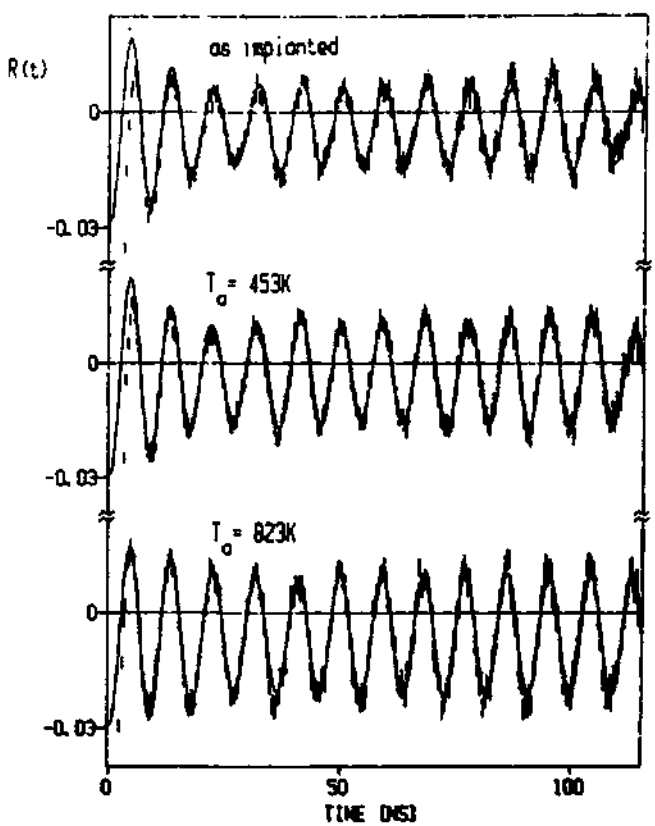

Fig. 7: PAC spectra of the system ^{111}CdCo after implantation of ^{111}In into fcc Co.

in the system ^{111}InNi studied by Hohenemser et al. [HOH77,SUT78], we associate this hyperfine field with an In_1-V_4 complex in which a substitutional In atoms traps 3 NN vacancies and relaxes along the <111> direction thus forming a cubic complex with four equally spaced vacancies around the interstitial In atom. Together with the ^{111}In activity a variable amount of inactive ^{111}Cd$^+$ ions are being implanted into the sample; it was found that the fraction f_2 decreases for increasing ^{111}Cd dose. A similar behaviour was found for annealed ^{111}InNi samples which were post-irradiated [SUT78,ALL83,VOS86]. Among the remaining two fractions, the one labeled 3 has the Larmor frequency of hcp-Co [LIN78], while the last fraction with ω_4 has not been unambiguously explained so far. The latter two fractions f_3 and f_4 survive the hcp→fcc phase transition temperature T_p=690 K. (Note that the whole sample stays in the fcc phase if heated above T_p and then cooled below T_p.)

By means of a LN cryostat with heatable sample, we also determined the temperature dependence of the Larmor frequencies in the range 100≤T≤390 K. The results for $\omega_1(T)$ and $\omega_2(T)$ are given in Fig. 9; $\omega_3(T)$ follows closely $\omega_2(T)$. Also given is the temperature variation of the bulk magnetization extrapolated from Ni and scaled with the Curie temperature T_c=1388 K of Co [CRA71]. The high field data $\omega_1(T)$ are well described by this parametrization and do not exhibit the anomalies found e.g. for the elements Ga, As, Ge and Sn in hcp-Co [SEN81]. Senba et al. [SEN81] have pointed out that the ^{111}CdCo hyperfine field in the fcc phase measured at 723K and 963K is also consistent with the bulk magnetization. In contrast, the frequency $\omega_2(T)$ of the $^{111}In_1$-V_4 complex decreases linearly with T with a coefficient $\Delta\omega_2/\omega_2\Delta T$=0.024 %K^{-1} and thus does not follow the bulk magnetization. Salm and Klepper [SAL79] have observed a similar linear decrease of the Larmor frequency in non-substuitutional sites in the system ^{19}FNi.

IV. Paramagnetic relaxation - the case Nd in Ni

Nuclear magnetic moments are very sensitive to the single-particle structure of a nuclear state. In γ-unstable (triaxially deformed) transitional nuclei, the alignment of one or several quasi-particles along the axis of collective rotation can have a strong influence on the shape; very convincing examples for such γ-driving forces have been recently found in the mass A ≈ 80 and 130 regions [LUH85,FRA83,PAU87]. While the (1qp) level structure of an odd-A nucleus directly reflects the deformation of the underlying core, (2qp) and (3qp) bands depend in a more hidden way on the collective shape of the nucleus. Hence, g-factors are needed to pin down the nature and angular momentum of the aligning particles which in turn depend on and influence collectivity.

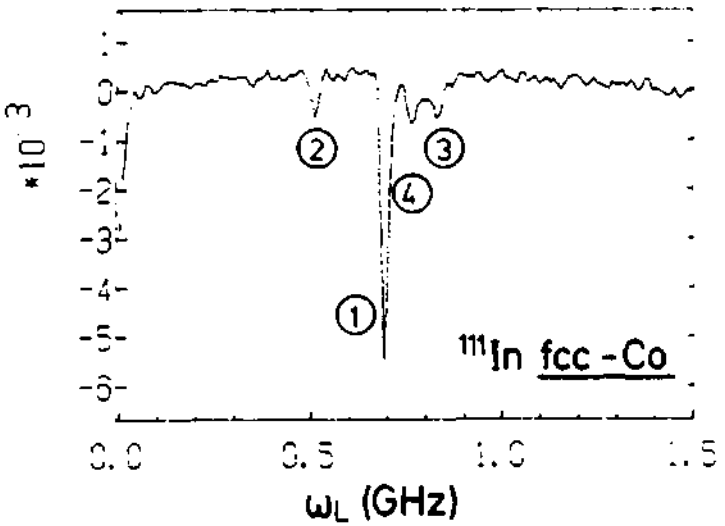

Fig. 8: Fourier spectrum of ^{111}Cd-fcc Co showing the four Larmor frequencies discussed in the text

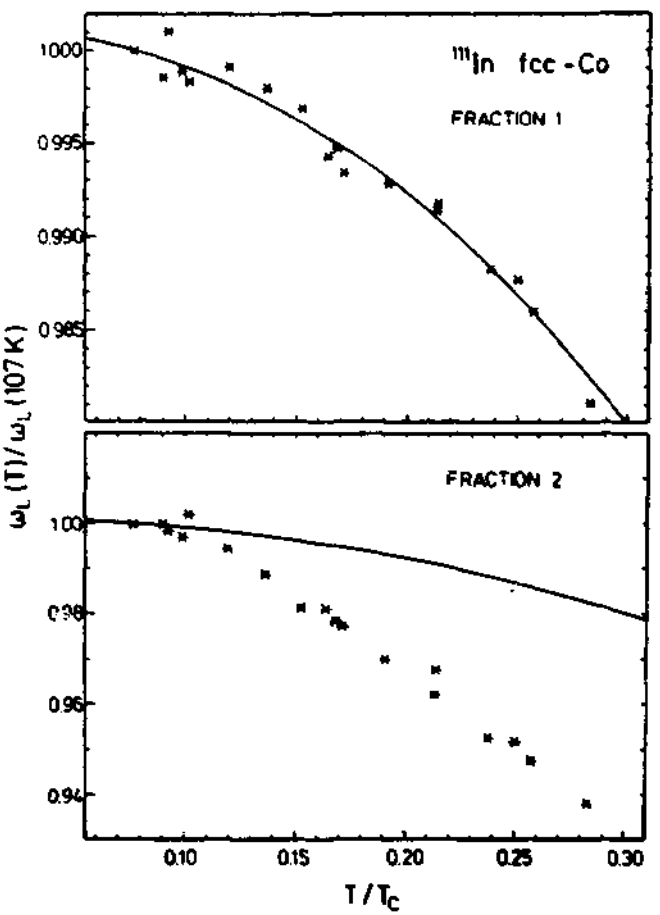

Fig. 9: Temperature variation of the Larmor frequencies of fraction 1 (substitutional) and 2 (InV_4 complex)

$$W(\theta,t;\uparrow\text{or}\downarrow) = 1 + A_2 Q_2 P_2(\cos(\theta \pm \omega_L t))\exp(-\lambda_2 t) + ..$$

and gives the time integral PAD

$$W(\theta,\downarrow\text{or}\uparrow) = 1 + 0.25 A_2 Q_2 G_{22}(1+3\cos(2\theta \pm 2\Delta\theta_2)*[1+\tan^2 2\Delta\theta_2]^{-1/2}) + ..$$

where
$$\tan 2\Delta\theta_2 = 2\omega_L \tau\,(1+\lambda_2 \tau)^{-1},$$
$$G_{22} = (1+\lambda_2 \tau)^{-1},$$
$$\lambda_2 = 2\,\omega_L^2\,\tau_c$$

and λ_2^{-1} and τ_c denote the relaxation resp. correlation times; note that λ_2 scales with g^2. The parameters ω_L and λ_2 can be fitted from the experimental quantities

$$\varepsilon(\theta) = [W(+\Delta,\downarrow)+W(-\Delta,\downarrow)-W(+\Delta,\uparrow)-W(-\Delta,\uparrow)]/\Sigma W,$$
$$S(\theta) = [W(+\Delta,\downarrow)+W(+\Delta,\uparrow)-W(-\Delta,\downarrow)-W(-\Delta,\uparrow)]/[\Delta\,\Sigma W],$$
$$\Sigma W = W(+\Delta,\downarrow)+W(-\Delta,\downarrow)+W(+\Delta,\uparrow)+W(-\Delta,\uparrow).$$

If one adopts the static field B_{st} = 150(36) T at LN temperature [KUG76], one obtains the mean g-factor of the 10^+_1 and 12^+_1 states in ^{134}Nd as g = +1.08(33) which value clearly proves $h_{11/2}$ proton alignment. On the basis of a Cranked Shell Model analysis of high spin states in ^{134}Nd, Paul et al. [PAU87] conclude that $h_{11/2}$ proton alignment drives the triaxial nucleus to a prolate shape, while $h_{11/2}$ neutron alignment leads to an energetically degenerate oblate band. The g-factor of the lowest 2^+ state in ^{134}Nd was found as g = 0.53(10) [BIL87b].

The observed γ-ray anisotropies are much smaller than expected from the Larmor precessions in the static field and indicate that in addition paramagnetic relaxation has to be taken into account ($\lambda_2 \neq 0$). A test experiment was therefore performed for the lowest 2^+ states in ^{146,148}Nd the g-factors of which have been determined previously: g(^{146}Nd)=0.22(3), g(^{148}Nd)=0.25(4) [KUG72]. Both nuclei were Coulomb excited by a 38 MeV ^{16}O beam and recoil implanted from a 1.5 mg/cm² ^{nat}Nd layer sputtered onto a 5 mg/cm² Ni foil. The γ radiation was measured in four Ge detectors at ±20° and ±(110° ±Δ), Δ=5°, in coincidence with projectiles backscattered into an annular silicon surface barrier detector. The resulting ε and S parameters are shown in Fig. 10. The measured precessions $\omega\tau(^{146}\text{Nd})$=-43(3$_6$) mrad and $\omega\tau(^{148}\text{Nd})$ = -248(3$^{3}_{21}$) mrad are in agreement with previous work [KUG72]. The ε parameters at 20° and 110° clearly show the relaxation effect as they deviate considerably from the τ_c = 0 curves (no relaxation). The other curves refer to τ_c = 50, 75 and 100 ps; the ε values in ^{148}Nd give at both angles the correlation time τ_c = 84(15) ps. The definition of the correlation time τ_c has been somewhat arbitrarely chosen as $\tau_c = \lambda_2/2\omega_L^2$ by replacing the unknown average fluctuating field of Nd by the static field B_{st} which causes the Larmor precession. If one

In collaboration with J. Billowes, G. D. Sprouse and others [BIL86,BIL87a,BIL87b], a series of g-factor measurements has been recently performed with the Stony Brook tandem-LINAC heavy ion facility. The time integral IMPAC or IMPAD techniques after recoil implantation into Fe and Ni backings by means of Coulomb excitation and heavy ion fusion reactions were used. We will discuss here the case Nd in Ni because it has provided some interesting results on the paramagnetic relaxation of this 4f element. Tab. 4.1 lists the excited states and reactions used in the experiments. The nucleus ^{136}Nd has two pronounced backbends at $I^{\pi}=10^{+}$ attributed to $h_{11/2}$ proton and neutron alignment; the estimated g-factors of these 10^{+} states are $g_p=1.1$ resp. $g_n=-0.2$ [HAM86]. The lifetime of the 3298 keV 10^{+} state is sufficiently long (τ=74 ps, [BIL87a]) as to produce a measurable Larmor precession in the large static hyperfine field B(Nd<u>Ni</u>)=150 T [KUG76].

Table 4.1: Nuclear states of Nd isotopes

A	E_x *(keV)*	τ *(ps)*	*g*	*Reaction; E_{beam} (MeV)*
134	295	92(6)[a]	0.53(10)[a]	^{76}Ge(^{60}Ni,4n); 235
136	3298	74(8)[a]	1.08(33)[a]	^{76}Ge(^{62}Ni,4n); 235
146	453	32(3)	0.22(3)[b]	^{146}Nd(^{18}O,^{18}O'); 38
148	300	123(3)	0.25(4)[b]	^{148}Nd(^{18}O,^{18}O'); 38

[a] *[BIL87a,b]* [b] *[KUG72]*

The IMPAD measurements for ^{134,136}Nd were done in the following way: The 3-layer sandwich target consisted of 0.7 mg/cm² Nd evaporated onto 5.5 mg/cm² Pb deposited onto an annealed 5 mg/cm² Ni foil. The Ni beams and the evaporation residues were slowed down in the Pb layer in order to avoid background reactions and transient field effects in the Ni backing. The target was polarized by an 0.13 T external magnetic field reversed every 2 min ($\downarrow\uparrow$), and kept at 80 K. Two Ge detectors operated in coincidence with a large solid-angle NE213 neutron detector were placed at angles $\theta_1=+120^{\circ}\pm\Delta$ and $\theta_2=-120^{\circ}\pm\Delta$, $\Delta=11.8^{\circ}$, and the four spectra labelled $W(+\Delta,\downarrow)$, $W(+\Delta,\uparrow)$, $W(-\Delta,\downarrow)$ and $W(-\Delta,\uparrow)$ were accumulated.

Assuming a purely magnetic hyperfine interaction in a static and fluctuating field, the time-differential PAD can be written [FRA65,ABR53] as

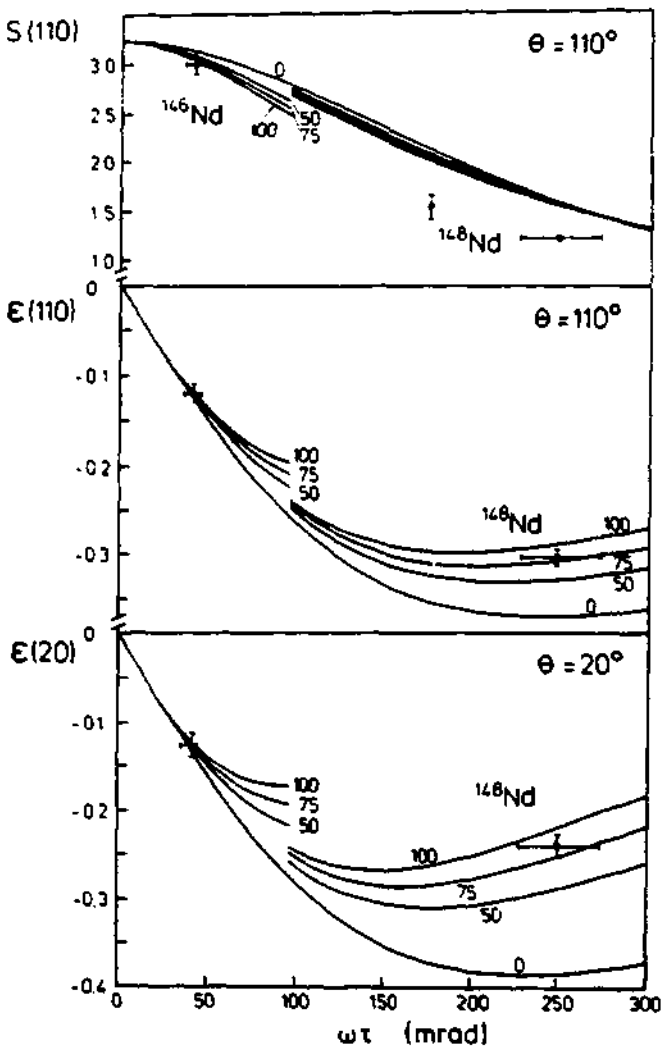

Fig. 10: The quantities S and ε defined in the text for the $2^+ \rightarrow 0^+$ transitions in ^{146}Nd and ^{148}Nd after Coulomb excitation with a 38 MeV oxygen beam and recoil implantation into Ni. The curves are labeled by τ_c = 0, 50, 75 and 100 ps. The deduced correlation time is τ_c = 84(15) ps.

uses the estimated 4f field reported by Kugel et al. [KUG76], B_{4f} = 420 T, one gets the correlation time $\tau_c' = (B_s/B_{4f})^2 \tau_c$ = 11 ps. This figure is by an order of magnitude larger than the correlation times measured time differentially for Nd in Sn, SnBi and SnAu alloys and extrapolated to 80 K [RIE83,RIE85].

Evidently more work is needed, in particular time differential measurements of Nd in Ni and other ferromagnets as well as for different temperatures to better understand the relaxation of this 4f elements in ferromagnetic, both in the context of nuclear magnetic moment measurements and for its own sake.

Acknowledgements

The authors are very thankful to their collaborators in the various parts of the experiments presented here, in particular to J. Kesten and J.W. Petersen (^{77}BrFe), to G. Weyer and J. Chevallier (^{111}InCo), and to J. Billowes, G.D. Sprouse, O.C. Kistner, S.L. Rolston, W.F. Piel and J.W.Noe (NdNi), for the permission to quote from unpublished work. We are indebted to W. D. Schmidt-Ott for performing the cyclotron irradiations and to H. Uhrmacher for his help with the IONAS implantations.

References

[ABR53] A.Abragam, R.V.Pound, Phys. Rev. 92 (1953) 943

[AKA83] H.Akai, N.Akai, J.Kanamori, J. Magn. Magn. Mat. 31/32 (1983) 551

[ALL83] C.Allard, G.S.Collins, C.Hohenemser, Hyp. Int. 15/16 (1983)387

[ALE74] R.B.Alexander, P.T.Callaghan, J.M.Poate, Phys. Rev. B9 (1975) 157

[AUE67] U.Auerbach, J.Braunsfurth, M.Maier, E.Bodenstedt, H.W.Flender, Nucl. Phys. A94 (1967) 427

[BER83] F.J.Bergmeister, M.Uhrmacher, K.P.Lieb, Hyp. Int. 14 (1983) 177

[BIL86] J.Billowes,C.H.Holbrow,T.Lauritsen,K.P.Lieb, R.G.Pillay, S.L.Rolston, G.D.Sprouse, Phys. Lett. 178B (1986) 145

[BIL87a] J.Billowes, K.P.Lieb, J.W.Noe, W.F.Piel Jr., S.L.Rolston, G.D.Sprouse, O.C.Kistner, Phys. Lett. (1987) in press

[BIL87b] J.Billowes, K.P.Lieb, J.W.Noe, W.F.Piel Jr., S.L.Rolston, G.D.Sprouse, O.C.Kistner, F. Christancho, submitted to Phye. Rev. C

[BOL87] W.Bolse, M.Uhrmacher, K.P.Lieb, Hyp. Int. (1987) in press

[BRA78] F.Brandolini, F.J.Bergmeister, K.P.Lieb, C.Rossi-

Alvarez, M.Uhrmacher, Hyp. Int. 5 (1978) 275
[CAL74] P.T.Callaghan, N.J.Stone, B.G.Turrell, Phys. Rev. B10 (1974) 1075
[CRA71] J.Crangle, G.M.Goodman, Proc. Roy. Soc. London A 321 (1971) 477
[FRA65] H. Frauenfelder, R.M. Steffen, in "Alpha-, Beta- and Gamma-Ray Spectroscopy", ed. K. Siegbahn (North Holland Publ. Comp., Amsterdam, 1965) p.997
[FRA83] S. Frauendorf, P.R. May, Phys. Lett. 125B (1983) 245
[HAM86] E.Hammaren, K.W.Schmidt, F.Grümmer, A.Faessler, B.Fladt, Nucl. Phys. A454 (1986) 301
[HOH77] C. Hohenemser, A.R. Arends, H. de Waard, H.G. Devare, F.Pleiter, S.A.Drentje, Hyp. Int. 3 (1977) 297
[KAN84] J.Kanamori, H.Akai, N.Akai, Hyp. Int. 17-19 (1984) 287
[KOI64] Y.Koi, A.Tsujimara, T.Hiram, Journ. Phys. Soc. Jap. A94 (1964) 1493
[KUG72] H.W.Kugel, R.R.Borchers, R.Kalish, Nucl. Phys. A186 (1972) 513
[KUG76] H.W.Kugel, L.Eytel, G.Hubber, D.E.Murnick, Phys. Rev. B13 (1976) 3697
[LIN78] B.Lindgren, S.Bedi, R.Wäppling, Phys. Scr. 18 (1978) 26
[LUH85] L.Lühmann, M.Debray, K.P.Lieb, W.Nazarewicz, B.Wörmann, T.Heck, J.Eberth, Phys. Rev. C31 (1985) 828
[PAU87] E.S.Paul, C.W.Beausang, D.B.Fossan, R.Ma, W.F.Piel Jr., P.K.Weng, N.Xu, submitted to Phys. Rev. C
[RAE84] F.Raether, F.J.Bergmeister, K.P.Lieb, M.Uhrmacher, H.Grawe, H.Haas, Hyp. Int. 20 (1984) 285
[RAE87a] F.Raether, K.P.Lieb, Hyp. Int. (1987) in press
[RAE87b] F.Raether, K.P.Lieb, J.Kesten, L.Ziegeler, J.W.Petersen, submitted to Hyp. Int.
[RAE87c] F.Raether, G.Weyer, K.P.Lieb, J.Chevallier, in prep.
[RIE83] D. Riegel, Hyp. Int. 15/16 (1983) 603
[RIE85] D. Riegel, Journ. Magn. Magn. Mat. 52 (1985) 96
[SEN81] M.Semba, P.Ragavhan, W.Semmler, R.S.Raghavan, Hyp. Int. 9 (1981) 453
[SUT78] R.M.Suter, M.Haoui, C.Hohenemser, Hyp. Int. 4 (1978) 711
[UHR75] M.Uhrmacher, A.Gelberg, F.Brandolini, A.M.Kleinfeld, K.P.Lieb, Phys. Lett. 56B (1975) 247
[UHR85] M.Uhrmacher, K.Pampus, F.J.Bergmeister, D.Purschke, K.P.Lieb, Nucl. Instr. Meth. Phys. Res. B9 (1985) 245
[VOS86] M.Vos, D.O.Boerma, F.Pleiter, Nucl. Instr. Meth Phys. Res. B15 (1986) 333
[WAA75] H.de Waard, Phys. Scr. 11 (1975)
[WEY86] G.Weyer, in "Solid State Reactions after Ion Implantation detected by Nuclear Methods", K.P.Lieb, M.Uhrmacher, eds. Göttingen (1986) p.81

RECENT RESULTS OF PAC APPLIED TO STUDY OF MAGNETIC ALLOYS

M. Rots
Instituut voor Kern- en Stralingsfysika, University of Leuven, B-3030 Leuven, Belgium

In this report two new applications of PAC in the study of magnetism will be introduced. The first topic is devoted to the problem of reentrance behaviour, the nature of which is still controversal especially in the case of AuFe alloys around 16at%Fe. Recently the applicability of PAC to the study of spin-glass freezing was investigated and the results in the reentrant concentration region were discussed in recent publications [1-4]. Here we add new results on the interplay between local atomic order and the appearance of the double magnetic transition: paramagnetic-ferromagnetic-spin glass upon cooling. In the second part we introduce preliminary PAC results on the study of antiferromagnetism in manganese and its alloys.

1. Local atomic order versus reentrant magnetic behaviour in $Au_{85}Fe_{15}$

The controverse on the low temperature behaviour of non-dilute AuFe alloys, especially the character of the double magnetic transition, depends heavily on whether or not alloy randomness can be assumed. A Mössbauer study at room temperature by Whittle and Campbell [3] led to the conclusion that in the concentration range 5-20 at%Fe the AuFe alloy is not a random solid solution. In the as-rolled state a tendency towards clustering was noticed, while heat treatment at 550° C induces atomic short range order or anticlustering. In an earlier Mössbauer work [4] on 17 at%Fe an increase in ordering temperature upon annealing was found, while ac-magnetic susceptibility measurements [5] on 14 and 15 at%Fe reflects the opposite behaviour. The broad spread in ordering temperatures among the different investigations illustrates this influence of the actual metallurgical state. Comparing hyperfine interaction results, Mössbauer and PAC spectroscopy [1], one notices a close similarity in the response, although the former technique probes on the Fe impurity itself while the latter senses the magnetic state by means of a foreign probe atom. This has led us to the conclusion that not a local

picture but rather long range magnetic interaction between statistically induced spin clusters of different sizes explains the temperature behaviour of the hyperfine field. The present study aims to verify this interpretation by investigating the PAC response for a 15 at%Fe sample (well within the cluster-glass region) to changes in the metallurgical state due to cold working and annealing.

The sample was prepared by induction melting under vacuum and cold rolling to foil thickness of 100μ. Between the production and actual use of the foil a period of 700 days room temperature ageing elapsed. The radioactive ^{111}In tracer was diffused into the foil during 4 hours at 900°C under H_2-atmosphere, terminated by a quench in liquid nitrogen. After measurement the same sample was cold rolled to foil thickness of 20μ and measured as such (AR-state). The sample was subsequently given a thermal treatment of 13 hours at 550°C (HT-1 state) and 4 hours at 900°C (HT-2 state) respectively.

We measure as a function of temperature the average hyperfine interaction, at the ^{111}Cd probe nucleus, originating from the distributed Fe impurities in the Au-lattice. This temperature dependence of the average interaction frequency is represented in Fig. 1 for the different metallurgical conditions of the sample.

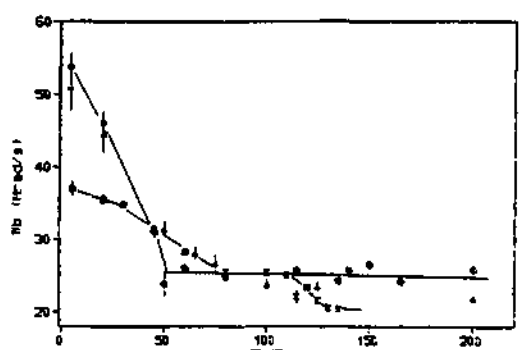

Fig.1. Hyperfine field vs. temperature for $Au_{85}Fe_{15}$ in different metallurgical states; □ : anneal 900°C+Q; ● : as-rolled; Δ: anneal 500°C+Q.

The salient features are as follows:

1. Under the initial treatment conditions the hyperfine field as a function of temperature closely ressembles our earlier result on the same concentra-

tion. The ordering temperature is 130K and around 80K a second increase in hf-interaction is clearly visible. However the 4.2 K hff value is somewhat lower than observed earlier.

ii. In the as-rolled state the hff behaviour changes completely. The ordering temperature drops to 50K, where the interaction strength steeply increases to a value substantially larger than under the previous condition. Moreover above 50K the average hf-interaction remains at the plateau seen between 80K and 110K in the previous run.

iii. in the annealed state (HT-1) the hf-interaction strength below 50K hardly changes, although the temperature behaviour above develops towards the two stages patern seen in the initial state but with a reduced ordering temperature located around 80K and an increased "background" interaction.

iv. The brief annealing at 900°C apparently does not fully restore the original alloy conditions in the sense that the hf-interaction strength, measured at T=20K and 200K only, are moderately reduced relative to the previous values.

The results clearly show that the hyperfine interaction strength at low temperature, but also its temperature variation, sensitively depends on the history of the alloy. The present measurement was done on a part of the same foil used earlier with the thermal treatment (4 hours at 900°C plus quench) identical. Nevertheless the hyperfine field at 4.2K equals 30.2(4)kG in the earlier measurement, while we observe 26.1(2)kG in the present one. The former sample was prepared after 10 days room temperature ageing, the latter after 700 days ageing. Subsequent cold working on the latter sample substantially increases the hyperfine field to 37(2)kG when measured in the fresh AR-state. Upon annealing at 550°C this high field value remains unchanged at 4.2K while at 20K a reduction can be noticed.

In the as-rolled state, due to clustering, the matrix remains with an effective Fe concentration reduced in respect to the nominal value. This clustering is seen here by an increased interaction strength at higher temperatures. The steep increase of hyperfine field around 50K marks the spinglass freezing of the depleted matrix. Short term annealing or room temperature ageing gradually dissolves the clustering thereby increasing the Fe concentration in the matrix as reflected by the increase in ordering temperature, weakening of the slope change around 50K and reduction of the low temperature hyperfine field.

2. Hyperfine field distributions in α-Mn.

One of the four allotropic forms of manganese stabilize at room temperature in the α-Mn phase, having a cubic structure with lattice constant a = 8.9135Å and 58 atoms per unit cell. The basis of the atomic arrangement is a simple body-centred cubic lattice with a cluster of 29 atoms associated with each lattice point. The structure contains four crystallographically inequivalent sites. Each type I atom at the bcc-lattice points is surrounded by an octahedron of type IV atoms of tetrahedral symmetry and somewhat further from the center four type II atoms, arranged tetrahedrally around the center. Finally the outermost atoms are 13 type III atoms in a polyhedron with cubic and octahedral faces, such that the whole cluster has tetrahedral symmetry. From space filling considerations, atoms on site I and II tend to have larger electronic radii to fill the relative larger volume of the CN16 coordination. In diluted alloys one expects that larger impurity atoms occupy preferentially site I and II, while smaller impurity atoms prefer the smaller volume associated with CN13 and CN12 coordination in site III or IV.
Neutron diffraction studies [6] on the magnetic structure revealed that below T_N = 95K an antiferromagnetic ordering sets in. A non-collinear spin model was proposed with relative large localized moments on site I and II but small moments on the other two sites. This proposal could be confirmed in NMR experiments [7] showing different hyperfine field proportional with the site moments. It is the purpose of present study to investigate the local moment picture as opposited to a spin-density-wave approach. The literature does not report any PAC work on the manganese system and therefore we restrict here to a survey of the first observations.

2.1. Site identification.

In the present study ^{111}Cd and ^{100}Rh will be used as probe for the hyperfine field distributions. From the atomic arrangement one may derive an electric field gradient almost zero at site I, different from zero but axially symmetric at site II, relatively large and non-axially symmetric at site III or IV. Measurements in the paramagnetic state reveal at the ^{111}Cd probe a quadrupole interaction strength $\frac{e^2Qq}{h}$ = 45(2)Mc with a broad distribution of

18Mc and η = 0 at T = 150K, while for ^{100}Rh probe at T = 293K we found $\frac{e^2Qq}{h}$ = 67.9(5)Mc with an asymmetry parameter close to η = 1. From this observation we derive that ^{111}In occupies site I or II and ^{100}Pd goes to site III or IV, consistent with what may be expected from atomic size consideration.

In addition to the quadrupole interaction observed in the α-Mn phase (produced by annealing at 620°C) we determined the quadrupole interaction strength in the β-Mn phase also. This phase was produced by annealing the sample at 900°C followed by a quench in ice water. We observe at 77K as well as 4.2K $\frac{e^2Qq}{h}$ = 1067(8)Mc and η = 0.11(1). The same sample was subjected to an isochronal anneal treatment followed by a measurement at T = 77K. Up to annealing temperatures of 500°C no significant changes in the interaction parameters were observed. After a brief anneal of 10 minutes at 600°C, however, the PAC spectrum changes drastically. This spectrum needs an analysis with the assumption of a magnetic interaction with two distinct sites. We find a fraction of almost 80% of probes experiencing a magnetic interaction of ω_B = 80(1)Mrad/s and width $\delta\omega_B$ = 10(3)%, while the remaining probes experience an interaction of ω_B = 42(17)Mrad/s. Obviously the α-Mn phase formation was reached at 600°C anneal and the sample shows up the antiferromagnetic ordering expected below 95K. The initial hyperfine interaction parameters measured for the electric quadrupole interaction in β-Mn could be restored by annealing at 900°C followed by a quench.

2.2. Determination of the magnetic ordering temperature.

Furtheron we concentrate on samples treated appropriate for the production of the α-Mn phase.

Different experiments using a veriety of techniques determined the Néel temperature in the vicinity of T_N = 95K for the pure α-Mn state, either decreasing or increasing when α-Mn alloys are considered. Shifts ΔT_N of the order of 10-20 degrees per at.% were observed [8] depending on the valence or size of the alloying element.

High purity Mn flakes of quoted purity 99.99% was used and the Indium concentration did not exceeded 200ppb, assuming that the radioactivity diffused

homogeneously throughout the sample. The ordering temperature could be measured very sensitively by following the hyperfine parameters from room temperature down to a temperature were they drastically change from almost T-independent quadrupole-type to T-dependent magnetic-type.
The observed Néel temperature was located at T_N = 120(2)K, substantially larger than found in any other experiment. Moreover this value turned out to be extremely sensitive to the ^{111}In loading, increasing up to T_N = 160K in cases where the In-Cd concentration was increased by a factor of ten. Compared with ΔT_N shifts quoted for alloys in the at% region, our value refers to a concentration region eight orders of magnitude smaller. We also performed measurements on α-Mn alloys and our preliminary results indicate that ΔT_N shifts of the same magnitude and sign are observed but still relative to our previous T_N = 120K value. Lattice expansion is a commonly accepted possible explanation for the increase of Néel temperature in α-Mn as well as β-Mn alloys. Because indeed indium may produce the largest effect in view of its large atomic size, the shift in Néel temperature remains anomalous. Since manganese oxidize quite readily case was taken to prepare the sample under high vacuum, but the annealing was done under H_2 atmosphere. Therefore the absorption of hydrogen may be partially responsible for our high Néel temperature.

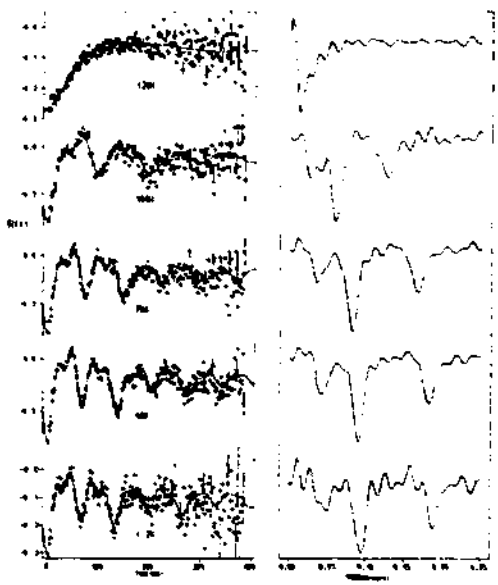

Fig.2. Typical PAC spectra for α-Mn (^{111}Cd) with their frequency distribution.

2.3. Magnetic hyperfine fields in α-Mn.

In fig. 2 some typical PAC spectra are displayed together with the frequency distribution. The data in the time domain where fitted according to the familiar expression for a randomly oriented magnetic interaction. The frequency distribution on the other hand was obtained using a multi-frequency mapping routine with 100 steps within the range 0-200 Mrad/s. Obviously the frequency distribution is peaked near to 45 and 94 Mrad/s, revealing the existence of two distinct sites. Over the whole temperature range down to 4.2K, the interaction frequencies corresponding to the two sites remain in a ratio close to 1:2, while the population of the highest interaction site amount 60%. All probes contribute to one or the other site and no paramagnetic fraction could be detected. The respective hyperfine fields at 4.2K equal 3.24(4)T and 6.46(2)T. The hyperfine field distribution widths equal 0.29(5)T and 0.22(3)T at the low and high field sites respectively and remain almost temperature independent. The temperature dependence of both hyperfine fields is shown in fig. 3. In the temperature region near to the ordering temperature ($T/T_N > 0.75$) the hyperfine field data nicely follow a power law.

$$\frac{H_{hf}(T)}{H_{hf}(4.2)} = D(1-T/T_N)^{\beta}$$

with $D = 1.18(5)$; $\beta = 0.42(3)$ for the low field site and $D = 1.174(3)$; $\beta = 0.316(2)$ for the high field site. The fitted Néel temperature then equals $T_N = 121.3(5)$K and $T_N = 120.14(5)$ respectively.

A remarkable jump in hyperfine field below T = 20K is observed at the low field site but not at the high field site. Moreover a further distinction between sites becomes apparent when the In-concentration increases. While the high field site remains almost unchanged, the low field site change to an interaction site reminescent of the β-Mn phase, together with an increase of the global ordering temperature.

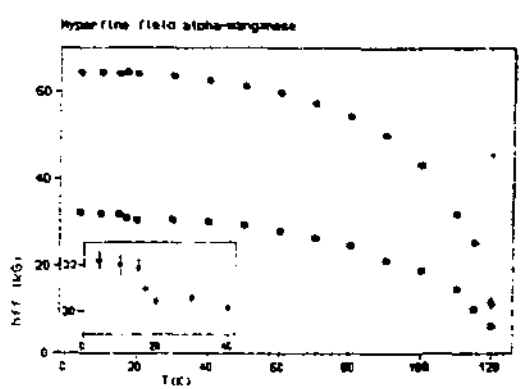

Fig.3. Temperature observation dependence of the hyperfine field in α-Mn at the two ^{111}Cd sites.

Assuming a localized moment model and the nf-field at ^{111}Cd proportional with the effective moment at each site, the expected field ratio between site I and site II equals 1.67, a value close to the observed ratio. On the other hand the lattice contribution to the electric field gradient at site II amounts $(1-\gamma_\infty)eq_{latt} = 1.10^{17}$ V/cm^2 to be compared with the observed value of eq = 0.39(2) 10^{17} V/cm^2, while the efg at site I equals zero. The measured spectrum at T = 150K, however, could be interpreted only in terms of a single probe environment. Moreover, the relative population in the high and low field sites being 3:2 is at variance with the atomic abundance 1:4 of type I to type II, indicating at least that In prefers site I rather than site II. The anomalous temperature dependence of the hyperfine field at T = 20K in the low field site, ressembles the jump in nf-field at the spin flip transition temperature, where the magnetization becomes parallel to the spin density wave vector, observed with the same technique in pure chromium.

2.4. Experiments under an external polarizing field.

In order to investigate the possible difference in nature of the magnetic sites observed, a serie of experiments was performed using an external magnetic field. The first noticed field effect concerns a substantial narrowing of the hyperfine field distribution at the low field site from 18% in zero field cooling to 5% after field cooling in B_{ext} = 4T, both measured without external field. At the high field site, however, the same narrow field distribution of 1.7% was observed in both cooling conditions.
In a next step the hyperfine fields observed at 4.2K and 77K were followed as a function of external field up to 4T. The results are summarized in fig. 4. For the high field site we observe at both temperatures the behaviour expected for an antiferromagnet under the influence of an external field. Depending on the relative orientation of the polarizing field and the local magnetic axis, in a polycrystalline sample one may observe a gradual rotation of the spins towards a perpendicular orientation when the external field approaches the spin-flop field strength. The observed hyperfine field B_{obs} therefore increases with B_{ext} according to

$$B_{obs} = a(B_{hf} + B_{ext}) + b\sqrt{B_{hf}^2+B_{ext}^2}$$

with a=1/3 and b=2/3 in low external fields, while a=0 and b=1 above the

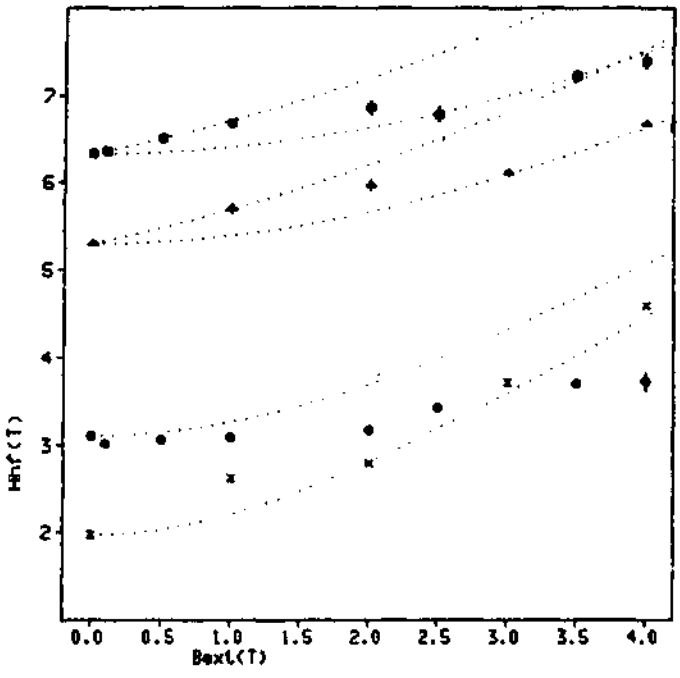

Fig.4. Dependence of the high and low field site as a function of external field, measured at 4.2K and 77K.

spin-flop field. The high field value obviously follows this behaviour, while the low field value do so approximately only at T = 77K. At 4.2K, on the contrary, the observed field at the low field site increases much too slowly. This different behaviour is illustrated even more clearly when the temperature dependence of the hyperfine field is measured with B_{ext} = 4T. In this case a maximum in the observed hf-field is observed around T = 20K for the low field site, while the high field site behaves normal. From the amplitude ratio between both frequency harmonics as well as the magnitude of the frequency itself, one derives that the hf-field is perpendicular to the external field at the high field site. The same is true for the low field site at 4.2K, but at higher temperatures the hf-field makes an angle of almost 80° with the external field.

References.

1. J. Van Cauteren, L. Hermans and M. Rots, Phys. Rev. B35 (1987) 1939
2. M. Rots and J. Van Cauteren, Phys. Lett. A120 (1987) 155
3. G.L. Whittle and S.J. Campbell, J. Phys. F15 (1985) 693
4. R.J. Borg and G.J. Dienes, J. Appl. Phys. 46 (1975) 99
5. S. Crane and H. Claus, Sol. Stat. Comm. 36 (1980) 461
6. T. Yamada, N. Kunitomi, Y. Nakai, D.E. Cox and G. Shirane, J. Phys. Soc. Jap. 28 (1970) 615
7. H. Yamagata and K. Asayama, J. Phys. Soc. Jap. 33 (1972) 400
8. T. Kohara and K. Asayama, J. Phys. Soc. Jap. 37 (1974) 393

RECENT DEVELOPMENTS IN PAC SURFACE STUDIES *

G. Schatz, T. Klas, R. Platzer, J. Voigt, and R. Wesche
Fakultät für Physik, University of Konstanz, D-7750 Konstanz
F.R. of Germany

1. Introduction

Recently interesting experiments have been reported where hyperfine techniques, like Mößbauer spectroscopy [1,2] and perturbed angular correlations (PAC) [3,4], have been applied to study surface phenomena. Especially PAC has proven to be rather powerful since surfaces can be prepared with an extremely low probe concentration, i.e. surfaces can be labelled with isolated radioactive probes. In such cases the hyperfine parameters, like the electric field gradient acting at the probe nuclei, can serve as a fingerprint to elucidate different probe sites at the surface, impurity-probe configurations and diffusion of impurities. In this paper most recent examples of PAC surface studies will be presented.

2. Surface studies with PAC

Most of the PAC surface work has been performed by utilizing the ^{111}In PAC probe. Several surfaces have been investigated so far, but the most complete body of data is available for copper surfaces. Therefore in the following the system ^{111}In on copper surfaces shall serve to demonstrate different aspects of PAC surface investigations.

2.1 Surface field gradients for the different Cu surfaces: Cu(100), Cu(110) and Cu(111)

Copper single crystals, cut accordingly, have been cleaned and annealed in UHV and checked with Auger-electron-spectroscopy and LEED. Radioactive ^{111}In probes have then been deposited at the surface with a concentration in the order of 10^{-4} of a monolayer. Experimental details can be found elsewhere.[5]

In Fig.1 PAC time spectra are shown for the three main orientations of the fcc copper system, namely Cu(111) (top), Cu(100) (middle) and Cu(110) (bottom). The samples have been annealed up to about 600 K for 20 minutes. In all cases the surface normal was lying in the γ-detector plane pointing under 45° between detectors. As one can see from the data most of the ^{111}In probes are exposed to well-defined electric surface field gra-

* This work was supported by the Deutsche Forschungsgemeinschaft through the Sonderforschungsbereich 306.

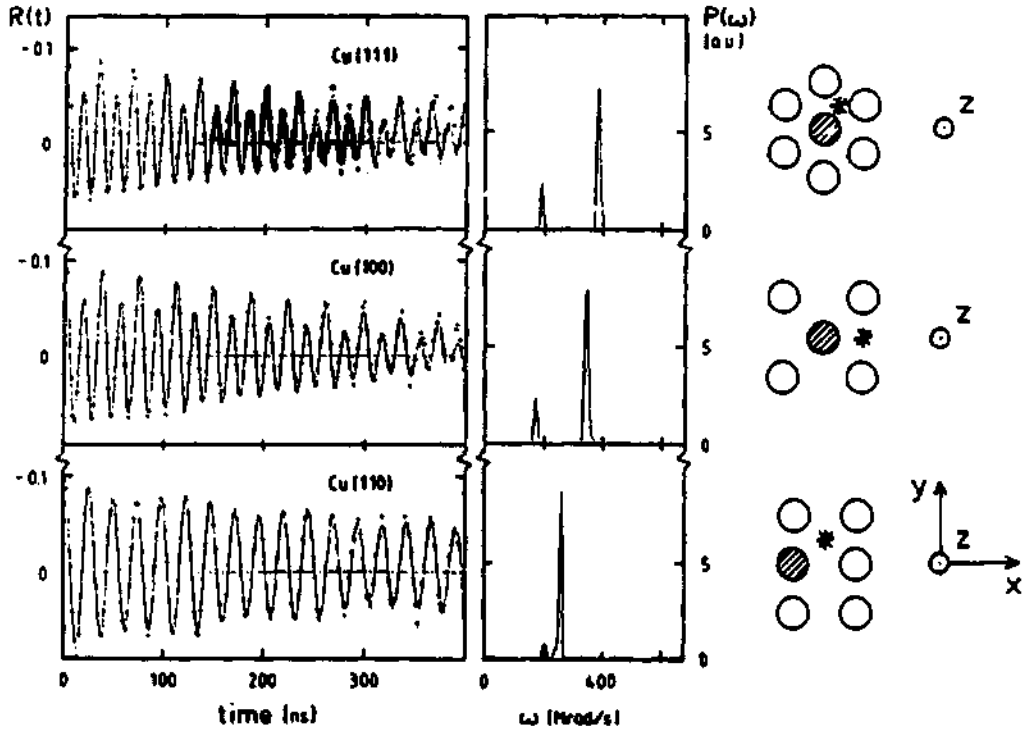

Fig.1: PAC time spectra together with their Fourier transforms for isolated ^{111}In probes on a Cu(111) (top), Cu(100) (middle) and Cu(110) (bottom) surface. The surface normals were lying in the detector plane under 45° with respect to two adjacent detectors. The time spectra are fitted with three frequencies corresponding to a unique electric field gradient. On the right-hand side the atomic arrangement for the corresponding Cu surface is shown and the measured principal-axis orientation is depicted. The possible ^{111}In sites, consistent with experiments are also indicated (dashed: substitutional site, star: hollow site).

dients, which is manifested by sharp transition frequencies seen in the Fourier analyses (right part). Due to the chosen geometrical arrangement, from the expected three transition frequencies (since the nuclear spin of the isomeric ^{111}Cd-level is I = 5/2) the second frequency is dominately seen. Since for Cu(111) and Cu(100) the ratio between first and second frequency is found to be 1:2, an axial-symmetric electric field gradient with asymmetry parameter $\eta = 0$ is deduced. The following electric field parameters have been found:

Cu(111) :	$V_{zz} = 9.8(15)\cdot10^{17}$ V/cm²	$\eta = 0$
Cu(100) :	$V_{zz} = 8.8(14)\cdot10^{17}$ V/cm²	$\eta = 0$
Cu(110) :	$V_{zz} = 7.7(12)\cdot10^{17}$ V/cm²	$\eta = 0.74(1)$

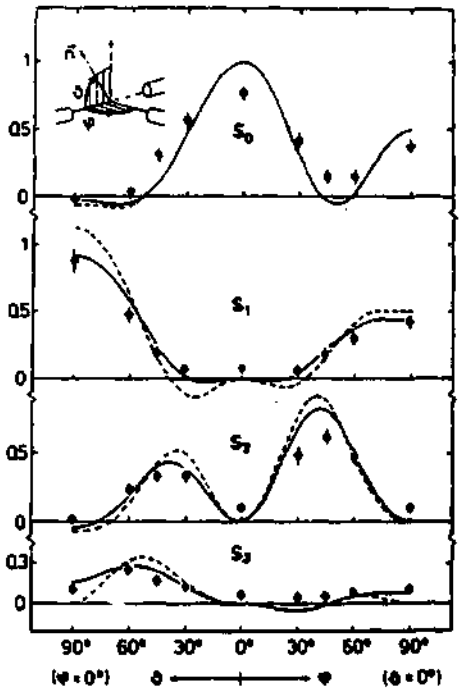

Fig.2: Dependence of the frequency amplitudes for isolated ^{111}In probes on a Cu(100) surface as a function of a selected set of angles between surface normal and γ-detector plane.

In order to determine the orientation of the principal axis system of the electric field gradient tensor PAC spectra for different geometrical arrangements have been recorded. Fig.2 shows an example for ^{111}In on Cu(100), where the angles of the surface normal with respect to the γ-detector plane has been varied (for definition of angles: see insert). The dashed curves are calculated by assuming the symmetry axis of the surface field gradient pointing along the surface normal and by neglecting the finite size of the sample and γ-detectors. The finite solid angle of the γ-detectors can be taken into account, which results in the solid lines in Fig.2. The agreement with the experimental data clearly establishes the fact that the symmetry axis of the electric-field-gradient tensor is directed perpendicular to the Cu(100) surface. Similiar experiments have been performed for the Cu(111) and Cu(110) surfaces. The obtained principal-axis orientation is depicted on the right side of Fig.1 together with the atomic arrangement for each surface. It is clear that the symmetry and the orientation of the electric field gradient reflects the symmetry of the surface atoms.

In the case of Cu(111) and Cu(100) only two sites of the ^{111}In probes can explain the experimental findings: firstly a substitutional site, i.e. In is incorporated in the topmost layer or, secondly, a hollow site, i.e. In is occupying a regular Cu site in the next (still empty) monolayer. Cluster

calculation by Lindgren [6] favour the substitutional terrace positions of ^{111}In on copper surfaces.

2.2 Surface field gradient at ^{111}In probes deposited at different depth from the surface

As it was demonstrated before, ^{111}In probes which are occupying substitutional sites in the topmost atomic layer are exposed to rather strong unique electric field gradients. The electric field gradient acting on to probe nuclei should be governed mainly by the next-neighbouring atoms and the conduction electrons in the neutral Wigner-Seitz cell. Therefore once the ^{111}In probes are surrounded by the 12 next neighbours in fcc Cu a vanishing electric field gradient is expected. This situation is valid already for ^{111}In probes one layer below the surface layer in Cu(100) and Cu(111), since then a complete next neighbour Cu-shell is present.

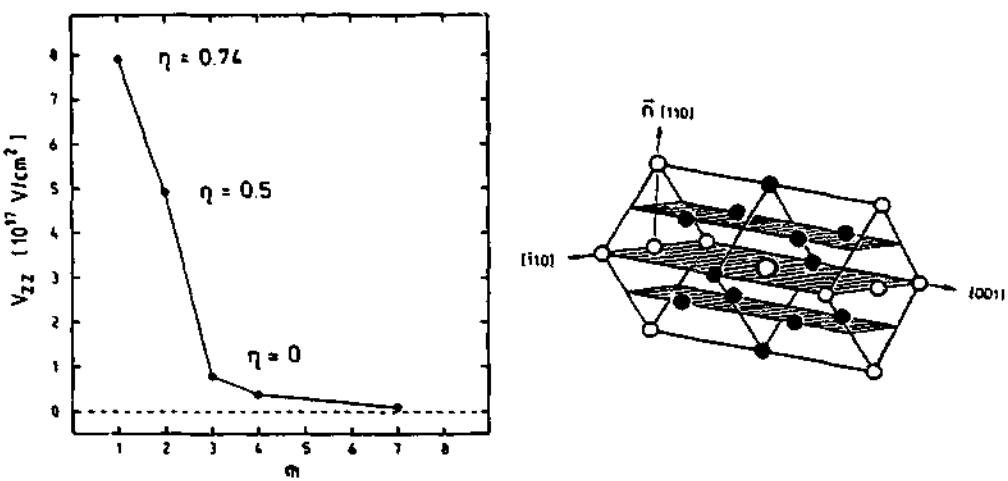

Fig.3: The largest component V_{zz} of the electric-field-gradient tensor measured at ^{111}In probes as a function of the depth from a Cu(110) surface. The asymmetry parameter η is also included. The inset illustrates the next neighbour arrangement around the substitutional ^{111}In probe atoms.

For Cu(110) the situation is different, here two additional Cu monolayers are needed on top of the ^{111}In probes to restore the complete coordination (see Fig.3, right side). This effect was investigated experimentally, by labelling Cu(110) surfaces with ^{111}In probes and successive coverage by additional copper. The result is shown in Fig.3 where the electric field gradient is shown for ^{111}In probes situated at different depth

from the surface. ^{111}In probes situated in the second layer are still exposed to a rather strong electric field gradient, which stems from the fact that ^{111}In is only surrounded by 11 Cu atoms. Only after coverage by two layers, i.e. ^{111}In is now situated in the third layer, the electric field gradient tends towards zero, as it should be for a cubic surrounding. This result shows that the electric field gradient can be used to determine the position of ^{111}In probes with respect to the surface layer. This opens the possibility to follow migration of probes perpendicular to the surface on an atomic scale.

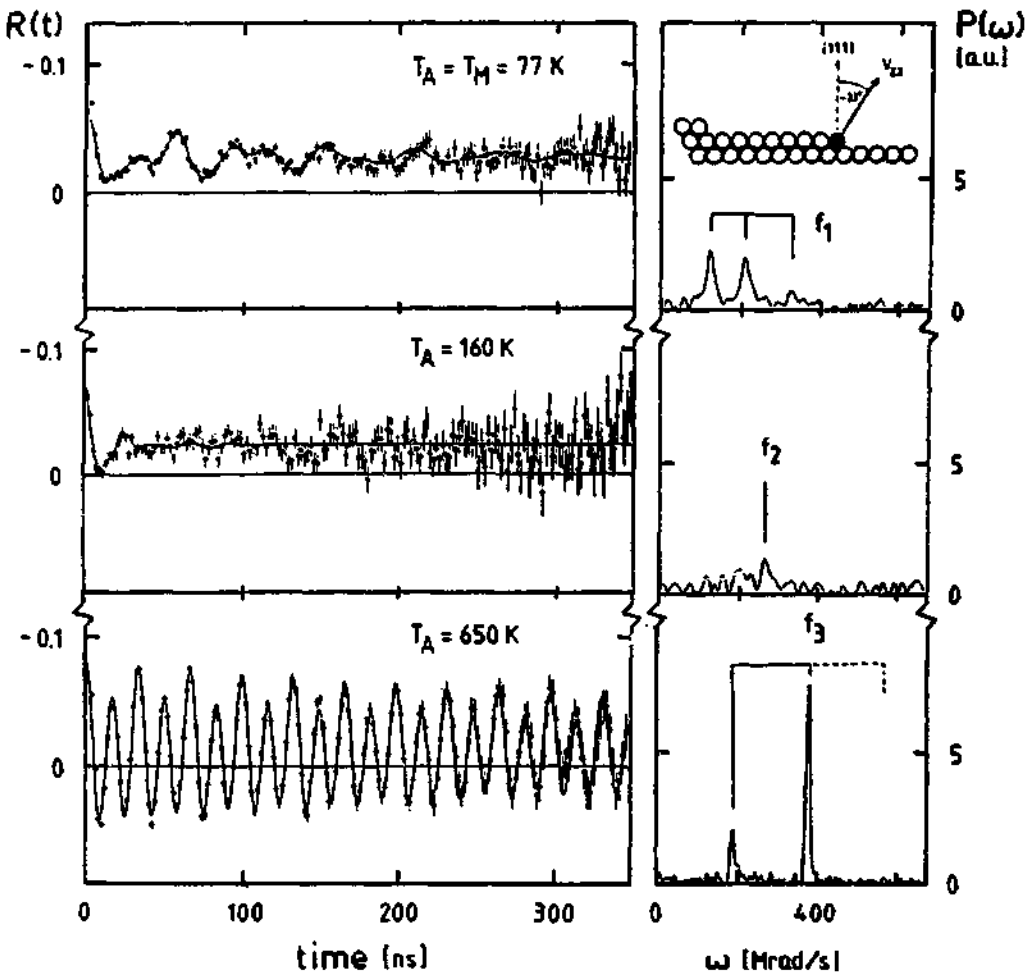

Fig. 4: PAC time spectra with Fourier transforms for isolated ^{111}In probes on a Cu(111) surface measured at T_M = 77 K after annealing for 20 min at three different annealing temperatures T_A. The insert illustrates the possible ^{111}In probe step sites denoted by the fraction f_i.

2.3 Step sites for ^{111}In on Cu(111) surfaces

As described above ^{111}In probes occupy terrace sites at copper surfaces after thermal treatment. The question arises through what paths the ^{111}In probes find such terrace sites after deposition at 80 K and successive annealing. In the case of ^{111}In on Cu(111) we tried to reconstruct the possible behaviour of the probes until they settle down at terrace sites. For this purpose a Cu(111) surface was prepared with a high number of steps.

In Fig.4 PAC spectra together with Fourier transforms are shown for three different annealing temperatures. The topmost spectrum was taken right after deposition of the ^{111}In probes, in this case a fraction f_1 is exposed to an electric field gradient with V_{zz} = 9.8(15)·10^{17} V/cm^2 and η = 0, exhibiting some distribution. Annealing up to 160 K results in completely undefined electric field gradients for all ^{111}In probes. Finally after annealing above 350 K the ^{111}In probes are occupying the above mentioned terrace sites (lower spectrum, fraction f_3). Closer inspection of the electric field gradient associated with f_1 shows that the z-axis of the principal-axis system is inclined under 33° to the surface normal. Our interpretation of these results is as follows. After deposition of the ^{111}In probes at 77 K they have landed on the surface in for example hollow sites in which they are highly mobile and are then trapped at steps at Cu(111) (fraction f_2). Further annealing releases the ^{111}In probes from the step sites, they may diffuse to impurities and imperfections at the steps characterized by a variety of electric field gradients. Finally at higher temperatures the ^{111}In probes enter the surface layer from the step configurations occupying regular terrace sites.

2.4 Indium Diffusion on Cu(100)

The labelling of copper surfaces by radioactive PAC probes offers the possibility to study diffusion processes. The basic concept hereby is trapping and detrapping of a certain species under consideration at the isolated ^{111}In probes. Trapping can be recognized by a detuning of the surface field gradient obtained for free ^{111}In probes.

We have performed experiments to investigate Indium diffusion on Cu(100) surfaces. [7] In a first step isolated ^{111}In probes have been deposited at Cu(100) and after annealing the PAC probes are exposed to a well-defined, axially symmetric electric field gradient (see Fig.6a). As can be seen in the Fourier transform the amplitude for ω_2 is dominant, which is consistent with the principal z-axis system of the field gradient being oriented perpendicular to the surface (see chapter 2.1).

In a next step the Cu(100) surface, marked with isolated ^{111}In probes, was covered at 77 K with about 7 % of a monolayer of natural Indium. The effect of this Indium deposition on to the PAC spectrum is that a broadening of the electric field gradient distribution from 1 % to 3.5 % occurs, however, without any significant shift of the average frequency (ω_2 = 344(1) Mrad/s). Now the sample was subjected to to an isochronal

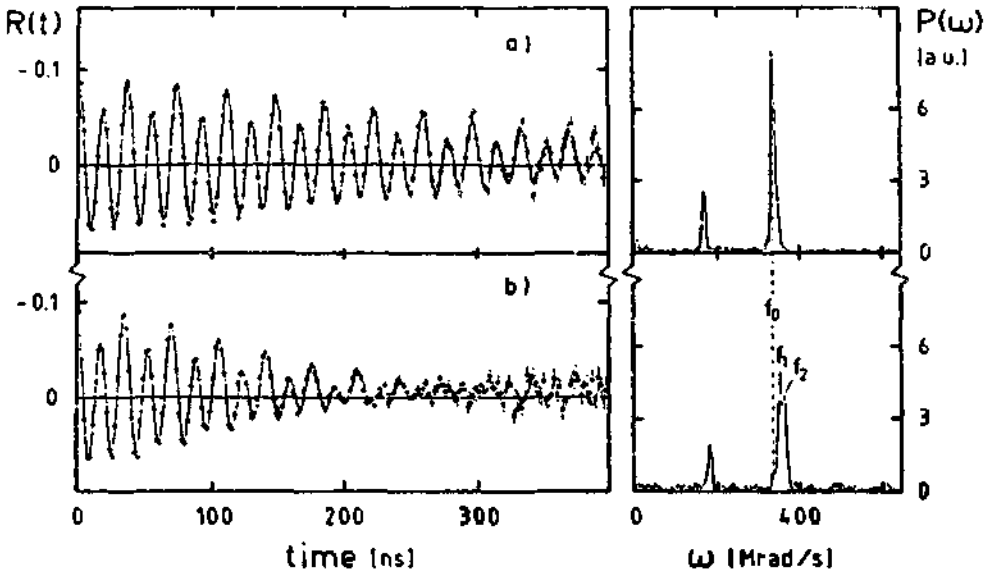

Fig.5: PAC time spectra and their Fourier transforms for isolated ^{111}In on a Cu(100) surface (measurement temperature: 77 K)
a) for a clean Cu(100) surface
b) for the Cu(100) surface covered with about 7 % natural Indium and annealed up to 580 K.

annealing program (annealing time: t_A = 20 min, measurement temperature: T_M = 77 K) to thermally activate diffusion of Indium atoms.

At an annealing temperature T_A = 200 K a frequency shift of the electric field gradient distribution of about 3 % to higher frequencies (ω_2 = 354(2) Mrad/s) is observed and at T_A = 240 K even another fraction with a higher frequency shift (ω_2 = 367(2) Mrad/s) appears. Over the entire annealing temperature range no other new frequencies occur. The PAC spectrum after annealing up to T_A = 580 K is shown in Fig.5b. The Fourier transform clearly shows the splitting of ω_2 into three fractions, the corresponding splitting of ω_1 is not resolved.

The annealing behaviour of the different fractions related to the three frequencies is depicted in Fig.6a. The fraction f_0 is characterized by ω_2 = 344 Mrad/s, which is the same as found for the Cu(100) surface without natural Indium deposition. Therefore we assume that this fraction of ^{111}In probes has no Indium at nearest-neighbour sites on the surface, the observed increase of the field-gradient broadening is due to Indium in the further surrounding. Heating the sample induces Indium diffusion and with our Indium coverage already one or two jumps are sufficient to form In-In pairs. This effect occurs at temperatures between 150 K and 200 K, the fraction of free Indium probes converts as indicated by a frequency shift of 3 %. At higher annealing temperatures the new fraction f_1 of In-In

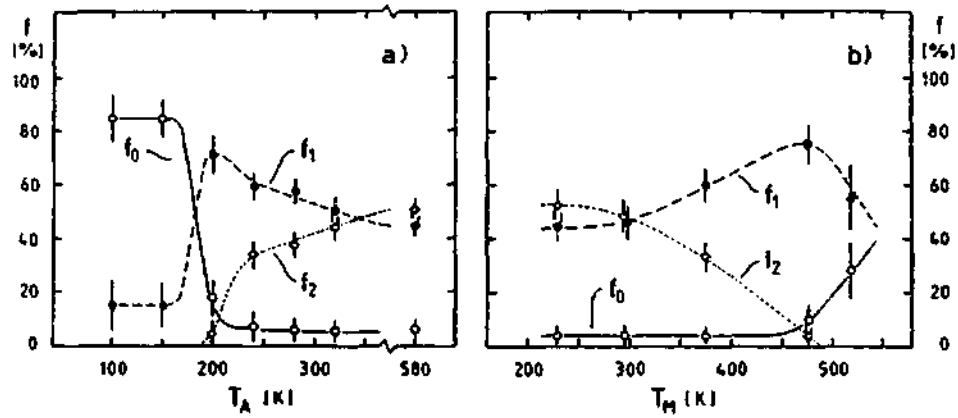

Fig.6: Fractions of ^{111}In probes, which are related to different In configurations, on a Cu(100) surface covered with about 7 % natural Indium
a) as a function of annealing temperature (t_A = 20 min)
b) as a function of measurement temperature.

pairs partially converts in a fraction f_2, which we might identify as small Indium clusters. The slow increase of f_2 at temperatures below 240 K can be explained by the fact that only few free In atoms are left to promote further cluster growth and therefore other clusters have to dissolve.

The ^{111}In fractions were also investigated as a function of PAC measurement temperature, which was kept for several hours typically. This experimental dependence is shown in Fig.6b. Now with increasing temperature the fraction f_2 is reduced in favour of f_1; finally above 470 K also the fraction f_1 starts to diminish, e.g. in our model now In-In pairs break up.

3. Conclusion

The field of employing hyperfine probes to surfaces is still at the beginning, however due to the experimental sophistication surface hyperfine fields can now be measured in a systematic way. Especially the utilization of the PAC method has led to a variety of interesting results, some of them have been indicated in this review. In conclusion, a summary of all the surfece hyperfine fields for free metal surfaces known up to now are listed in Table 1. This table demonstrates that a remarkable progress has been achieved recently in the field of surface hyperfine fields.

Table 1: Magnetic hyperfine fields and electric field gradients at free metal surfaces. [a]

Surface	Probe	Method	B_{hf} (T)	V_{zz} (V/cm²)		η	Orientation of Principal axis
Au (100)	^{111}In	(PAC)	-	1.2(2)	$\cdot 10^{16}$ [a]	0	z ⊥ surface
Cu (100)	^{111}In	(PAC)	-	8.8(14)	$\cdot 10^{17}$	0	z ⊥ surface
Cu (110)	^{111}In	(PAC)	-	7.7(12)	$\cdot 10^{17}$	0.74(1)	z ⊥ surface y ∥ [110]
Cu (111)	^{111}In	(PAC)	-	9.8(15)	$\cdot 10^{17}$	0	z ⊥ surface
Fe (110)	^{57}Fe	(ME)	30.9(4)	3.29	$\cdot 10^{17}$	0 [b]	z ⊥ surface
In (111)	^{111}In	(PAC)	-	4.7(8)	$\cdot 10^{17}$	0.44(4)	z ⊥ surface
Mo (110)	^{111}Cd	(PAC)	-	4.0	$\cdot 10^{17}$	0.2	
W (110)	^{8}Li	(NMR)	-	0.0(4)	$\cdot 10^{15}$		
W (110)	^{9}Li	(NMR)	-	-1.1(1)	$\cdot 10^{15}$		z ⊥ surface
W (110)	^{23}Na	(NMR)	-	-4.74(3)	$\cdot 10^{16}$	0.07(1)	z ⊥ surface

[a] two probe sites observed. [b] assumption by authors

4. References

1) J. Korecki and U. Gradmann, Phys. Rev. Lett. 55 (1985) 2491
2) J. Korecki and U. Gradmann, Europhys. Lett. 2 (1986) 651
3) W. Körner, W. Keppner, B. Lehndorff-Junges, and G. Schatz, Phys. Rev. Lett. 49 (1982) 1735
4) T. Klas, J. Voigt, W. Keppner, R. Wesche, and G. Schatz, Phys. Rev. Lett. 57 (1986) 1068
5) J. Voigt, Diplomarbeit, University of Konstanz (1986)
6) B. Lindgren, Hyperfine Interactions 34 (1987) 217
7) T. Klas, J. Voigt, W. Keppner, R. Platzer, R. Wesche and G.Schatz, Hyperfine Interactions 34 (1987) 677
8) G. Schatz, T.Klas, R. Platzer, J. Voigt, and R. Wesche, Hyperfine Interactions 34 (1987) 555

NEW PERMANENT MAGNETS INVESTIGATED BY MOSSBAUER SPECTROSCOPY

J.P. SANCHEZ

CENTRE DE RECHERCHES NUCLEAIRES 67037 STRASBOURG Cedex, France

I - INTRODUCTION

A permanent magnet is a material able to produce a steady magnetic field after being magnetized. Materials suitable for this purpose should give rise to large hysteresis i.e. high remanence B_r and large coercive field H_c. The measure of the quality of a permenent magnet is usually described by its energy product $(BH)_{max}$. The relevant parameters of a permanent magnet are illustrated by the hysteresis loop plotted as magnetic induction B versus the magnetic field strenght H (figure 1). It is obvious,

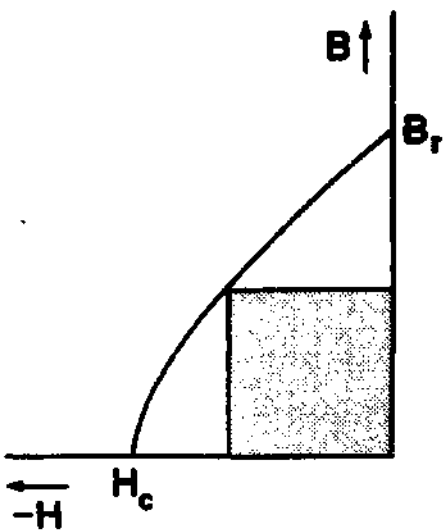

Figure 1 - Second quadrant of hysteresis loop, or demagnetization curve of permanent magnet. The energy product $(BH)_{max}$ is given by the area of the shaded rectangle.

that for practical use the material should order magnetically at a temperature well above RT. It follows, that the main conditions required for good permanent magnet properties are : a) high Curie temperature, b) large spontaneous magnetization (B_r is intimately linked to it), c) large uniaxial anisotropy (one of the primary sources for a high coercive field). These conditions may be fulfilled by alloying 3d transition metals with rare-earth (RE) elements. Indeed, until very recently (1983), Sm-Co intermetallics were known as the laurels of high performance magnets, $(BH)_{max} \simeq 30$ MG Oe. Prices of the raw materials and erratic supply of Co have however impeded growth of the Sm-Co market.

The status of the RE based permanent magnets changed dramatically, when in the late 1983, Sumitomo metals /1/ and General Motors /2/ announced the discovery of a cheap high performance magnet, related to the $Nd_2Fe_{14}B$ phase, with an energy product as high as 40-45 MG Oe (or $\sim$ 350 KJ/m^3). The importance of Nd-Fe-B materials for permanent magnet technology has initiated considerable scientific investigation around the world and specially in Europe, where the European Communities decided to support an Concerted European Action on Magnets (CEAM). One of the aims and objectives of these researches was to characterize and determine the intrinsic properties of alloys with the $Nd_2Fe_{14}B$ structure and of other RE-Fe-B phases as well.

The elucidation of the basic properties of these materials, which is complicated by the coexistence of large number of low-symmetry atomic sites, requires a combination of experimental methods. Among these, Mössbauer spectroscopy is attractive for the elucidation of the local magnetic and structural properties from hyperfine interactions at both the iron and RE elements. This microscopic tool has provided a variety of useful

informations concerning the local magnetic moments, the magnetic structure and spin reorientation effects. The analysis of the quadrupole interaction data (^{155}Gd, ^{161}Dy) allowed the first experimental evaluation of the second order RE crystal field parameters, a key to understand the magnetocrystalline anisotropy in these materials (i.e. easy axis or easy plane). It has also been possible to deduce the Fe-RE exchange interactions from the temperature dependence of the RE sublattice hyperfine fields (^{161}Dy). Moreover, the Mössbauer spectroscopy has been shown to be very suitable for phase analysis, determination of the iron site preference and for the study of hydrogen adsorption properties.

In this paper, we will first summarize the structural and bulk magnetic properties of the $RE_2Fe_{14}B$ phases. The contribution of the Mössbauer spectroscopy to the knowledge of the intrinsic properties of these new permanent magnets will then be given.

II - CRYSTAL STRUCTURE AND BULK MAGNETIC PROPERTIES OF THE $RE_2Fe_{14}B$ COMPOUNDS

II.1. - Crystal structure

The crystal structure of the $Nd_2Fe_{14}B$ phase was determined by powder neutron diffraction /3/ and single crystal X-ray measurements /4,5/. Subsequent works showed that the RE elements form a series of isostructural compounds with the $Nd_2Fe_{14}B$ structure (the Eu compound, however, does not exist). The structure is tetragonal (space group $P4_2/mnm$); it includes two structurally distinct RE sites and six non-equivalent Fe sites, all of which possess point symmetries lower than axial symmetry (Figure 2, Table 2). It is interesting to notice that the RE atoms occupy the center of an hexagonal

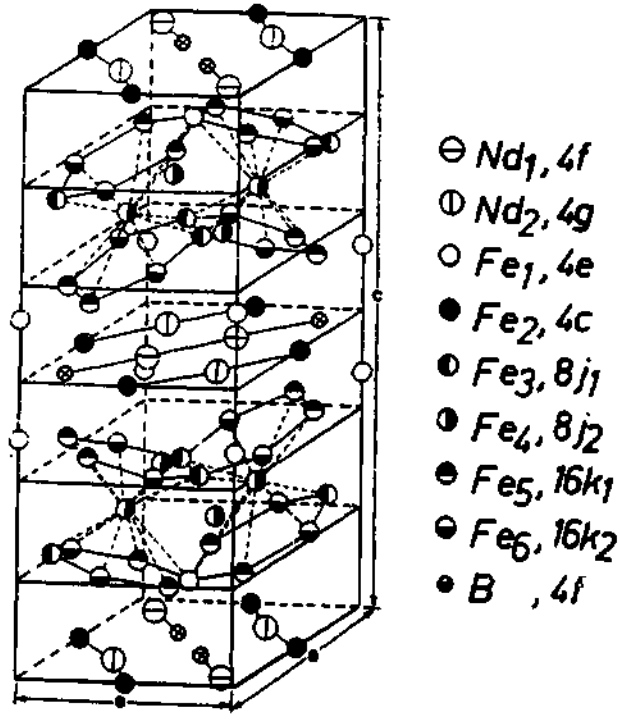

Figure 2 – Crystal structure of $Nd_2Fe_{14}B$ after Herbst et al. /3/. The c-axis is not to scale. The notation of the site follows the convention of Givord et al. /4/.

prism as in the $RECo_5$ structure. The other points which deserve attention are the occurrence of very short Fe-Fe distances i.e. 2.39 Å (j_1-K_2) and the similarity of the Fe(j_2) site with the dumbell 2c or 4f sites in the hexagonal or rhombohedral $REFe_{17}$ structures /6/ (the j_2 (2c, 4f) sites are situated on the midpoint between the centers of Fe hexagons stacking along the c-axis).

Table 1 - Atomic sites, number and type of nearest neighbours (CN) and average distances. The notation of the sites follows the covention of Givord et al. /4/. Notice that Nd site designed by g corresponds to the f site in the Herbst et al. /3/ paper.

Atom	Site	CN and average distances		
		Nd	Fe	B
Nd_1	4f	(3) 3.71	(16) 3.23	(1) 2.89
Nd_2	4g	(2) 3.79	(16) 3.11	(2) 3.25
Fe_1	4e	(2) 3.19	(9) 2.59	(2) 2.09
Fe_2	4c	(4) 3.25	(8) 2.53	-
Fe_3	$8j_1$	(3) 3.30	(9) 2.55	-
Fe_4	$8j_2$	(2) 3.10	(12) 2.70	-
Fe_5	$16K_1$	(2) 3.06	(9) 2.58	(1) 2.10
Fe_6	$16K_2$	(2) 3.17	(10) 2.54	-
B	4f	(3) 3.13	(6) 2.10	-

II.2. - Bulk magnetic properties

The magnetic properties of the $RE_2Fe_{14}B$ series have been reviewed by Buschow /7/, Coey /8/ and Givord /9/. It has been shown that they are governed by the Fe-Fe and RE-Fe exchange interactions and by the RE single ion anisotropy, at least at low temperature where the 4f anisotropy usually dominates the 3d one.

Investigations of the alloys with non-magnetic RE showed that the mean iron moment ($\sim$ 2.1 μ_B) is slightly smaller that the value of 2.2 μ_B of α-Fe /10/. This moment reduction was ascribed to electron transfert and hybridation effects.

The Curie temperatures (figure 3) are relatively low compared to iron metal (T_c = 1043 K). This is attributed to the occurrence of Fe-Fe bonds shorter than 2.5 Å which favour antiferromagnetism .

Analysis of magnetization data of $Y_2Fe_{14}B$ single crystal allowed to conclude that the c-direction is the easy direction of magnetization for the iron sublattice. The anisotropy constant K_1 which is rather small (7.05 x 10^6 erg/cm^3 at 4.2 K) has a peculiar temperature dependence /11, 12/.

From the values of the spontaneous magnetization at low temperature it was concluded that the Fe and RE sublattices couple ferromagnetically for light RE and antiferromagnetically in the case of heavy RE /10/. It should be noticed that the Fe-RE interactions almost constant for heavy RE is about twice as large for light RE (Pr or Nd). This effect is attributed by Givord to different 4f-5d overlap accross the series /13/.

The RE anisotropy which is related to the crystal field acting at the RE sites determines at low temperature the magnetic structures of the non-S RE alloys. At RT the direction of the bulk magnetization (excepted for the Yb compound) is strongly correlated to the sign of the second order α_J

Stevens coefficients (figure 3). This suggest the dominance, at RT, of the second order crystal field terms (B_2^0, B_2^2) in determining the RE anisotropy, and in turn the bulk anisotropy. At high temperature (i.e. close to T_c) the iron anisotropy overrules the RE anisotropy and the c-direction is the easy direction (excepted for the Sm compound). Thus, the uniaxial iron anisotropy competes with the RE anisotropy when $\alpha_J > 0$ (figure 3). Spin reorientations, as expected, have been observed in $Er_2Fe_{14}B$ (323 K /12/), $Tm_2Fe_{14}B$ (315 K /12/) and $Yb_2Fe_{14}B$ (115 K /14/). Another type of spin reorientation transitions occurs in $Nd_2Fe_{14}B$ (150 K) and $Ho_2Fe_{14}B$ (58 K /12/) at low temperatures (the net magnetization becomes inclined with respect to the c-axis); 4th order crystal field terms should be considered in these cases /15/. Notice that the actual magnetic structure of $Nd_2Fe_{14}B$ has not yet been

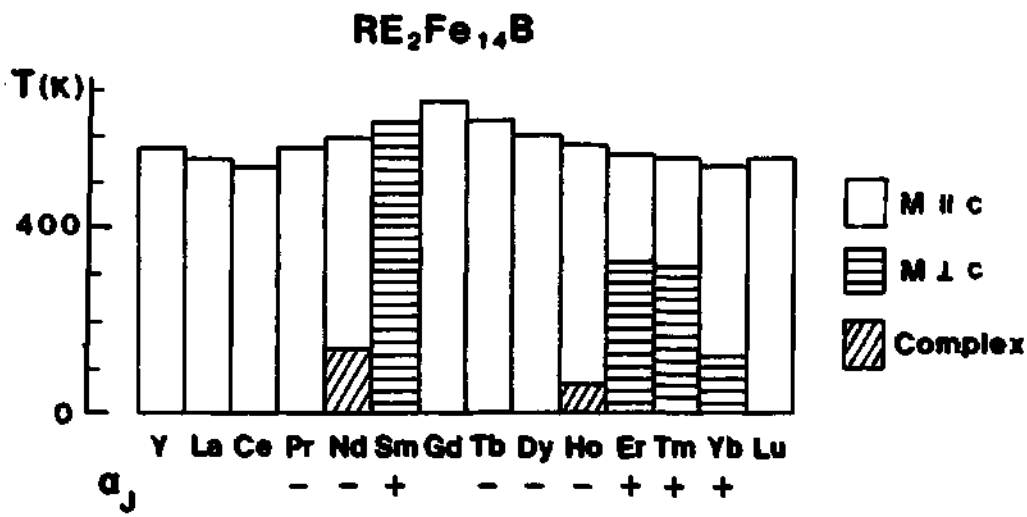

Figure 3 : Curie temperature, second order Stevens factor for different RE and easy axis direction in $RE_2Fe_{14}B$ alloys.

completely solved ; preliminary work by Givord indicates that the structure is non-collinear with several RE sublattices.

Although RE-Fe-B magnets have very high $(BH)_{max}$, their Curie temperatures and anisotropy fields are relatively low. Thus, many efforts have been devoted to improve their high temperatures properties by atom substitutions in the $Nd_2Fe_{14}B$ or $Pr_2Fe_{14}B$ phases /16,17,18/. Co substitution for Fe increases dramatically the Curie temperature but has negative effects, both the spontaneous magnetization and the anisotropy field decrease. The anisotropy, and therefore the coercitivity, can be improved by replacing Nd or Pr by RE with uniaxial anisotropy ($\alpha_J < 0$). Dy or Tb seems to be the best candidates however, the spontaneous magnetization decreases owing to the antiparallel coupling of the Dy and Fe moments.

III - MOSSBAUER MEASUREMENTS IN THE $RE_2Fe_{14}B$ ALLOYS AND RELATED PHASES

III.1. - Iron sublattice properties : local moments and site preference of iron

Numerous ^{57}Fe Mössbauer investigations of the $RE_2Fe_{14}B$ alloys were undertaken with the emphasis to obtain informations on the magnetic properties of the Fe sublattice /19,20,21/. Complex Mössbauer spectra were observed as expected owing to the occurrence of six iron sites of low symmetry in addition to the presence of Fe-base impurity phases (α-Fe, $REFe_4B_4$ or RE_2Fe_{17}). Thus, constraints need to be included in the data analyses, i.e., the intensities of the six subsites were maintained proportional to the occupation numbers deduced from the crystal structure (16:16:8:8:4:4). It should be noticed that when the magnetization is not in the c-direction, some sites that are crystallographically equivalent become magnetically

inequivalent /22/. This further complication was never taken into account in the fitting model ; it shows up by a mere broadening of the resonance lines.

In all cases, the quadrupole interaction was treated as a first order perturbation of the magnetic interaction i.e. the effective quadrupole splitting is given by :

$$D_Q = 1/4\ e^2qQ\ (3\cos^2\theta - 1 + \eta \sin^2\theta \cos 2\Phi) \qquad (1)$$

where (θ, Φ) define the direction of the hyperfine field in the electric field gradient (efg) tensor principal axes.

Due to the complexities of the spectra and the limited resolution, there was no unique way to fit the data ; but some general agreement exists for the hyperfine field values of the three major sites $16K_1$, $16K_2$ and $8j_2$ but some discrepancies exist for $8j_1$ and the weaker 4c and 4e patterns (Table 2 - figure 4). Nevertheless, the average hyperfine field appears to be insensitive on the fitting model. The assignment of the different Fe sites was made by reference to the systematics of the hyperfine parameters established in the RE-Fe intermetallics, i.e., a monotonic correlation exist between the hyperfine field and the number of n.n. Fe atoms (Table 1). The hyperfine pattern with the largest H_{hf} was assigned to the structural site $8j_2$ which present 12 n.n. Fe ; as already pointed out the coordination of this site is comparable to the dumbell site in RE_2Fe_{17} alloys which also present an enhanced H_{hf} value /20/.

The evaluation of the efg parameters was far more difficult owing to the low symmetry of the Fe sites ; large asymmetry parameters and arbitrary orientations of the efg axes were predicted from point charge calculations /20/. Friedt et al. /20/ showed however, that the $8j_2$ site which has

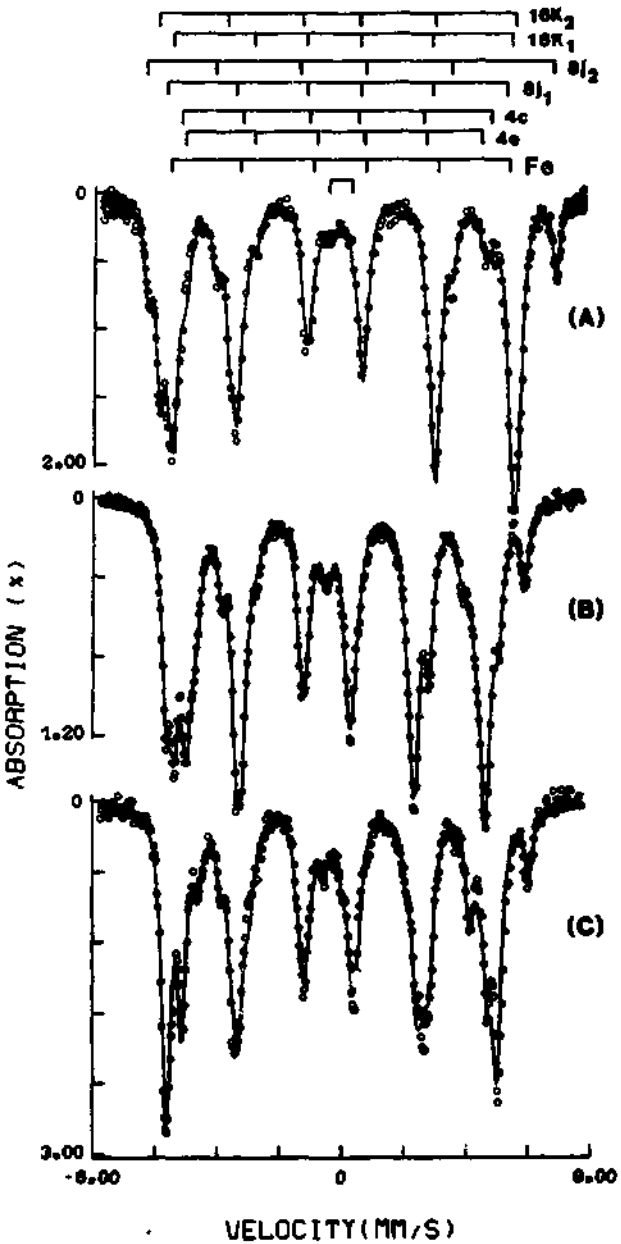

Figure 4 - ^{57}Fe Mössbauer spectra of $Dy_2Fe_{14}B$ at 4.2 K (A) and 295 K (B) ; and of $Dy_2Fe_{14}BH_{3.5}$ at 295 K (C) /23/.

the largest quadrupole interaction was of nearly axial symmetry ($\eta \simeq 0$) along the c-direction. This favourable circumstance was used to detect spin reorientation transition (see below).

The rare-earth dependence of the average hyperfine field at 300 K is presented in Figure 5. For non-magnetic RE (including Y), the average hyperfine field is shown to decrease from La to Lu. The Ce compound is somewhat anomalous, Ce is tetravalent and its T_c is depressed. The iron hyperfine fields are larger with magnetic RE (the maximum value is observed for Gd); they follow roughly the De Gennes law, $H_{hf} \propto (g_J-1)J$.

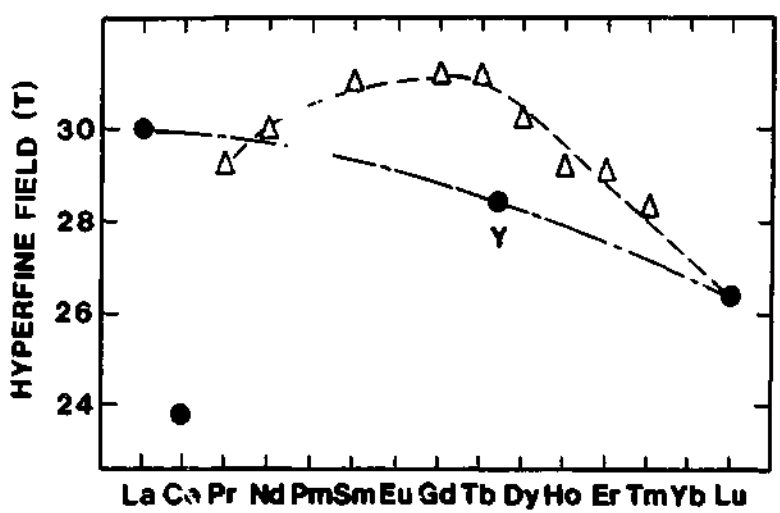

Figure 5 - RE dependence of the mean iron hyperfine field at RT (adapted from /21/).

The magnetic moments deduced from Mössbauer effect are compared in Table 2 with those obtained by neutron scattering measurements /24/ ; only crude agreement between the two sets of results was obtained. Notice,

Table 2 - Values of the hyperfine fields acting on ^{57}Fe nuclei at the six Fe sites in $Y_2Fe_{14}D$ at 4.2 K. The value of the iron moment was estimated from the hyperfine field corrected for the dipolar field /21/ using the relation 1 μ_B = 15 T. The last line corresponds to the moments deduced from polarized neutron scattering experiments /24/.

	$16K_2$	$16K_1$	$8j_2$	$8j_1$	4c	4e	average	
H_{hf} (T)	34.4	32.5	38.1	32.1	32.4	32.0	33.7	
H_{hf}-H_{dip}(T)	34.6	32.5	38.8	32.7	31.5	32.0	33.9	/20/
$\mu(\mu_B)$	2.31	2.17	2.59	2.18	2.10	2.13	2.26	
H_{hf} (T)	34.3	32.1	36.9	35.2	30.3	35.3	33.9	
H_{hf}-H_{dip}(T)	34.5	32.1	37.6	35.8	29.4	35.3	34.1	/21/
$\mu(\mu_B)$	2.30	2.14	2.51	2.39	1.96	2.35	2.27	
$\mu(\mu_B)$	2.25	2.25	2.80	2.40	1.95	2.15	2.32	/24/

however, that the probing of magnetic moments by these two methods are not strictly equivalent and, that the neutron measurements are rather unsensitive to the polarization of the conduction electrons.

The other point which deserves attention is the demonstration by Mössbauer effect measurements of a small anisotropy (1 - 2.5 %) of the iron magnetization /14, 21/. The occurrence of a minute Fe orbital moment was evidenced from the observation of a discontinuity of the average hyperfine field when the Fe magnetization changes its direction from parallel to perpendicular to the c-axis. It was furthermore shown by Fruchart et al. /21/ that the local iron anisotropy has opposite sign for the 16 K and $8j_2$ sites; these authors suggest that this may be the reason for the unusual temperature dependence of the iron anisotropy in $Y_2Fe_{14}B$.

^{57}Fe Mössbauer measurements in $RE_2(Fe_{1-x}Co_x)_{14}B$ alloys have been undertaken with the aim to obtain informations on the site preferences /17, 25, 26/. The data confirmed the preferential occupation of the $8j_2$ site by the iron atoms while the opposite holds for the $16K_2$ site (Figure 6).Table 1 shows that $8j_2$ site in $Nd_2Fe_{14}B$ has the highest number (12) of n.n. 3d atoms at the largest average distance (2.70 Å). In contrast $16K_2$ site has 10 n.n. 3d atoms at a mean distance of 2.54 Å. Thus, as pointed out by Van Noort and Buschow /25/, the preferential site occupancy of Co and Fe atoms is mainly linked to the smaller size of Co atoms. The Co atoms by occupying the smaller size suppress the weakest Fe-Fe exchange interactions and thus enhance T_c. Deppe et al. /26/ showed, furthermore, that the average hyperfine field decreases with the Co content when $x > 0.1$.

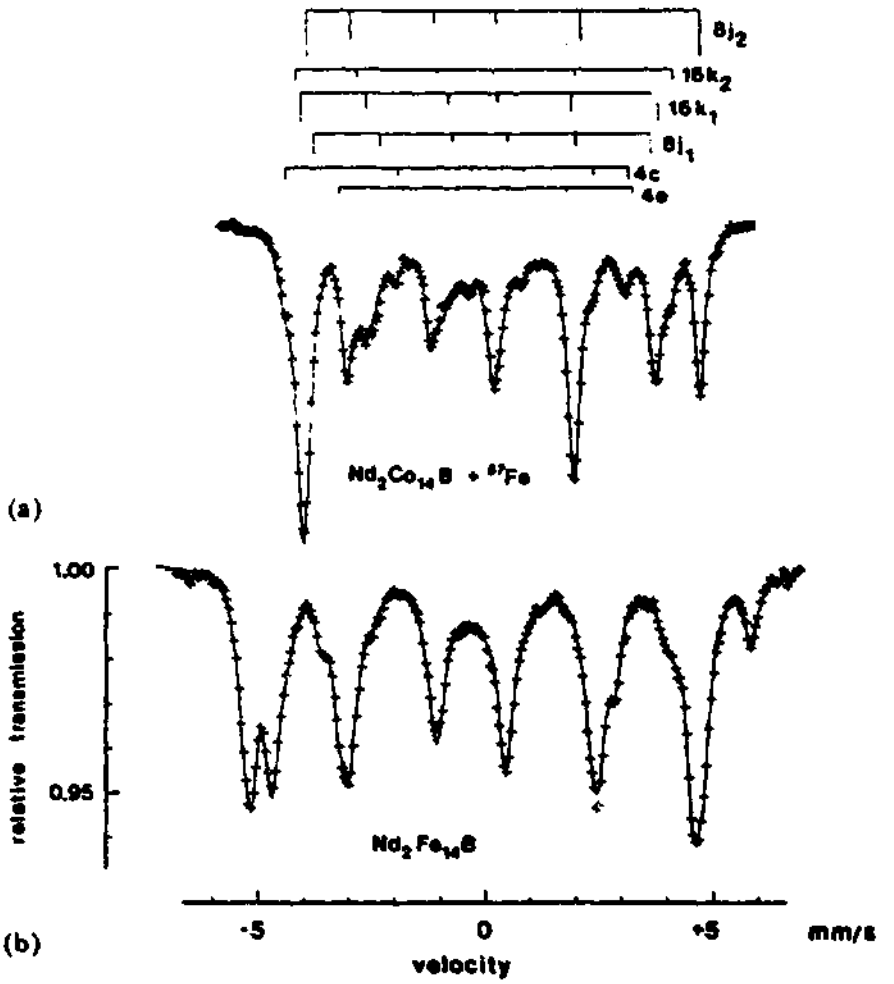

Figure 6 - ^{57}Fe Mössbauer spectrum at RT of $Nd_2Co_{14}B$ doped with 2 % ^{57}Fe (a). The $Nd_2Fe_{14}B$ spectrum (b) is shown for comparison /25/.

III.2. - Rare-earth sublattice properties : crystal field, local moments and exchange interactions

Measurements of the hyperfine parameters (Figures 7 to 9) at the two RE sites in the $RE_2Fe_{14}B$ alloys have been performed using the ^{155}Gd /27, 28/, ^{161}Dy /20, 21/ and ^{166}Er /29/ Mössbauer isotopes (^{169}Tm measurements were mentionned in /7/ but not yet published, ^{174}Yb Mössbauer experiments by G. Czjzek et al. are in pregress).

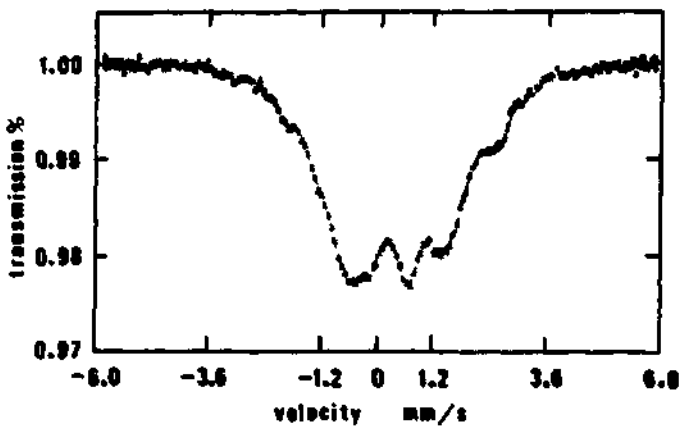

Figure 7 - ^{155}Gd Mössbauer spectrum of $Gd_2Fe_{14}B$ at 4.2 K /27/.

The magnetic hyperfine field acting on the RE nuclei in $RE_2Fe_{14}B$ alloys (Table 3) is commonly described as a sum of several contributions :

$$H_{hf} = H_{4f} + H_{cp} + H_{op} + H_n(RE) + H_n(Fe) \qquad (2)$$

H_{4f} represent the field produced by the 4f localized electrons (orbital plus spin dipolar contribution); H_{cp} is the core polarization field,

$H_{cp} \simeq -10\,(g_J-1)J$(Tesla) ; the last three terms stand for the conduction electron contribution due to the RE own polarization (H_{op}) and to the neighbouring magnetic atoms, H_n(RE) and H_n(Fe). For S-state ions (Gd^{3+}) the 4f field vanishes to zero. Thus, the ^{155}Gd hyperfine field data (Table 3) allow a direct estimate of the field produced by the conduction electron polarization, $H_{ce} \equiv H_{op} + H_n(RE) + H_n(Fe)$, along the $RE_2Fe_{14}B$ series. Strictly speaking H_{op} and H_n(RE) are proportional to the RE spin whereas H_n(Fe) is proportional to the iron sublattice magnetization. The larger contribution to H_{ce} is provided by H_n(Fe); hence, the ^{155}Gd data actually provide an upper limit for H_{ce} which is taken as + 49 T for site 4f and + 62 T for site 4g. The intra ionic fields ($H_i \equiv H_{4f} + H_{cp}$) at both the ^{166}Er (757 T, average) and ^{161}Dy (568 T and 566.5 T) nuclei are very close to the respective free ion values (Table 3). Thus the hyperfine fields imply that J_z is nearly fully saturated in $RE_2Fe_{14}B$ alloys, in agreement with magnetization data.

Table 3 - Hyperfine fields at the ^{155}Gd, ^{161}Dy and ^{166}Er nuclei in $RE_2Fe_{14}B$ alloys. A positive Gd hyperfine field means that the field is parallel to the RE sublattice magnetization.

Site	H_{hf}(T)		
	^{155}Gd	^{161}Dy	^{166}Er
4f	+ 15.3 (2)	616 (2)	
			812 (5)
4g	+ 27.6 (2)	628 (2)	
Free ion	- 34.0 (2)	563 (11)	765 (8)

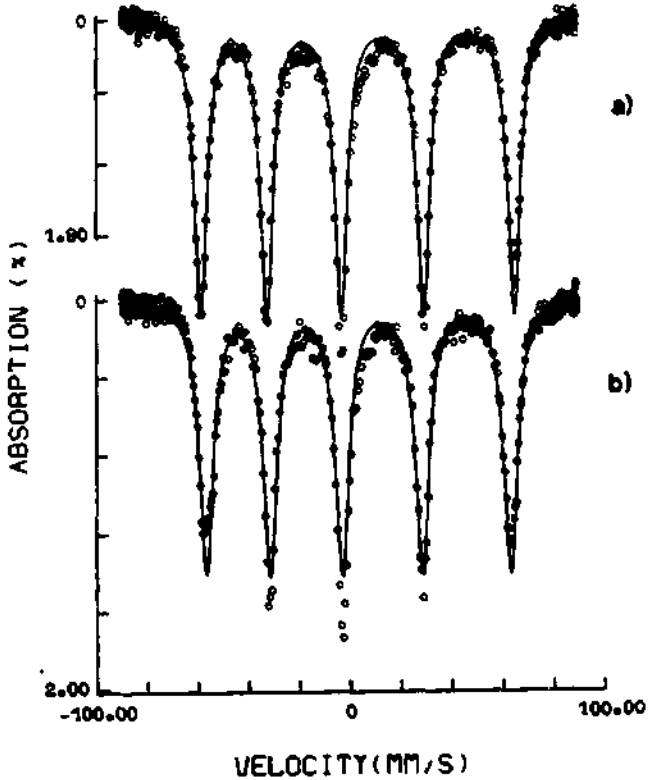

Figure 8 - ^{166}Er Mössbauer spectra of $Er_2Fe_{14}B$(a) and $Er_2Fe_{14}BH_{2.6}$(b) taken at 4.2K /29/.

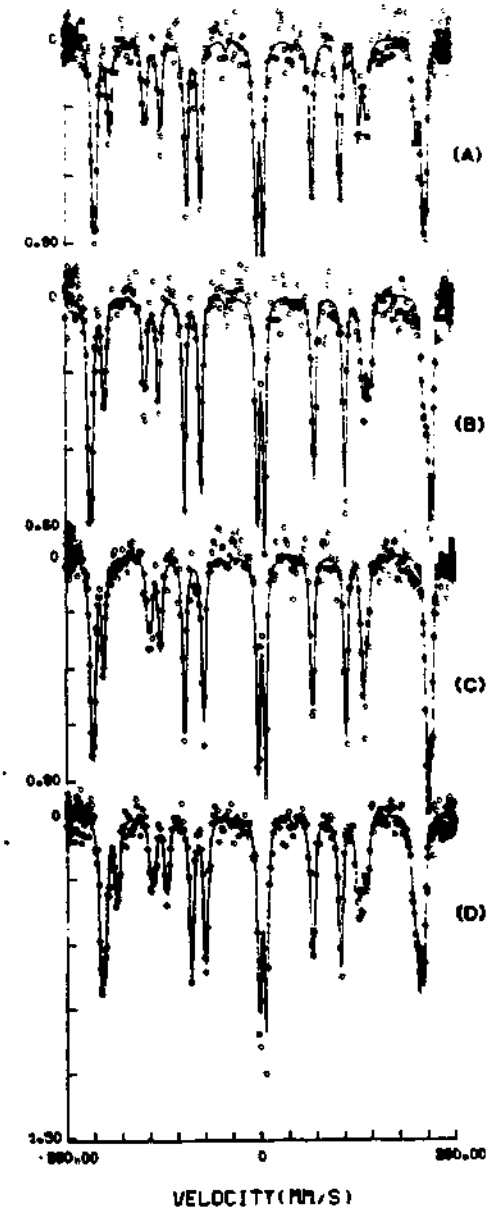

Figure 9 - ^{161}Dy Mössbauer spectra of $Dy_2Fe_{14}B$ at (A) 77 K, (B) 4.2 K and in $Dy_2Fe_{14}BH_{3.3}$ at (C) 4.2 and (D) 77 K /20, 23/.

The electric field gradient (efg) acting at the RE sites is the sum of a 4f contribution eq^{4f} and of a lattice contribution eq^{lat}. The possible contribution from the conduction electron is included in eq^{lat} :

$$eq = eq^{4f} + eq^{lat} \qquad (3)$$

At low temperature the second term is treated as a perturbation of the dominant and essentially axial eq^{4f} :

$$e^2q_zQ = e^2q_z^{4f}Q + 1/2\ e^2q_z^{lat}Q\ (3\cos^2\theta - 1 + \eta^{lat}\sin^2\theta\cos 2\varphi) \qquad (4)$$

where (θ , φ) are the polar angles defining the direction of the RE moment (Z-axis) in the lattice efg system of axes (z).

For S-state ions (Gd^{3+}) the 4f efg vanishes to zero. This allows us to calculate the lattice quadrupole coupling constant for the non-S RE ions (Table 4).

The orientation of the lattice efg principal axes with respect to the crystallographic reference frame deduced from symmetry considerations and point charge calculations /11,20/ was confirmed by the ^{155}Gd data. One axis coincides with the crystal c-axis and the other two are in the (a, b) plane (Figure 10). Thus, the polar angles (θ , φ) can be deduced when the orientation of the RE moments is known. Notice that we assumed in Table 4 that the Er moments are along the a-axis. Actually, this is only true for the net Er moment ; a fan magnetic structure was predicted for $Er_2Fe_{14}B$ /30/.

Table 4 - Measured quadrupole interaction parameters in $RE_2Fe_{14}B$ alloys and estimated contribution from the lattice to the total quadrupole coupling constant at the ^{161}Dy and ^{166}Er nuclei as calculated by scaling from the ^{155}Gd data /28/ (with Q (^{155}Gd) = 1.30 b, $Q^*(^{166}Er)$ = -1.59 b and Q (^{161}Dy) = 2.35 b). $e^2q^{4f}Q$ is estimated according to Eq.4.

Site	^{155}Gd		^{161}Dy		^{166}Er	
	4f	4g	4f	4g	4f	4g
e^2qQ (mm/s)	-3.50(9)	+5.05(9)	115(2)	114(2)	12.3(5)	
$e^2q^{lat}Q$ (mm/s)	-3.50(9)	+5.05(9)	-21.3	+30.8	+4.60	-6.63
η^{lat}	0.61(7)	0.35(3)	0.61	0.35	0.61	0.35
(θ,φ)	(0,0)	$(\pi/2,\pi/2)$	(0,0)	$(\pi/2,\pi/2)$	$(\pi/2,\pi/4)$	$(\pi/4, 0)$
$e^2q^{4f}Q$ (mm/s)	0	0	136.3	134.8	14.6	14.5
$e^2qQ^{free\ ion}$ (mm/s)	0	0	140(7)		16.3(7)	

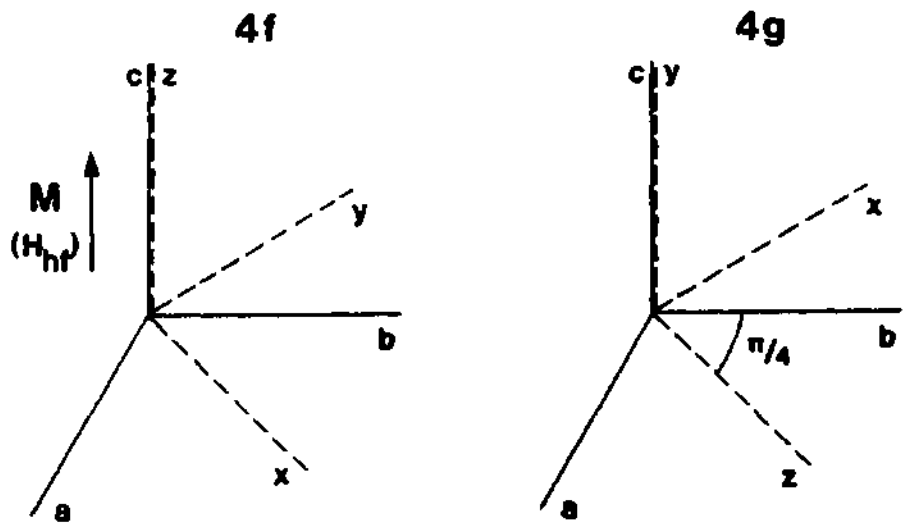

Figure 10 - Orientation of the lattice efg principal axes with respect to the crystallographic reference frame. The direction of RE sublattice magnetization (or hyperfine field) corresponds to the situation occurring in the Gd or Dy compound.

The estimated 4f contribution to the quadrupole coupling constant in $Dy_2Fe_{14}B$ and $Er_2Fe_{14}B$ (Table 4) show that they are very close to the free ion values. Actually a minute crystal field admixture was observed for the Er compound.

In conclusion both the hyperfine field and the quadrupolar data indicate a nearly free ion behaviour for the non-S RE compounds, as expected when the exchange dominates the crystal field interaction.

The ^{155}Gd data are of special interest owing that the determination of the efg acting at the Gd nuclei provided a direct information on the second order crystal field terms which determine the RE anisotropy. B_2^0 and

B_2^2 can be scaled from the efg parameters using the relations :

$$B_2^0 = -\frac{\alpha_J \; eq^{lat} \langle r^2 \rangle_{4f} (1-\sigma_2)}{4(1-\gamma_\infty)} \; ; \; |B_2^2| = |B_2^0| \; \eta^{lat} \qquad (5)$$

Separating the factors which vary from one RE ion to another, Bogé et al. /28/ defined universal parameters A_2^m by $B_2^m = (1-\sigma_2)\,\alpha_J \langle r^2 \rangle_{4f} A_2^m$. The A_2^m parameters being approximatively constant for all RE in the $RE_2Fe_{14}B$ series. It follows that $A_2^0 = -\frac{eq^{lat}}{4(1-\gamma_\infty)}$ and $|A_2^2| = |A_2^0|\,\eta^{lat}$ in the efg principal axes system. It is customary to use the c-axis as reference system for the crystal field ; thus, for site 4g the coordinate system has to be rotated by 90°. The values for A_2^m deduced from the ^{155}Gd efg data are listed in Table 5 along with the values resulting from point charge calculations /11/. The A_2^0 values have about the same magnitude and are positive for both RE sites. This means that the c-axis is an easy axis for RE ions with $\alpha_J < 0$ while an easy plane is favoured when $\alpha_J > 0$.

Table 5 - Experimental values of the second order crystal field parameters A_2^0 and A_2^2 (referred to c-axis) derived from ^{155}Gd efg data (γ_∞ =-92) and point charge calculations /28/.

Site		A_2^0 (K/a_0^2)	$\lvert A_2^2 \rvert$ (K/a_0^2)
4f	from efg	600(17)	414(49)
	cal.	1900	500
4g	efg	661(19)	1298(27)
	cal.	1400	1600

Informations about the physical parameters describing the exchange interactions between the RE ions and the Fe sublattice may be derived from the temperature dependence of the hyperfine field acting at the RE sites. Berthier et al. /31/ deduced the experimental variation of the Dy moments with temperature from $H_{hf}(T)$ by assuming that the temperature dependence of $H_n(Fe)$ can be neglected below 400 K and starting from $M^{Dy} = 10\ \mu_B$ at 4.2 K (Figure 11). The magnetic exchange interaction (H_{ex}^{Dy}) acting on Dy moments

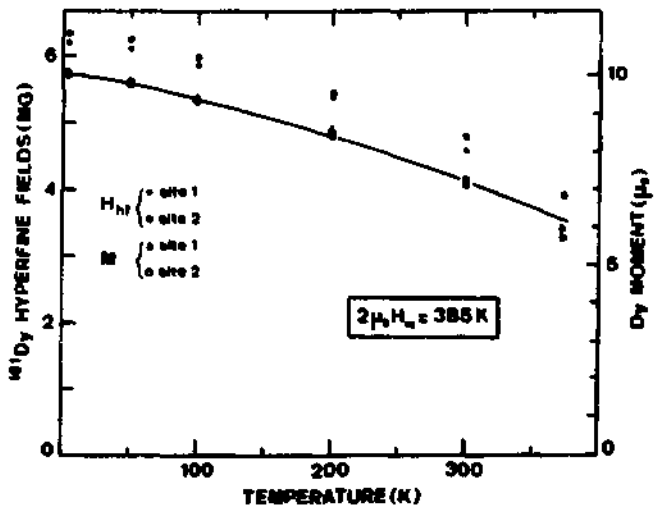

Figure 11 – Experimental temperature dependence of the Dy hyperfine field in $Dy_2Fe_{14}B$ and deduced temperature dependence for the Dy moments. The solid curve represents the best fit to the data with a Brillouin function (see text) /31/.

was obtained from the fit of the experimental points to the Brillouin function :

$$M^{Dy}(T) = M^{Dy}(0)\ B_{15/2}\ (2S\ \mu_B\ H_{ex}^{Dy}/kT) \qquad (6)$$

with the exchange field assumed to be proportional to the Fe sublattice magnetization, $M^{Fe}(T) = M(T) - M^{Dy}(T)$, obtained from magnetization measurements on a single crystal. The value of $2\,\mu_B H_{ex}$ = 385 K at 4.2 K was found to be in good agreement with other estimates /27/.

III.3. - Magnetic structures and spin reorientation phenomena

The two types of spin reorientation phenomena encountered in $RE_2Fe_{14}B$ alloys have been investigated thoroughly by Mössbauer effect measurements in powdered and magnetically aligned samples /14, 20-22, 32-36/.

Spin reorientations where the Fe magnetization changes its direction from c-axis to basal plane, as the temperature is decreased, were detected by following the temperature dependence of the outermost right hand resonance line belonging to the $6j_2$ pattern (Figure 12). The reduction by a factor of about -2 of D_Q (Eq. 1) for the $6j_2$ site, when crossing the spin reorientation transition from above, is consistent with a 90° rotation of the moments.

The data obtained with magnetically aligned samples are more informative since the rotation of the moments can be followed more easily and their orientations with respect to the crystallographic axes may be provided by complementary X-ray diffraction measurements.

The Fe spin reorientation are detected by observing the relative intensity change of the $\Delta m = 0$ ^{57}Fe Mössbauer resonance lines (Figure 13). This method relies on the fact, for magnetically split ^{57}Fe spectrum, the intensities of the six lines are (ideally) in the ratios $3:Z(\alpha):1:1:Z(\alpha):3$, where α is the angle between the gamma-ray wavevector and the hyperfine field (or magnetization) direction, and $Z(\alpha)$ =

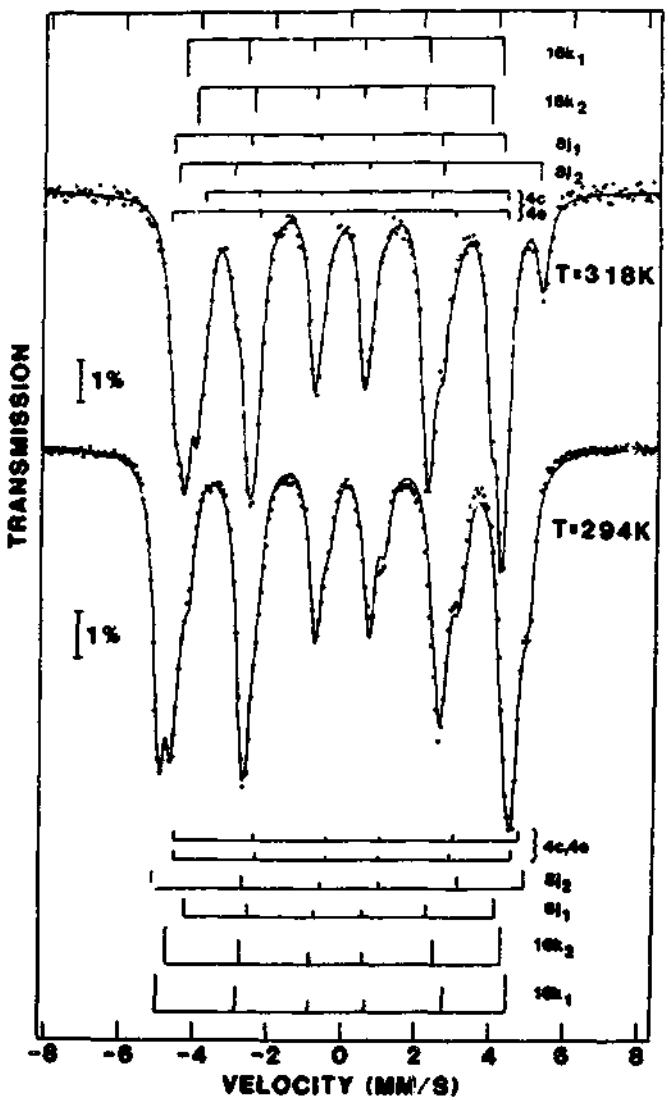

Figure 12 - ^{57}Fe Mössbauer spectra of $Tm_2Fe_{14}B$ above and below the spin reorientation transition /22/.

$4 \sin^2\alpha / (1 + \cos^2\alpha)$. Thus, for an absorber whose spins are initially aligned parallel to the gamma-ray direction, a 90° spin reorientation will manifest itself as a $Z(\alpha)$ change from 0 to 4 (Figure 13).

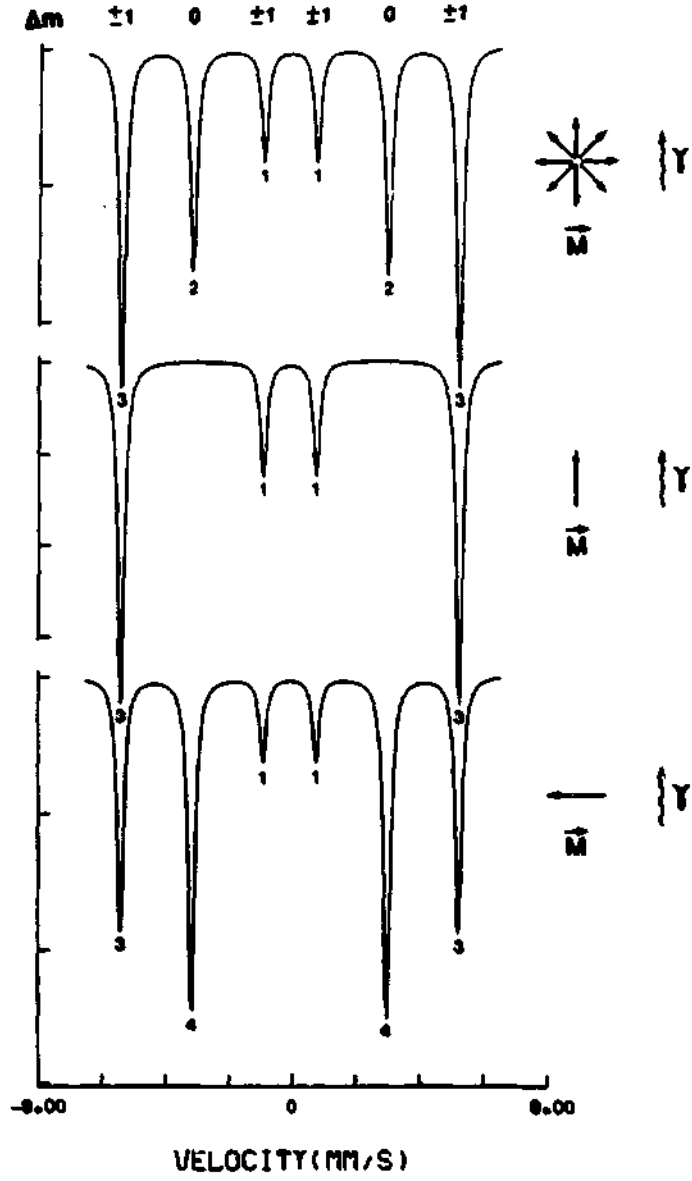

Figure 13 - Principle of the method for determining the orientation of the Fe magnetic moments from the relative intensities of the six resonance lines of a magnetically split spectrum (see text).

For $Er_2Fe_{14}B$ /33/ and $Tm_2Fe_{14}B$ /21/ the ^{57}Fe Mössbauer spectra change dramatically around respectively 328 and 316 K (Figure 14), in clear demonstration for a spin reorientation occurring at these temperatures, with the spins rotating from c-axis to basal plane when the alloys are cooled. The residual intensity in $\Delta m = 0$ above the spin reorientation temperature is due to imperfect alignment of the powder.

For the cases of $RE_2Fe_{14}B$ compounds with RE = Y, Ce, Pr, Tb, Dy, Lu /21, 33/ no change of the relative resonance areas was observed in the temperature range investigated (4.2 K - 350 K). It was concluded that the Fe spins remained aligned parallel to the c-axis (Figure 14). It was furthermore shown, by ^{161}Dy Mössbauer spectroscopy /33/, that the Dy moments are collinear with the Fe spins between 300 and 4.2 K (Figure 15).

Spin cantings of the Fe sublattice in $Ho_2Fe_{14}B$ /21/ and $Nd_2Fe_{14}B$ /32/ at low temperatures were clearly evidenced from the change in the $\Delta m = 0$ line intensities. The canting angles with respect to the c-axis were deduced to amount 30° for both samples.

The change of the reorientation temperature (T_{sr}) by partial substitution of Er by another RE in $(Er\text{-}RE)_2Fe_{14}B$ alloys was investigated by ^{57}Fe Mössbauer spectroscopy in $(Er_{1-x}Gd_x)_2Fe_{14}B$ /35/ and $(Er_{1-x}Dy_x)_2Fe_{14}B$ /34, 36/ magnetically oriented samples. The study of T_{sr} as a function of x in $(Er_{1-x}RE_x)_2Fe_{14}B$ compounds is a means of testing microscopic models for the crystal electric field (CEF) and exchange interactions in these alloys.

The data for $(Er_{1-x}Gd_x)_2Fe_{14}B$ were quantitatively explained in terms of a Hamiltonian which included second order CEF terms, RE-Fe interaction, plus an uniaxial anisotropy due to the Fe sublattice /35/.

A rapid decrease of T_{sr} with x was observed in $(Er_{1-x}Dy_x)_2Fe_{14}B$ alloys, as expected from competition between the uniaxial anisotropy of Dy

Figure 14 - ^{57}Fe Mössbauer spectra of magnetically aligned $Dy_2Fe_{14}B$ and $Er_2Fe_{14}B$ powder samples. Alignment at 360 K along the γ-propagation axis in a field of 1.7 T and freezing in paraffin/epoxy resin. Measurement of the Dy alloy at (A) 295 K, (B) 4.2 K and of the Er alloy at (C) 328 K, (D) 295 K /20/.

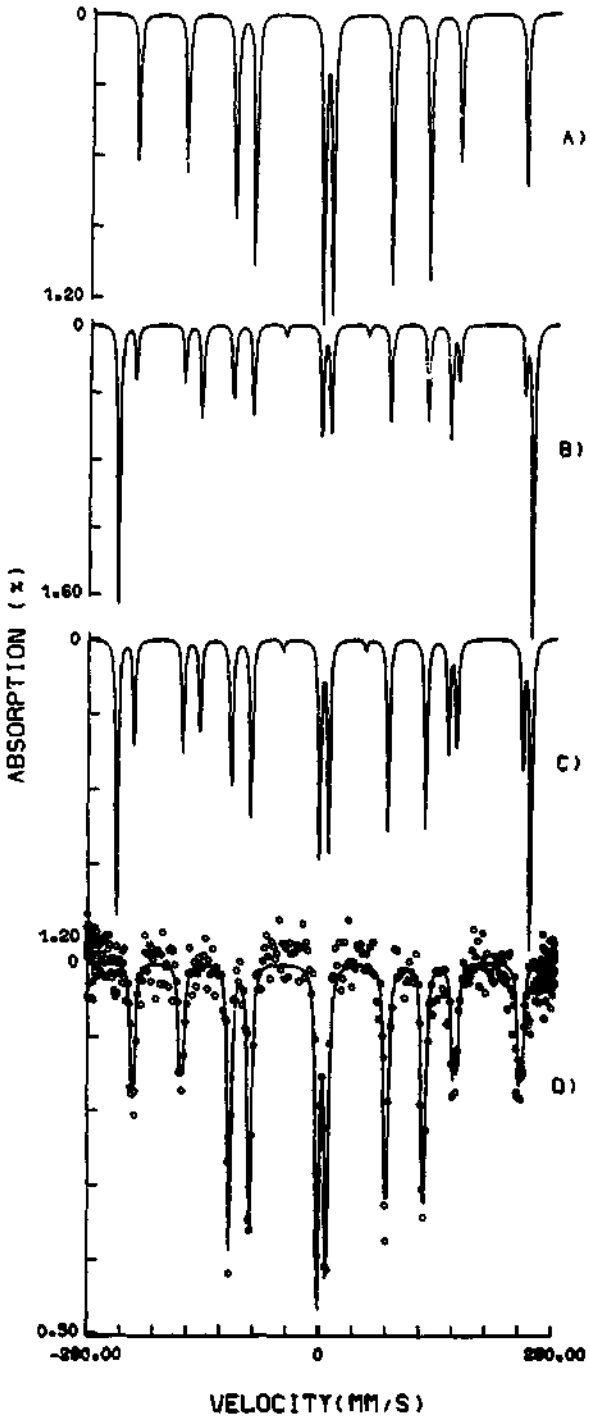

Figure 15 - Calculated ^{161}Dy Mössbauer spectra for oriented samples : (A) $M^{Dy}//\gamma$, (B) $M^{Dy}\perp\gamma$ and (C) non-oriented samples. (D) ^{161}Dy Mössbauer spectrum at 4.2 K of a magnetically oriented $Dy_2Fe_{14}B$ sample ($H_{ext}//\gamma$) /33/.

and the basal anisotropy of Er (Figure 16). In addition, these measurements revealed that the spin reorientation occurs gradually over some tens of K when x > 0 /36/. More interesting was, however, the necessity to include 4th and 6th order CEF terms in the Hamiltonian for a quantitative description of the T_{sr} vs x data in the whole x concentration range (Figure 16).

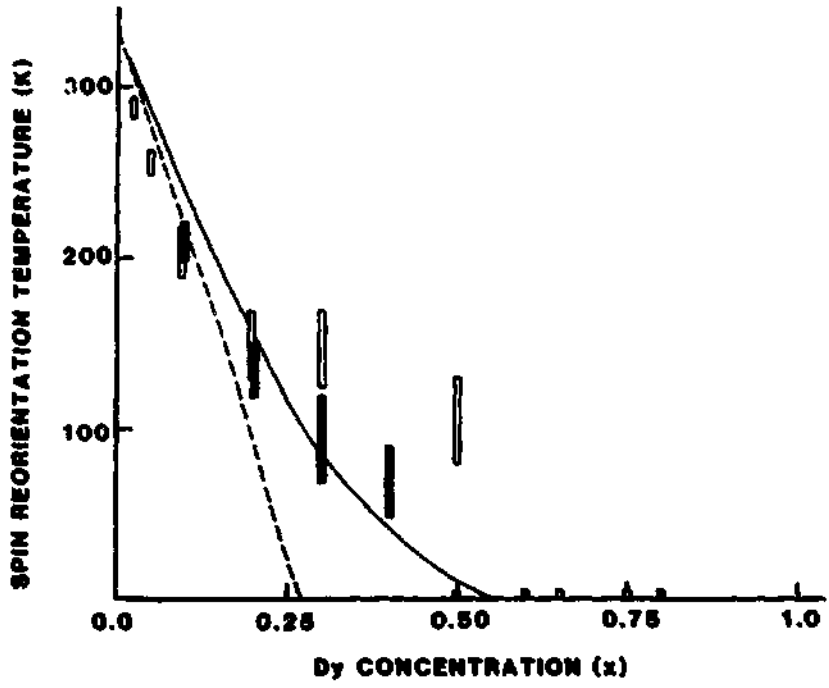

Figure 16 - Spin reorientation temperature as a function of x for $(Er_{1-x}Dy_x)_2Fe_{14}B$. Experimental data : black bars /36/, white bars /34/. Calculated values : using 2nd order CEF terms only (dashed curve), using 2nd, 4th and 6th order CEF terms (full curve) /36/.

III.4. - Hydrogen dependence of the hyperfine interactions

The hydrides of $RE_2Fe_{14}B$ alloys were studied essentially for their structure and intrinsic magnetic properties. However, charging and decharging with hydrogen was shown to be a useful method for powder decrepitation prior permanent magnet processing.

The $RE_2Fe_{14}B$ alloys absorb large quantities of hydrogen (2-5 atoms per formula unit) while preserving their crystal structure. Increase of Curie temperature and saturation magnetization (M_s) coupled with large decrease of magnetic anisotropy and coercive field were observed /8, 37-41/.

^{57}Fe Mössbauer measurements on the $RE_2Fe_{14}BH_x$ (RE = Y, Dy, Er) alloys were reported /20, 23, 39-41/. The data showed that the average hyperfine field increases (2- 3 %) on hydrogenation (Figures 4 and 17). The increase of the average Fe moment was however insufficient to account for the observed enhancement of T_c ; volume expansion and electronic factors must be considered too. It was noticed that the hyperfine field for all six sites changes on hydrogenation (Figure 7). This suggested that the iron anisotropy is not completely dominated by the contribution of any one of the sites. Another point which deserved attention was that the relative increase of the saturation magnetization ($\sim$ 6 %) for the Yttrium compound was almost twice as great as that of the average hyperfine field. Thus, the proportionality, 1 $\mu_B \equiv$ 15 T, between H_{hf} and M_s was questionned in these hydrides /39/.

Finally, it was shown that the combination of the ^{57}Fe Mössbauer results and bulk magnetization data on $Dy_2Fe_{14}BH_x$ /40, 41/ allows to determine that the magnetic structure of these hydrides is canted.

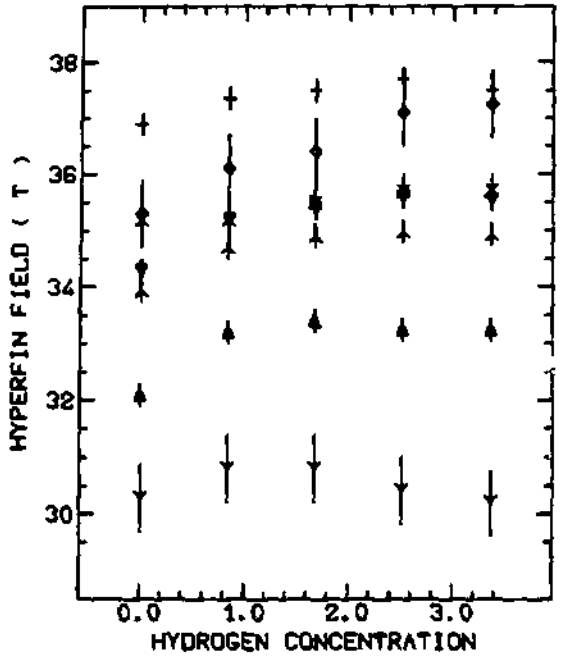

Figure 17 - ^{57}Fe hyperfine field at the six Fe sites of $Y_2Fe_{14}BH_x$ at 4.2 K. $16K_1(\Delta)$, $16K_2(\nabla)$, $8j_2(+)$, $8j_1(x)$, $4c(Y)$, $4e(\diamond)$, average (λ) /39/.

The influence of hydrogen on the hyperfine parameters at the RE site was investigated by ^{161}Dy and ^{166}Er Mössbauer spectroscopies /20, 23, 29, 40/. The spectra of the hydrides are shown together with those of the virgin samples in Figures 7 and 8. The data are collected in Table 6.

In the hydrides the hyperfine fields were significantly reduced in comparison to the virgin samples. This may arise from changes in the contribution of the conduction electron polarization on hydrogenation and /or/ (Er hydride) from crystalline field admixture. The decrease with hydrogen of the ^{161}Dy isomer shift is consistent with the trend established in the RE-Fe

intermetallic hydrides, i.e., a charge transfer from the RE 6s orbital onto the H atoms.

Table 6 - ^{161}Dy and ^{166}Er hyperfine parameters in the $RE_2Fe_{14}BH_x$ (RE = Dy,Er) alloys at 4.2 K. The isomer shift δ_{IS} for ^{161}Dy refers to the $(Gd,Dy)F_3$ source at RT /20, 29/.

Site	$Dy_2Fe_{14}B$	$Dy_2Fe_{14}BH_{3.3}$	$Er_2Fe_{14}B$	$Er_2Fe_{14}BH_{2.6}$
4f	616(2)	610(2)		
H_{hf}(T)			812(5)	786(5)
4g	628(2)	622(2)		
4f	115(2)	130(2)		
e^2qQ(mm/s)			12.3(5)	12.8(5)
4g	114(2)	125(2)		
4f	1.8(2)	1.4(3)	-	-
δ_{IS}(mm/s)				
4g	2.2(1)	1.8(3)	-	-

On hydrogenation one observe a large increase of the quadrupole coupling constant for the Dy compound whereas it stays almost constant for the Er compound. The K_1 anisotropy constant is known to decrease in the hydrides /8, 41/; thus the B_2^0 (and therefore $e^2q^{lat}Q$) are expected to decrease too on hydrogenation, i.e. the total quadrupole coupling constant should increase. This was indeed observed in the Dy compound. In the Er hydride the constancy of e^2qQ was reasonably assigned to a decrease of the lattice part

(opposite to the 4f contribution) which would be compensated by a decrease of the 4f contribution via crystal field admixture. Concomitantly, the decrease of H_{hf} was relatively larger for Er($\sim$ 3 %) than for Dy ($\sim$ 1 %) on hydrogenation.

III.5. - Phase analysis, properties of the $RE_{1+\varepsilon}Fe_4B_4$ alloys

The $RE_2Fe_{14}B$ compounds do not melt congruently, the alloys of stoichiometric compositions are, thus, not single phase. The amount of foreign phases depends somewhat on the annealing treatment. This shows up in the Mössbauer spectra (igure 4) by additional patterns : more often a paramagnetic doublet attributed to a new tetragonal phase $RE_{1+\varepsilon}Fe_4B_4$ /42-44/ which probably plays a role in magnetic hardening processes.

All compounds of the $RE_{1+\varepsilon}Fe_4B_4$ series are paramagnetic at RT but most of them order ferromagnetically at low temperatures ($T_c \leq 37$ K). Such low temperatures are closely related to the absence of magnetic moment on Fe which was inferred from magnetization and Mössbauer measurements /45-47/. ^{57}Fe Mössbauer spectra for all compounds are doublets with quadrupole splittings in the 0.52-0.60 mm/s range. Line broadenings below T_c, due to the occurrence of a small magnetic splitting, were observed only in two cases, namely RE = Dy and Sm. Analysis of the spectra of simultaneous magnetic and quadrupolar interactions revealed the magnetization to be parallel to the c-axis for Sm and perpendicular to the c-axis for Dy /47/. These results are consistent with a 2nd order CEF mechanism for anisotropy; the negative sign of the A_2^0 CEF term being deduced from ^{155}Gd /48/ and ^{161}Dy /49/ Mössbauer measurements. It is of interest to notice the giant value of the A_2^0 term

(-2450 ± 50 K/a_0^2) due to the peculiar structure of the $RE_{1+\epsilon}Fe_4B_4$ alloys (for the $RE_2Fe_{14}B$ phases A_2^0 amounts only 660-680 K/a_0^2).

Acknowledgments

This work was partially supported by the Commission of European Communities through the CEAM programme. The collaboration of J.M. Friedt, A. Vasquez, H.R. Rechenberg, P. L'Héritier and R. Fruchart, at different stages of the CEAM project, is gratefully acknowledged.

REFERENCES

/1/ M. Sagawa, S. Fujimura, M. Togawa and Y. Matsuura, J. Appl. Phys. 55, 2083 (1984)

/2/ J.J. Croat, J.F. Herbst, R.W. Lee and F.E. Pinkerton, J. Appl. Phys. 55, 2078 (1984)

/3/ J.F. Herbst, J.J. Croat, F.E. Pinkerton and W.B. Yelon, Phys. Rev. B29, 4176 (1984)

/4/ D. Givord, H.S. Li and J.M. Moreau, Solid State Comm. 50, 497 (1984)

/5/ C.B. Shoemaker, D.P. Shoemaker and R. Fruchart, Acta Cryst. C40, 1665 (1984)

/6/ J.F. Herbst, J.J. Croat and W.B. Yelon, J. Appl. Phys. 57, 4086 (1985)

/7/ K.H.J. Buschow, Materials Science Reports 1, 1 (1986)

/8/ J.M.D. COEY, J. Less-Comm. Met. 126, 21 (1986)

/9/ D. Givord, Proceedings of the Workshop on Nd-Fe Permanent Magnets, Brussels, 1984, ed. I.V. Mitchell (Commision of the European Communities, Brussels, 1984) p.131

/10/ S. Sinnema, R.J. Radwanski, J.J.M. Franse, D.B. de Mooij and K.H.J. Buschow, J. Magn. Magn. Mat. 44, 333 (1984)

/11/ D. Givord, H.S. Li, R. Perrier de la Bâthie, Solid State Comm. 51, 857 (1984)

/12/ S. Hirosawa, Y. Matsuura, H. Yamamoto, S. Fujimura and M. Sagawa, J. Appl. Phys. 59, 873 (1986)

/13/ J.P. Gavigan, D. Givord, H.S. Li, P. Tenaud and T Viadieu, Proceedings of the 3rd International Conference on Magnetic Materials (Szczyck - Bika, sept.86) to appear

/14/ P. Burlet, J.M.D. Coey, J.P. Gavigan, D. Givord and C. Meyer, Solid State Comm. 60, 723 (1986)

/15/ E.B. Boltich and W.E. Wallace, Solid State Comm. 55, 529 (1985)

/16/ Y. Matsuura, S. Hirosawa, H. Yamamoto, S. Fujimura and M. Sagawa, Appl. Phys. Lett. 46, 308 (1985)

/17/ F. Bolzoni, J.M.D. Coey, J. Gavigan, D. Givord, O. Moze, L. Paretti and T. Viadieu, J. Magn. Magn. Mat. 65, 123 (1987)

/18/ H. Fujii, W.E. Wallace and E.B. Boltich, J. Magn. Magn. Mat. 61, 251 (1986)

/19/ H.M. van Noort, B.D. de Mooij and K.H.J. Buschow, J. Less. Comm. Met. 115, 155 (1986)

/20/ J.M. Friedt, A. Vasquez, J.P. Sanchez, P. L'héritier and R. Fruchart, J. Phys. F : 16, 651 (1986)

/21/ R. Fruchart, P. L'Héritier, P. Dalmas de Reotier, D. Fruchart, P. Wolfers, J.M.D. Coey, L.P. Ferreira, R. Guillen, P. Vulliet and A. Yaouanc, J. Phys. F : 17, 483 (1987)

/22/ D.C. Price, R.K. Day and J.B. Dunlap, J. Appl. Phys. 59, 3585 (1986)

/23/ J.M. Friedt, J.P. Sanchez, P. L'Héritier and R. Fruchart, Proceedings of the Workshop on Nd-Fe Permanent Magnets, Brussels, 1984, ed. I.V. Mitchell (Commission of the European Communities, Brussels, 1984) p.179

/24/ D. Givord, H.S. Li and F. Tasset, J. Appl. Phys. 57, 4100 (1985)

/25/ H.M. Van Noort and K.H.J. Buschow, J. Less Comm. Met. 113, L9 (1985)

/26/ P. Deppe, M. Rosenberg, S. Hirosawa and M. Sagawa, Proceedings 31st Annual Conference on Magnetism and Magnetic Materials, November 1986, Baltimore, to be published in J. Appl. Phys.

/27/ M. Bogé, J.M.D. Coey, G. Czjzek, D. Givord, C. Jeandey, H.S. Li and J.L. Oddou, Solid State Comm. 55, 295 (1985)

/28/ M. Bogé, G. Czjzek, D. Givord, C. Jeandey, H.S. Li and J.L. Oddou, J. Phys. F 16, L67 (1986)

/29/ J.P. Sanchez, J.M. Friedt, A. Vasquez, P. L'Héritier and R. Fruchart, Solid State Comm. 57, 309 (1986)

/30/ M. Yamada, Y. Yamaguchi, H. Kato, H. Yamamoto, Y. Nakagawa, S. Hirosawa and M. Sagawa, Solid State Comm. 56, 663 (1985)

/31/ Y. Berthier, M. Bogé, G. Czjzek, D. Givord, C. Jeandey, H.S. Li and J.L. Oddou, J. Magn. Magn. Mat. 54-57, 589 (1986)

/32/ H. Onodera, Y. Yamaguchi, H. Yamamoto, M. Sagawa, Y. Matsuura and H. Yamamoto, J. Magn. Magn. Mat. 46, 151 (1984)

/33/ A. Vasquez, J.M. Friedt, J.P. Sanchez, P. L'Héritier and R. Fruchart, Solid State Comm. 55, 783 (1985)

/34/ D. Niarchos and A. Simopoulos, Solid State Comm. 59, 669 (1986)

/35/ A. Vasquez and J.P. Sanchez, J. Less Comm. Met. 127, 71 (1987)

/36/ H.R. Rechenberg, J.P. Sanchez, P. L'Héritier and R. Fruchart, to be published in Phys. Rev. B

/37/ K. Oesterreicher and H. Oesterreicher, Phys. Status Solidi (a), 85, K61 (1984)

/38/ P. Dalmas de Réotier, D. Fruchart, P. Wolfers, P. Vulliet, A. Yaouanc, R. Fruchart and P. L'Héritier, J. Phys. (Paris) 46, C6, 249 (1985)

/39/ J.M.D. Coey, A. Yaouanc and D. Fruchart, Solid State Comm. 58, 413 (1986)

/40/ L.P. Ferreira, R. Guillen, P. Vulliet, A. Yaouanc, D. Fruchart, P. Wolfers, P. L'Héritier and R. Fruchart, J. Magn. Magn. Mat. 53, 145 (1985)

/41/ J.M.D. Coey, A. Yaouanc, D. Fruchart, R. Fruchart and P. L'Héritier, to appear in the Proceedings of the International Symposium on the Properties and Applications of Metal Hydrides V, Maubuisson, France, May 25-30, 1986

/42/ A. Bezinge, H.F. Braun, J. Muller and K. Yvon, Solid State Comm. 55, 131 (1985)

/43/ D. Givord, J.M. Moreau and P. Tenaud, Solid State Comm. 55, 303 (1985)

/44/ D. Givord, J.M. Moreau and P. Tenaud, J. Less Comm. Met. 123, 109 (1986)

/45/ D. Niarchos, G. Zouganelis, A. Kostikas and A. Simopoulos, Solid State Comm. 59, 389 (1986)

/46/ H.R. Rechenberg, A. Paduan-Filho, F.P. Missell, P. Deppe and M. Rosenberg, Solid State Comm. 59, 541 (1986)

/47/ H.R. Rechenberg and J.P. Sanchez, Solid State Comm. 62, 461 (1987)

/48/ M. Bogé et al. to be published

/49/ H.R. Rechenberg and J.P. Sanchez, to be published

SOME BIOLOGICAL APPLICATIONS OF THE MOSSBAUER EFFECT.

E.R. Bauminger, Racah Institute of Physics, Jerusalem, Israel

Abstract: Two different biological applications of the Mossbauer effect are described: a) In Mossbauer studies of blood samples obtained from patients with thalassemia, ferritin like iron in large quantities was observed. Desferral was found to remove excess iron from serum, but not from red blood cells. b) Mossbauer measurements of myoglobin and ferritin, showed different dynamical behaviour of the iron in the two proteins. Measurements as function of iron concentration show a gradual change from almost myoglobin like dynamics in iron poor ferritin to a first order phase transition in the dynamics of iron rich ferritin.

Among the many works which have been performed, utilizing the Mossbauer effect in studies of problems in biology and medicine[1], I am going to describe as an example only two different applications. The first application is in the study of blood diseases and has been performed in Jerusalem several years ago with my late collegue S. Ofer, and with E.A. Rachmilewitz from the Hadassah Medical School[2]. The second application is in the study of protein dynamics[3]. This work was also started several years ago with my late collegues S.G. Cohen and S. Ofer, and is continuing with I. Nowik in Jerusalem, in collaboration with P. Harrison and A. Treffry from the Biochemistry Department in Sheffield, England.

a)Thalassemia.

Introduction - In recent years the Mossbauer effect (ME) has been found to be a powerful tool for investigating the iron containing compounds of blood cells. In the Mossbauer spectra, different "fingerprints" are obtained for each iron component whose concentration is larger than 10×10^{-6} g/cc in samples nonenriched in Fe^{57}. Using the ME the iron content of human blood cells and blood serum obtained from patients with various hemoglobinopathies, has been investigated.

The main component of blood is hemoglobin. Hemoglobin is built around the heme molecule. Heme is built around an iron atom, which is bound to four nitrogen atoms; one additional bond is connected to the protein via an amino acid and one bond is free to bind and release oxygen. If oxygen is bound to the sixth position - we have oxy-hemoglobin - if the sixth bond is empty, we have deoxy-hemoglobin.

Normal hemoglobin contains 4 subunits, 2 alpha-chains and 2 beta-chains.

The difference between the alpha- and beta-chains is in the sequence and structure of the amino acids in the globin chains, which are attached to the heme molecule. In thalassemia either alpha- or beta-chains are not synthesized in adequate quantities.[4] In alpha-thalassemia there is an excess of beta-chains, in beta-thalassemia an excess of alpha-chains. In beta-thalassemia, the excess of alpha-chains cannot form stable tetramers. The life span of the red cells is shortened and hemolitic anemia results. Alpha-thalassemia (HbH disease) is usually less severe, as beta tetramers are more stable. In beta-thalassemia many of the RBCs produced in the bone marrow, do not reach the peripheral blood. The deficiency of RBCs in the blood results in a compensating over-activity of the bone marrow and in the presence of a large number of reticulocytes (young RBCs) in the blood stream. Beta-thalassemia is the most widespread abnormality of Hb in the world and is found in large numbers in the Mediterranian area and in China. The life span of thalassemic patients is about 20 years and the disease is responsible for the death of about 100,000 children per year throughout the world. The death usually results from iron overload in the cardiac muscle.

In the Mossbauer spectra of blood samples of thalassemic patients, a well defined spectrum, different from that of oxy - or deoxy - hemoglobin, has been found. This additional spectrum is identical to that obtained in the iron storage compound ferritin. The amounts of ferritin-like iron were comparable to those of hemoglobin iron and were particularly large in reticulocytes (young RBCs). Comparison of the amount of ferritin-like iron detected by the ME in hemolysates and the amount of ferritin detected by immunoradiometric assays showed that not all the ferritin-like iron found by the ME can be accounted for by the present immunoradiometric assays employed. The effect of medication on the iron content of the erythrocytes and of the serum of these patients showed that desferral removes iron from the serum, but has no effect on the iron content of RBCs.

Materials and Methods. - The Mossbauer spectra were obtained by using a conventional spectrometer. A 100 mCi source of ^{57}Co in rhodium, which was maintained at room temperature, was used. The 14.4 keV gamma rays were detected using a Harwell proportional counter operating at about 5×10^4 counts/s. For most measurements about 1 ml of the material investigated was sealed in lucite containers of about 1.5 cm^2 cross section and stored in

liquid nitrogen before measurement. For measurements, the samples were held in cryostats enabling absorption measurements to be made at any temperature between 4.1 K and 300 K. Most measurements were performed at 85 K. In measurements performed on serum and hemolysates, where the iron concentrations were small, lyophilized (freeze dried) samples were used. Typically, the lyophilized absorber with a volume of 1.2 cc was prepared from 10 ml serum or hemolysate.

Least squares computer fits to the experimental spectra were performed, taking the hyperfine interaction parameters corresponding to each subspectrum and the relative intensity of the subspectra as free parameters. Lorentzian line shapes were assumed.

The diagnosis of the disease in each case was made by common medical techniques. Blood samples from patients getting regularly blood transfusions were obtained at least 60 days after the last transfusion. For some of the measurements the RBCs were separated by differential centrifugation into samples containing mainly young RBCs (reticulocytes and normoblasts), and samples containing mainly old RBCs. The hemolysates were prepared by lysis of the RBCs and subsequent centrifugation at 15000 rpm for 20 min[5].

Results: - Normal RBCs: The only compound in normal RBCs, which contains iron in a concentration above 10×10^{-6} g/cc, is hemoglobin (Hb). Usually the Mossbauer spectra consist of two doublets, one corresponding to deoxy-Hb and the other to oxy-Hb. Exact computer analysis of the oxy-Hb subspectra at various temperatures, shows that these cannot be fitted by a doublet consisting of two Lorentzian lines. Very good fits to the oxy-Hb subspectra can be obtained by a superposition of 2 quadrupole doublets with different splittings and different line widths and equal intensities. This phenomenological procedure for fitting the oxy-Hb spectrum is required as the lines do not have an exact Lorentzian shape.

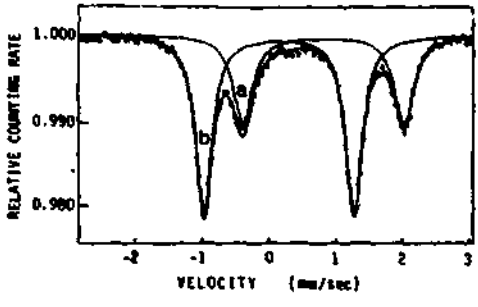

Fig. 1. Fe^{57} Mossbauer spectrum at 82 K of normal RBCs; subspectrum (a) cooresponds to deoxy-Hb, subspectrum (b) to oxy-Hb.

probably due to relaxation effects[6]. A spectrum obtained in normal Hb is shown in fig. 1 and the parameters obtained from the computer fits at 85 K are given in table 1.

Thalassemic RBCs: In Mossbauer spectra of RBCs obtained from patients with alpha or beta thalassemia, varying amounts of a third component, in addition to oxy and deoxy-Hb, were seen. An example of such spectra at various temperatures is shown in fig. 2. Fig. 3 displays the spectrum obtained at 4.1 K. The parameters of the third component obtained from computer fits at all

Table 1. Mossbauer parameters of subspectra corresponding to oxyhemoglobin, deoxyhemoglobin and ferritin found in RBCs.

	T (K)	Line Width (mm/sec)	eqQ/4 (mm/sec)	Isomer shift[a] (mm/sec)	H_{eff} (kOe)
Deoxy-Hb	85	0.32(2)	1.15(2)	0.92(1)	
Oxy-Hb site I	85	0.24(2)	1.09(2)	0.27(1)	
site II		0.38(2)	0.95(2)	0.27(1)	
Ferritin in RBCs	4.1	0.7(1)	<0.05	0.48(2)	496(3)
	82	0.54(2)	0.33(2)	0.46(1)	
	200	0.44(2)	0.35(2)	0.43(1)	
	263	0.46(2)	0.34(2)	0.38(1)	
Rat Liver Ferritin	4.1	0.5(2)	<0.05	0.47(2)	498(3)
	82	0.50(2)	0.35(2)	0.40(1)	
	200	0.48(2)	0.35(2)	0.42(1)	
	263	0.46(2)	0.35(2)	0.38(1)	

[a] relative to iron metal at room temperature.

temperatures are identical to those obtained in ferritin or hemosiderin[7,8] and are given in table 1. Ferritin is the iron storage protein in mammals. It consists of a core of FeOOH of about 70 Å in diameter, surrounded by a protein shell with an outer diameter of about 120 Å. The iron compound in hemosiderin is identical to the iron compound in ferritin, but the protein shell may be partially or completely absent. The iron core is antiferromagnetic and displays the phenomena of superparamagnetism due to its small size. At 4.1 K its Moasbauer spectrum consist of a well defined

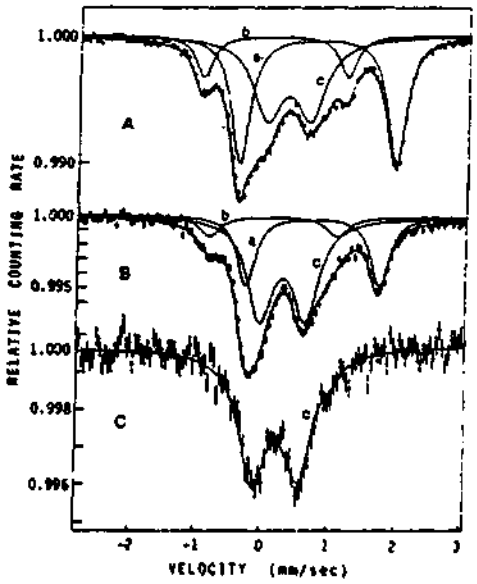

Fig. 2 - Fe^{57} Mossbauer spectra of RBCs obtained from a patient with beta thalassemia. Spectra A,B and C were obtained at 82, 200 and 263 K, respectively. Subspectrum (a) corresponds to deoxy-Hb; (b), to oxy-Hb and (c), to the ferritin-like compound.

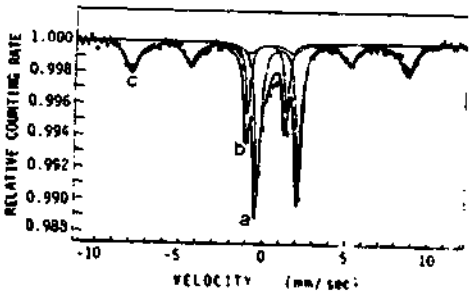

Fig. 3 - Fe^{57} Mossbauer spectrum at 4.1 K of RBCs obtained from a patient with beta thalassemia. Subspectra (a),(b) and (c) as in fig.2.

magnetic sextet. As seen from fig. 2, the temperature dependences of the f-factor of Hb and ferritin are very different. The f factors can be deduced from the spectral areas and the absolute amount of Fe in ferritin or in normal RBCs measured by other techniques. The ratio of the amount of ferritin-like iron to Hb iron (denoted by R) was in thalassemic RBCs between 3% and 50%, whereas in RBCs of normal controls, the R values are less than 1%. These results correspond to an absolute concentration of 3 to 50×10^{-15}g of ferritin-like iron per single thalassemic RBC, as compared with 100×10^{-15}g Hb iron in one normal RBC. In 1 gram of packed cells there are about 10^{10} RBCs; thus there are between 0.03 and 0.5 mg ferritin-like iron in 1 gm of thalassemic packed cells.

The peripheral blood of thalasaemic patients contains a comparitively large amount of young RBCs (about 10% of reticulocytes). It was known before that apoferritin synthesis is greatly enhanced in thalassemic

reticulocytes[9]. The question arises, whether this apo erritin contains iron already in the reticulocytes or is filled with iron only in later stages. Samples with significantly different concentrations of reticulocytes were prepared by differential centrifugation. Some samples contained as much as 85% reticulocytes. The R values were determined for samples containing significantly different concentration of reticulocytes and mature RBCs. The R values obtained in the reticulocyte rich fraction were about three times larger than the R values in the reticulocyte poor fraction. The amount of ferritin like iron in reticulocytes was between 2.5 and 8 times that of ferritin like iron in mature RBCs. The results are summarized in table 2.

Table 2. Ratio of ferritin-like iron to Hb iron and absolute amounts of ferritin-like iron and Hb iron per blood cell in RBCs of 17 patients.

	R^*	F^{**} 10^{-15} g	Hb iron/cell 10^{-15} g
Normal RBCs	R<0.01	F<1	100
Thalassemic old RBCs	0.15<R<0.54	10<F<40	70
Thalassemic retic.	0.40<R<1.6	20<F<110	50

* R = (ferritin like iron)/(Hb iron) in mature RBC
** F = (ferritin like iron)/cell

The presence of intracellular unstable Hb is common to the disorders in which ferritin-like iron has been detected in the RBCs. In a few cases 1 ml of whole blood contained as much as 250×10^{-6} g ferritin-like iron - as compared to about 2×10^{-6} g in normal blood. This may be a consequence of the high rate of intracellular denaturation of Hb during the accelerated and ineffective erythropoesis in these diseases.

The large difference in the amount of ferritin-like iron between reticulocytes and mature RBCs may be explained by two alternative hypotheses: 1) Appreciable amounts of ferritin-like iron are somehow removed from the RBCs during the life span of the RBCs; 2) These reticulocytes which contain large amounts of ferritin-like iron are destroyed before reaching maturation. The mature RBCs, as old surviving cells, contain more stable Hb and less ferritin-like iron.

Hemolysates of Thalassemic RBCs: Hemolysates are solutions of hemoglobin, obtained by rupturing RBCs. The amount of ferritin in hemolysates was determined hitherto by immunoradiometric assay (IRMA). IRMA determines the amount of a protein by using antibodies reacting with this specific protein. It can be performed only on solutions. Two distinct types of ferritin, spleen type and heart type ferritin, are known. Until recently, the ferritin in hemolysates was assayed using antibodies to spleen type ferritin only. Comparison of the amount of ferritin detected by the ME and by IRMA with antibodies to spleen type ferritin, showed that only about 10% of the ferritin-like iron detected by ME could be accounted for by this IRMA technique. In order to solve this discrepancy - IRMA, with antibodies to heart and spleen type ferritin, were performed on hemolysates and the ME measured on the same samples[5]. In order to increase the accuracy of the estimates of ferritin-like iron by the ME some of the measurements were performed on lyophilized hemolysates. Fig. 4 shows the dependence of the f factor of lyophilized ferritin, oxy- and deoxy-hemoglobin on temperature. The f-factor of lyophilized Hb drops off much faster than the f-factor of lyophilized ferritin - and therefore in measurements taken at room temperature on lyophilized samples, the subspectrum corresponding to ferritin sticks out much more than in spectra taken at 80 K on frozen samples. This is even more pronounced if the Hb in the sample is reduced to deoxy-Hb before measurement. This can be achieved by stirring the sample in a N_2 atmosphere or by adding Na-dithionite to the sample. Fig. 5 shows the spectrum obtained in the lyophilized sample at room temperature (A) and in the frozen sample at 80 K, of the same hemolysate (B). The lyophilized sample was prepared from 8 cc hemolysate.

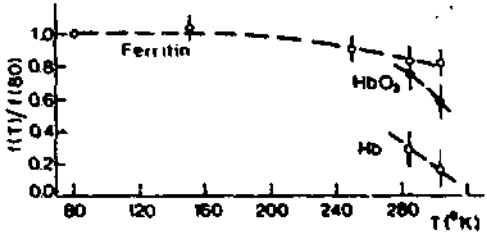

Fig. 4. - The temperature dependence of the f-values of lyophilized oxy-Hb (full dots), deoxy-Hb (open circles) and ferritin (open diamonds).

By IRMA the amount of whole ferritin (protein + iron core) is determined, whereas, the ME measures the amount of ferritin-like iron only. The iron/protein ratio in ferritin molecules is between 0 (in apoferritin) and 0.56 (in ferritin completely filled with iron). In

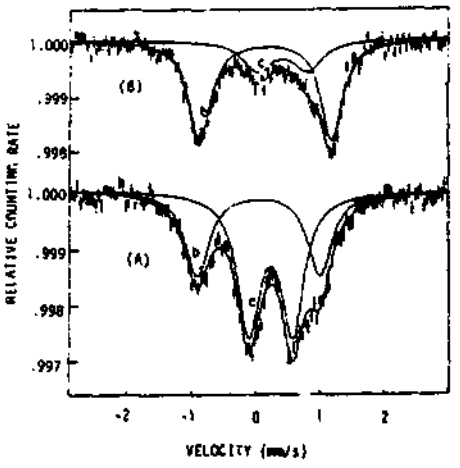

Fig. 5. - Fe^{57} Mossauer spectra in (A) a lyophilized sample of hemolysate at room temperature of a patient with beta thalassemia and (B) a frozen sample of hemolysate at 85 K of the same patient. Subspectra (b) correspond to oxy-Hb and (c) to ferritin.

normal cells the amount of ferritin-like iron is too small to be detected by the ME. By IRMA, $0.12x10^{-15}$g heart type ferritin and $0.024x10^{-15}$g spleen type ferritin per normal cell were detected. The spleen type concentration in the hemolysates as measured by IRMA could account for only 0.1 of the ferritin-like iron detected by the ME. IRMA studies of heart type ferritin showed much larger amounts of heart type ferritin than of spleen type ferritin, explaining the large discrepancies between the ME and IRMA found earlier. In some cases there is an appreciably greater amount of ferritin-like iron present in the whole erthrocytes than in the hemolysates, indicating that in these cases, some of the ferritin-like iron is in an insoluble or membrane-bound form (like hemosiderin). In most hemolysates the iron to ferritin ratio is still larger than 0.56. The difference between the amount of ferritin determined by the IRMA technique and by the ME technique has thus been greatly diminished - but not eliminated. The two possible explanations for this discrepancy are: 1) Previous studies have shown that ferritin may undergo a process of polymerisation. This process appears to be associated with digestion of the protein moiety, resulting in a high iron/protein ratio.[10] A similar process may occur in grossly iron loaded red cells. It may be that the ferritin-like iron measured, is a combination of iron found in intact ferritin molecules and iron found in denatured soluble ferritin polymers. 2) At the present time two types of ferritin have been identified , one reacting with antibodies for spleen ferritin and the other reacting with antibodies for heart ferritin. It is possible that other immunologically distinct types of ferritin exist, which do not react with these antibodies and which could not be detected by the IRMA used heretofore.

Human Blood Serum - It was known previously that blood serum of patients with

hemoglobinopathies contains an increased amount of ferritin. Normal serum contains less than 0.1×10^{-6} g/cc of ferritin, as determined by IRMA - an amount much too small to be detected by ME[11]. The Mossbauer measurements were all carried out on lyophilized samples obtained from about 10 cc of serum. One of the spectra obtained at 85 K is shown in fig. 6(A). The parameters of the spectra at all temperatures are identical to those of ferritin. Among the 17 cases investigated - 6 had less than 1×10^{-6} g ferritin-like iron per 1 cc serum, 4 had more than 2.5×10^{-6} g/cc and 7 had an amount between 1 and 2.5×10^{-6} g/cc. Repeated tests on the same patients did not show significant changes in the iron concentrations with time, when no iron chelating agent was administered to the patients. The amount of ferritin-like iron found in the serum does not seem to be correlated with the amounts found in the RBCs of the same patients. The amount of ferritin detected by IRMA in thalassemic patients' blood serum is smaller than 1×10^{-6} g/cc[12]. It remains to be seen if using antibodies to heart type ferritin, the amounts of ferritin seen by IRMA will be similar to those detected by the ME.

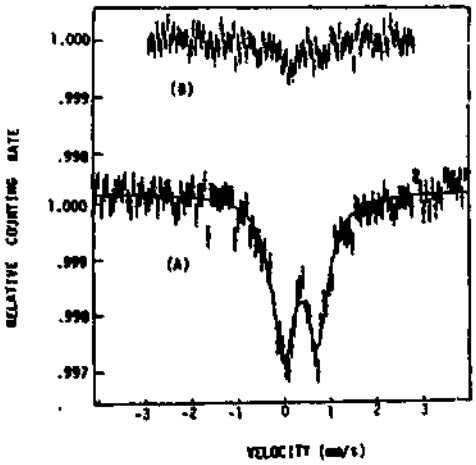

Fig. 6. - Fe^{57} Mossbauer spectra at 85 K in lyophilized serum of a patient with beta thalassemia; (A) before treatment with desferral (B) after treatment with desferral.

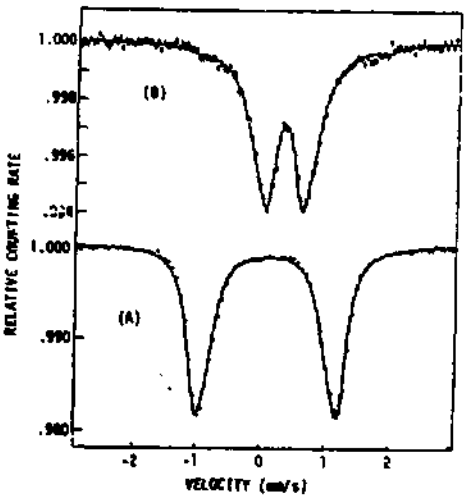

Fig. 7. - Fe^{57} Mossbauer spectra at 85 K (A) in frozen RBCs of a patient with hemochromatosis and (B) in lyophilized serum of the same patient.

In one case of hemochromatosis, a hereditary defect in the regulation of iron absorption resulting in toxic accumulations of tissue iron, an especially large quantity, 40×10^{-6} g/cc ferritin-like iron, was detected in the serum. The spectra obtained in the serum and RBCs of this patient are shown in fig. 7. Although the iron concentration in the serum is so large - no ferritin-like iron could be detected in the RBCs. By IRMA the largest concentrations of ferritin found heretofore in the serum was 7×10^{-6} g/cc[12].

The Influence of Medication - Some of the thalassemic patients were treated with desferral, a chelating agent which is known to remove excess iron from the body. Mossbauer spectra performed on RBCs and serum of these patients, revealed that whereas the desferral removes most of the ferritin-like iron from the serum (fig. 6, A and B), it has no effect on the ferritin-like iron content of the RBCs. It seems thus that the ferritin-like iron is well protected inside the RBCs and is invulnerable to this medication.

Conclusions: The Mossbauer effect has shown that large amounts of ferritin are present in RBCs of patients with various hemoglobinopathies. As a result of the Mossbauer studies it became clear that the IRMA technique using spleen type antibodies detects only a small fraction of the ferritin present in hemolysates and that most of ferritin in hemolysates is heart type. It was shown that RBCs of thalassemic patients contain up to 50 times more ferritin like iron than normal RBCs. There is about 3 times more ferritin iron in thalassemic reticulocytes than in mature thalassemic RBCs. The serum of some patients with thalassemia contain 25 times more ferritin iron than normal serum. RBCs of one patient with hemochromatosis did not contain more ferritin like iron than normal, but his serum contained 400 times more ferritin like iron than normal serum. There is thus no correlation between the amount of ferritin like iron in the serum and in the RBCs. Medication removes ferritin like iron from the serum, but not from the RBCS.

b) Protein Dynamics.

Introduction: - A completely different problem to which the Mossbauer effect has been applied is the problem of protein dynamics.[13-17] Proteins are large macromolecular systems, which contain large amounts (about 50%) of water. Many different kinds of proteins exist and they fulfill different functions. The proteins are not rigid structures and their dynamic properties are of

fundamental interest in biology and biophysics. It is well known e.g. that Hb can release and bind oxygen only due to the movement of part of the molecule - which closes and opens a pocket into which the oxygen is admitted. The iron is known to sit in the nitrogen plane in oxy Hb and above it in deoxy Hb. How do these motions occur? Ferritin admits storage iron into its core through the channels in the apoferritin protein _ these channels also must open up to admit the iron and to release it. Can these motions be studied by the Mossbauer Effect?

The lucky circumstances which enable the use of the Mossbauer Effect in protein dynamics studies are: 1) that Fe is such a good Mossbauer nucleus, and 2) that the time scales involved (10^{-8} sec) fit those of protein dynamics in a region which cannot be studied by other methods.

The Model: - Mossbauer Spectra of the proteins above a certain temperature, reveal characteristic and peculiar features in that in addition to the presence of relatively sharp lines, like in solids, there are also very broad lines extending to Doppler velocities of several cm/sec.

Usually the ME is observed in solids, where it gives sharp absorption lines with a natural line width of about 0.2 mm/sec in Fe^{57}. Broad absorption lines are observed for colloidal particles in a viscous liquid, where the width of the line is proportional to the diffusion constant or the viscosity of the fluid. The combination of sharp and broad lines corresponds to a state intermediate between solid and liquid _ a state of "proteinic matter". Characteristic spectra are shown in fig. 8. Spectra like this have been observed in oxy and met myoglobin, oxy and deoxy-Hb, Co-Hb and ferritin crystals. They have also been observed in other polymers and macromolecular systems.(18)

These spectral shapes can be explained as being due to the motion of the iron-atom in a restricted volume. The iron atom performs bounded diffusion which is connected to large scale motions of the protein. The onset of this motion occurs at a certain temperature T_c, above which the additional broad lines appear in the spectra. Above this temperature there is usually also a sharp decrease in the overall area of the Mossbauer spectra as function of temperature.

The spectra can be explained using a model for bound diffusion based on

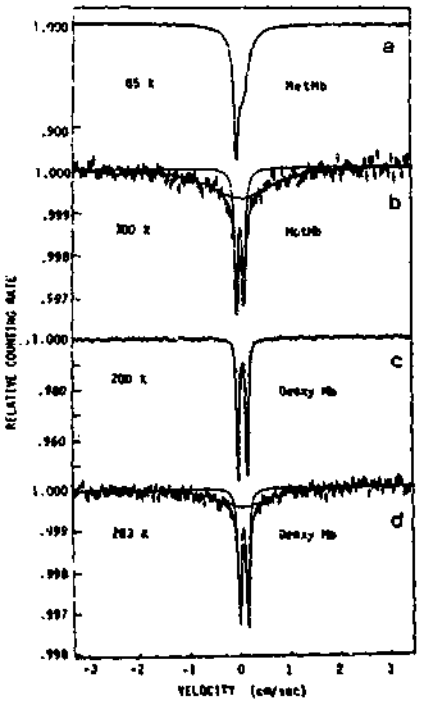

Fig. 8. - Typical Fe^{57} spectra obtained in met-Mb and Deoxy-Mb below and above T_c.

the Brownian motion of an overdamped harmonic oscil ator.[19] The model deals with a particle of mass m bound to a center by a harmonic force $m\omega^2 r$, damped by a frictional force $m\beta dr/dt$ and acted upon by random forces F(t), which follow the equation of motion: $md^2r/dt^2+m\beta dr/dt+m\omega^2 r=F(t)$. If we denote by $\alpha=\omega^2/\beta$, the ratio between the harmonic and damping force constants, and $D=k_bT/m\beta$ the diffusion constant, the msd $\langle x^2\rangle_s=k_bT/m\omega^2=D/\alpha$. The spectra are fit with 2 free physical parameters: with D - the diffusion constant and either with α - which is also the relaxation rate of the ensamble average of x, $\langle x\rangle=x_0\exp(t/\tau_c)$, or with the msd $\langle x^2\rangle_s=D/\alpha$. Slow collective motions are characterized by the value of $\alpha=2.5\times10^8$, which corresponds to τ_c of 4×10^{-9} sec, and $\langle x^2\rangle_s=0.017A^{\circ 2}$. Fast collective motions correspond to large values of α ($\alpha>2\times10^9 sec^{-1}$), low damping and $\tau_c<5\times10^{-10}$ sec. The lines shapes obtained as function of α with fixed D, are shown in fig. 9. For large α (strong binding) a narrow Lorentzian line of natural width is obtained, corresponding to the normal line in a solid. For very small α, we obtain a single wide Lorentzian line of width ($\Gamma+2\hbar k^2D$) as expected for free diffusion. At intermediate values of α, spectral shapes like those observed in proteins are obtained. These can be approximated as the sum of two components, one narrow component of natural width Γ_o and the other broad component of width $\Gamma=2\hbar k^2D$

The area under the Mossbauer line is always proportional to the Mossbauer efficiency f, which in the harmonic approximation gives the mean square displacement of the Mossbauer nucleus $\langle x^2\rangle$, through $f=\exp(-k^2\langle x^2\rangle)$, where k is the wave number of the gamma ray. ($k = 1/0.137A^{\circ -1}$ for the 14.4 keV gamma ray of Fe^{57}). At 0 K, f is close to unity. From the temperature dependence of the

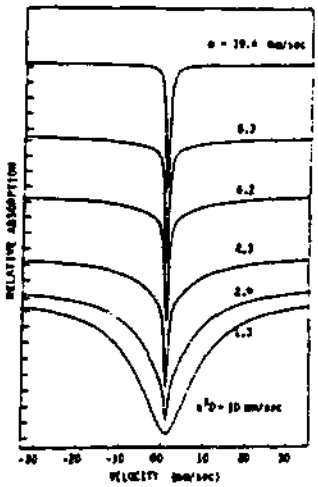

Fig. 9. - Mossbauer spectra of harmonically bound particles containing Fe^{57} in Brownian motion as a function of the parameter $\alpha = \omega^2/\beta$, for a fixed value of the diffusion constant $D=1.4\times10^{-9}cm^2/sec$ corresponding to a value of $\hbar k^2 D$ equal to 10mm/sec in units of the Doppler velocity ($\hbar\Gamma$ was fixed at a value of 0.75 mm/sec).

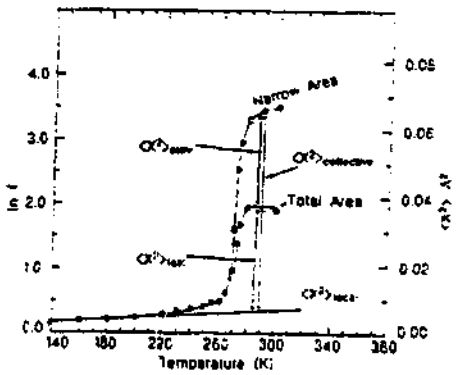

Fig. 10. - Decomposition of $\langle x^2\rangle_{total}$ into $\langle x^2\rangle_{slow}$, $\langle x^2\rangle_{fast}$ and $\langle x^2\rangle_{local}$.

areas of the narrow (elastic) and broad (quasi-elastic) components, we can obtain different mean square displacements of the Fe nuclei.

Fig. 10 shows -ln(narrow area)=-ln f(narrow) and -ln(total area) as function of temperature for iron rich ferritin. At low temperatures only the narrow solid like spectrum is observed. At T_c the change in ln f becomes much steeper than below it and the spectra are composed of narrow and broad subspectra. Assuming independent degrees of freedom, we can write the recoilless fraction at a particular temperature, f(narrow), caculated from the area of the narrow component, as the product of the partial recoilless fractions f_{fast} and f_{slow}, that is $f(narrow)=f_{fast}\cdot f_{slow}$. The Mossbauer fraction associated with the sum of the elastic and quasielastic resonance f(total) is equal to $f_{fast}\cdot f_{slow}$, which is the f-factor of the slow collective motions, which are characteristic of the motions within the protein, is thus given by $f(narrow)/f(total)=f_{slow}$. We get therefore from $-\ln f(total)=k^2\langle x^2\rangle_{fast}$, from $-\ln f(narrow)-(-\ln f(total))=k^2\langle x^2\rangle_{slow}$ and from

$-\ln f(\text{narrow}) = k^2 \langle x^2 \rangle_{total}$.

Below T_c, $\langle x^2 \rangle$ is associated with the local thermal vibrations of the individual iron atoms around their equilibrium positions, like in any solid. As illustrated in fig. 10, the total msd derived from the area of the narrow component, can be thus resolved into 3 different modes of motions: a) $\langle x^2 \rangle_v$ the value obtained by linear extrapolation from the values of $\langle x^2 \rangle$ below T_c. b) $\langle x^2 \rangle_{total} - \langle x^2 \rangle_v = \langle x^2 \rangle_{coll}$ gives the msd associated with large scale motions of parts of the protein, including the iron. These motions can be subdivided into two parts: $\langle x^2 \rangle_{slow}$ and $\langle x^2 \rangle_{fast\ collective}$. $\langle x^2 \rangle_{slow}$, corresponding to slow collective motions, responsible for the appearance of the broad lines, is given by the difference between $\langle x^2 \rangle_{total}$, derived from the area of the narrow line, and $\langle x^2 \rangle_{fast}$, derived from the total area. $\langle x^2 \rangle_{fast\ collective}$ is given by the difference between $\langle x^2 \rangle_{fast}$ and $\langle x^2 \rangle_v$. The broad lines associated with the fast collective motions are so broad that they are lost from the spectra.

Results: - Fig. 11 shows the results obtained in met Mb and in ferritin. A comparison between the results in met Mb and ferritin shows that whereas in Met Mb the transition is gradual - in ferritin it is a first order transition at higher T_c, but the msd's in both proteins are very similar - except $\langle x^2 \rangle_v$ - which points to stronger binding of Fe in ferritin. In order to understand better the similarity and difference between the two proteins - we have to take a closer look at ferritin.

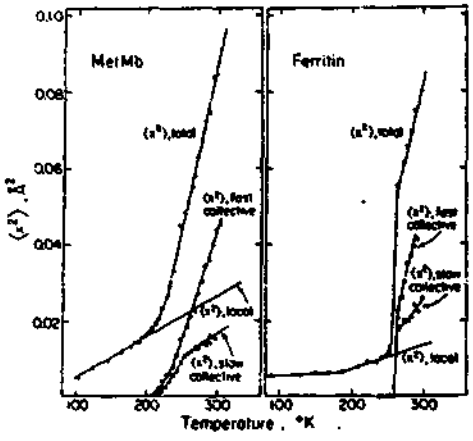

Fig. 11. - Values of msds in metMb and in ferritin.

The ferritin molecule consists of a roughly spherical shell with an outer diameter of about 125A° and an inner diameter of about 80A° and is composed of 24 subunits. The cavity might be filled with crystalline particles, mainly ferrihydrate, FeOOH, with some inorganic phosphate adsorbed on the iron core crystallites. Completely filled it can accommodate up to 4,500 iron atoms within one ferritin molecule. Two types of

channels lead through the protein shell: 6 hydrophobic channels and 8 hydrophilic channels, which can bind metal ions. The inner surface of the cavity is lined with loose hydrophilic residues.

We first compared the dynamics of the iron which goes in first with the dynamics of th iron that which goes in last. For this purpose we loaded the ferritin with 56 atoms of Fe^{57} and then added 3600 atoms of natural iron per

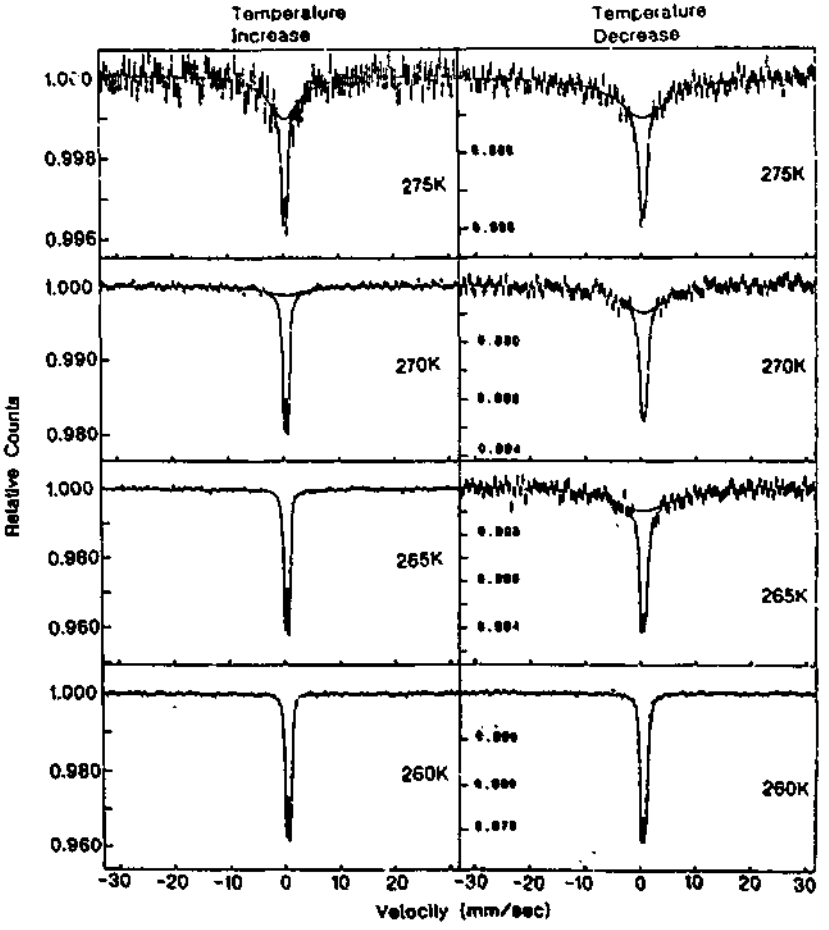

Fig. 12. - Fe^{57} Mossbauer spectra of iron-rich ferritin as the temperature is increased and as the temperature is decreased.

ferritin molecule. Then we loaded ferritin first with 3600 atoms of natural iron and then added 56 atoms of Fe^{57} per ferritin molecule. We could not see any difference between the different samples. Some spectra, around T_c, are shown in fig. 12.

From these spectra one observes that as the temperature is increased there is still only a narrow spectrum, as in the frozen state, at 265 K, and at 270 K a weak broad line appears. As the temperature is decreased the wide line is still seen at 265 K and disappears at 260 K. We thus see that there is a very snarp transition in the dynamic behaviour at 271 K as the temperature is increased and at 264 K as the temperature is decreased. We can see this in the intensity ratio of broad to narrow lines and in the total and narrow spectral areas as shown in fig. 13. We could not detect any change in the hyperfine parameters (quadrupole splittings and isomer shifts) at these temperatures, which shows that no change in the chemical environment is

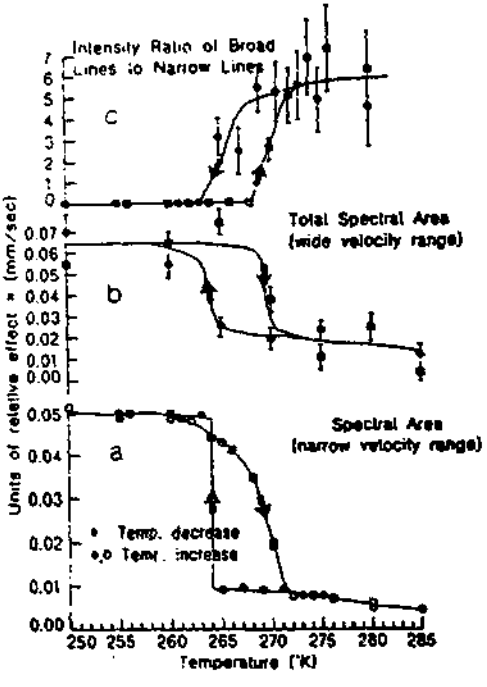

Fig. 13. - Hysteresis effects in the dynamics of iron rich ferritin.

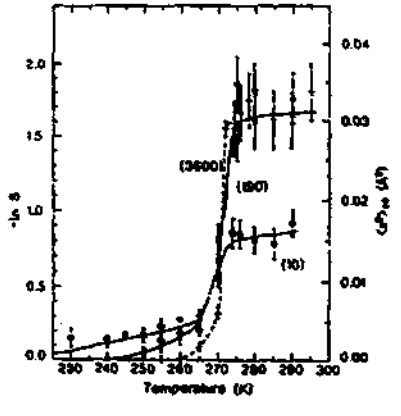

Fig. 14. - $\langle x^2 \rangle_{slow}$ in ferritin containing 10, 190 and 3600 Fe atoms per ferritin molecule.

occuring. In other samples with less than 190 Fe per ferritin molecule, significant differences in the dynamical behaviour compared to the iron-rich ferritin were found. As the amount of Fe per ferritin molecule decreases the transition gets less sharp. In iron poor ferritin (10 Fe^{57} per ferritin molecule) almost no hysteresis (<2°K) is seen and the broad lines appear already at 230 K. The results in the various types of ferritin are compared in fig. 14, which shows $\langle x^2 \rangle_{slow}$ for three different concentration of iron. In Mb the transition is very smooth - starting at about 220 K - yet the overall displacements above 270 K are about the same. (If they were significantly different - they would not be observed by the ME).

Conclusions: - The work points to two puzzles: a) Why is the transition sharp in iron rich ferritin at 271 K, amooth in myoglobin starting at 220 K and in between in "iron poor" ferritin (<190 Fe per molecule) ? b) How is it that two such different proteins - one in which the iron is an integral part of the protein and the other in which the iron forms an aggregate within the protein shell - give so similar msds?

The answer to a) lies probably in the state of water. 1) In myoglobin the water is probably adsorbed in small groups and has lost the properties of free water - melting at 220 K and thus freeing additional degrees of freedom at this temp. 2) In iron rich ferritin the bulk of the iron is in the core, where the water behaves almost as free water with a first order melting phase transition at 271 K and a supercooled glass transition at 264 K. 3) In iron poor ferritin a larger part of the iron is attached directly to the protein shell - and therefore feels more the water attached to the protein shell which is similar to the water in Mb and is very different from normal water. The spectra we observe here are a superposition of spectra due to the iron near the protein shell and the inner core iron. b) These results indicate that the iron core is composed of subaggregates which are not rigidly connected to each other. Each subaggregate is bound strongly to a protein subunit and is driven by its dynamics. The similarity might be explained by the picture of "hinge motions" of the helix structures in the proteins, overdamped in the outer viscous "glycerol-like" layer of the protein.

This work shows that via the ME _ which probes the iron dynamics, one can learn about dynamical structure and different kinds of water in the proteins. Different kinds of water in proteins have been suggested also by x-ray

studies, dialectric constant studies and specific heat studies in lyzosomes.

References

(1) Dickson, D.P.E., in Mossbauer Spectroscopy Applied to Inorganic Chemistry, ed. G.J. Long, Vol. 1, p. 339 (1984)

(2) Bauminger, E.R., Cohen, S.G., Ofer, S. and Rachmilewitz, E.A., Proc. Natl. Acad. Sci. USA 76, 939 (1979).

(3) Nowik I., Bauminger E. R., Cohen, S. G. and Ofer S., Phys. Rev. A31,2291 (1985).

(4) Weatherall, D.J. and Cegg, J.B., The Thalassemic Syndromes, 2nd ed. (Blackwell Scientific Publ., Oxford) 1972.

(5) Jacobs, A., Peters, S.W., Bauminger, E.R., Eikelboom, J., Ofer, S. and Rachmilewitz, E.A., British Journal of Haemotology 49, 201 (1981).

(6) Lang, G. and Spartalian, K., In Mossbauer Effect Methodology 10, 169 (1976)

(7) Fishbach, F.H., Gregory, D.W., Harrison, P.M., Joy, T.G. and Williams, J.M., J. Ultrstr. Res. 37, 495 (1971).

(8) Boas, J.F.and Window, B., Aust. J. Phys. 19, 573 (1966).

(9) Eylar, E.H. and Matioli, G., Nature 208, 661 (1965).

(10) Williams, M.A. and Harrison, P.M., Biochemical J. 110, 265 (1968).

(11) Bexkorovainy, A., Biochemistry of Nonheme Iron (Plenum Press) p.253 (1980).

(12) Milder, M.S., Cook, J.D., Strey, S. and Finch. C.A., Medicine 59, 34 (1980).

(13) Cohen, S.G., Bauminger, E.R., Nowik, I., Ofer, S. and Yariv J., Phys. Rev. Letters, 46, 1244 (1981).

(14) Mayo, K.H., Parak, F. and Mossbauer, R.L., Phys. Letters 82A, 468 (1981).

(15) Parak, F., Frolov, E.N., Mossbauer, R. L. and Goldanskii, V.I., J. Mol. Biol. 145, 825, (1981).

(16) Bauminger, E.R., Cohen, S.G., Nowik, I., Ofer, S. and Yariv, J., Proc. Natl. Acad. Sci. (U.S.) 80, 736 (1983).

(17) Parak, F. and Knapp, E.W., Proc. Natl. Acad. Sci. (U.S.) 81, 7088 (1984).

(18) Bauminger, E.R., Nowik, I., Ofer, S. and Heitner-Wirguin, C., Polymer 26, 1829 (1985).

(19) Nowik,I., Bauminger, E.R., Cohen, S.G. and Ofer, S., Phys. Rev. 31A, 2291 (1985).

LATTICE DYNAMICAL EFFECTS AND TEMPERATURE DEPENDENCE OF MÖSSBAUER ISOMER SHIFT IN ^{67}ZnO*

W. Potzel
Physik-Department E15, Technische Universitat Munchen,
D-8064 Garching, Federal Republic of Germany

Abstract: Using the high-resolution 93.3keV transition in ^{67}Zn we studied the temperature dependence of the Lamb-Mossbauer factor (LMF), the center shift (CS) and the quadrupole interaction in ZnO single crystals. The temperature range for this high-energy Mossbauer resonance could be extended up to liquid nitrogen temperature (77.3K). The mean-square atomic displacements show very little anisotropy. The results on the LMF can well be described by the Debye model with Θ_D^{LMF}~317K. The quadrupole interaction is e^2qQ/h= (2.401±0.004)MHz at 4.2K and it is independent of temperature within 1%. At 77.3K the center shift has changed by 9.0μm/s compared to its value at 4.2K. Already at low temperatures phonon-induced electron transfer from zinc to oxygen is observed. The shift caused by charge transfer shows a T^4-dependence at low temperatures, in agreement with recent theoretical calculations.

*This work has been funded by the German Federal Minister for Research and Technology (BMFT) under contract Nr. 03-KA1TUM-4 and by the Kernforschungszentrum Karlsruhe.

1.) Introduction

Almost exactly two years ago, at the XX. Zakopane School on Physics I introduced ^{67}Zn Mossbauer spectroscopy as a highly sensitive tool for measuring small changes in the r-ray energy /1-3/. In particular, I discussed the Cu-Zn alloy system /4/. In the same presentation I also tried to show that the ^{67}Zn resonance is in addition very suitable for investigating lattice dynamical effects. As an example I discussed Zn metal and pointed out the enormous anisotropy of the recoil-free fraction /5,6/.

In the present paper I want to employ this sensitivity to investigate a combined effect in ZnO, the second-order Doppler effect of lattice dynamical origin and the temperature dependence of the isomer shift, caused by a variation of charge density at the Zn atom.

Mossbauer experiments were performed with single crystals of ZnO. This material crystallizes in a hexagonal (wurtzite) structure. Each Zn atom is surrounded by a tetrahedron of O atoms. The tetrahedron is slightly distorted. Already several years ago it was demonstrated that covalency effects play an important role in the Zn-O bond /7,8/. This fact is emphasized by Fig. 1, where the isomer shift is plotted versus the electronegativity (Pauling) of the ligand for various Zn-compounds. The s-electron density at the Zn nucleus is reduced with increasing electronegativity of the ligand. This behaviour is easily understood /7,8/ in terms of 4s and 4p electrons of Zn participating in the bonding. In a simplifying picture: if the electronegativity of the ligand is increased the probability of finding 4s and 4p electrons at the Zn site is diminished and the s-electron density at the Zn nucleus is reduced. Surprisingly, even for ZnF_2 covalency effects are by no means negligible /8/. Also in this lecture it will turn out, that the covalent part of the Zn-O bond is very important.

Through refinements of the experimental techniques we were able to extend the measuring temperature upwards to 80K despite the small Lamb-Mossbauer factor caused by the relatively high gamma-ray energy and low mass of the resonant nucleus. Therefore we could derive mean-square atomic displacements and mean-square atomic velocities for

^{67}Zn in the temperature range between 4 and 80K. We observed phonon-induced charge transfer from zinc to oxygen. At low temperatures this charge transfer shows a T^4-dependence as predicted theoretically by K. N. Shrivastava /9/. This is the first time that a T^4-dependence of the charge transfer has been observed experimentally. In addition, the temperature dependence of the electric field gradient in ZnO was determined with high precision.

2.) Experimental Details

Measurements were performed in standard transmission geometry with a piezoelectric quartz spectrometer as described earlier /5/. The drive system which is a compact unit containing both, source and absorber, was suspended by soft springs inside a sealed stainless-steel container filled with He exchange gas at reduced pressure /5/. The temperature of the ZnO single crystal source could be increased by a small heating coil. In this manner it was possible to keep the absorber temperature below 12K even at a source temperature of 80K. The temperatures of source and absorber were determined by semiconductor devices.

Due to the small recoilfree fraction at higher temperatures experiments become increasingly difficult, in particular at liquid nitrogen temperature. One could argue that it would be advantageous to heat the absorber rather than the source and compensate the smaller recoilfree fraction at elevated temperatures by increasing the absorber thickness. This, however, can not be done here, since the electronic (photo-electric) absorption cross section is the factor limiting absorber thickness /3,10/. The problem can only be overcome by using strong radioactive sources and fast counting electronics, i. e. by measuring small resonance absorption effects with high statistical accuracy.

The ^{67}Ga ($T_{1/2}$=78h) activity was produced in situ by 28MeV proton bombardment of ZnO single crystals at the cyclotron of the Kernforschungszentrum Karlsruhe. The ZnO single crystals were disks of 4mm diameter and of 0.5mm thickness. They were cut with the c-axis perpendicular to the crystal faces. After irradiation the samples were annealed in oxygen atmosphere at ~970K for six hours and thereafter

slowly cooled (50K/h) to room temperature. Mossbauer spectra were recorded with the c-axis at 0° and 45° with respect to the direction of observation of the gamma rays.

The absorber consisted of ^{67}ZnO powder, enriched to 85.2% in ^{67}Zn. The thickness was 963 mg ^{67}Zn/cm^2. Details of the absorber preparation are given elsewhere /10/.

The spectrometer was calibrated using the known quadrupole splittings in ^{67}Zn metal /2,11/ and in ^{67}ZnO /2/ at 4.2K. The gamma rays were detected by an intrinsic Ge diode of 10mm thickness and 40mm diameter coupled to a fast preamplifier. In order to achieve high counting speed and simultaneously good energy resolution a fast double differentiating main amplifier was used /12/. Count rates up to 200 000 s^{-1} in the 93.3keV window were obtained. The signal-to-noise ratio was determined once a day by recording pulse height spectra at the actual counting rate via a high speed analog-to-digital converter. Typical values for the signal-to-noise ratio were 60 - 70%.

3.) Results and Discussion

A. Lamb-Mossbauer Factor

Figs. 2 and 3 display Mössbauer absorption spectra recorded at source temperatures between 4.2 and 77.3K for orientations of the ZnO single crystal of ϑ=0° and 45° of the c-axis with respect to the direction of observation of the 93.3keV gamma rays.

Due to the hexagonal structure of ZnO an electric field gradient is present at the Zn nucleus both, in the source as well as in the absorber. If ϑ=0°, the quadrupole interaction in the source leads to relative intensities of the emitted lines of 0:2:1 /13/, whereas at ϑ=45° we have three lines with relative intensities of 1.36:1:2 assuming that the anisotropy of the mean-square atomic displacements is negligible. The quadrupole interaction in the ZnO powder absorber leads to three absorption transitions of equal intensities. Thus the absorption spectra with ϑ=0° exhibit five peaks with relative intensities of 1:2:1:3:2 and those with ϑ=45° have seven peaks with relative intensities of 2:1:2:4.36:1:1.36:1.36. The line separations

are a direct measure of the main component of the quadrupole tensor and the asymmetry parameter η /2/. The spectra were least-squares fitted to a superposition of five (resp. seven) independent Gaussian lines.

The Lamb-Mossbauer factor and the mean-square atomic displacements are derived from the total area under the absorption lines after correction for non-resonant background radiation.

The angular dependence of the recoil-free fraction $f(\vartheta)$ for an axially symmetric lattice is given by

$$f(\vartheta)=\exp\left\{-\vec{k}^2[\langle x^2\rangle_\perp+(\langle x^2\rangle_\parallel-\langle x^2\rangle_\perp)\cos^2\vartheta]\right\} \qquad (1)$$

where $\vec{k}$ is the wave vector of the gamma radiation and $\langle x^2\rangle_\perp$ and $\langle x^2\rangle_\parallel$ denote the mean-square atomic displacements perpendicular and parallel to the c-axis, respectively. In Fig. 4 the mean-square atomic displacements $\langle x^2\rangle_\perp$ and $\langle x^2\rangle_\parallel$ for ZnO are plotted versus temperature. The solid lines are fits by the Debye model with effective Debye temperatures of $\Theta_D^{LMF}=(319\pm6)$K and (315 ± 5)K, respectively. The Debye model fits the data points quite well indeed. Still, the Debye model renders itself to be insufficient for a description of the phonon frequency spectrum in ZnO /14/. Above ~50K the values for $\langle x^2\rangle_\parallel$ tend to be slightly larger than those for $\langle x^2\rangle_\perp$, however, just outside our present limits of error. If at all, there is very little anisotropy of the mean-square atomic displacements at low temperatures. This is in perfect accordance with the similarity of the Gruneisen parameters $\gamma_\parallel$ and $\gamma_\perp$ deduced from thermal-expansion coefficients and related data /15,16/, which implies that the elastic anisotropy of the crystal must be small. This result is in sharp contrast to the situation in Zn metal, where an enormously large anisotropy was found /5/.

B. Center Shift

A change with temperature of the center shift is clearly visible in Figs. 2 and 3. At 77.3K it has increased to a value of (9.0) ± 0.03)μm/s as compared to 4.2K.

The temperature variation of the center shift CS can be written /17,18/:

$$(\partial CS/\partial T)_p = (\partial S_{SOD}/\partial T)_p + (\partial S/\partial T)_V + (\partial S/\partial \ln V)_T \cdot (\partial \ln V/\partial T)_p \qquad (2)$$

The first term represents the second-order Doppler shift (SOD). The second term describes the explicit temperature dependence of the isomer shift S at constant volume due to changes of the electron density which may be caused by the electron-phonon interaction upon the electronic states. The third term gives the volume dependence of S caused by thermal expansion of the lattice. Although there are no high pressure Mössbauer data on ZnO available at present, the contribution of the third term to the center shift can be estimated to be negligibly small. The total volume contraction between 4.2K and 80K is smaller than $1 \cdot 10^{-4}$ /15,16/. The s-electron density ρ is calculated for $^{67}Zn^{2+}$ in a tetrahedral environment of O^{2-}-ions to vary proportional to the inverse seventh power of interatomic distance R /19/, i. e. $\Delta\rho \simeq -(7/3)(\Delta V/V)\rho$ with $\rho \sim 7.5$ a.u. for R ~ 2Å /20/. Together with the known value of $\delta\langle r^2\rangle$ /7,21/ we estimate $\Delta S \sim 0.08 \mu m/s$, or only ~0.9% of the center shift observed between 4.2 and 77K. Thus, to a very good approximation, the center shift is due to the second-order Doppler shift (SOD) and the explicit temperature dependence of the isomer shift (ETS).

The main problem is the separation of the SOD from the CS /22/. We attempt to achieve this by using specific heat data C_p /23-25/. Since the volume change is rather small up to T~100K the specific heat C_V can very well be approximated by the experimental data C_p in this temperature range. As demonstrated by Fig. 5 the change in specific heat C_V follows closely the curve calculated within the Debye model if a Debye temperature of $\Theta_D^{SD}=(275\pm3)$K is chosen and the assumption is made, that only acoustic phonons play a role at low temperatures. When these low-frequency phonons are excited, the whole ZnO-molecule moves together. Optical phonon frequencies appear to lie much higher indeed.

When the temperature of a harmonic crystal is increased, the change of the total energy is twice the change of the mean kinetic energy:

$$M_{Zn}\Delta\langle v_{Zn}^2\rangle + M_O\Delta\langle v_O^2\rangle = \Delta E \qquad (3)$$

where E is the total energy of the lattice, and M_{Zn}, M_O, $\langle v_{Zn}^2\rangle$, and $\langle v_O^2\rangle$ are the gram atomic weights and mean-square atomic velocities of Zn and O, respectively.

We consider the two limiting cases of high resp. low temperatures. At high temperatures in thermodynamic equilibrium the mean kinetic energies for Zn and O change by equal amounts. Then eq.(3) reduces to

$$\Delta\langle v_{Zn}^2\rangle = 1/(2M_{Zn})\Delta E \qquad (4)$$

In ZnO at high temperatures the second-order Doppler shift, $S_{SOD} = -\Delta\langle v^2\rangle/(2c)$, is connected to the specific heat by:

$$S_{SOD} = -\Delta T \cdot C_V/(4M_{Zn}c) \qquad (5)$$

where c is the velocity of light and ΔT is the difference in temperature. The line shift S_{SOD} can therefore be predicted by integrating eq. (5) with known specific heat. The broken line labeled S_{SOD}^H in Fig. 6 indicates the temperature dependence of the second-order Doppler shift as calculated from the specific heat, if the assumption would be valid that eq.(5) also holds at low temperatures.

In the second limiting case of low temperatures, the change of $\langle v^2\rangle$ between 0K and temperature T is given by /22/:

$$\langle v^2\rangle_T - \langle v^2\rangle_{T=0} = (3A^4/5)\cdot(k_B/M)\cdot\vartheta_0\cdot\left(T/\vartheta_0\right)^4 \qquad (6)$$

At low temperatures this increase in $\langle v^2\rangle$ is the same for zinc and oxygen. It is caused by the very long-wavelength acoustic vibrations which are the first to be excited. Since in these modes groups of atoms move together, the motion of a particular atom does not depend on its mass, force constants, or local surroundings, but only on the bulk elastic constants of the crystal. In eq.(6) M is the mass of a ZnO molecule. The value of ϑ_0 is obtained by fitting a T^3-dependence to the low-temperature specific heat data with the condition that the total number of modes allowed is three times the number of ZnO molecules. The curve labeled

S^L_{SOD} in Fig. 6 is calculated using eq.(6) with ϑ_o=275K. Up to ~50K S^L_{SOD} lies considerably below the data points obtained experimentally for CS (s. Fig. 6). This is true also for the value at 19.4K, where S^L_{SOD}=(0.066±0.002)μm/s and CS=(0.080±0.003)μm/s. The fact that the observed CS is larger than both, S^H_{SOD} and S^L_{SOD}, demonstrates that the explicit temperature dependent isomer shift plays a decisive role already at cryogenic temperatures.

In order to determine the ETS quantitatively, the derivation of the SOD for the zinc atoms at intermediate temperatures is required. This is a formidable task. It requires modern cluster calculations, which in particular allow a determination of force constants. At present such calculations are not available. However, we can say that the ETS has to be within a certain region: it has to be at least as large as the difference between the experimental values for CS and the curve S^L_{SOD} (i. e. ETS>ETS_{min}) and it has to be smaller than the difference between CS and the curve S^H_{SOD} (i. e. ETS<ETS_{max}). Furthermore, ETS has to approach ETS_{min} at low temperatures and ETS_{max} at high temperatures. To get a more quantitative estimate we took $S_{SOD}=S^L_{SOD}$ at 19.4K and $S_{SOD}=S^H_{SOD}$ at 297.9K (the highest temperature, for which specific heat data are available) and used a spline interpolation for the temperature range in between. This spline curve is also shown in Fig. 6. The ETS is then given as difference between CS and the spline curve. In Fig. 7 the ETS is plotted versus temperature.

The change of ETS is such, that the s-electron density $\rho(0)$ at the Zn nucleus is reduced with increasing temperature. Anharmonic effects, like lattice contraction, can not explain the observed ETS. As estimated above, the shift caused by lattice contraction is about a factor of 50 smaller than ETS. In addition, lattice contraction is expected to increase $\rho(0)$ due to the larger covalency of the Zn-O bond /7/. Therefore our data clearly demonstrate the presence of ETS. Most likely it is caused by phonon-induced processes which involve the electronic structure.

Changes in the s-electron density at the Mossbauer nucleus as a result of the electron-phonon interaction have been calculated /9,26-28/ and experimentally investigated in some conducting /18,29-31/

as well as insulating systems /32,33/. In all cases, phonon-induced effects have been observed only at high temperatures, where however other effects, like thermal expansion, are large. In ZnO the electron-phonon interaction appears to be important already at cryogenic temperatures.

K. N. Shrivastava has theoretically investigated two types of phonon-induced processes for the case of ^{57}Fe: dynamical configuration mixing and dynamical charge transfer /9/. In the case of ZnO, dynamical configuration mixing can be neglected, since the 3d-shell of Zn is completely filled and the 4d-levels lie energetically too high to be involved in the chemical bond. Dynamical charge transfer, however, appears to play the important role. As stated earlier /7,8/, the chemical bond in ZnO is partially covalent. The dynamical phonon-induced electron transfer from partially occupied 4s- and 4p-orbitals of zinc to the neighbouring oxygen atoms is mediated by the orbital lattice interaction. Such an electron transfer indeed decreases the s-electron density $\rho(0)$ at the zinc nucleus. From our measured value of ~3.5μm/s (at 77.3K) we estimate a charge transfer which corresponds to a fraction of 0.01 of a 4s-electron.

The temperature dependence of the dynamical charge transfer was predicted /9/ to cause ETS to vary according to

$$ETS = K \cdot T^4 \cdot \Phi(T) \qquad (7)$$

where K is a constant containing the electronic matrix elements. In Ref.9 the Debye approximation was used with

$$\Phi(T) = \int_0^{\Theta/T} z^3 (e^z - 1)^{-1} dz \qquad (8)$$

where Θ is an effective Debye temperature.

From our measurements we derive $K=(3.0\pm1.0)\cdot10^{-8}\mu m \cdot s^{-1} \cdot K^{-4}$ and $\Theta=(275\pm3)K$. The relatively large error in the value for K is mainly due to the uncertainty in the spline interpolation. The full line in Fig. 7 is calculated with these parameters. Considering the relatively simple spline interpolation, the agreement with our experimental data is very good. In addition, the value of Θ agrees

perfectly with the Debye temperature θ_D^{sp} derived from specific heat data in this temperature range. At low temperatures $\Phi(T)$ is temperature independent to good approximation (if $(\theta/T)>7$, the deviation of $\Phi(T)$ from $\Phi(0)=\pi^4/15$ is less than 5%). Therefore

$$ETS = K\cdot(\pi^4/15)\cdot T^4 \qquad (9)$$

Unfortunately, for ^{67}Zn-systems calculations, in particular of the constant K, are still missing. From experimental point of view the high-resolution spectroscopy of the 93.3keV transition makes it possible to determine phonon-induced transfer effects with high precision.

C. Quadrupole Interaction

As demonstrated by Fig. 8 the electric field gradient tensor (efg) is independent of temperature between 4.2 and 77.3K within $\sim 1\cdot 10^{-2}$. We get $e^2qQ/h = (2.401 \pm 0.004)$MHz at 4.2K and for the ratio $e^2qQ(4.2K)/e^2qQ(77.3K) = 1.009 \pm 0.010$. Within our experimental errors the asymmetry parameter is found to be $\eta=0$ at all temperatures. Our data on ZnO are corroborated by time-differential perturbed-angular correlation (TDPAC) measurements using, however, the probe ^{111}Cd as an impurity in ZnO /34,35/. The TDPAC-results exhibit very little change up to ~70K, a slow decrease of the quadrupole interaction up to ~300K and an exponential increase above ~400K. In addition, the TDPAC-data show a reduction of the quadrupole coupling constant at low temperatures by ~2% in ZnO single crystals as compared to ZnO powder. With our measurements we find a small but systematic difference between CS for $\vartheta=0^\circ$ nd for $\vartheta=45^\circ$. This is an indication for a slightly smaller efg in ZnO single crystals as compared to ZnO powder. However, in order to determine this difference more precisely, we have to improve the statistical accuracy of our measurements as well as the temperature stability of our experimental set-up.

Neither the TDPAC nor the Mossbauer results are fully understood at present. The electric field gradient can surprisingly well be

described within a point charge model /36/ assuming complete ionicity in ZnO (i. e. Zn^{2+} and O^{2-}). The point charge model predicts a temperature independent efg if the change caused by a lattice contraction parallel to the c-axis is compensated by the change due to the lattice contraction perpendicular to the c-axis. The application of the point charge model, however, has to be considered doubtful, since the chemical bond in ZnO is partially covalent. As stated earlier /7,8/, a clear indication of this fact is the much more negative isomer shift which was found for ZnF_2. In fact, an investigation of the electric quadrupole interaction in ZnF_2 demonstrated, that even this compound is not fully ionic /8/. The phonon-induced electron transfer from zinc to oxygen also stresses the partially covalent character of the Zn-O bond. Although the electron transfer decreases the charge at the zinc site, the symmetry of the charge distribution, which is reflected in the quadrupole interaction, remains virtually unchanged. An improvement of our understanding of the dynamical charge transfer process and of electric field gradients and their temperature dependence requires highly detailed theoretical calculations.

4.) Conclusions

The 93.3keV transition in ^{67}ZnO was used to investigate the temperature dependence of the quadrupole interaction, the Lamb-Mossbauer factor, and the center shift. The quadrupole interaction is independent of temperature within 1% between 4.2 and 77K. The mean-square atomic displacements were found to show very little anisotropy. Most interesting is the variation of the center shift with temperature. Mossbauer effect is the only method to measure mean-square atomic velocities in the solid directly. Already at low temperatures (~20K) phonon-induced electron transfer from zinc to oxygen causes a significant contribution to the center shift. The shift due to charge transfer shows a T^4-dependence. The charge transfer amounts to only ~0,01 of a 4s-electron at 77.3K and decreases $\rho(0)$, the s-electron density at the ^{67}Zn nucleus. Although the change of $\rho(0)$ is exceedingly small, the high energy resolution of the 93.3keV transition makes it possible to determine such effects with high precision.

Acknowledgements

We would like to thank Dr. H. Schweickert, K. Assmus, and W. Maier at the cyclotron of the Kernforschungszentrum Karlsruhe for the numerous source irradiations.

References

/1/ W.Potzel. Condensed Matter Studies by Nuclear Methods. Proceedings of XX. Winter School on Physics, Zakopane 1985 edts. J. J. Bara, K. Ruebenbauer, Z. Stachura. Vol.2, p. 294

/2/ W.Potzel, Th. Obenhuber, A. Forster, and G.M. Kalvius. Hyperfine Interactions 12, 135 (1982)

/3/ P. Helisto, E. Ikonen, T. Katila, W.Potzel, and K. Riski. Phys. Rev. B30, 2345 (1984)

/4/ Th. Obenhuber, W. Adlassnig, U. Narger, J. Zankert, W. Potzel, and G.M. Kalvius. Europhys. Lett. 3, 989 (1987)

/5/ W. Potzel, W. Adlassnig, U. Narger, Th. Obenhuber, K. Riski, and G.M. Kalvius, Phys. Rev. B30, 4980 (1984)

/6/ Th. Obenhuber, W. Adlassnig, J. Zankert, U. Narger, W. Potzel, and G.M. Kalvius, Hyperfine Interactions 33, 69 (1987)

/7/ A. Forster, W. Potzel, and G.M. Kalvius, Z. Physik B37, 209 (1980)

/8/ W. Potzel, and G.M. Kalvius, Phys. Lett. 110A, 165 (1985)

/9/ K. N. Shrivastava, Hyperfine Interactions 24-26, 817 (1985)

/10/ W. Potzel, A. Forster, and G.M. Kalvius, J. Phys. (Paris) 37, C6-691 (1976)

/11/ Th. Obenhuber, A. Forster, W. Potzel, and G.M. Kalvius, Nucl. Instrum. Methods 214, 361 (1983)

/12/ W. Potzel and N. Halder, Nucl. Instrum. Methods, 226, 418 (1984)

/13/ G.J. Perlow, L.E. Campbell, L.E. Conroy, and W. Potzel, Phys. Rev. B7, 4044 (1973)

/14/ C. Schafer, W. Potzel, W. Adlassnig, P. Pottig, E. Ikonen, and G. M. Kalvius, to be published

/15/ H. Ibach, Phys. Stat. Sol. 33, 257 (1969)

/16/ B. Yates, R.F. Cooper, and M.M. Kreitman, Phys. Rev. B4, 1314 (1971)

/17/ R.V. Pound, G.B. Benedek, and R. Drever, Phys. Rev. Lett. 7, 405 (1961)

/18/ G.M. Rothberg, S. Guimard, and N. Benczer-Koller, Phys. Rev. B1, 136 (1970)

/19/ K.N. Shrivastava, Phys. Rev. B13, 2782 (1976)

/20/ S.C. Abrahams and J.L. Bernstein, Acta Cryst. B25, 1233 (1969)

/21/ A. Svane and E. Antoncik, Phys. Rev. B33, 7462 (1986)

/22/ R. M. Housley and F. Hess, Phys. Rev. 146, 517 (1966)
/23/ Y. S. Touloukian and E. H. Buyco, Thermophysical Properties of Matter, Vol. 5, p. 290, Plenum, New York 1970
/24/ K. Clusius and P. Harteck, Z. Physik. Chem. 134, 243 (1928)
/25/ R. W. Hillar, J. Am. Chem. Soc. 50, 2653 (1928)
/26/ R.V. Kasowski and L.M. Falicov, Phys. Rev. Lett. 22, 1001 (1969)
/27/ K.N. Shrivastava, Phys. Rev. B1, 955 (1970)
/28/ K.N. Shrivastava, Phys. Rev. B7, 921 (1973)
/29/ R.M. Housley and F. Hess, Phys. Rev. 164, 340 (1967)
/30/ D.L. Williamson, in Mossbauer Isomer Shifts, edited by G. K. Shenoy and F. E. Wagner (North-Holland, Amsterdam, 1978)
/31/ G. Kaindl, D. Salomon, and G. Wortmann, in Mossbauer Isomer Shifts, Ref. 30
/32/ G.M. Kalvius, U. F. Klein, and G. Wortmann, J. Phys. (Paris) 35, C6-139 (1974) and references therein.
/33/ H. K. Perkins and Y. Hazony, Phys. Rev. B5, 7 (1972)
/34/ H. Wolf, S. Deubler, D. Forkel, H. Foettinger, M. Iwatschenko-Borho, F. Meyer, M. Renn, and W. Witthuhn, 14th Int. Conf. on Defects in Semiconductors, Paris, France, 1986, in print
/35/ F. Meyer, S. Deubler, M. Plank, W. Witthuhn, and H. Wolf, 7th Int. Conf. on Hyperfine Interactions, Bangalore, India, 1986, in print
/36/ F.W. de Wette, Phys. Rev. 123, 103 (1961)
/37/ The data point shown at 19.4K in Figs. 6 and 7 was obtained with a powdered sample of ZnO in a supplementary experiment. The agreement with the single crystal data is excellent.

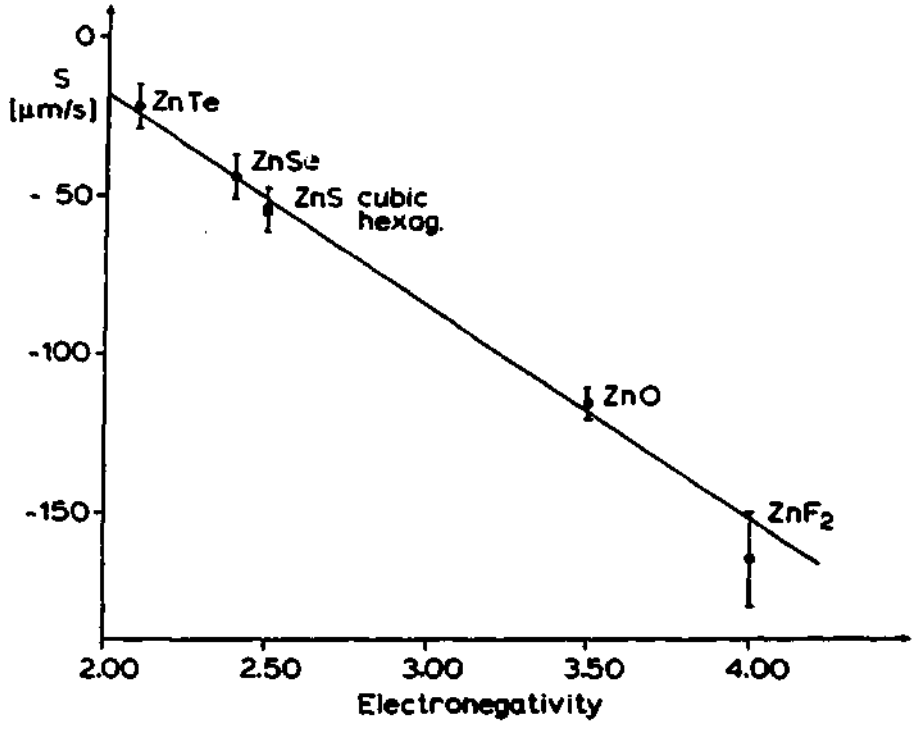

Fig.1: Isomer shifts vs. Pauling electronegativity of the ligands for various divalent Zn compounds. All shifts are given with respect to a $^{57}CoCu$ source.

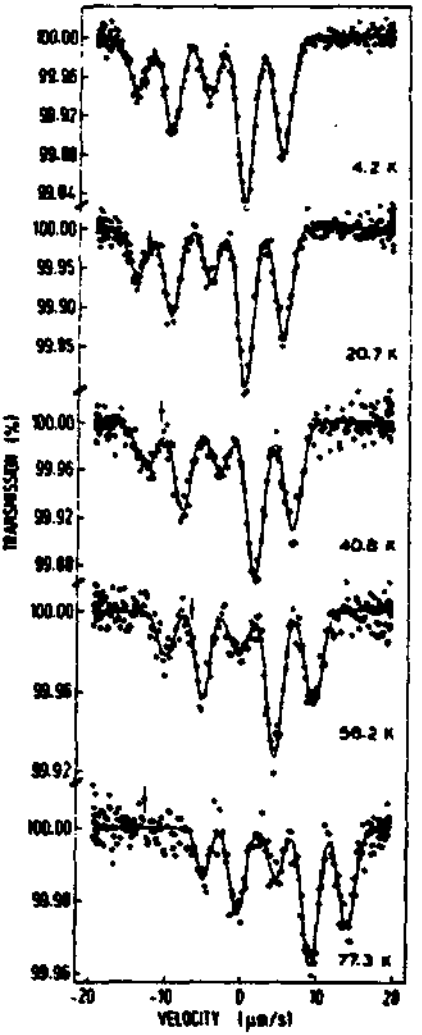

Fig.2: Mössbauer absorption spectra recorded at source temperatures between 4.2K and 77.3K. The source is a $^{67}CoAlMg$ single crystal with the c-axis parallel to the direction of observation of the 93.3keV gamma-rays.

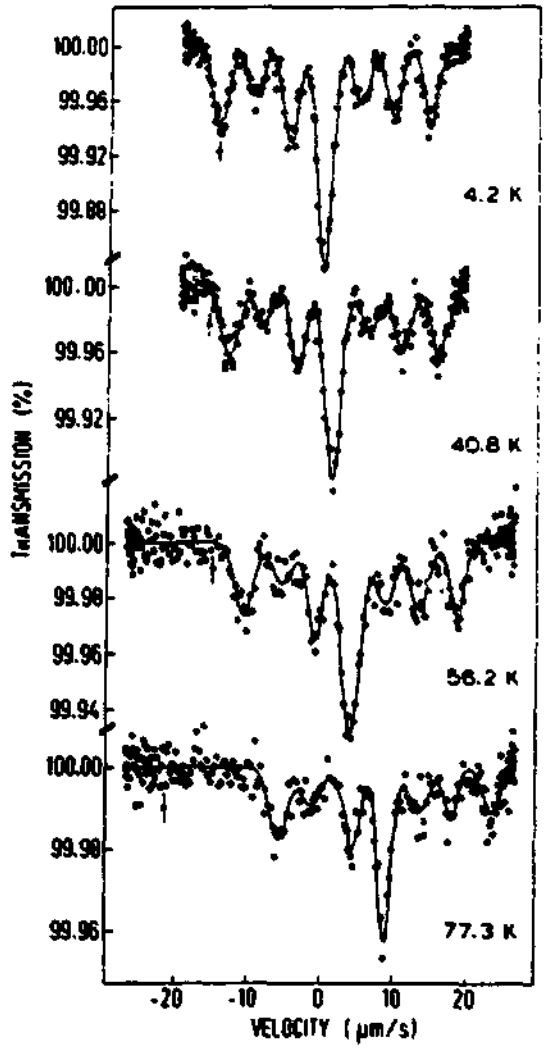

Fig.1: Mössbauer absorption spectra obtained at source temperatures between 4.2K and 77.3K. The c-axis of the $^{57}CoInO$ single crystal forms an angle of 45° with respect to the direction of observation of the 93.3keV gamma rays.

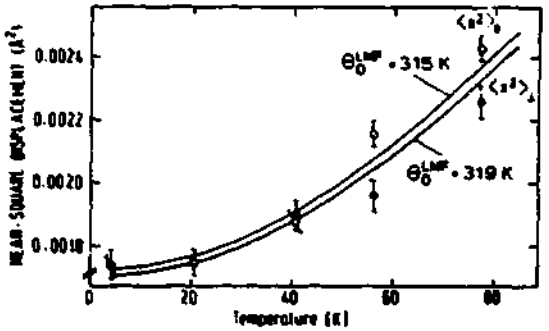

Fig. 4: Mean-square atomic displacements in ZnO, parallel and perpendicular to the c-axis. The solid lines are fits by the Debye model with Debye temperatures of Θ_D^{LMP}=315K and 319K, respectively.

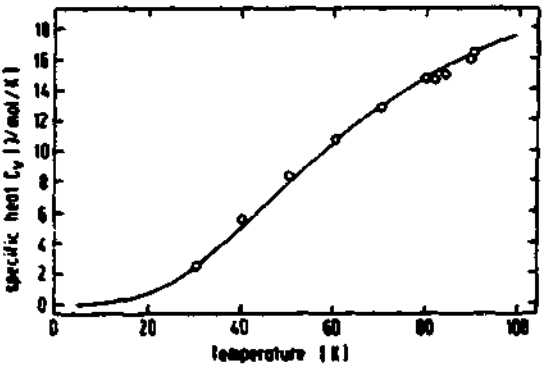

Fig. 5: Specific heat of ZnO within the temperature range covered by the Mössbauer experiments. The best fit by the Debye model in the temperature range (T≥80K) gives a Debye temperature of Θ_D^{SP}=275K. The specific heat data are taken from Refs. 23-25.

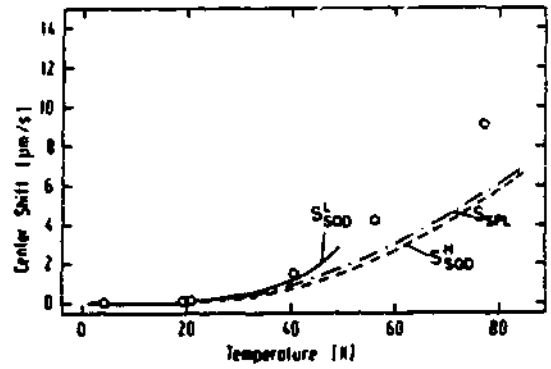

Fig.6: Center shift at various temperatures. The error bars are smaller than the open circles representing the data points /37/. S^L_{SOD} and S^H_{SOD} correspond to the second-order Doppler shift as calculated from specific heat data for the low and high temperature limit, respectively. S_{SPL} denotes the second-order Doppler shift as calculated from a spline interpolation between the low and high temperature limits (s. text).

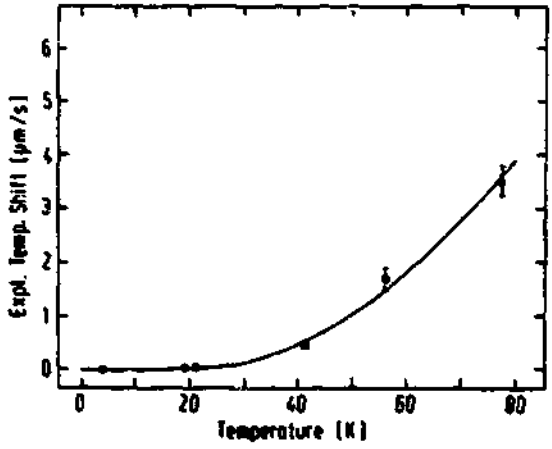

Fig.7: Explicit temperature dependence of the isomer shift (ETS). ETS is the difference between CS and S_{SPL} of Fig. 6. The solid line is a fit to the data using equation ETS=K·T^4+c(T). At low temperatures a T^4-dependence is observed.

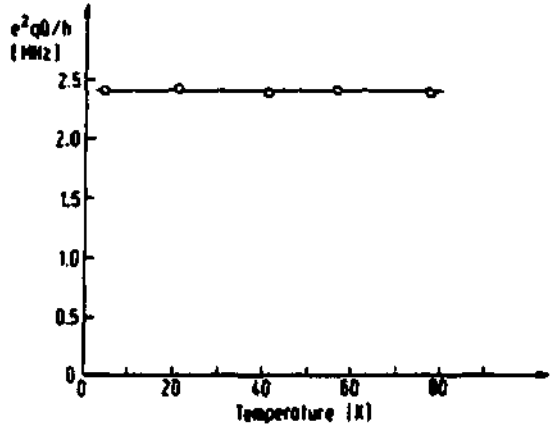

Fig.1: Quadrupole interaction in ^{67}ZnO at various temperatures. The change of e^2qQ/h between 4.2K and 77.3K is smaller then 1%.

THE USE OF CLUSTER CALCULATIONS FOR THE INTERPRETATION OF HYPERFINE INTERACTION IN SOLIDS

S. Nagel, Institute of Mineralogy, University of Marburg, D-3550 Marburg, W-Germany.

ABSTRACT

Wave functions from cluster calculations have been used to analyze the source of electric field gradients in solids in order to provide an understanding of experimentally measured quadrupole interaction. Contrary to previous assumptions based on the ionic model, it turned out that electric field gradients are mainly determined by valence states, especially by those which are unoccupied in the ideal ionic state.

I. INTRODUCTION

The present contribution will be mainly concerned with quadrupole coupling which is the interaction of the nuclear quadrupole moment Q with the second derivative of the electrostatic potential at the nuclear site $V_{i,j} = \partial^2 V(r)/ x_i x_j$ (in the following also denoted as electric field gradient EFG) which is described by the Hamiltonian

$$H = \frac{eQ}{2I(2I-1)} (V_{xx} I_x + V_{yy} I_y + V_{zz} I_z) \qquad (1)$$

The knowledge of the interrelation between the EFG and the electronic structure is the essential basis for an exploitation of experimental quadrupole coupling data in order to gain information about chemical bonding. Unfortunately the EFG provides only integral information about the total charge distribution $\rho(r)$:

$$V_{zz} = \int \rho(r) (3\cos^2\theta - 1)/r^3 \, d^3r \qquad (2)$$

which allows quite different models for the electron distribution to fit with observed quadrupole coupling data. Therefore, it should be required that an adequate model be also consistent with independent experimental information such as that from x-ray diffraction. However, the integrand in eq. 2 has its main contributions from regions close to the nucleus and there is hardly an alternate technique which allows to obtain reliable information about this region. Therefore, also most of the approaches in solid state theory are not interested in an accurate description of the small r region.

II. THE IONIC MODEL

The traditional understanding of field gradients in solids is based on the antishielding concept[1-4]. Here it is assumed that an "external" field gradient originating from the crystal ions is amplified through the response of the charge distribution around the resonating nucleus:

$$V_{zz} = (1-\gamma_\infty) \, {}^{ex}V_{zz} \qquad (3)$$

This approach has motivated a great effort to calculate more exact antishielding factors as well as lattice sums. However, shielding corrections turned out to be considerably different

when calculated for free ions or for ions within a surrounding charge distribution[5,6]. Furthermore the model completely neglects covalency and charge transfer.

III. ALL-ELECTRON CALCULATIONS

Recently some groups have begun to calculate EFGs in solids from first principles using band structure[7,8] as well as cluster approaches[9,10] the latter of which consider only a limited number of atoms. Contrary to band structure methods, the cluster approximation allows also to treat impurities for which a great number of nuclear resonance data exist. In the presently applied approach the remainder of the lattice is considered by exposing the cluster to an external potential $^{ext}V_i$ which is different for each cluster ion i and which is the exact Coulomb potential the ion would experience in an infinite crystal. This kind of stabilization of the cluster guarantees the approximate equivalency of those centers which are equivalent in the crystal.

The technique for solving Schrödinger's equation for the cluster is based on the scattered-wave technique[11] which has been modified in some points[12]. The method is at the same level of approximation as the KKR and APW band structure methods and is characterized by a local-density approximation for the exchange operator and a muffin-tin approximation of the potential . The latter involves a spherical average of the potential in spheres around the nuclei which allows numerical integration of the radial Schrödinger equation and thus a considerable exactness of the wave functions close to the nucleus.

The method has been previously applied to a number of different crystal structures[13-15] and it has been shown that it is capable to produce EFG tensors which are in good agreement with experimental quadrupole coupling constants. Furthermore, also isomer shifts and magnetic hyperfine fields could be successfully calculated. One of the most important results of these studies was that the overwhelming contributions to the EFG may originate from orbitals which would be empty in the ideal ionic state such as e.g. 4p orbitals of Fe^{3+}. In the case of hexagonal metals the importance of valence p-orbitals has been deduced from empirical arguments[16] which hes been recently confirmed by very accurate band structure calculation[8].

IV. RESULTS

The origin of EFG in ionic systems will be analyzed in more detail in the following part for the examples of $M=Al^{3+}$, Ga^{3+}, and Fe^{3+} in the garnets $Y_3M_5O_{12}$ as well as for Au^+ and Au^{3+} in $Cs_2Au_2Cl_6$. In all cases the clusters have been restricted to the coordination shell. In the case of the garnets, the metal ions occupy an octahedral position with point symmetry $\bar{3}$ as well as a tetrahedral position with symmetry $\bar{4}$. Both, the octahedra as well as the tetrahedra are elongated along the symmetry axes. Thus, in both cases the EFG is axially symmetric and the coordinate systems may be chosen with z along the symmetry axes. The contribution from a partioular wave function to Vzz is then

$$V_{zz} = 4/5 \langle r^{-3} \rangle_p (n_x - n_z) + 4/7 \langle r^{-3} \rangle_d (2n_{xy} - n_{xz} - n_{yz}) \qquad (4)$$

Table 1
Calculated and experimental contributions to V_{zz} in e/a_B^3 for YAG and YGaG

	YAG		YGAG	
	oct.	tet.	oct.	tet.
V_{zz}^{ion}	-0.011	-0.014	-0.032	-0.016
V_{zz}^{lat}	-0.049	-0.131	-0.254	-0.376
V_{zz}^{tot}	-0.060	-0.145	-0.286	-0.392
V_{zz}^{exp}	±0.018	±0.171	±0.148	±0.468

Table 2
Atomic orbital populations and V_{zz} for Al in YAG and Ga in YGAG.

	octahedral pos.		tetrahedral pos.	
	Al	Ga	Al	Ga
n_s	1.9986	1.9996	1.9962	1.9989
n_p	1.9984	1.9995	1.9948	1.9985
V_{zz}	0.0027	0.0031	0.0117	0.0078
n_{p_x}	0.0337	2.0227	0.0159	2.0143
n_{p_y}	0.0536	2.0398	0.0281	2.0182
n_{p_z}	0.0217	2.0181	0.0137	2.0264
V_{zz}	-0.0014	-0.0518	-0.0027	-0.0600
n_s	0.1474	0.1813	0.0753	0.0981
n_p	0.1506	0.1865	0.0826	0.1093
V_{zz}	-0.0505	-0.1326	-0.1389	-0.3170
n_s	0.2727	0.4434	0.1483	0.2732
q^{tot}	2.04	1.80	2.50	2.30
V_{zz}	-0.048	-0.254	-0.131	-0.376

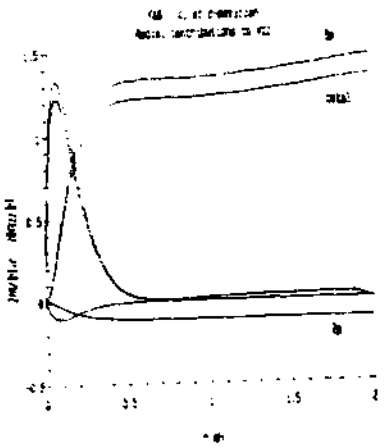

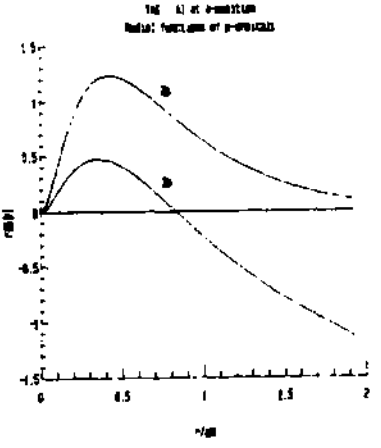

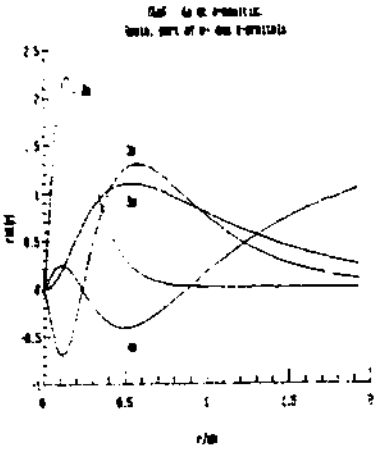

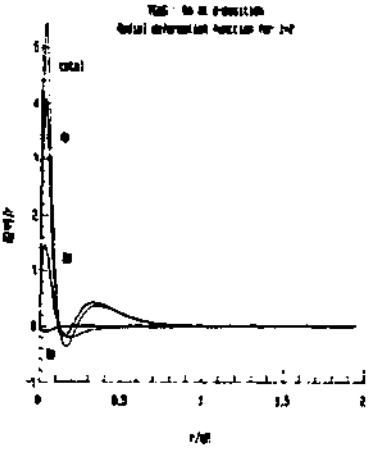

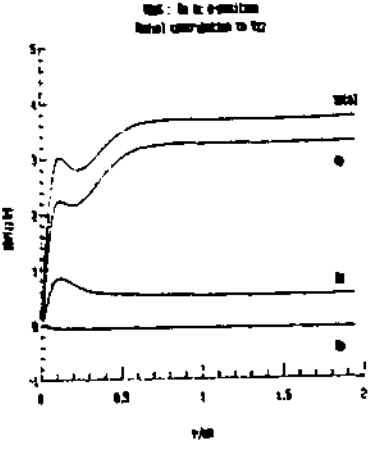

where $\langle r^{-3}\rangle = \int R(r)/r\, d^3r$ with the respective radial function R(r) of p- or d-orbitals which are occupied by $n_\uparrow$ or $n_\downarrow$ electrons, respectively. The total V_{zz} may be analyzed by expanding the total charge distribution into spherical harmonics:

$$\rho(r) = \Sigma_{l,m} R_{l,m}(r)\, Y_{l,m}(r) \qquad (5)$$

which leads to

$$V_{zz} = {}_0\int^{\infty} R_{2,0}(r)/r\, dr \qquad (6)$$

All values will be given in atomic units $a_B = 0.529\text{Å}$, $V_{zz}[V/cm^2] = 9.7\ 10^{17}\ V_{zz}[e/a_B^3]$. Table 1 gives the total calculated V_{zz} in comparison with experimental values for the Al- and Ga garnets[17,18]. $^{ion}V_{zz}$ is the contribution from the ion itself whereas $^{ex}V_{zz}$ is the lattice contribution. The overall agreement between experimental and calculated values is reasonable although the calculation underestimates the difference between octahedral and tetrahedral sites. Table 2 gives the orbital populations and individual contributions to V_{zz} for the core p orbitals (i.e. Al 2p and Ga 3p) and for the valence d- and p-orbitals. It is obvious from the table that in both cases the dominating contributions arise from the charge transferred from oxygen to the uppermost p-orbitals which is most probable for p_z-orbitals because of the elongation of the polyhedra. The 2p of Al and 3p of Ga contribute to V_{zz} with opposite sign as in this case it is more probable for the p_z-orbitals to loose charge. The radial parts of representative atomic orbitals as well as the radial deformation function $\rho 2(r)$ from eq. 6 and its integral are shown in figure 1-5. They show the dominating role of the uppermost p-orbitals for $R_2(r)$ which has its maximum within the first node of this orbital. V_{zz} converges to it's final value within a distance of less than 0.5 a_B.
Table 3 gives similar information for Fe^{3+} at the tetrahedral position in YIG. Here it may be seen that a significant contribution to V_{zz} arises also from a partial occupation of minority spin d-orbitals.

$Cs_2Au_2Cl_6$ contains gold with two different valencies. Au^+ is in a strongly compressed octahedron with two short Au-Cl distances and 4 long ones whereas the opposite situation is found for Au^{3+}. Mößbauer measurements have been carried out by Stanek[19] at different pressures who assigned a large quadrupole splitting of 5.02 mm/s to Au^+ and a small one of 1.17 mm/s to Au^{3+} and who postulated considerable influence of 5d-6s hybridization from the pressure dependence of the quadrupole splitting. The results of a cluster calculation with the positional parameters at zero pressure are given in table 4. In fact a considerable amount of $5d_{z^2}$-6s hybridization has been found for Au^+ leading to a positive V_{zz} from the depletion of the d_{z^2}-orbital. This is, however, overcompensated by the strong negative contribution of the 6p orbitals leading finally to a negative V_{zz}. The situation is reversed for Au^{3+}. However, here it is the large negative contribution to V_{zz} from the depleted d-orbital which determines the negative sign of the total V_{zz}. The relative magnitudes of the EFG for Au^+ and Au^{3+} are opposite compared to the experimental assignments although the order of magnitude is correct. From the calculation this may be due to the limited clus-

Table 3
Atomic orbital populations and V_{zz} for Fe^{3+} at tetrahedral position in YIG

	spin	spin	sum	
n_x	0.9965	0.9958		
n_z	0.9951	0.9940		3p
V_{zz}	0.0229	0.0301	0.0531	
n_{xy}	1.0472	0.1625		
n_{x^2}	1.0196	0.2599		3d
n_{z^2}	1.0601	0.1156		
Vzz	-0.0329	-0.1058	-0.1387	
n_x	0.0264	0.0155		
n_z	0.0303	0.0198		4p
V_{zz}	-0.1001	-0.1102	-0.2103	
n_s	0.0649	0.0597		
q^{lat}	1.62			
V_{zz}^{lat}	-0.434			
V_{zz}^{val}	-0.011			
Vzz^{tot}	-0.445			
V_{zz}^{tot}	-0.535	(Q(^{57}Fe)=0.18)		

Table 4
Atomic orbital populations and V_{zz} for Au^{+} and Au^{3+} in $Cs_2Au_2Cl_6$

	Au^{+}	Au^{3+}	
n_x	1.9999	1.9957	
n_z	1.9945	1.9999	5p
V_{zz}	0.3769	-0.2968	
n_{xy}	1.9567	1.0307	
$n_{x^2-y^2}$	1.9717	2.1659	
n_{z^2}	2.0544	2.1493	5d
n_{xz}	1.8851	2.0049	
Vzz	1.3833	-8.0668	
n_s	0.0274	0.1103	
n_z	0.1069	0.0283	6p
V_{zz}	-3.9061	3.6726	
n_s	0.2308	0.2976	
q^{lat}	0.68	0.88	
V_{zz}	-2.19	-4.72	

Table 5
Atomic orbital populations and V_{zz} for Zn. $ZnZn_8Zn_8$ cluster in comparison with bandstructure results from Ref. 8

	cluster	bandstructure
V_{zz}^{core}	-----	-0.003
n_{z^2}	2.044	
n_{x^2}	2.033	
n_{xz}	2.026	
Δn_d	0.028	-0.010
V_{zz}	-0.013	-0.099
n_s	0.333	
n_z	0.221	
Δn_p	0.112	0.041
V_{zz}	0.548	0.546
n_e	1.432	
V_{zz}^{ion}	-0.059	-0.059
V_{zz}	0.476	0.386
V_{zz}^{exp}	0.370	

ter or to the importance of core polarization which is not sufficiently accountted for on the basis of a muffin-tin potential. However, we feel that the general features of bonding and their influence on the EFG are correctly described.

Finally, the applicability of the cluster approach to metallic systems shall be considered. Table 5 gives the results for a cluster with 13 Zn atoms in comparison with a recent band structure result[8]. Again the importance of the asymmetric 4p occupation may bec seen and the 4p contribution to V_{zz} is almost the same as the band structure result.

V. CONCLUSIONS

It may be concluded that the interpretation of quadrupole coupling based on the cluster calculations is considerably different from that based on the ionic model. The dominating contributions were found to arise from the uppermost valence orbitals which are loosely bound to allow easy adjustment to a deformation of the surrounding. Nevertheless the dominating contributions come from regions very close to the nucleus. The reason for this is the orthogonality of the valence p-orbital to the core p-orbitals with nodes and large oscillations close to the nucleus. V_{zz} converges to its final value almost within a distance from the nucleus which is smaller than the first node of the valence p-orbital. This shows that any theory used for the calculation of EFG tensors must be capable to accurately describe the wave functions in this region.

REFERENCES

1) R. Sternheimer and H. Foley, Phys. Rev. 102, 731 (1956)
2) A. Dalgarno, Adv. Phys. 11, 281 (1962)
3) R.J. Bersohn, J. Chem. Phys. 29, 236 (1958)
4) E. Brun and S. Hafner, Z. Krist. 117, 63 (1962)
5) P.C. Pattnaik, M.D. Thompson, and T.P. Das, Phys. Rev. B16, 5390 (1977)
6) A.C. Beri, Taesul Lee, .P. Das, and R.M. Sternheimer, Phys. Rev. B28, 2335 (1983)
7) P. Blaha, K. Schwarz and P. Herzig, Phys. Rev. Lett. 54, 1192 (1985)
8) P. Blaha, K. Schwarz, and P.H. Dederichs, Phys. Rev. Lett., in press
9) D. Guenzburger and D.E. Ellis, Phys. Rev. B22, 4203 (1980)
10) D.E. Ellis and D. Guenzburger, Phys. Rev. B31, 114 (1985)
11) K.H. Johnson, J. Chem. Phys. 45, 3085 (1966)
12) S. Nagel, Mol. Phys. 48, 161 (1983)
13) S. Nagel, J. Phys. Chem. Solids 46, 743 (1985)
14) S. Nagel, J. Phys. C: Solid State Phys. 18, 3673 (1985)
15) S. Nagel, J. Phys. Chem. Solids 46, 905 (1985)
16) E. Bodenstedt, B. Perscheid, and S. Nagel, Z. Phys. B 63, 9 (1986)
17) K.C. Brog, W.H. Jones, C.M. Verber, Phys.Lett.20, 258 (1966)
18) E. Zubkovsky, Thesis, University of Zürich (1981)
19) J. Stanek, J. Chem. Phys. 76, 2315 (1982)

WIS-87/35/May-PH

Nuclear Polarization Induced by Tilted Multi-foils and Application to Quadrupole Interaction Studies in Solids

E. Dafni*
Department of Nuclear Physics
The Weizmann Institute of Science
76100 Rehovot, Israel

Abstract

The quadrupole interaction of high spin isomers in non-cubic metals is usually measured by the TDPAC technique. However, in such experiments on *aligned* nuclei only the magnitude of the coupling constant can be measured, not the sign. The tilted foils technique provides means to *polarize* the isomers and thereby determine also the sign of the interaction. Applications of the combined tilted foils-TDPAD technique are discussed. As a specific example we consider the signs of the EFG for Ce impurities in Gd.

Introduction

Quadrupole interaction studies of high spin isomers in non-cubic metals are usually motivated by nuclear physics considerations. However, there are cases where such experiments are of interest also from the solid state point of view. In these experiments the coupling constant e^2qQ/h is determined where eq is the electric field gradient in the solid and Q is the nuclear quadrupole moment. If Q is known, then the EFG can be determined. There are several reasons to perform solid state oriented experiments in-beam:

i Large choice of nuclear probes with suitable mean-lives in the range 10^{-8}-10^{-5} sec.

ii Recoil implantation of the probe (impurity) into any desired host.

iii Extremely dilute inpurity-host systems or pure systems.

However, as shown below, in a conventional experiment on *aligned* nuclei, one cannot measure the sign of the interaction; sign determination requires nuclear polarization. The present work considers a procedure for polarizing high spin isomers prior to the implantation into the non-cubic host and measuring the sign of the quadrupole interaction, along with its magnitude. Specific examples for applications are discussed.

* Incumbent of the Arye Dissentshik Career Development Chair

2. TDPAD for Aligned and Polarised Nuclei

In a "conventional" TDPAD experiment, isomers are populated in a spin aligned state. As a result, the angular distribution of decay γ-ray is anisotropic:

$$W(\theta,\phi) = \sum \rho_q^{\lambda\dagger} A_q^\lambda D_{qq}^\lambda.$$

where ρ_q^λ are the statistical tensors constructued from the density matrix:

$$\rho_q^\lambda = \sum_{mm'} (-1)^{I+m} < I - mIm'|\lambda q >< m|\rho|m' >$$

A_q^λ are the γ-ray angular distribution coefficients and D_{qq}^λ are the rotation matrices. For aligned nuclei, $\rho_0^2 \neq 0$. Since for γ-radiation $A_q^\lambda = 0$ for odd λ, one observes γ anisotropy only for even values of λ (i.e. alignment). If we now introduce quadrupole interaction during the nuclear lifetime,

$$K(Q) = \frac{3m^2 - I(I+1)}{4(2I+1)} e^2 qQ$$

(axial symmetry is assumed), spin rotation is induced and the statistical tensors develop in time:

$$\rho_q^\lambda(t) = \sum_{\lambda' q} G_{\lambda\lambda'}^{qq'}(t) \rho_{q'}^\lambda(t=0)$$

where for $\lambda + \lambda'$=even,

$$G_{\lambda\lambda'}^{qq'}(t) = \sum_n S_{nq}^{\lambda\lambda'} cos(n\omega_0 t)$$

These functions are observed by time differential measurements of the γ-anisotropy and the value of $|\omega_0| \propto eqQ$ is deduced. It is apparent that for $\lambda + \lambda'$=even there is no sensitivity to the sign of ω_0.

On the other hand, for vector polarised nuclei $\rho_0^1 \neq 0$. We now consider the case of $\lambda + \lambda'$=odd and the observed functions are:

$$G_{\lambda\lambda'}^{qq'}(t) = -i \sum_n S_{nq}^{\lambda\lambda'} sin(n\omega_0 t)$$

which are sensitive to the sign of Q. The physical picture is that we start from polarized nuclei and induce spin rotation in a preferred sense (depending on the sign if ω_0) thereby producing alignment which was not there before. Fig. 1 shows the TDPAD signals for aligned and polarized ^{144}Gd(10^+) isomers implanted into Gd single crystal. Fig. 2 shows how many nuclear quadrupole moments are known as a function of the spin[1] and demonstrate the difficulty to measure the sign at high spins.

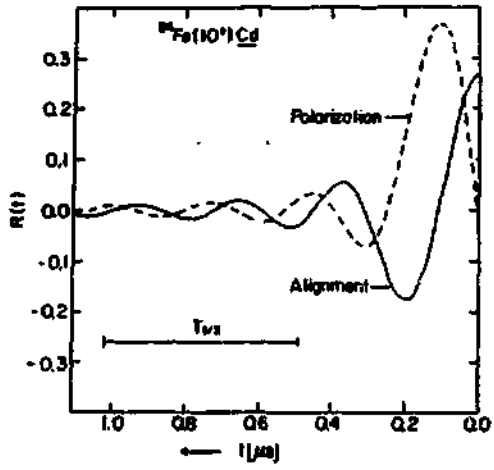

Fig. 1: TDPAD signals for aligned (solid line) and polarised (dashed line) nuclei. The curve for polarisation depends on the sign of ω_0 while the curve for alignment does not.

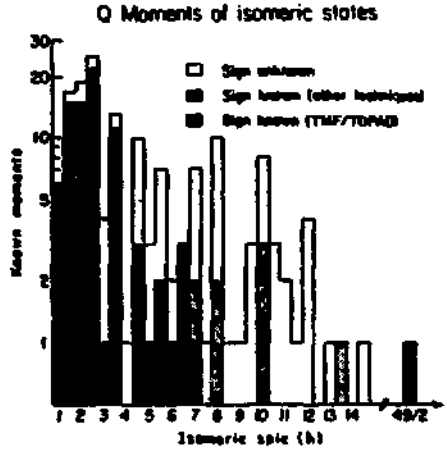

Fig. 2: A compilation of known Q-moments (from data of ref. 1 updated at 1983). The dotted areas represent signs determined by the MTF/TDPAD technique and discussed in the present treatise.

3. Tilted Foil Polarization

We consider ions which emerge from the surface of a foil with their velocity vector at an oblique angle with the normal to the foil. It is known that an electronic spin polarization is produced by an interaction at the exit surface which polarizes the orbital momentum of the atomic states[2]. Such atomic polarization can, in turn, interact with the nucleus via magnetic hyperfine coupling and thus provide a technique for polarizing nuclear high-spin levels. A large improvement in the experimental sensitivity is achieved by allowing the excited nuclear levels to interact with many polarizing foils (MTF interaction).

Two distinct types of nuclear spin manipulations can be obtained with the multifoil interaction. For $\omega_L t \ll 1$ and $N \gg 1$, where ω_L is the average Larmor frequency during flight in vacuum, t is the flight time between two successive foils and N is the number of foils, the angular distribution of decay γ-ray undergoes a precession similar to that in an external magnetic field. This precession (in an effective M Gauss field) has been used to measure g-factors of high-spin short-lived levels in ^{54}Fe, ^{84}Sr and ^{108}Sn. For $\omega_L t \gg 1$, a net *nuclear polarization* is induced. Briefly, the polarization process is as follows: under the condition of $\omega_L t \gg 1$ there is a transfer of polarization from the atomic system to the nucleus (manifested as odd-rank terms in the statistical tensor representation of the density matrix). At long precession times the original sense of $\vec{I}$ and $\vec{J}$ is lost and they assume the average direction of $\vec{F}$ (fig. 3). The introduction of an array of parallel carbon foils results in a regeneration of the electronic polarization at the exit from each foil; the electronic polarization is transferred successively to the nuclei after each foil, resulting in an appreciable cumulative nuclear polarization.

The mathematical formalism which describes the build-up of nuclear polarization P_I in the tilted-multifoil geometry is described in detail in ref. 3. The values of P_I can be calculated either in a classical vector-coupling scheme or with the formalism of statistical tensors evolving in time due to a polarized hyperfine interaction. P_I depends on the atomic polarization P_J, on the number of foils N and on the ratio I/J. Under the asymptotic condition $\omega_L t \gg 1$ the two calculations result in very similar values for P_I. Fig. 4 presents such results for typical cases of I=10, 49/2.

The basic feature of the nuclear polarization build-up is clearly seen from figs. 3,4: the value of P_I increases as I increases provided enough polarizing foils are used. The nuclear polarization can considerably exceed the atomic polarization – an effect understood in terms of more effective transfer of P_J to P_I (if $I \gg J$).

In the following we present measurements of *signs* of quadrupole moments of high-spin nuclear levels – one of the important applications of the MTF method. These measurements also simultaneously determine the induced polarization, P_I. Nuclear polarization induced by tilted foils in low spin long-lived light ions was observed by other groups

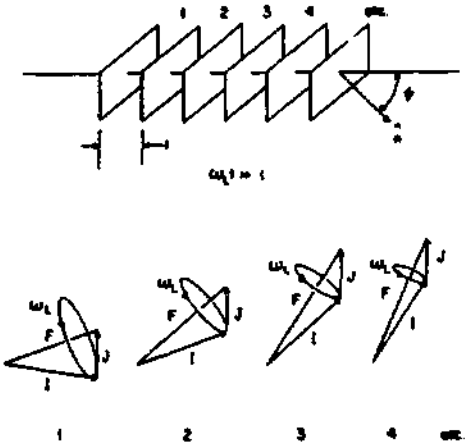

Fig. 3: Multistep transfer of polarization to the nuclear ensemble by a multifoil array.

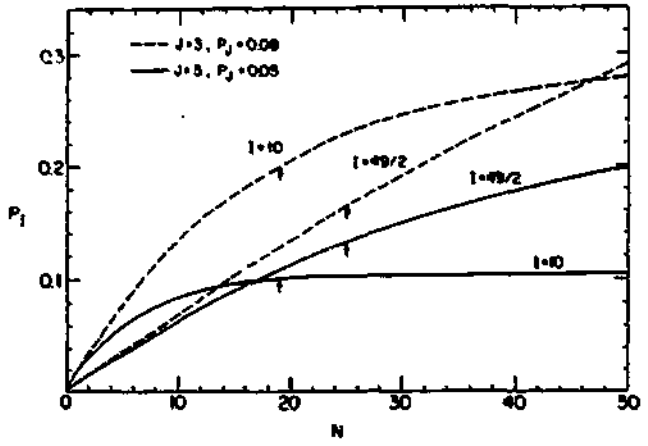

Fig. 4: Nuclear polarization P_I induced by passage through N tilted foils. The flight time between successive foils is assumed to obey the condition $\omega_L t \gg 1$ (see text). The arrows indicate the number of foils actually used in experiments.

via optical spectroscopy[4], β-NMR[5] and Coulomb excitation[6] measurements.

4. Signs of quadrupole interactions

The conventional techniques available to determine the sign of the quadrupole splitting in non-cubic metals: the Mössbauer effect, nuclear orientation at low temperatures, $\beta - \gamma$ correlations, asymmetric Coulomb excitation and polarized neutron capture, are not suitable for short-lived high-spin isomers and till recently no signs of quadrupole moments of high spin states were measured (fig. 1). On the other hand, the nuclear polarization discussed above can now be used to determine signs as well as the magnitudes of Q.

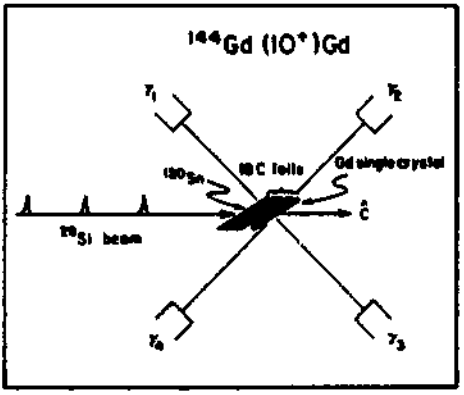

Fig. 5: Experimental set-up used in the ^{144}Gd experiment.

We consider, as an example, the measurement for the ^{144}Gd(10^+) and the ^{147}Gd($13/2^+, 27/2^-$ and $49/2^+$) isomers[7]. The Gd isomers were populated by fusion evaporation reactions with pulsed ^{28}Si beams and 600-μg/cm^2 isotopically enriched Sn targets, tilted with the normal at 60° to the beam (fig. 5). The recoiling reaction products passed through arrays of equally spaced 4-8μg/cm^2 carbon foils and stopped in a single crystal of Gd, oriented with the ĉ axis along the beam direction. The total flight time through the multi-foil stack, during which the polarization is built up was a few nanoseconds. In a second stage, after stopping in the hexagonal Gd host, the polarised nuclear spins experience a precession due to the hyperfine quadrupole interaction with the internal electric field gradient (EFG); the sense of the rotation depending on the sign of Q, and the sign of the EFG. The number of carbon foils (ranging from N=18-24) and the interfoil distances were chosen to maximize the induced nuclear polarization, given the g-factors and recoil velocities (so that $\omega_L t \gg 1$) and to minimize the stopping in the

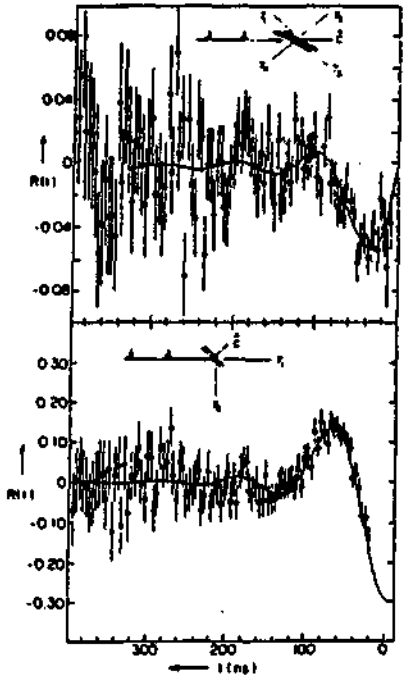

Fig. 6: Upper part: Ratio function R(t) (see text) for polarized ^{144}Gd(10^+) nuclei. The amplitude of the observed modulation is proportional to the induced polarization P_I and the frequency is proportional to $|Q|$. The solid line represents a best fit to the data (see text). A quadrupole moment of an opposite sign would result in an opposite modulation in the ratio function (dotted line).
Lower part: R(t) for *aligned* ^{144}Gd(10^+) nuclei.

carbon foils and frames. The tilt direction (left or right relative to the beam) was alternated periodically, corresponding to measurements with polarization up and down.

Four coaxial Ge(Li) detectors were used to accumulate time spectra of decay γ rays of interest. Ratio functions of the normalized and background subtracted time spectra of counters situated at $\pm 45°$ (and $\pm 135°$) to the beam were performed in such a way that

the nuclear lifetime is divided out. These functions were fitted to the expression

$$R(t) = -\frac{3}{2} P_I F_2 \sum_{n=o}^{n_{max}} S_{n1}^{12} sin(n\omega_o t),$$

where $P_I = < Iz > /[I(I+1)]^{1/2}$ is the nuclear polarization induced by the multifoil array and F_2 is the γ-ray angular distribution coefficient; S_{n1}^{12} are geometrical coefficients and ω_o is proportional to the quadrupole moment Q times the external EFG. The data for ^{147}Gd($49/2^+$) are shown in Fig. 6. The magnitude of the induced polarization is determined from the amplitude of the observed quadrupole oscillation and was found to be $P_I = 0.10(3)$ and P_I=0.16(3) for ^{144}Gd(10^+) and ^{147}Gd($49/2^+$), respectively.

Table 1

Q-moment measurements: the values of $T_{1/2}$, g and |Q| are from previous experiments; sign of Q determinations and P_I values are from the measurements discussed here.

State	$T_{1/2}$[ns]	g	P_I	Q[e.fm^2]
^{54}Fe10^+)	357	+0.728	0.18(5)	+29.7(4)
^{88}Zr(8^+)	1700	-0.18	0.06(2)	+51(3)
^{90}Zr(8^+)	120	+1.36	0.05(1)	-51(3)
^{134}Ce(10^+)	308	-0.187	0.12(3)	+132(12)
^{142}Sm(7^-)	170	-0.06	-	+112(27)
^{144}Gd(10^+)	130	+1.276	0.10(3)	-146(6)
^{147}Gd($13/2^+$)	22.2	-0.037	-	-73(7)
^{147}Gd($27/2^-$)	26.8	+0.840	0.11(2)	-126(8)
^{147}Gd($49/2^+$)	510	+0.446	0.16(3)	-324(18)

A similar procedure, in both the experiment and analysis, has been performed for several other measurements which are summarized in table 1. From the values of the induced polarization P_I one can obtain information regarding the atomic ensemble, e.g. the average atomic polarization $\langle P_J \rangle$ and the average atomic spin $\langle J \rangle$[7]. The nuclear structure relevance of these studies is discussed elsewhere, here we give only one illustrative example, the 8^+ isomers in ^{88,90}Zr. The 8^+ level in ^{88}Zr is described in terms of a two-neutron holes $(\nu g_{9/2})^{-2}$ configuration while the 8^+ level in ^{90}Zr is presumed to be a two-protons, $(\pi g_{9/2})^2$ state (supported by g-factor measurements). The respective magnitudes |Q| of both quadrupole moments have been measured[8] to be the same, indicating similar effective charges for $g_{9/2}$ protons and neutron holes around $A \approx 90$. With

the present determination[9] of positive Q for the 8^+ state in ^{88}Zr and negative Q for the 8^+ state in ^{90}Zr, the shell model picture of particles and holes for these nuclei receives further and direct confirmation.

5. Sign of the EFG for Ce in Gd

While we have a large amount of experimental data on the EFG tensor for many impurity-host systems[1], so far there is no convenient model to predict the magnitude or sign of the EFG for any given system. There are, however, systematics related to specific groups of systems. Considering the transition metal hosts, including Gd which has a (spherical) half-filled $4f$ electronic shell, we find that for any sp or d metal impurity where the sign of the EFG is known, it depends only on the host[1,10,11] (Table 2). (There is one exception, Fe in Ti). For example, in Gd the EFG is always positive. The question raised was if one can also extend these systematics to rare earth impurity ions where the EFG is strongly influenced by the $4f$ electrons.

Table 2

Sign of the EFG in Transition Metal Hosts

Host impurity	Ti	Co	Zr	Gd	Lu	Hf	Re	Os
Fe	−	−					−	−
Co		−						
Cd	+		+			+		
Gd				+				
Lu					+			−
Hf	+		+		+	+		−
Ta						+	−	
W				+				
Re					+		−	
Os					+		−	−
Ir				+			−	−
Au		−		+	+		−	
Hg							−	

We have measured the quadrupole interaction of polarized ^{138}Ce(10^+) nuclei in Gd. From the fit in Fig. 7 we derive a positive value for ω_o. ^{138}Ce(10^+) has a predominant $\nu h_{11/2}^{-2}$ nuclear structure which is certain to have a positive quadrupole moment. There-

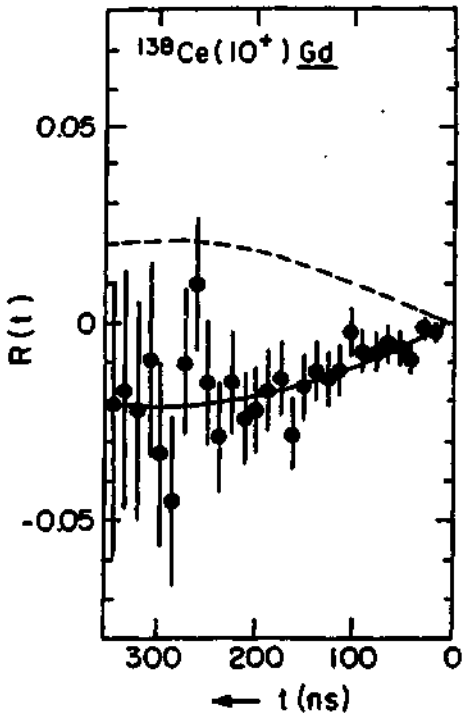

Fig. 7: Ratio function R(t) for ^{138}Ce(10^+) isomers implanted in Gd single crystal. In this case, the sign of Q is known from nuclear physics arguments and the sign of the EFG is determined.

fore, we deduce that also the EFG for Ce in Gd is positive. This result was later used in our studies of other rare earth ions in Gd.

6. Conclusions

A novel technique to polarise high spin isomers by arrays of tilted foils was presented. Implantation of the polarized isomers into non-cubic metallic environments enables the measurement of the quadrupole coupling constants, including the sign of the interaction. Examples were given to specific cases of interest to nuclear or solid state physics.

References

1. For a compilation of known quadrupole moments see R. Vianden, Hyperfine Interact. 16, 1091 (1983) and references therein.

2. H.G. Berry and M. Hass, Ann. Rev. Nucl. Part. Sci. 32, 1 (1982) and references therein.

3. G. Goldring and Y. Niv, Hyperfine Interact. 21, 209 (1985).

4. See, for example, H. Winter and H.J. Andrä, Z. Phys. A291, and F.Q. Lu, J.Y. Tang and B.I. Deutch, Phys. Rev. C25, 1476 (1982).

5. O. Ohsumi et al. Proc. 6th Int. Sym. on Polarization Phenomena in Nuclear Physics, Osaka, Aug. 1985, p. 272.

6. B.I. Deutch and Y. Nojiri, Hyperfine Interact. 15, 135 (1983).

7. E. Dafni, J. Bendahan, C. Broude, G. Goldring, M. Hass, E. Naim, M.H. Rafailovich, C. Chasman, O.C. Kistner and S. Vajda, Phys. Rev. Lett. 53 (1984) 2473; E. Dafni, J. Bendahan, C. Broude, G. Goldring, M. Hass, E. Naim, M.H. Rafailovich, C. Chasman, O.C. Kistner and S. Vajda. Nucl. Phys. A443, 135 (1985).

8. P. Raghavan, M. Senba, Z.Z. Ping, A. Lopez-Garcia, B.A. Brown and R.S. Raghavan, Phys. Rev. Lett. 54, 2592 (1985).

9. J. Bendahan, C. Broude, E. Dafni, G. Goldring, M. Hass, E. Naim and M.H. Rafailovich, Phys. Rev. C33, 1517 (1986).

10. R.E. Watson, R.M. Sternheimer and L.H. Bennett. Phys. Rev. B30, 5209 (1984).

11. H. Ernst, H. Hagn and E. Zech, Phys. Rev. B19, 4460 (1979).

Invited talk Presented at
XXII International School of Physics
Zakopane, Poland
May 9-13, 1987

Experiments in Atomic and Applied Physics Using Synchrotron Radiation*

K. W. Jones
Brookhaven National Laboratory, Upton, New York 11973 USA

ABSTRACT

A diverse program in atomic and applied physics using x rays produced at the X-26 beam line at the Brookhaven National Synchrotron Light Source is in progress. The atomic physics program studies the properties of multiply-ionized atoms using the x rays for photo-excitation and ionization of neutral atoms and ion beams. The applied physics program builds on the techniques and results of the atomic physics work to develop new analytical techniques for elemental and chemical characterization of materials. The results are then used for a general experimental program in biomedical sciences, geo- and cosmochemistry, and materials sciences. The present status of the program is illustrated by describing selected experiments. Prospects for development of new experimental capabilities are discussed in terms of a heavy ion storage ring for atomic physics experiments and the feasibility of photoelectron microscopy for high spatial resolution analytical work.

*Work supported in part by Fundamental Interactions and Processes and Techniques Branches, Division of Chemical Sciences, Office of Basic Energy Sciences, US DOE under Contract DE-AC02-76CH00016; applications to biomedical problems by the National Institutes of Health as a Biotechnology Research Resource under Grant No. P41RR01838; applications in geochemistry by National Science Foundation Grant No. EAR-8618346; and applications in cosmochemistry by NASA Grant No.NAG 9-106.

Introduction

The National Synchrotron Light Source (NSLS) at Brookhaven National Laboratory (BNL) is a high intensity source of x rays that gives new opportunities for research in atomic and applied physics. This paper describes work in both areas that has been done with x ray beams at the NSLS X-26 beam line that show how new types of experiments are made possible by the use of synchrotron radiation. In atomic physics it is shown that measurements of fluorescent radiation on dilute gas targets can now be done so that it is possible to study the light emitted by atoms in an isolated environment. In applied physics work it is shown that it is now possible to detect the presence of as few as 10^7 atoms in a volume of 10^{-9} cm^3 by the use of synchrotron radiation induced x-ray emission (SRIXE) methods. An example of the application of the SRIXE method is given.

The equipment that is now used can be improved in many different ways in the future. In atomic physics it may be possible to add a cooled heavy ion storage ring (CHISR) in close proximity to the NSLS so that it will be possible to study photoexcitation and ionization of multiply-charged ions with high precision. For applied physics it may now be timely to consider the use of photoelectron microscopy as a complement to the detection of fluorescent x rays. Consideration of the use of such an approach to sub-micron resolution imaging is given.

The combination of descriptions of present experimental results with plans for future developments is intended to show the scope and vitality of the research based on the use of NSLS x ray beams in a succinct manner. A full description of the topic goes beyond the scope of this paper.

(Some references to papers and abstracts on crucial aspects of the work are given in References 1-18).

The entire program that is described here represents the work of scientists from the BNL Department of Applied Science Division of Atomic and Applied Physics: B. M. Johnson, M. Meron, B. M. Gordon, A. L. Hanson, and J. G. Pounds, and from The University of Chicago Department of the Geophysical Sciences: J. V. Smith, M. L. Rivers, and S. R. Sutton. We have also had many collaborators from many different institutions who have left a strong imprint on the program.

It is appropriate to mention specifically a long-term interaction between the Institute of Nuclear Physics at Cracow, the Department of Applied Science Division of Atomic and Applied Physics at Brookhaven, and the Kosciuszko Foundation of New York in this contribution to the Proceedings of the XXI Zakopane Winter School. This interaction has made it possible for visitors from Cracow to spend extended periods of time at Brookhaven. The experiments described here have benefited in many ways from invaluable contributions by A. Z. Hrynkiewicz, J. Kajfosz, M. Cholewa, W. M. Kwiatek, and B. Rajchel during their visits. We hope to see our joint ventures continue and to be able to report further results at subsequent meetings in Zakopane!

Characteristics of the NSLS X-26 Beam Line

The NSLS is an electron storage ring that ran at 2.5 GeV with maximum stored electron currents of ~ 200 mA and average beam lifetimes of around ~ 8 hours. The photon flux produced at the experimental station 20 m from the electron orbit is given in Figure 1. The low-energy cutoff is produced by windows and filters used in the path of the beam.

The actual mechanical layout of the beam line is shown in Figure 2. Beryllium windows are used to separate the beam line vacuum system from the machine vacuum for greater ease in doing experiments. The apparatus in the experimental enclosure (hutch) was arranged so that atomic and applied physics could be done simultaneously. A photograph of the hutch interior is shown to the left in Figure 3. The magnet system at the left sideof the hutch is a Penning-type ion trap for atomic physics work and on the right side is the x-ray fluorescence microprobe system used for trace element measurements.

Measurement of Fluorescent Radiation from Argon Following K-Shell Ionization

Measurements of fluorescent radiation from dilute atomic targets are useful for obtaining atomic data that can be used to provide benchmarks data for improving theoretical atomic structure models and for determining cross sections or rate coefficients for very low energy ion-atom collision processes. With synchrotron radiation from the NSLS the photon flux at the sample position is high enough to make such measurements with target densities corresponding to target pressures in the region of 10^{-10} torr or approximately 3×10^{6} atoms/cm^{3}. Parenthetically, note that the determination of fluorescent radiation is the basis of the SRIXE method, with detection limits now running around 10^{6-7} total atoms. Values quoted for target densities depend on the assumptions made for detection system efficiencies, data accumulation times, and backgrounds. The above values are, therefore, to be considered as approximate.

The first experiment that was done at the X-26 beam line on fluorescent radiation for atomic physics purposes was the study of the radiation produced

following the K-shell photoionization of argon (13). This could be done with filtered white radiation since the contribution from the L-shell ionization cross section is less than 10% of the K-shell cross section at the energies considered. The production rate of K vacancies in argon can be easily calculated by calculating the integral of the product of photon flux and cross section over the photon energy distribution. The value obtained is roughly 6×10^3 K vacancies/s for a target density of 10^7 atoms/cm^3, which is adequate for experimental work even though low.

The fluorescent photons produced in the wave length region from 50 to 150 nm were analyzed with a 0.2-m normal incidence spectrometer with a 600 g/mm toroidal grating. This instrument was operated with a resolution of 0.2 nm. A typical spectrum that was obtained for a pressure of 50 mtorr is shown at the bottom of Figure 4. The upper spectra indicate the predicted appearance of lines from individual ionization stages (Ar I to Ar VIII).

Analysis of the data showed that the intensities of the spectral lines were strongly affected by collisions with neutral argon ions. Measurements of the relative intensities of the spectral lines as a function of pressure thus give values for the rate coefficients for charge neutralization in ion-atom collisions at energies around 100 meV. The results of such experiments are now being analyzed.

The mechanisms by which the K vacancy is filled after production results in the further ionization of the atom. For argon a distribution of charge states is produced with values as high as 6 or 7 and a maximum at 4. It is therefore possible to examine a wide range of ions in the course of a single experiment. Figures 5 and 6 show the results of two measurements (16) of the

charge-state distribution using a Penning ion trap and a recoil-time-of-flight apparatus on the X-26 beam line.

The results of the first experiments show the feasibility of atomic photoionization studies. Improvements are under way. The photon flux delivered to the target will be increased by several orders of magnitude by the addition of focussing mirrors in the beam line. This will increase the signal/background and make possible measurements at lower target densities. The use of time-resolved spectroscopy to take advantage of the natural bunching of the synchrotron beam will improve the accuracy of the rate coefficient measurements.

X-Ray Microscopy (SRIXE) Measurements

The use of x-ray fluorescence for analytical measurements has been an established method for many years. The synchrotron light source has catapulted it into a new era because of the high polarization and high brilliance (photons/source area/solid angle/energy interval/s), brightness (photons/solid angle/energy interval/s) and flux (photons/mrad horizontal/energy interval/s) of the x rays emitted. The introductory work described here relies only on the high flux. Further developments of the beam line using mirrors will utilize the high brightness and brilliance of the source.

The SRIXE system that we have used is simple, albeit very powerful. The measurements are carried out after the x-ray beam passes through a window and into the laboratory. Beam intensity is monitored with an ion chamber. Fluorescent x rays are detected at 90 degrees to the incident beam, a position which minimizes the background of Compton-scattered photons. Our measurements

used a 30-mm^2 Si(Li) detector with a resolution of around 155 eV for 5.9-keV Mn K-x rays. Sample positions were changed using stepping-motor-driven x-y-θ translators. Beam positions could be set to about 1 micrometer. The beam size was defined by tantalum slits with a spacing that could be adjusted using stepper motor driven micrometers. Minimum beam size was 10 micrometers. A computer was used to control the system so that maps could be easily made of the spatial distribution of specific elements. Thus, what we have is a very versatile system for high energy x-ray microscopy measurements. A photograph of the arrangement is shown in Figure 3. The present system is a refined version of one that was originally used in experiments at the CHESS facility at Cornell University (1).

The detection limits for the system defined by the Currie criterion (ref) were determined by measuring the spectra of various standard reference materials. The results obtained for a home brew of various elements at the 10 parts per million (wet weight) level dispersed in a 20-micrometer slice of gelatin is shown in Figure 3. The conditions for the irradiation are shown in the figure. The minimum detection limits extracted from this data are shown in Figure 7.

The x-ray microscope (XRM) has been used for many investigations in the biomedical and earth sciences. A specific example to illustrate how it can be used is the work on trace element distributions in the rat brain by Kwiatek et al. (19) In this investigation measurements were made of trace elements in the brain for control animals and for animals that had ingested varying amounts of lead. It is known that lead is a toxic element and that it changes the function of the brain. Changes and interactions in the trace element distributions can thus be expected to occur. It is impossible to make

measurements at very low concentration levels with good resolution by other techniques than PIXE (proton-induced x-ray emission) so that the PIXE should be a truly quantitative improvement in the tools available to the biologist.

The concentration of iron in the rat cerebellar cortex can be taken as a specific example from the above work on the rat brain. Figure 8 shows a conventional photomicrograph of a coronal section of the cerebellar cortex. Structures in the cortex called the molecular and granule cell layers and the white matter tract are indicated. Figure 9 is a photograph taken at higher resolution that shows more details of the three regions. Figure 10 shows a portion of a 30 x 40 pixel map of the iron distribution found in the same region shown in Figure 9. Each pixel was 100 micrometers on a side. White represents highest iron concentrations and black represents the lowest. The three pronged region in white, (iron concentration is high), corresponds to the fiber tract region. This experiment will be part of the Ph.D. thesis to be submitted to the Institute of Nuclear Physics in Cracow by W. M. Kwiatek.

Future Direction in Atomic Physics

Recently there has been much interest in building storage rings for heavy ions. The advantage of the storage ring is that the effective ion current is enhanced because of the high characteristic revolution frequency of the ions in the ring. It seems to be feasible to fill a ring with around 10^{10} ions and to get effective currents close to 10^{16}/s. The interaction rates that are produced will then be many orders of magnitude greater than if experiments were done with ordinary types of ion sources. Rings to date have been proposed for study of electron- ion or ion-ion (or atom) collisions.

We have proposed (11,14) building a storage ring at the NSLS so that it would be possible to do precision photon excitation and ionization experiments using synchrotron radiation. Experiments using electron and ion beams as probes would also be done.

The science that could be done at this facility would cover many crucial areas of atomic physics. A first discussion of the topic has been published (14). Perhaps the most important point to make at this time is to establish the luminosities that are achieved in various types of beam experiments. A tabulation is given in Table 1 taken from Ref. 14. This shows that the storage ring will substantially extend the range of feasible experiments that can be done in investigating the properties of multiply-charged ions.

The ring requires an elaborate ion source for best operation. At BNL we are fortunate to have a powerful three- stage Tandem facility to use as an injector. These machines produce heavy ions with energies in the region of several hundred MeV and with charge states from fully stripped around Z = 22 to about 50% stripped at lead or gold.

The geographical layout of the proposed ring at BNL is shown in Figure 11 to show how the existing photon and ion facilities can be used to feed the storage ring. A detailed design study for the ring is now in progress.

Future Direction in Applied Physics

A great need in the Applied Physics Program is the development of new methods for characterizing materials at spatial resolutions around 1 micrometer or less. Prospects for doing this by x-ray imaging seem to be limited by the difficulty encountered in the production of focussing x-ray

optics of high quality. Thus, it is necessary to consider other types of approach to the problem.

A possible approach seems to be to adopt the methods of electron microscopy to the problem. In this case the x rays would be focussed as tightly as possible so that a spot with as high an x ray flux is formed. Rather than raster a target past this x ray beam in order to form an image it is possible to image the electrons produced in the irradiated area by using electron microscopy techniques. Focussing and imaging of electrons is a well studied problem that can easily be used at sub-micrometer resolutions. The field of photoelectron microscopy has been reviewed by Griffith (20). The high flux of synchrotron photons may now make it feasible to use electron spectroscopy/microscopy methods with high spatial resolution.

Professor A. Z. Hrynkiewicz has worked with the BNL group during several visits on the development of some of these ideas. What we propose to do is adapt (21) a Siemens ELMISCOP IA transmission electron microscope for use at the synchrotron. In order to do this we discard the first sections of the machine that are used to form the electron beam. The synchrotron beam is then used to irradiate a sample at approximately the normal position. Electrons that are emitted are focussed with an immersion type lens and that produces an object for the remainder of the microscope. The imaged electrons can then be detected with a position sensitive microchannel plate array and the image stored in a computer for final enhancement and analysis.

Additional analysis of the electron optics will be done before going further with the project. The addition of electron energy analysis is desirable and a more refined analysis of the production rates and backgrounds would also be helpful. The results of our first assessment are very

encouraging and we have hopes that we will be able to make images at the 100 nm resolution level with this instrument sometime in the future.

Conclusions

It is hoped that the material presented here will give some idea of the scope of work that the BNL Division of Atomic and Applied Physics is carrying out in atomic and applied physics using synchrotron radiation. Most importantly, we hope that the reader will feel the scientific content of the field is large and the questions to be answered important.

References

1. A. L. Hanson, H. W. Kraner, K. W. Jones, B. M. Gordon, R. E. Mills, and J. R. Chen. Trace element measurements with synchrotron radiation. IEEE Trans. Nucl. Sic. NS-30, 1339-1342 (1983).

2. B. M. Gordon. Uses of synchrotron radiation. NeuroToxicology 4, 13-22 (1982).

3. J. R. Chen, N. Martys, E. C. T. Chao, J. A. Minkin, C. L. Thompson, A. L. Hanson, H. W. Kraner, K. W. Jones, B. M. Gordon, and R. E. Mills. Synchrotron radiation determination of elemental concentrations in coal. Nucl. Instrum. Methods 32, 241-245 (1984).

4. B. M. Gordon and K. W. Jones. Design criteria and sensitivity calculations for multielemental trace analysis at the NSLS x-ray microprobe. Nucl. Instrum. Methods B3, 241-245 (1984).

5. A. L. Hanson, K. W. Jones, B. M. Gordon, J. G. Pounds, W. M. Kwiatek, G. J. Long, M. L. Rivers, and S. R. Sutton. Trace element measurements using white synchrotron radiation. Nucl. Instrum. Methods B24/25, 400-404 (1987).

6. P. Spanne and M. L. Rivers. Computerized microtomography using synchrotron x rays. Nucl. Instrum. Methods B24/25, 1063-1067 (1987).

7. S. R. Sutton, M. L. Rivers, and J. V. Smith. Applications of x-ray fluorescence to extraterrestrial materials. Nucl. Instrum. Methods B24/25, 405-409 (1987).

8. K. W. Jones, B. M. Gordon, A. L. Hanson, W. M. Kwiatek, and J. G. Pounds. X-ray fluorescence with synchrotron radiation. Ultramicroscopy, in press.

9. R. D. Glauque, A. C. Thompson, J. H. Underwood, Y. Wu, K. W. Jones, and M. L. Rivers. Measurement of femtogram quantities of trace elements using an x-ray microprobe. Proc. 36th Ann. Denver Conf. on Applications of X-Ray Analysis, Denver, Aug. 1987, to be published.

10. J. R. Chen, E. C. T. Chao, J. A. Minkin, J. M. Back, W. C. Bagby, M. L. Rivers, S. R. Sutton, B. M. Gordon, A. L. Hanson, and K. W. Jones. Determination of the occurrence of gold in an unoxidized Carlin-type ore sample using synchrotron radiation. Nucl. Instrum. Methods B22, 394-400 (1987).

11. K. W. Jones, B. M. Johnson, and M. Meron. Design considerations for a combined synchrotron-light source and heavy-ion storage ring atomic physics facility. Nucl. Instrum. Methods B24/25, 381-390 (1987).

12. K. W. Jones, B. M. Johnson, J. B. Hastings, M. Meron, V. O. Kostroun, and T. H. Kruse. Studies of ion beam photon interactions at the National Synchrotron Light Source. IEEE Trans. on Nucl. Sci. NS-30, 1026-1029 (1983).

13. B. M. Johnson, M. Meron, A. Agagu, and K. W. Jones. Atomic physics and synchrotron radiation: the production and accumulation of highly-charged ions. Nucl. Instrum. Methods B24/25, 391-396 (1987).

14. K. W. Jones, B. M. Johnson, M. Meron, B. Crasemann, Y. Hahn, V. O. Kostroun, S. T. Manson, and S. M. Younger. Science with synchrotron radiation and a heavy-ion storage ring. Comm. At. Mol. Phys. 20(1), 1-18 (1987).

15. K. W. Jones, B. M. Johnson, and M. Meron. PHOBIS, A PHOton Beam Ion Source for production of multiply-charged atoms. Phys. Lett. 94A, 377-380 (1983).

16. D. A. Church, S. D. Kravis, I. A. Sellin, C. S. O, J. C. Levin, R. T. Short, M. Meron, B. M. Johnson, and K. W. Jones. Studies of confined thermal multi-charged ions produced by synchrotron radiation. Phys. Rev. Lett., submitted.

17. R. T. Short, C. S. O, J. C. Levin, I. A. Sellin, B. M. Johnson, M. Meron, K. W. Jones, and D. A. Church. Synchrotron radiation inner-shell photoionization of atomic and molecular gases. Nucl. Instrum. Methods B24/25, 417-419 (1987).

18. M. Meron, B. M. Johnson, K. W. Jones, and D. A. Church. Prospects for experiments with trapped multi-charged ions produced by VUV synchrotron radiation. Proc. Symposium on Atomic Spectroscopy and Highly-Ionized Atoms (SASHIA), Hickory Ridge, Illinois, Aug. 1987, to be published.

19. W. M. Kwiatek, G. J. Long, K. R. Reuhl, A. L. Hanson, K. W. Jones, and J. G. Pounds. Distribution of Fe, Cu, Zn, and Hg in the mouse cerebellum. Toxicologist 7(1), 302a (1987).

20. O. Hayes Griffith and Gertrude F. Rempfer. Imaging: photoelectron microscopy and related techniques, in Advances in Optical and Electron Microscopy, Vol. 10, R. Barer and V. E. Coslett, eds. (Academic Press, London).

21. W. Engel. Proc. 6th Intern. Congress Electron Microscopy, Kyoto, 1968, pp. 217-218.

Table II. Luminosities of photon-ion/atom interactions using 0.1% bandwidth synchrotron radiation with a photon current at the target of about $5 \cdot 10^{15}$ photons/s, which is based on design parameters of the NSLS for a 5-pole superconducting wiggler, assuming 5 mr horizontal acceptance and full vertical acceptance.

System	Luminosity ($cm^{-2}\ s^{-1}$)
Gas target (pressure = 10^{-6} torr)	$1.76 \cdot 10^{26}$/(cm length)
Singly-charged ion source (10 keV energy, 10 μA current)	$1.4 \cdot 10^{23}$ (for crossed beams of 1 mm height) $1.4 \cdot 10^{23}$/(cm merging length)(0.1 cm^2 beam area) $1.4 \cdot 10^{22}$/(cm merging length)(1 cm^2 beam area)
Kingdon Ion Trap (PHOBIS, see Ref. 22)	$5 \cdot 10^{22}$/(cm length)
ECRIS and EBIS (100 pnA, 10 keV/amu, for Ar^{+17})	$2.2 \cdot 10^{20}$ (for crossed beams of 1 mm height) $2.2 \cdot 10^{20}$/(cm merging length)(0.1 cm^2 beam area) $2.2 \cdot 10^{19}$/(cm merging length)(1 cm^2 beam area)
CHISR (10 MeV/nucleon)	
For $(\frac{\Delta p}{p}) = 10^{-2}$ (No point in bunching because space charge limit is exceeded)	
$N = 1.2 \cdot 10^{10}$ (Ar^{+17})	$2 \cdot 10^{22}/cm^2$ (1 cm merging length, 1 cm^2 area)
For $(\frac{\Delta p}{p}) = 2 \cdot 10^{-3}$	
$N = (8 \cdot 10^{8})$	$1.3 \cdot 10^{21}$ unbunched $1.6 \cdot 10^{22}$ bunched

Figure Captions

Figure 1. NSLS photon flux at the experimental position 20 m from the electron orbit. Units for the flux are shown at the top of the figure and are in photons/s/mA/eV/mm^2. The electron energy is 2.52 GeV. The curves show the effect of beryllium windows that are incorporated in the beam line and of additional aluminum filters that are used to harden the beam for specific experiments.

Figure 2. Plan and elevation views of the beam line showing the simplicity of the design and the in-line arrangement that makes it possible to do two experiments simultaneously.

Figure 3. Composite figure showing photographs of the experimental area. At the top left an overall view is given of an atomic physics experiment (a Penning ion trap in this case) and the x-ray fluorescence apparatus at the right. The photograph at the lower left shows a view of the details of the x-ray fluorescence apparatus. The figures at the right show x-ray fluorescence spectra obtained for a gelatin standard containing elements at the 10 parts-per-million (wet weight) level and from a thin section of kidney. Additional details are given for each spectrum in the figure.

Figure 4. Fluorescence spectrum recorded in the wave length region from 500 to 1500 A. The radiation was emitted following K-shell ionization using filtered synchrotron radiation (see Figure 1), (Ref. 13).

Figure 5. Distribution of charge states in argon following K-shell ionization using filtered synchrotron radiation. The ions were observed in a Penning ion trap (Ref. 16).

Figure 6. Distribution of charge states in argon following K-shell ionization using filtered synchrotron radiation. The ions were observed using a time-of-flight technique (Ref. 16).

Figure 7. Minimum detection limits determined for trace elements in a 20-micrometer thick gelatin standard. Values are normalized to an electron current of 77 mA, target area of 2.5×10^{-5} cm^2, and counting time of 300 s.

Figure 8. Photomicrograph of a coronal section of the rat cerebellar cortex. Features of interest and a scale are indicated in the photograph.

Figure 9. Photomicrograph of a small section of the ceronals ection of rat cerebellar cortex shown in Figure 8. The size and features are shown on the figure.

Figure 10. Distribution of iron in the cerebellar cortex in the region approximately the same as that shown in the photomicrograph of Figure 9. The light pixels show a higher concentration in the region of the fiber tract.

Figure 11. Map of Brookhaven National Laboratory showing the location of the National Synchrotron Light Source, Tandem Accelerator Laboratory, and the proposed heavy-ion storage ring. The length of the tunnel from the Tandem Laborstory to the storage ring is about 140 m.

X26C Beamline, photons sec^{-1} mA^{-1} eV^{-1} mm^{-2}

Vert. ang.	.05	Radius (m)	6.87	Horiz. ang (mr)	.05
Scale	1	Current (mA)	1	Bandwidth (eV)	
Energy (GeV)	2.52	n poles	1		

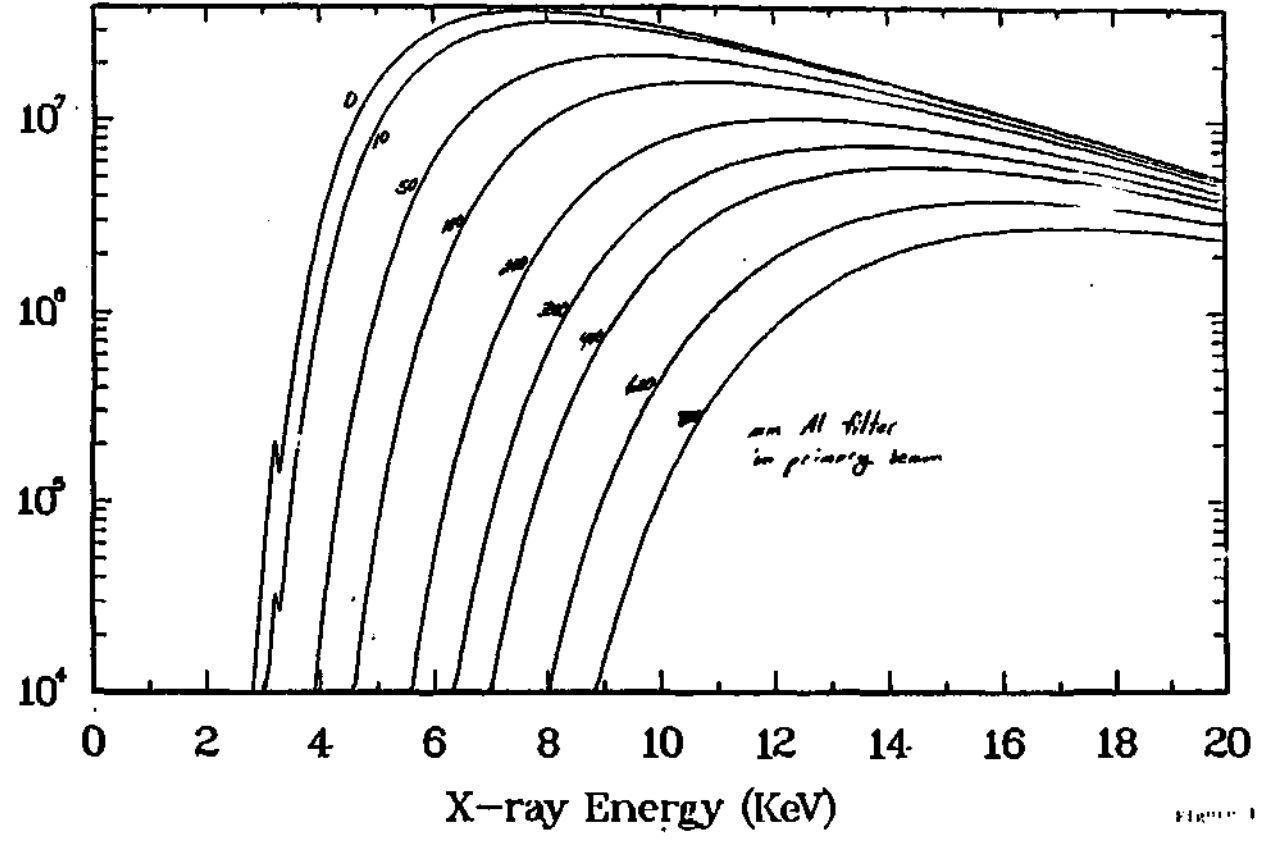

Figure 1

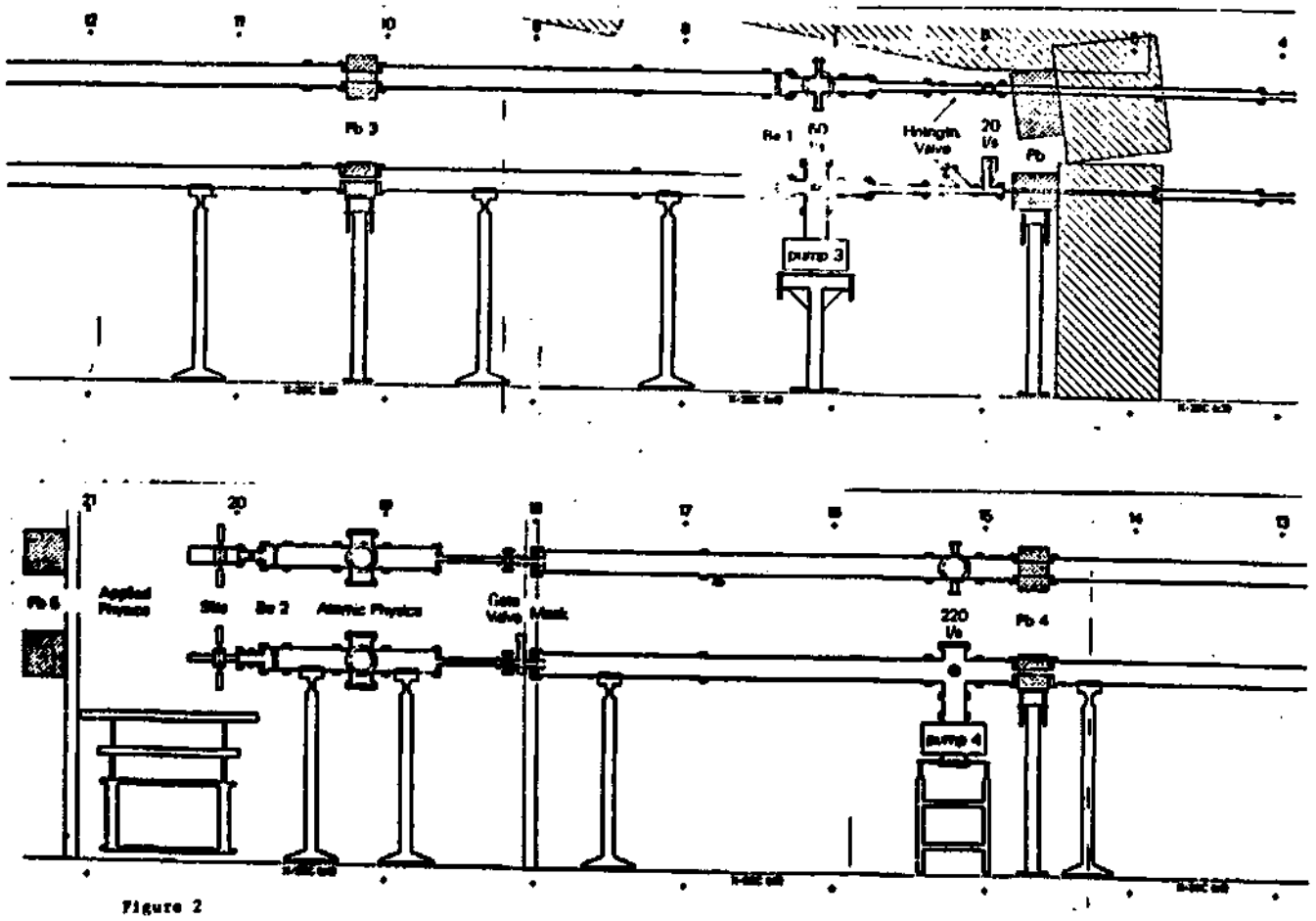
Pb 3
Be 1
60 l/s
Hastings Valve
20 l/s
Pb
pump 3
Applied Physics
Be 2
Atomic Physics
Gate Valve
Mask
220 l/s
Pb 4
pump 4

Figure 2

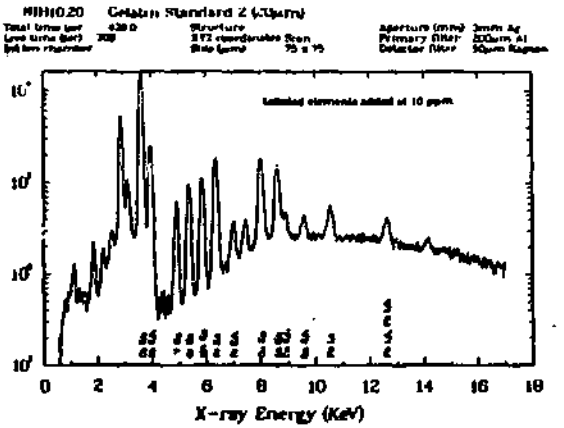
X-ray Energy (KeV)

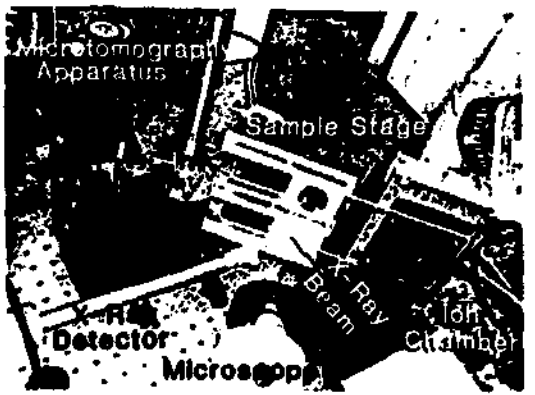
Microtomography Apparatus
Sample Stage
X-Ray Beam
Ion Chamber
X-Ray Detector
Microscope

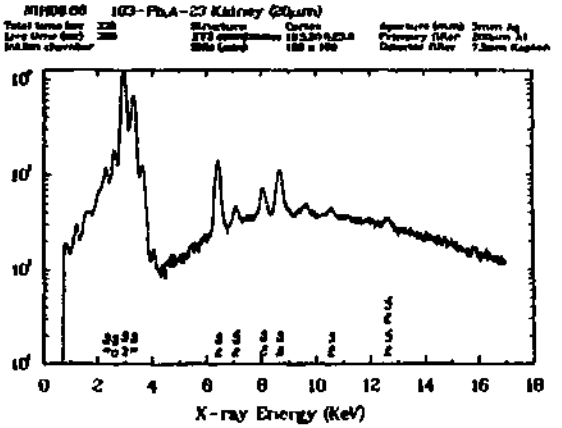
X-ray Energy (KeV)

Figure 3

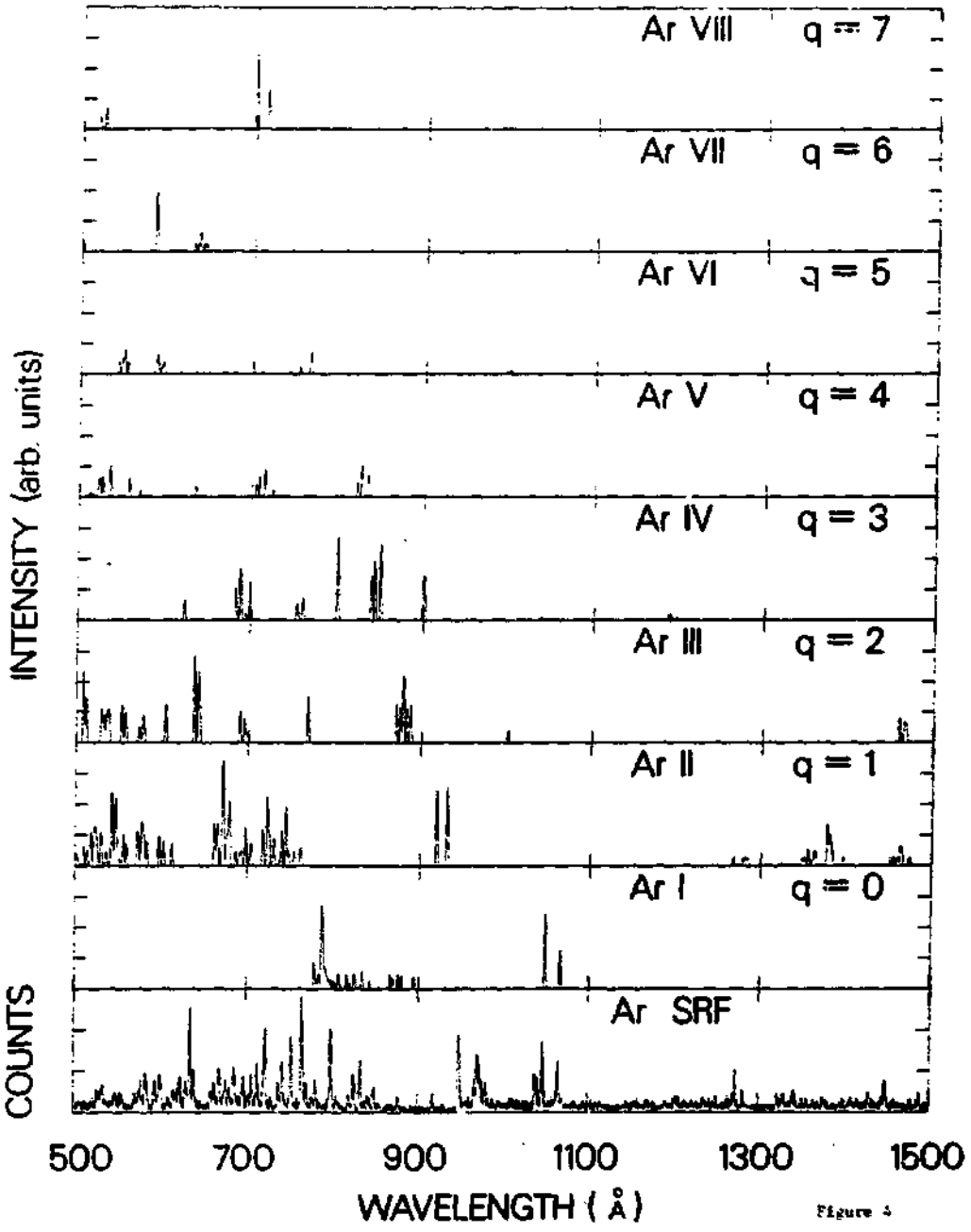
Ar VIII q = 7
Ar VII q = 6
Ar VI q = 5
Ar V q = 4
Ar IV q = 3
Ar III q = 2
Ar II q = 1
Ar I q = 0
Ar SRF
INTENSITY (arb. units)
COUNTS
500
700
900
1100
1300
1500
WAVELENGTH (Å)

Figure 4

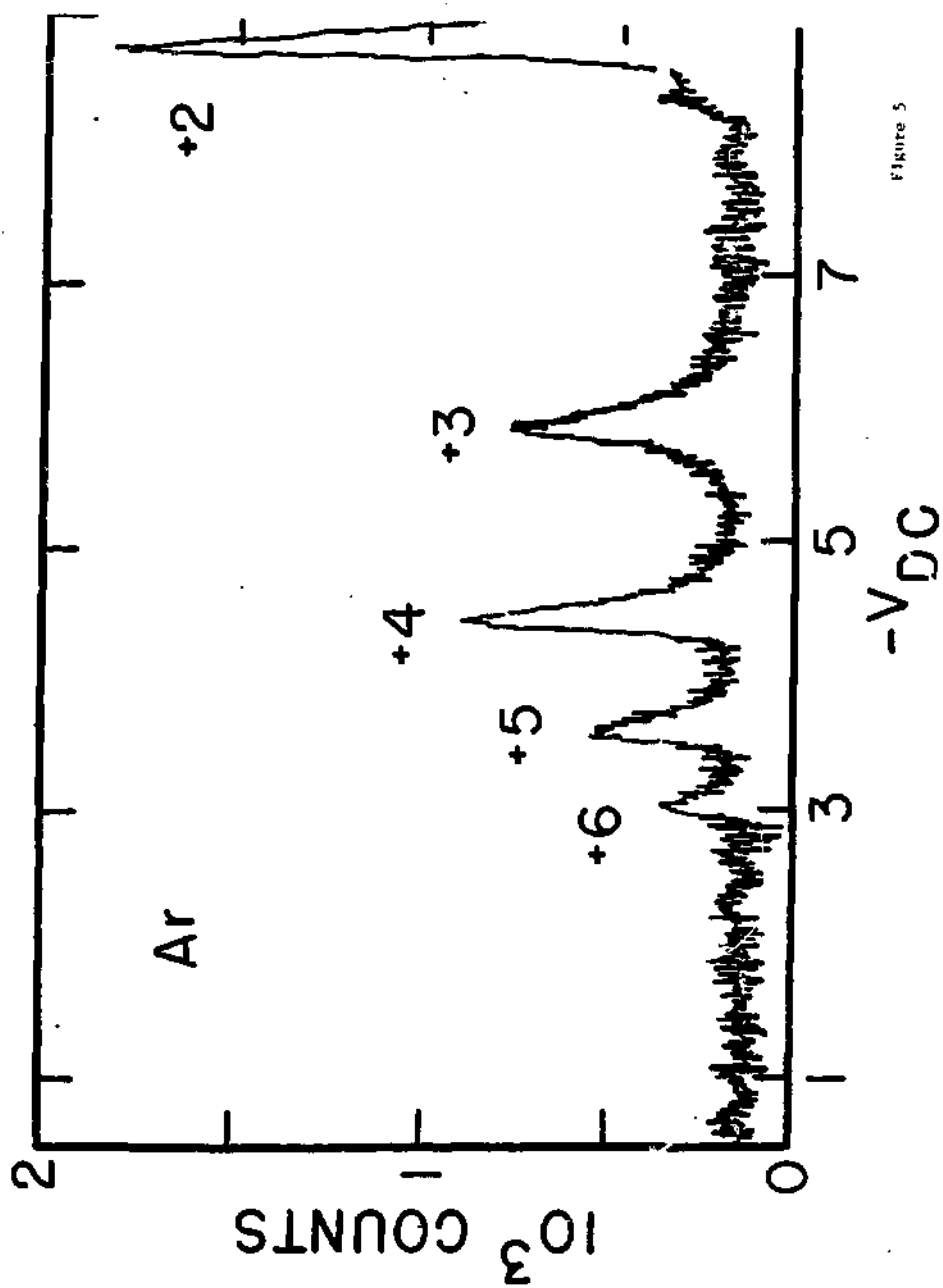

Figure 5

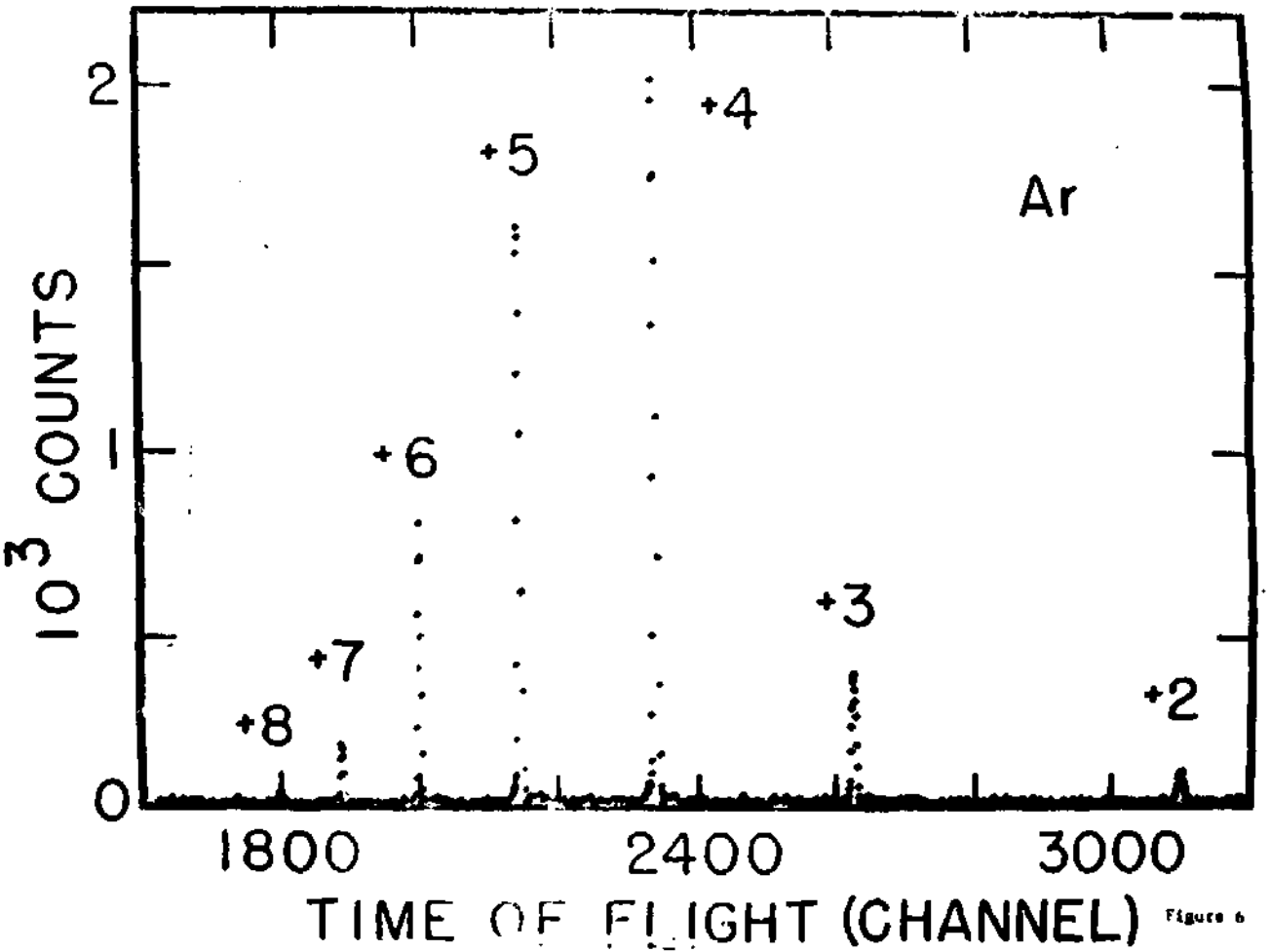
2
1
0
10^3 COUNTS
+4
+5
Ar
+6
+3
+7
+8
+2
1800
2400
3000
TIME OF FLIGHT (CHANNEL)

Figure 6

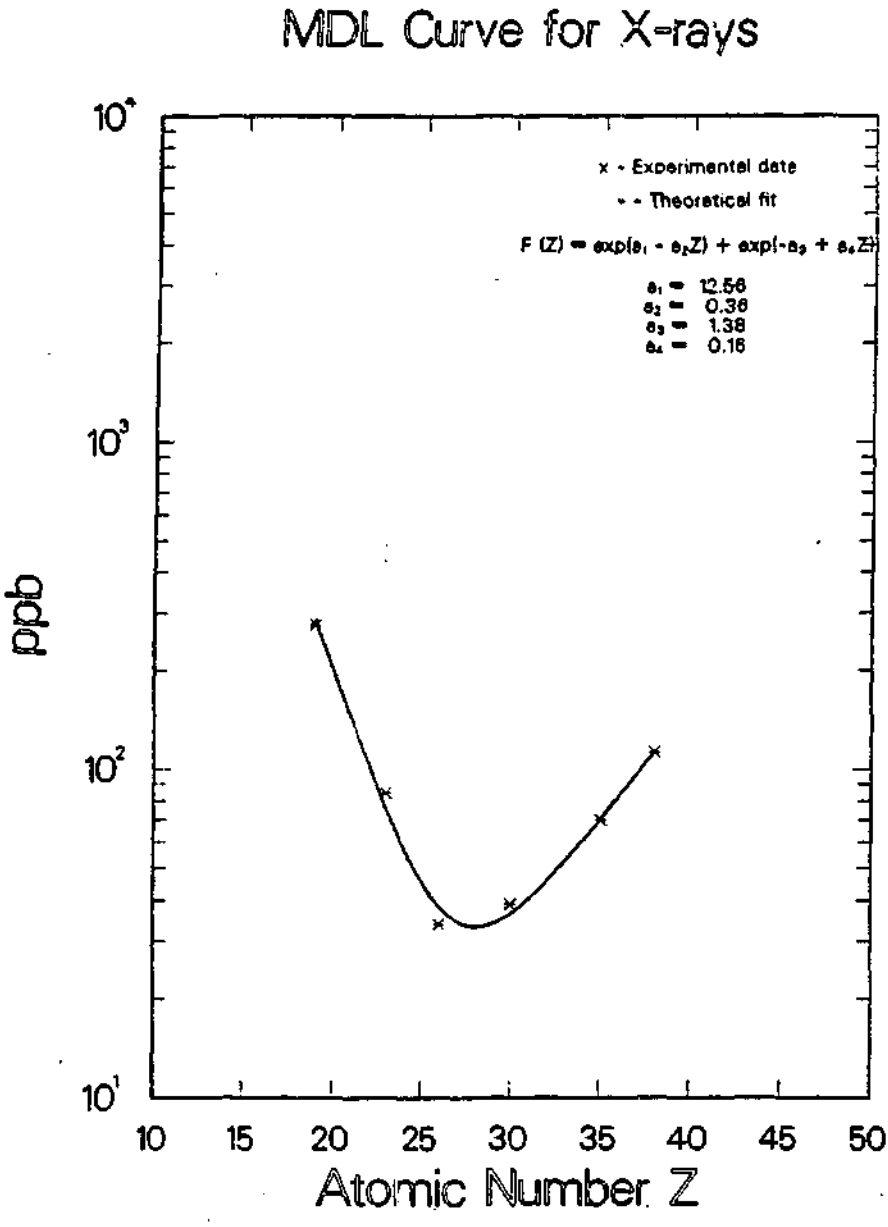
MDL Curve for X-rays
x - Experimental date
- - Theoretical fit
F (Z) = exp(a1 - a2Z) + exp(-a3 + a4Z)
a1 = 12.56
a2 = 0.36
a3 = 1.38
a4 = 0.16
ppb
10^4
10^3
10^2
10^1
10
15
20
25
30
35
40
45
50
Atomic Number Z

Figure 7

Figure 8

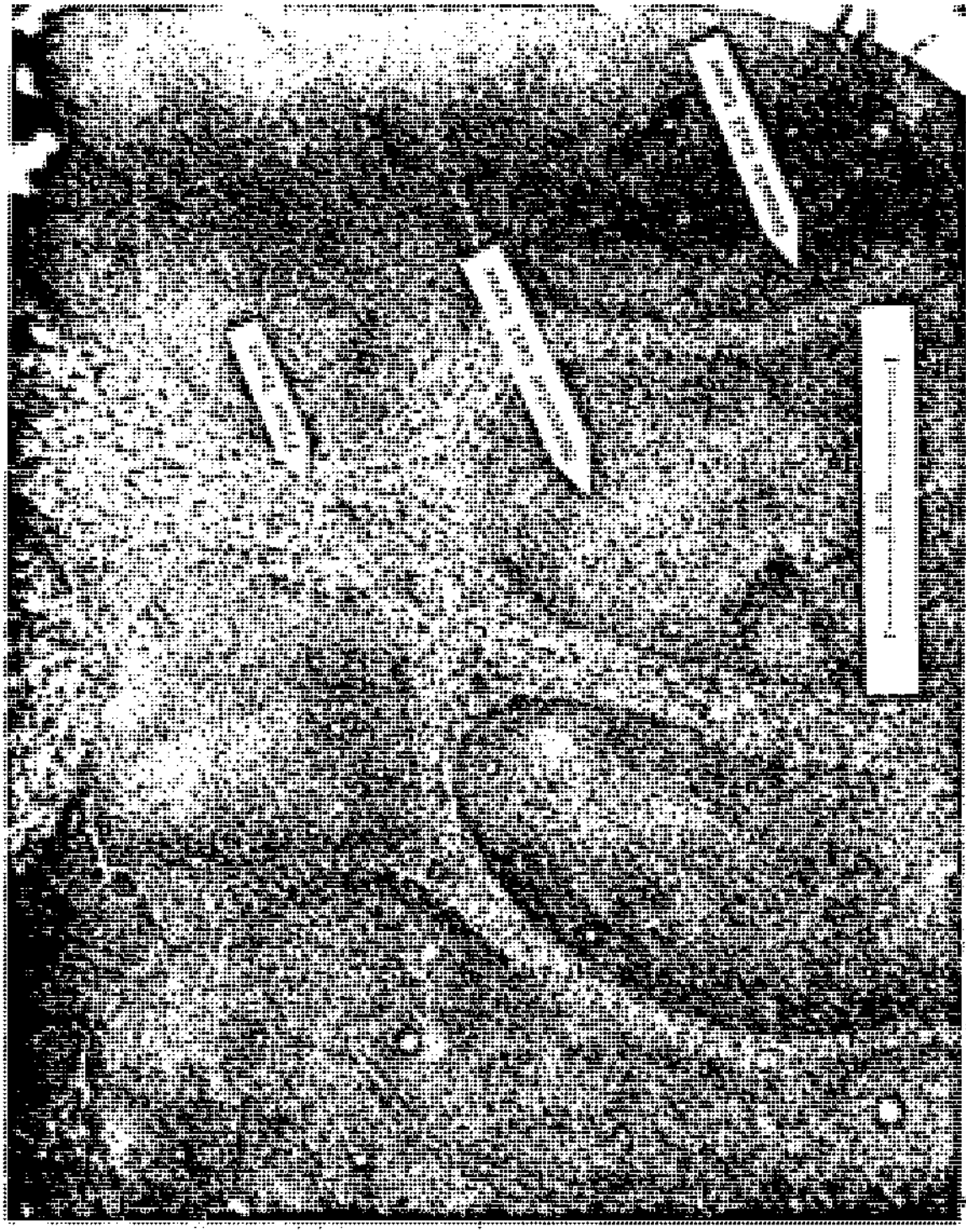

Figure 9

Figure 10

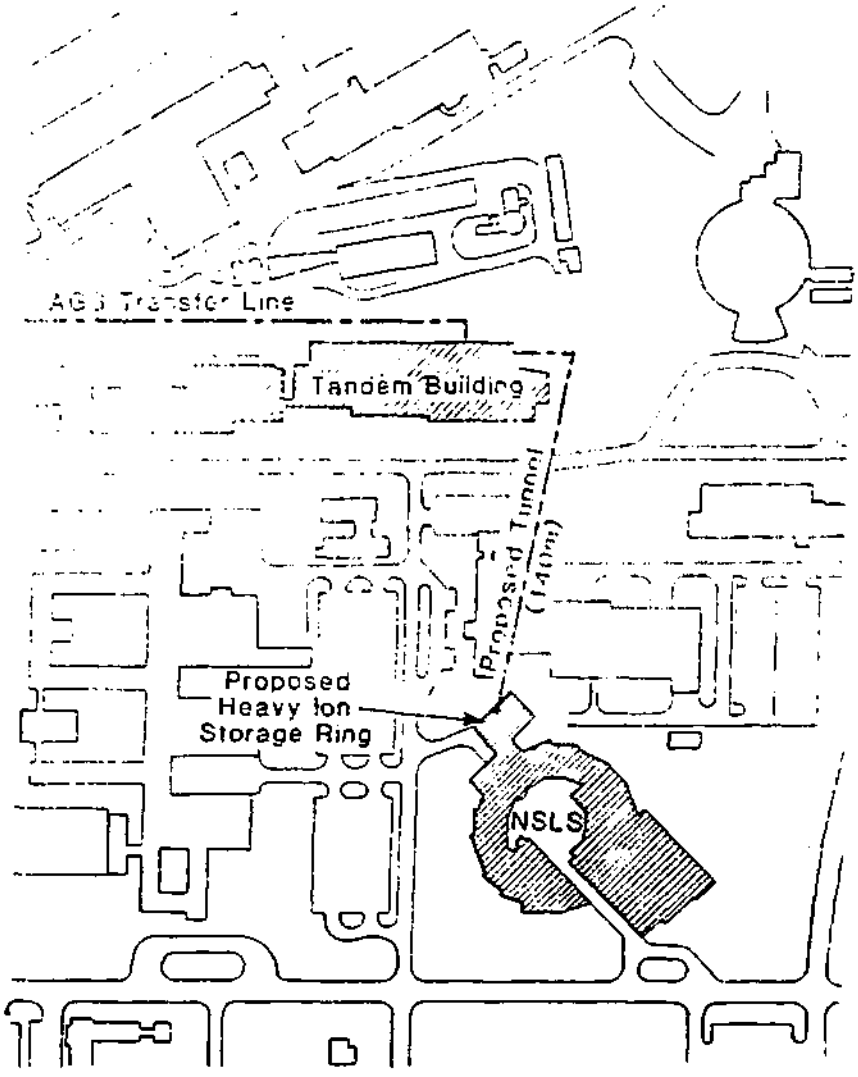
AGS Transfer Line
Tandem Building
Proposed Tunnel
Proposed
Heavy Ion
Storage Ring
NSLS

Figure 11

LIST OF GIVEN LECTURES NOT PUBLISHED IN PROCEEDINGS

1. LOW TEMPERATURE NUCLEAR ORIENTATION
   M. Finger
2. APPLICATIONS OF DEPTH - SELECTIVE CONVERSION ELECTRON MÖSSBAUER SPECTROSCOPY IN MATERIALS SCIENCE
   W. Keune
3. FIELD GRADIENTS AND KNIGHT SHIFTS IN SIMPLE METALS
   H. Haas
4. PRESSURE INDUCED MAGNETIC PHASE TRANSITIONS IN Fe - INVAR ALLOYS
   M.M. Abd-Elmeguid
5. RARE EARTH IONS AS LOCAL PROBES FOR AMORPHOUS STRUCTURES
   G. Czjzek

SEMINARS

LIST OF SEMINARS

MAGNETOSTATIC AND MÖSSBAUER INVESTIGATION OF MAGNETIC PROPERTIES OF $Fe_{3-x}V_xAl$ ALLOYS WITH DO_3 TYPE STRUCTURE
E. Popiel, M. Tuszyński, W. Zarek 285

CONVERSION ELECTRON MÖSSBAUER SPECTROSCOPIC STUDY ON PHOSPHORUS IMPLANTED IRON
H. Reuther 290

LOCAL STRUCTURE IN MELT-SPINNING Cu-Fe ALLOYS
T.J. Panek, G. Barton 293

THE LOCALISATION OF DISPLACED ATOMS BY BACKSCATTERING OF PLANAR CHANNELED IONS FOR SMALL DEPTH
J. Czerbniak, M. Moneta, D. Pawłowski 296

SYNCHROTRON RADIATION AND ITS APPLICATION
V.I. Raiko 299

LOCAL MAGNETOCRYSTALLINE ANISOTROPY IN $/Y_{1-x}Nd_x/_2Co_{14}B$ COMPOUNDS OBSERVED BY NMR
H. Figiel

LIST OF POSTERS

INFLUENCE OF HIGH PRESSURE THE HYPERFINE INTERACTION PARAMETERS IN LAVES PHASE COMPOUNDS: $/Y_{0.9}Hf_{0.1}/Fe_2$ AND $/Zr_{0.9}Hf_{0.1}/Fe_2$
M. Budzyński, M. Subotowicz, H. Niezgoda, H. Spustek, W. Tanska-Krupa and R. Wasiewicz 302

THE ROLE OF PIXE AND PIGE MEASUREMENTS IN GEOLOGICAL STUDIES
S. Szymczyk, J. Kajfosz, E. Dutkiewicz 305

ZX SPECTRUM - AN INTELLIGENT TERMINAL FOR A MÖSSBAUER 2331 SPECTROMETER IN A CAMAC SYSTEM
J. Holeczek, E. Popiel 310

HYPERFINE FIELDS AND SPIN POLARIZATION OF Ce IN $GdAl_2$ AND $DyAl_2$

E. Wäckelgård, E. Karlsson, B. Lindgren, A. Mayer, A. [illegible] Lewicz

MÖSSBAUER STUDY OF [illegible]

M. Chocázy, [illegible] Nieczyński, T.J. Panek

Magnetostatic and Mössbauer Investigation of Magnetic Properties of $Fe_{3-x}V_xAl$ alloys with DO_3 Type Structure.

E. Popiel; M. Tuszyński; W. Zarek
Institute of Physics-Silesian University Katowice

The ternary $Fe_{3-x}V_xAl$ alloys were prepared by arc melting of stoichiometric quantities of Fe,V and Al in an argon atmosphere. After melting and powdering of the ingots, a special, long-time thermal treatment was used for obtaining a DO_3 type structure of the sample.

X-ray studies for each sample were done and showed that this structure was obtained for samples with $0 \leq x \leq 1.1$ only. Samples with $1.1 < x \leq 1.5$ exhibited B_2 type structure while the samples with $x > 1.5$ exhibited A_2 type structure.

In further part of this seminar I want to show the results from magnetostatic and Mossbauer measurements for samples with $0 \leq x \leq 0.65$ only.

The ideal DO_3 type structure for binary alloy of Fe_3Al is shown in Fig.1, where 4a and 8c sites are occupied by Fe atoms only when 4b sites are occupied solely by Al atoms.

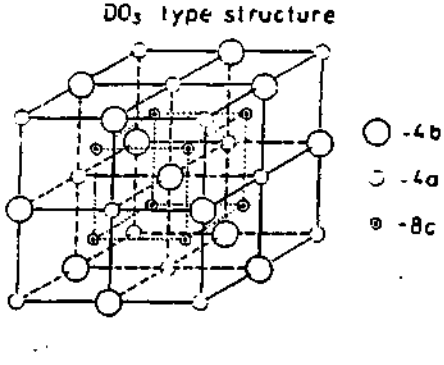

Fig. 1

This complicated structure can be described as a composition of four independent, fcc sublattices with the same lattice constant. In this ideal structure each Fe atom has eight other atoms as nearest neighbours (nn). Fe atom from 4a sites has eight other Fe atoms as nn (from 8c sites), while Fe atom from 8c site has four others Fe atoms (from 4a sites) and four Al atoms (from 4b sites) as nn [1,2]

The substitution of some Fe atoms in such structure by other 3d metal, nonmagnetic atoms can break magnetic interaction and change the magnetic structure of such substitutional ternary alloys. In our samples, V atoms were such nonmagnetic substitutes.

From precise x-ray studies, when the intensities of Bragg reflections were measured, the degree of DO_3 structure order and probabilities of occupation by Fe, V and Al atoms of sublattices 4a,4b,8c were

determined for each sample. When these probabilities are known, the distributions of the Fe atoms with different magnetic surroundings in nn shell can be calculated for each sample [3]. In the Fig.2 the probabilities for a few samples are given in the table. The distributions of the number of Fe atoms with different numbers of other Fe atoms in nn shell, calculated from binomial formula [3] are shown on the left side of Fig.2.

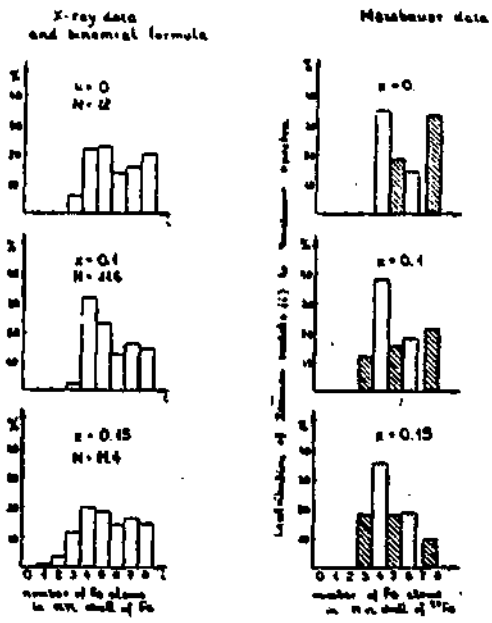

Fig. 2

The magnetic properties of Fe atom in the alloys strongly depend on the numbers of other magnetic atoms in its nn shell.

Magnetostatic and Mossbauer investigations of the magnetic properties of $Fe_{1-x}V_xAl$ alloys ($0 \le x \le 0.6$) showed that V atoms play an important role in the disordering of the magnetic structure of these alloys.

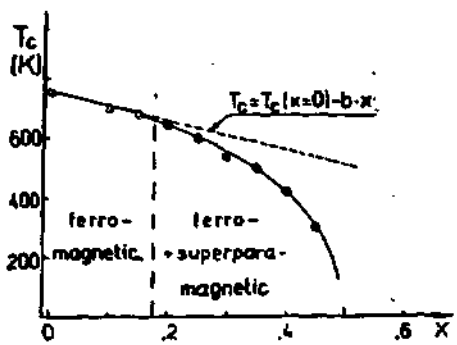

Fig. 3

This sample group can be divided into the two subgroups, if the magnetic behaviour of these alloys is studied. Those alloys with low V concentration ($x < 0.8$) behave as typical ferromagnetic bodies. The Curie temperature (T_C) of these alloys decreases linearly with the increase of x (left side of Fig.3) which suggests that V atoms do not have a local magnetic moment and are diluted as paramagnetic atoms in these alloys.

The Mossbauer absorption spectra, measured at room temperature(RT) for low V concentration samples, are shown in Fig.4. Each of these spectra is the superposition of several Zeeman sextets. The distri-

bution of these sextets is drawn schematically above each spectrum. On the right side of Fig.2 are shown the contributions of each Zeeman sextet to the spectra. It is seen that with increasing of x the contribution of the so-called " 7-8 nn sextet " decreases, suggesting that V atoms have a slight site-preference for 8c sites, normally occupied by Fe atoms. In Fig.3, the H_{hf} intensities, corresponding to each sextet, as the function of V concentration, are shown. The values of these H_{hf} suggest which number of Fe atoms in nn shell of ^{57}Fe are responsible for each Zeeman sextet [4].

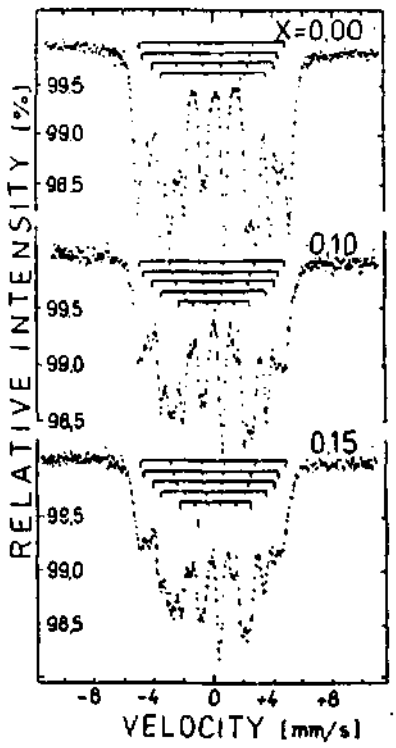

Fig. 4

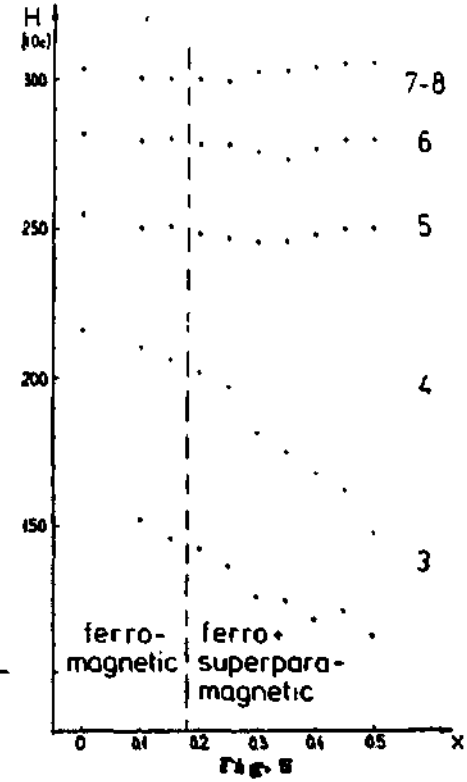

Fig. 5

For alloys with higher V concentrations (0.2 ≤x≤ 0.5) the magnetic behaviour of the samples is much more complicated. The T_C for these alloys decreases nonlinearly with the increase of x (right side of Fig.3).

As an example of magnetostatic results for this group of samples, magnetization for $Fe_{2.6}V_{0.4}Al$ alloys, as a functions of temperature and magnetic field intensity (insert) are given in Fig.6. The rather high magnetization for temperatures above T_C indicates that in these samples "particles" with large magnetic moment exist. Moreover - for these temperatures the variation of magnetization with an external,

magnetic field intensity (insert) is strongly nonlinear, which indicates too, on the existence of "particles" with large, magnetic moments in the sample. In Fig.7 the evolution of Mossbauer spectra, measured at RT with the increase of V concentration is shown. Shapes of these spectra indicate that two phases coexist in these alloys.

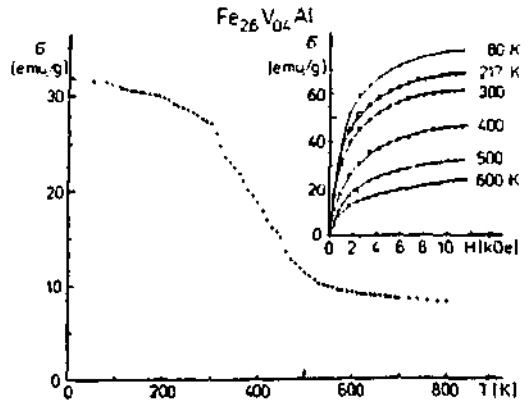

Fig. 6

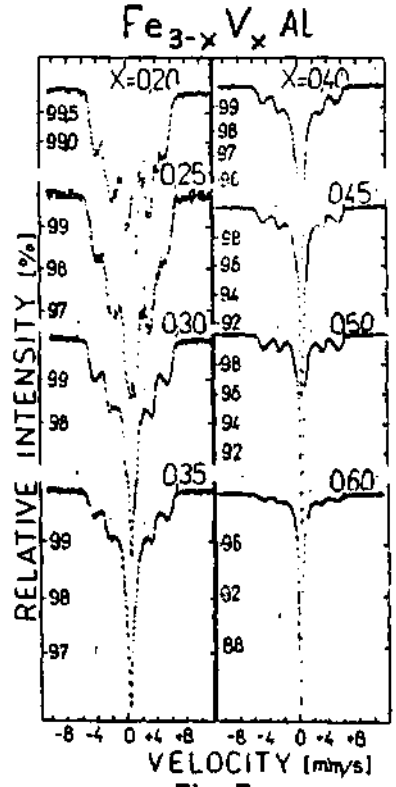

Fig. 7

Previous results suggest that one phase is ferromagnetic, where disorder grows with the increasing of x, - the second is superparamagnetic, which contains the "particles" with large, magnetic moments in the temperatures above T_C. The ferromagnetic phase for these spectra is presented by a multiline subspectrum. It can be resolved for the same number of Zeeman sextets, as the spectra for the samples with low V concentrations. The intensities of H_{hf} fields, corresponding to each sextet, are shown on the right part of Fig.4. The changes of H_{hf} fields with x are unusual for sextets, corresponding to ^{57}Fe probes with 3 and 4 other Fe atoms in the nn shell.

The superparamagnetic phase is presented at these spectra by a single broad, central line. The width of this line decreases with the increase of x, but the contribution of this line to the spectrum increase with increasing V concentration.

The contributions of the ferro- and superperamagnetic phases, obtained from the Mossbauer spectra, are shown in Fig.8. In magnetostatic measurements the alloy - x=0.8 is considered as a pure superparamagnetic phase, while in Mossbauer measurements, the ferromagnetic

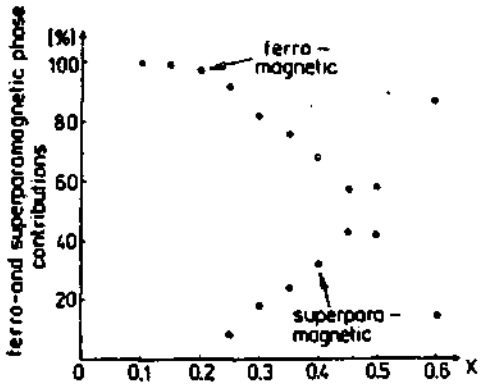

Fig. 8

phase is visible in the samples where x is up to 0.8.

For the sample where x=0.6, one Mossbauer measurement at RT with perpendicular magnetic field (H=2.5 kOe) was taken. The multiline subspectrum - representing the ferromagnetic phase - changes a little but normally, like Zeeman sextet in perpendicular magnetic field.

The central, single line-representing the superparamagnetic phase decreases in the external field. From detailed calculation it follows that in this measurement, the contribution of superparamagnetic phase decreases from 86% (without field) to 69% . This may suggest that in this magnetic field the greatest clusters, whose large magnetic moments flip slowly, are stabilized, giving the contribution to the ferromagnetic phase.

The work was partly supported by the Institute of Physics, Polish Academy of Sciences.

References:

[1]- H. Okamato; P.A.Beck; Met. Trans. 8,568 (1971)
[2]- W.B. Pearson; Handbook of Lattice Spacing and Structures of Metals and Alloys. vol. 2, p.681 (Pergamon Press, London 1967)
[3]- W. Cable; L. David; R. Parra; Phys. Rev.,B16,1132 (1977)
[4]- P. A. Beck; Met. Trans., 8, 2015 (1971).
J. Less Common Metals.28, 193 (1972)

CONVERSION ELECTRON MÖSSBAUER SPECTROSCOPIC STUDY ON PHOSPHORUS IMPLANTED IRON

H. Reutner
Central Institute of Nuclear Research Rossendorf of the Academy of Sciences of the GDR
Post Box 19, Dresden, 8051, GDR

In recent years ion implantation has been established as a method of surface improvement of metals.
Implantation of phosphorus in steel results in an improved corrosion behaviour attributet to the formation of an amorphous or microcrystalline layer as a consequence of the high energy deposition during implantation [1]. By the aid of the conversion electron Mössbauer spectroscopy it is possible to get informations on the structure of the implanted layers. First results were presented in [2] and this paper is the progress report.
Implantation of phosphorus in iron can result either in the embedment of the implanted ion on interstitial sites or in the amorphization of the disturbed range or in the formation of iron phosphides.
The maximum solubility of phosphorus in iron is 4.52 %. Implantation doses of 1 to 5 * 10^{17} cm^{-2} phosphorus ions let increase the phosphorus content in the implanted region up to 33 atom %. Therefore the iron phosphides Fe_3P, Fe_2P, and FeP, single or together, are expected to form. Fe_3P is ferromagnetic, Fe_2P and FeP are paramagnetic at room temperature [3]. FeP possesses one, Fe_2P two and Fe_3P three identical iron sites [4]. Therefore the Mössbauer spectra of iron phosphides should consist of one quadrupole doublet for FeP, two quadrupole doublets for Fe_2P, and three six-line-pattern for Fe_3P.
Implantation was carried out on a research implanter. Implantation conditions are given in Table 1. The Mössbauer measurements were described in [2].

Table 1: Parameters for Phosphorus implantation in iron

Sample	Dose in cm^{-2}	Energy in keV	Current density in $\mu A/cm^2$	Vacuum in Pa
P1	1 * 10^{17}	50	6	~ 10^{-4}
P2	5 * 10^{17}	50	4	~ 10^{-4}
P3	1 * 10^{17}	100	4	< 10^{-4}
P4	5 * 10^{17}	100	5	< 10^{-4}
P5	1 * 10^{17}	200	5	< 10^{-4}
P6	5 * 10^{17}	200	5	< 10^{-4}

Fig. 1 shows the Mössbauer spectra of the phosphorus implanted iron samples. All spectra contain the six-line-pattern of alpha-iron. Its portion lies between 100 % for sample P1 and 47 % for sample P4, and the line width are remarkable greater than that obtained at standard alpha-iron.

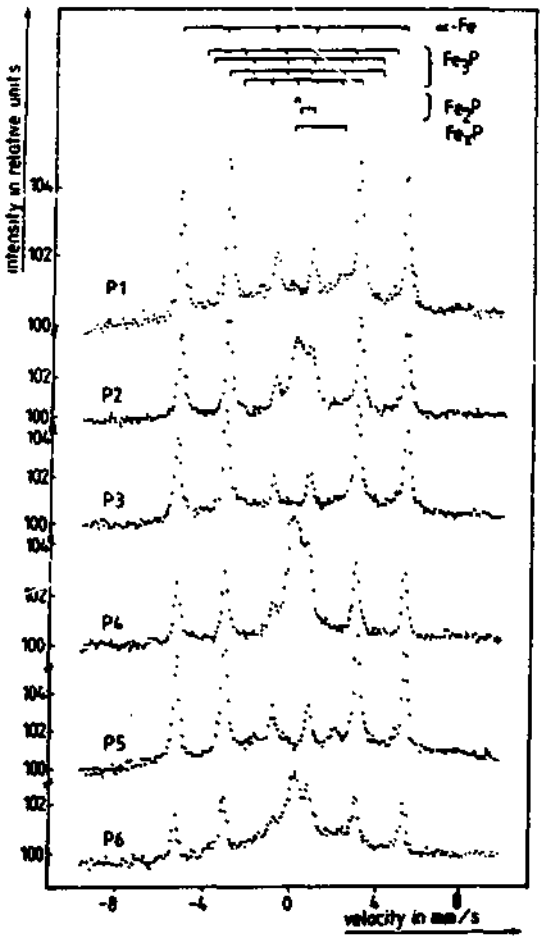

Fig. 1: Mössbauer spectra of phosphorus implanted iron

In sample P3 Fe_3P could be detected whereas the highly implanted samples P2, P4, and P6 contain Fe_3P. The lines of the two quadrupole doublets are very broad. In the spectrum of sample P5 a further magnetic component with a magnetic field of about 20.2 Tesla was found.

To study the crystallization effects all samples were annealed in a vacuum furnace for 1 h at subsequently increasing temperatures followed by a quick cooling and the Mössbauer measurement. The pressure during annealing was $1 \cdot 10^{-3}$ Pa and lower.

As an example for the highly implanted samples Fig. 2 shows the results obtained at sample P2. Up to 400 °C there is no general change in the components of the spectra. At 435 °C the lines of Fe_3P get narrower and at 468 °C the spectrum is completely transformed. The portion of Fe_3P is vanished, instead of it Fe_2P is formed. At 700 °C its portion begins to decrease.

Amorphous iron-phosphorus alloys are ferromagnetic, their Mössbauer spectra are sextets with very broad lines whose intensity properties strongly deverge from that of alpha-iron. The short range order of the metallic glasses is similar to the structure of Fe_3P [5]. Such portions only could be detected in the spectra of samples P1, P3, and P5. Samples implanted with $5 \cdot 10^{17}$ cm^{-2} phosphorus ions behave total otherwise. Besides the alpha-iron portion no further magnetic component, that is, no Fe_3P could be detected but instead of it amorphous portions whose structure by reason of their hyperfine parameters must be similar to Fe_3P. Annealing the samples a precipitation of Fe_3P takes place.

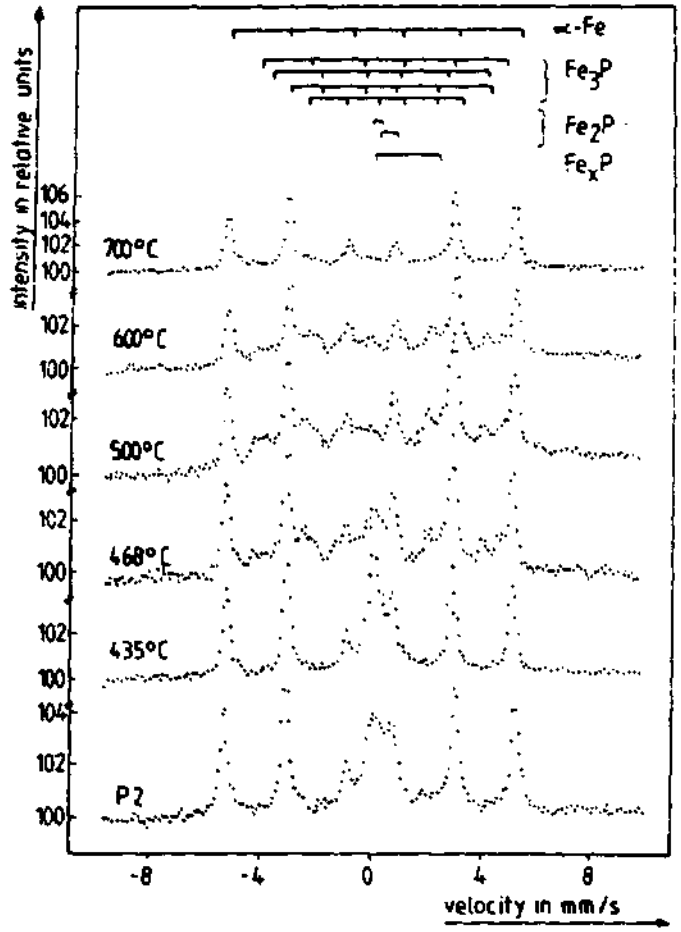

Fig. 2: Mössbauer spectra of the annealed sample P2

Between 400 °C and 500 °C the Fe_3P is converted into Fe_2P. The transformation is all at once without any coexistence between the two phosphides.

References

[1] C. R. Clayton et al., in: Ion Implantation Metallurgy, Ed. by C. M. Preece and J. K. Hirvonen, New York 1980, p.65
[2] H. Reuther, phys. stat. sol. (a) 93 (1986) 201
[3] O. Kubaschewski, Iron-Binary Phase Diagrams, Berlin 1982
[4] S. Rundquist, Ark. Kemi. 20 (1962) 67
[5] M. Eibschütz et al., J. Phys. E: Met. Phys. 14 (1984) 505

LOCAL STRUCTURE IN MELT-SPINNING Cu-Fe ALLOYS

T.J.Panek and G.Barton#

Institute of Physics & Chemistry of Metals, Silesian University, 40-007 Katowice, Bankowa 12, Poland
 # Adam Opel AG, Rüsselsheim, FRG

The Cu-Fe alloys have been extensively investigated and the iron atoms in solid solution Cu-Fe, Fe in coherent f.c.c. precipitate and on its surface, Fe in the ferromagnetic b.c.c. phase have been detected by the use of the Mössbauer spectroscopy [1]. The clustering of iron atoms, early stage of γ-Fe precipitation and its magnetic properties continue to be of interest to studies.
Fast quenching techniques have proved effective in extending the range of supersaturated solutions of Fe in Cu matrix as well as Cu in Fe matrix. One from the among of these methods - the ribbon spinning techniques (rst) - enable the preparation of alloys in amorphous phase or in crystalline one with ultrafine grains and new metastable phases in comparison to the alloys produced by the conventional method. Although single b.c.c. phase or single f.c.c. phase are not extended by rst [2] as much as in sputtered Fe-Cu alloys but it is found that samples Cu-Fe up to 15at% of iron containing significant fraction of Fe in γ-Fe can be obtained readily on quenching from liquid phase [3] for the magnetic properties investigation of γ-Fe. The character of spin-glass of rapidly quenched Cu-Fe alloys is responsible for both isolated Fe atoms and the magnetic clusters of iron as was shown in [4] up to 9at% of Fe in these alloys.
The main reason for the present interest in the splat cooling Cu-Fe is concentrated on the study of iron atom states in these alloys with wide range of Fe concentration.

Cu-Fe alloys containing iron from 1wt% to 100% with natural abundance of Fe were prepared by melt-spinning method in the Technical University of Clausthal-Zellerfeld (FRG) with the rate of cooling about 10^7K/s. The ribbons of alloys are 2 mm width and about 35 μm thick. X-ray diffraction measurements confirmed that the samples are polycrystallic materials. The standard Mössbauer spectrometer was used to examine these samples at room temperature (RT).

For rst Cu-Fe alloys of small Fe content (to 5at%) the spectra are similar to these one for the samples supersaturated in a solid state and the Cowley's parameters of short-range atomic ordering are close to the values of these parameters for the alloys supersaturated below the melting point [5]. This suggest that strong clustering of iron atoms already takes place in a liquid phase.
In alloys rich in iron (c>0.09) there is a clearly the three phase system : Cu-base - Fe solid solution, α-Fe phase and γ-Fe phase: as was visible on RT Mössbauer spectra of $Cu_{1-c}Fe_c$ where c = 0.1 to 0.6. These spectra showed similar behaviour with A) non-magnetic subspectrum due to combinations of Fe in Cu-Fe solid solution, iron atoms clusters, γ-Fe and its surface states and B) magnetic subspectrum due to α-Fe phase formation. For c>0.9 only magnetic components (B) were observed.

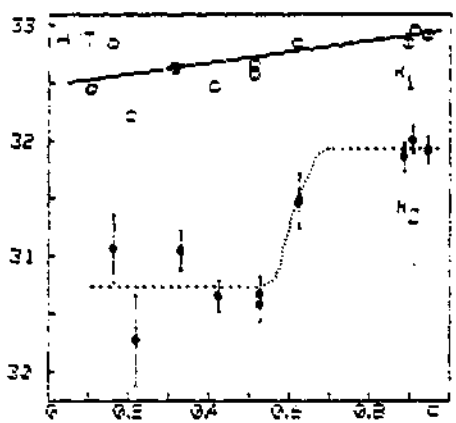

Fig. 1 show the values of the hyperfine magnetic field (hmf) as a function of iron concentration in Cu-Fe alloys. Open circle - H_1 - the largest component of hmf. The value of fitting procedure error is marked for each point.

The measured spectra were fitted using: - a single Lorentzian line to represent the γ-Fe and the other one to represent Fe atoms in Cu-Fe solid solution (Fe monomers), - a doublet to model Fe in iron clusters and γ-Fe surface states [1,5], - a two Zeeman's sektet with intensity ratios $I_{1,6}:I_{2,5}:I_{3,4}$ = 3:2:1 to fit the magnetic pattern (B) of these spectra. The two Zeemans are the smallest number of components which reasonably well describe the B subspectra of all Cu-Fe Mössbauer spectra. On the other hand it is adequate to the interpretation of the concentrated Au-Fe alloy spectra introduced by Gonser et al. [6], assumes the spectra to be a superposition of two magnetic hyperfine spectra. This mo-

del was developed recently by Violet et al. [7] and it is based on assumptions: i) The Fe atoms reside in two well-defined and distinct chemical states or environments. One environment will be enriched and other depleted relative to c; c-average bulk concentration of the alloy. There is a distribution of chemical states within each of the two environments. ii) The observed magnetic hyperfine field (H) depends only on the temperature and the local Fe concentration. iii) The variable of the recoilles fraction for the above range of Fe concentration is negligible.

The obtained magnetic hyperfine field data is presented on Fig. 1. The values of first component (H_1) slightly dependence on iron concentration (c) agree to relation $H_1=32.5(1+0.015c)(T)$ while the second component (H_2) is almost constant up to c:0.6 (H_2 equal about 30.7T) and increase to the value $H_2=31.9T$ for c more than 0.7. This implies that in the Cu rich region the environment of the iron atom in α-Fe depends on iron concentration in alloys and the local copper atoms concentration is greater than solubility limits of Cu in α-Fe near the melting point.

***Acknowledgements:** This work was supported by the Polish Ministry of Science and Higher Education within Project CPBP 01.06*

REFERENCES

1. U.Gonser and M.Ron in "Applications of Mössbauer Spectroscopy", ed. R.L.Cohen; Academic Press, New York (1980) vol.II p.281
2. Y.Nakamura, K.Sumiyama and N.Kataoka; Hyperfine interactions 28 (1986) 1029
   Y.Nakamura and K.Sumiyama; ICAME-1983 Alma Ata, Abstract p.232
3. G.L.Whittle, S.J.Campbell and A.Calka; Hyperfine interactions 28 (1986) 993
4. I.Okamoto, T.Miyazaki, H.Takashi;phys.stat.sol.(a)97 (1986) 993
5. T.J.Panek and J.Kansy; J.Phys.F: Metal Phys.12 (1982) 269
   T.J.Panek in "Condensed Matter Studies by Nuclear Methods", ed. J.J.Bara, K.Ruebenbauer and Z.Stachura; Kraków 1985 p. 425
6. U.Gonser, R.W.Grant, C.J.Meechan, A.H.Muir,Jr, and H.Wiedersich J.Appl.Phys.36 (1965) 2124
7. C.E.Violet, S.P.Verrill, D.J.Balaban and R.J.Borg; Hyperfine Interactions 28 (1986) 985

THE LOCALISATION OF DISPLACED ATOMS BY BACKSCATTERING OF PLANAR CHANNELED IONS FOR SMALL DEPTH

Jerzy Czerbniak, Marek Moneta, Bogdan Pawlowski

Instytute of Physics, University of Lodz
Nowotki 149/153, 90-236 Lodz

The backscattering technics (RBS) under channeling condivions is often applied for position localisation and evaluation of the number of atoms introduced from outside into the crystal lattice [1]. In the case of planar channeling characteristic maxima at the beginning part of energy spectra are observed, due to the oscylatory motion of an ion in the interplanar continous potential Y(y) [2,3]. The ion beam density across the channel changes with penetration depth x and tends to statistical equilibrium for depth greater than about 100 nm. There are such places in the planar channel, where atoms introduced from outside or shifted from lattice position can not be detected through the channeled ion beam or can be detected with greater probability in comparison with the case of random direction of incident ion beam. The energy loss of channeled ions depends upon the number of collisions with electrons and turns out to be higher for ions moving close to the crystal plane and lower for ions moving near the center of the channel than the average energy loss. It is even possible, that atoms placed at the same depth under the crystal surface but differently shifted in the channel,can cause backscatterig of ion beam in a such way, that each gives a component to different maximum of the RBS-energy spectrum. In order to investigate such phenomena, the dynamic equation of motion of channeled ion was solved taking into account the local electron density across the channel and the loss of energy along the ion trajectory. Having the set of trajectories $y=y(x, y_0, \varphi_0)$ versus depth or $y=y(E, y_0, \varphi_0)$ versus

energy loss /φ_0, y_0 - the angle and position of incidence of ion between the planes/, the ion flux density across the channel was found and the scattering probability for ions approaching crystal atoms was calculated [4]. In order to evaluate the influence coming from atoms shifted relatively to the plane, computations were performed assuming gaussian type of distribution in the region of 10-80 nm from the surface. Typical results are presented below.

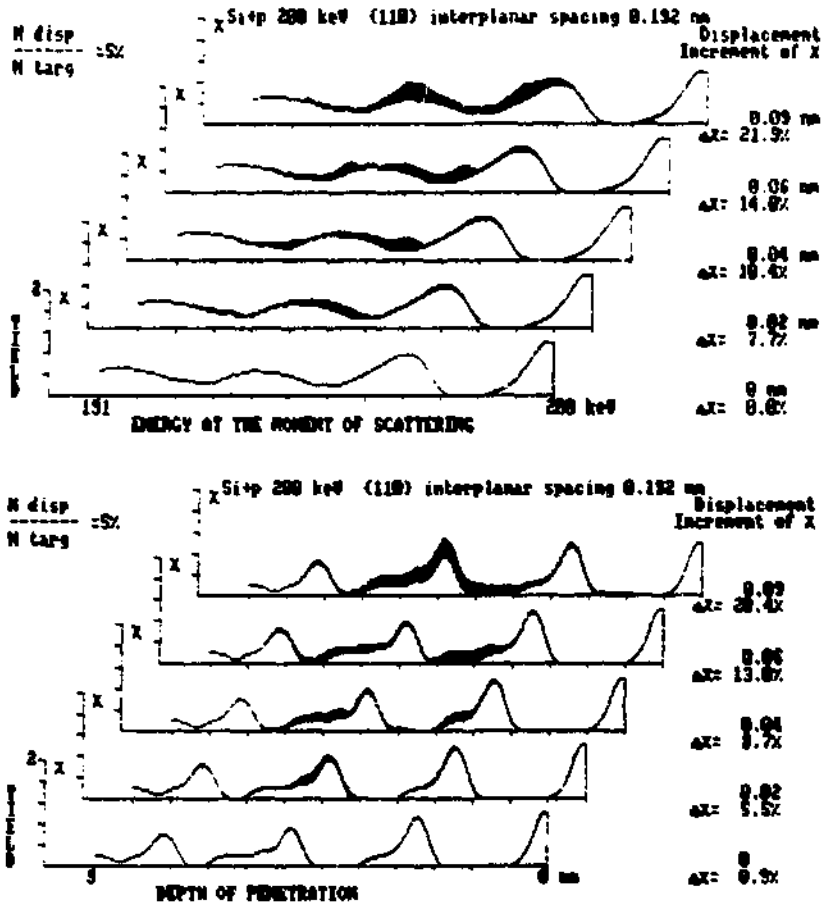

Fig.1.

The shape of calculated depth spectra differs from the shape of energy loss spectra. This is the result of the fact, that local electron density across the channel is not constant. The great deal of interpretation of experimental RBS data have been done up to now, assuming constant electron density (linear transformation between depth and energy scale).As is seen in Fig.1 such transformation for small depth is not satisfactory. The RBS measurements of planar channeled ions can be performed for different crystal planes. The analysis of such data accompanied by the method presented above allows one to obtain the relative density of shifted atoms of the order of 1-5%, and position with the accuracy of the order of thermal vibration amplitude. This work was supported in part under contract CPBP 01.09.

References

1. L.C. Feldman,J.W. Mayer and S.T. Picraux, Materials Analysis by Ion Channeling (Academic Press,New York,1982)
2. J.U. Lindhard, Mat. Fys. Medd. Dan. Vid. Selsk. 34, 34(1965)
3. F. Abel, G. Amsel, M. Bruneaux, C.Cohen and A. L'Hoir Phys. Rev. B12, N4617(1975)
4. J. Czerbniak, M.Moneta, Phys. Letters V117a, No7, 389(1986)

SYNCHROTRON RADIATION AND ITS APPLICATION.

V.I.Rajko

Institute of Molecular Genetics, USSR Academy of Sciences

Synchrotron Radiation (SR) emitted by high energy electron or positron storage rings is becoming a popular tool for science and industry. This radiation has unique properties, namely: high brightness, spectral coninuity, collimation and polised emission. It is increasingly applied in X-ray microscopy, chemistry, medicine, biology, material analysis, etc.

In nuclear spectroscopy SR makes it possible in principle to excite any single level. With all this one can study not solely nuclear scattering but the whole cascade of disintegration from the excited state and metastable levels. It is possible to conduct Moessbauer's experiments on SR beam with any nuclei possessing levels suited by the energy and the width. Here study /1/ is known where SR diffraction on Moessbauer's nuclei was observed at the storage ring "VEPP-3" in Novosibirsk, and the temporal distribution of the diffracted radiation was measured. In a recent study /2/ a similar experiment was performed and the spectral distribution of scattered quanta was measured on the storage ring "DORIS" in Hamburg. In X-ray topography of cristals SR is used in studies devoted to the interaction between radiation and atoms, molecules and condensed matter. The wide range of SR energies make it possible to cover the whole region of typical atomic energies above the laser region.

A growing part of SR users is made up by biologists. In the Institute of Molecular Genetics at Moscow X-ray structural stadies of biomolecules on SR were initiated in 1973. In 1979 the multi-channel (16,000) X-ray diffractometer on the basis of a multi-wire proportional shamber was put into operation on storage ring "VEPP-3" /3/. In the early 80s in IMG developed instrumentation for X-ray protein cristallography and for circular dichroism and fluorescence studies in the region of vacuum

ultraviolet radiation for the "SIBIRIA" storage rings at Moscow. The "SIBIRIA" complex consist of two storage rings and it is a facility for dedicated use of SR, the spectral output is shown in Fig.1. The complex was developed by the Institute of Nuclear Physics, Siberian Division of the USSR Academy of Sciences for the Kurchatov Institute of Atomic Energy. Since 1968 the small storage ring "SIBIRIA-1"(electron energy - 0.4-0.5 GeV) was used for short wave studies up to soft X-ray /4/, and it will serve as an injector for the large storage ring "SIBIRIA-2" (electron energy - 2.5 GeV). "SIBIRIA-2" will provide the source of hard X-ray radiation now under construction.

A set of wavelength shifters and undulators is provided for in the storage ring "SIBIRIA-2". To protect the personnel against radiation all the equipment in experimental hall is contained in protective chambers connected to the storage ring by vacuum channels. Control, monitoring, data acquisition, processing and output functions are computer-controlled /5/.

The complex of dedicated SR sources in Moscow will allow fundamental studies to be carried out at the contemporary level.

REFERENCES

1. А.И.Чечин и др., ЖЭТФ, 37, 11, 531-534, 1983.
2. G.Gerau, Nucl.Instr.Meth., A 246, 362-364, 1986.
3. Т.Д.Мокульская и др., Кристаллография, 27, 785-790, 1982.
4. Ю.П.Бузулуков, 6 Всесоюзное совещание по использованию синхротронного излучения СИ-84, Новосибирск, 1984.
5. Проспект "Техснабэкспорт", Внешторгиздат, № 36М737, Москва, 1984.

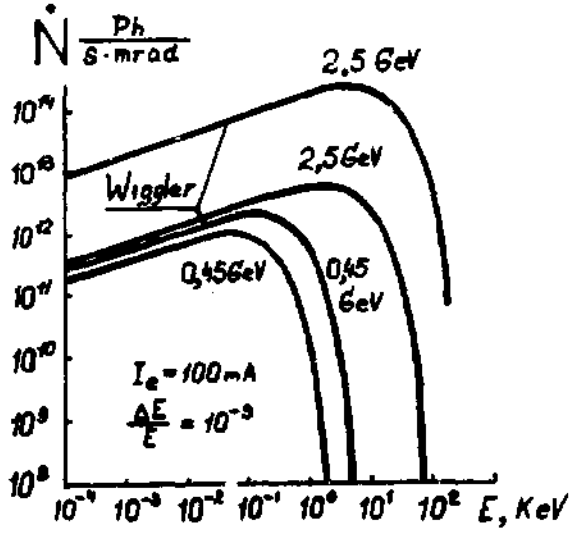

Fig.1 SR spectral distribution for "Siberia".

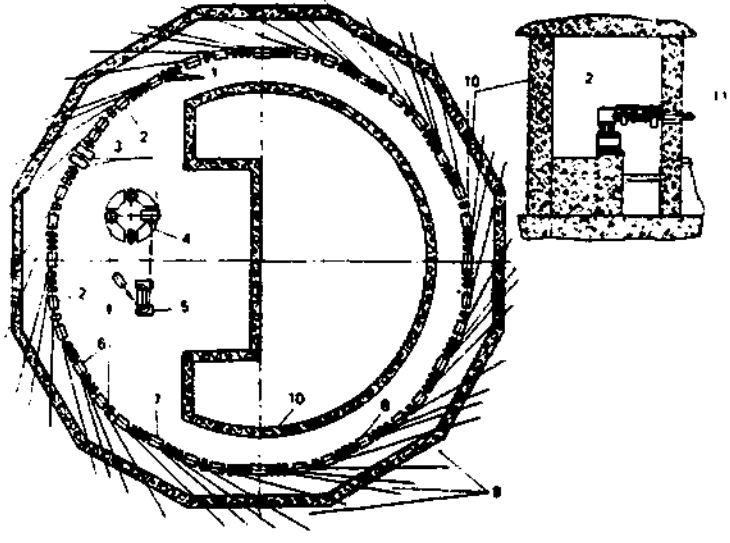

Fig.2 Lay-out of the complex "Siberia": 1-lenses; 2-bending magnets;3-RF cavity;4-"Siberia-1"; 5-microtron;6-Wigglers;7-superconducting Wigglers;8-undulators;9-SR beams;10-biological protection;11-SR extraction channel.

M. Podgórski, M. Subotowicz, H. Niezgoda, H. Spustek
K. Tańska-Krupa and R. Wasiewicz

Department of Experimental Physics, Institute of Physics,
M. Curie-Skłodowska University, 20-031 Lublin, Poland

INFLUENCE OF HIGH PRESSURE ON THE HYPERFINE INTERACTION PARAMETERS IN LAVES PHASE COMPOUNDS : $(Y_{0.9}Hf_{0.1})Fe_2$ AND $(Zr_{0.9}Hf_{0.1})Fe_2$

The influence of pressure on the hyperfine interaction parameters has been studied for some years but it still is little known. For some years the intensive and comprehensive studies of Laves phase compounds RFe_2 (where R is the rare earth element) have been performed. Hyperfine interactions in these compounds have been investigated, including the dependence of interaction parameters on the distance between ions and so-called "lantanic squeezing" [1].

The samples of $(Y_{0.9}Hf_{0.1})Fe_2$ and $(Zr_{0.9}Hf_{0.1})Fe_2$ were obtained by melting the stoichiometric quantities of initial components in the induction or arc furnace in the inert gas atmosphere. The annealing of samples in vacuum (10^{-6}Tr) at temperature 1250K for 200 hours has been carried out to increase or to reconstruct their homogenity. After they had been exposed for 100 hours to a neutron flux $\Phi = 7 \cdot 10^{13} n/cm^2 sec$ they were annealed once again to remove the radiation defects.

High pressure was produced in Bridgman's anvil pressure chamber. The anvils were made from sintered carbide alloy. The pressure was measured by means of a tensometer stuck into the interior wall of the chamber.

TDPAC measurements have been performed for (133-482)keV cascade in ^{181}Ta (after the β^- decay of ^{181}Hf). A standard spectrometer has been used, with BaF_2 and NE 111 scintillators working with XP 2020 Q photomultiplier. The time resolution was equal to $2\tau_0 = 0.9 - 1.9$ ns. Measurements were performed for

polycrystalline samples, without the external magnetic field.

It has been assumed that the measured hyperfine magnetic field is the sum of the fields originating from core polarization (B_{hf}^{CP}) and conduction electrons polarization (B_{hf}^{CEP}):

$$B_{hf}=B_{hf}^{CP}+B_{hf}^{CEP}$$

The hyperfine field B_{hf}^{CP} connected with the core polarization is of exchange interaction origin. It is antiparallel to the magnetic moment acting on the atom. The B_{hf}^{CEP} contribution is proportional to the magnetic moment localized near the nuclear sampler. Taking into account the results of [2,3] one can estimate the contribution of both components to B_{hf} on the Ta nuclei at room temperature: $B_{hf}^{CP} \cong +1.8$ T and $B_{hf}^{CEP} \cong -16.2$ T in YFe_2 and $B_{hf}^{CP} \cong +11.4$ T and $B_{hf}^{CEP} \cong -17.9$ T in $ZrFe_2$.

. Because of lantanic squeezing [1], experienced by atoms occupying the R positions, the external pressure leads mainly to the decrease of the value of the megnetic moment localized in this position and consequently to the decrease of B_{hf}^{CP}. Because of opposite signs B_{hf}^{CP} and B_{hf}^{CEP} and reciprocal relation between them, it leads to the increase of the amplitude of magnetic field observed on Ta nuclei (see table II). In the above considerations we assumed that B_{hf}^{CEP} does not change with the pressure, or its decrease with the pressure growth is considerably smaller than in the case of B_{hf}^{CP}. The decrease of Fe magnetic moment does not necessarily lead to the reduction of fields induced on Ta (transferred hyperfine fields). It is true, if this field is compensated by the decrease of overlapping of the wavefunctions of Fe(3d) - Ta(6s), like in the case of YFe_2 [4].

On the contrary, the decrease of the localized moments of Fe nuclei connected with the increase of the pressure, causes the magnetic field reduction ($\partial \ln B_{hf}/\partial p < 0$), because the B_{hf}^{CP} contribution is very small in this case.

The difference between values $\partial \ln B_{hf}/\partial p$ measured in R

positions for Y(Zr) and Ta is caused probably by the fact that the contributions from the core polarization for 5d ions are the greatest in the whole periodic table (and are equal to 73 T /unpaired spin/) Certainly, the induced localized magnetic moment on Ta impurity atoms will be different from the intrinsic moment of Y(Zr) atoms in YFe_2 or $ZrFe_2$ compounds, as far as its value is concerned.

Table II

Sample	Nuclear sampler	B_{hf} (T) at p=0	$\partial \ln\lvert B_{hf}\rvert/\partial p$ (10^{-4} kbar^{-1})	Temp. (K)	Lit
$(Y_{0.9}Hf_{0.1})Fe_2$	^{181}Ta	-14.4(1)	11.0(1)	300	*)
YFe_2	^{89}Y	-22.0(1)	0.7(3)	4.2	[4]
YFe_2	^{57}Fe	-21.3(1)	-4.2(2)	4.2	[4]
$(Zr_{0.9}Hf_{0.1})Fe_2$	^{181}Ta	-6.5(1)	22.3(3)	300	*)
$ZrFe_2$	^{89}Zr	-12.6(1)	11.1(3)	4.2	[4]
$ZrFe_2$	^{57}Fe	-22.2(1)	-7.3(1)	4.2	[4]

*) our experiment

Acknowledgements

The authors acknowledge the financial support of the Government's Central Programm of the Fundamental Research CPBP-01.09. in the realization of the present paper.

References.

1. E.Burzo. Angew.Phys. 32(1971)127.

2. Z.Z Akselrod, M.Budzynski, T.Khazratov, B.A.Komissarova, L.N.Kryukova, S.J.Reiman, G K.Ryasnyi and A.A.Sorokin Hyp.Int.14 (1983) 7.

3. Z.Z.Akselrod, M.Budzynski, B.A.Komissarova, L.N.Kryukova, G.K.Ryasnyi and A.A.Sorokin phys.stat.sol. (b) 119 (1983) 667.

4. T.Dumelov, P.C.Riedi, P.Mohn, K.Schwarz and Y.Yamada J.Magn.Mat. 54-57 (1986) 1081.

THE ROLE OF PIXE AND PIGE MEASUREMENTS IN GEOLOGICAL STUDIES

S.Szymczyk, J.Kejfosz, E.Dutkiewicz
Institute of Nuclear Physics, 31-342 Kraków, Poland

INTRODUCTION

The PIXE and PIGE /Proton Induced X-ray and Gamma-ray Emission/ methods are now fairly well developed and the range of their applications is still increasing. In the Institute of Nuclear Physics /INP/ in Cracow these techniques have for eleven years been widely applied in medicine, agriculture and environmental protection. In these fields the possibility of analyzing a large number of elements accurately and simultaneously by PIXE technique is fully exploited. However, in the last three years the geological applications increase in number and in the appreciation of their value. The feasibility of PIXE and PIGE analysis in geological material was proposed seven years ago on the 2nd PIXE Conference in Lund by Carlsson and Akselsson [1]. In this paper we want to demonstrate the great usefulness of these methods in geological studies, on a number of practical applications. One can stress, that now an explosion of geological studies is observed; the old geological conceptions are revised on the basis of newly available experimental results /among others PIXE/ .[2]

EXPERIMENTAL ARRANGEMENT

The determination of elemental composition was made using PIXE technique. A proton beam of 2.6 MeV energy from a small C-48 cyclotron at INP was focursed to a diameter of 6 mm on the analysed thick targets which have been pressed into pellets / ϕ 10mm/. In the PIXE assembly in INP we use a characteristic technique: the target-chamber with an intermediate air pressure. This improvement of PIXE analytical technique was described in ref. 3 and the method proved satisfactory and especially useful for the analysis of insulating targets as most of the geological samples.

The PIXE analyse, which are inapplicable to light elements with Z lower than 12, were supplemented by the PIGE method with high sensitivity for B, F, Li and medium sensitivity for Na, Mg, and Al elements.

FIELD OF COLLABORATION AND SUBJECTS OF STUDY

Four years ago we started in collaboration with A. Przybylowicz, a geophysicist from the Academy of Mining and Metallurgy systematic studies of geological materials of the serpentinite rocks from Lower Silesia. Interesting results presented at conferences [4,5] and in journals [4–6] stimulated several laboratories from the Geological and Mineralogical Departments to extend their investigations by PIXE and PIGE methods. Then we have received the dolomites from Upper Silesia delivered by S.Śliwiński, the kaolins from Lower Silesia by P.Łyszowirski, the samples of natural salt by A.Świątek, granities and gneisses from the Sudeten and Lower Silesia by A.Salmas-August /Wrocław University/, zinc ores by a Geological Firm in Kraków. All these studies and their results will be discussed in special publications and reports in topical literature. Here some illustrative examples will be presented and some methodological questions of interest in geological studies discussed.

The range of concentration values obtained in PIXE analysis is shown in Table I : column 2 for 54 representinite rocks in the Sudeten foreland by A.Przybylowicz /AGH Kraków/; column 3 for 27 granities and gneisses, collected in the Lower Silesia by A.Salmas-August /University in Wrocław/.

Element	Range of contents /ppm/		Element	Range of contents /ppm/	
	Serpentinities	Granites and gneisses		Serpentinities	Granites and gneisses
1	2	3	1	2	3
Si %	13,1–22,0		Ga	Sing.det.<6	17det.4,1–450
S	170–2700		As	"	Sing.det.2,2
Cl	90–620		Se	4 det.1,6–2,3	3 det.1,3–3,4
K	40–135		Br	1,2–9,7	0,6–150
Ca	2500–11900	100–58000	Rb	1,2–77	2,6–6300
Sc		380–690	Sr	2,2–27,4	49–6900
Ti	27–730	0,2–1800	Y	3,3–26,4	1,3–63
Cr	630–2020	6–2500	Zr	4–40	30–10100
Mn	50–2160	6–17000	Nb	Sing.det.17	-
Fe %	3,6–14,4	0,014–21	Ag	-	2det.ca1500
Ni	1200–3400	19det.10–300	Cs	-	sing.det.100
Cu	2 det.7,5;320	0,9–1350	Ce	-	" 20000
Zn	12–420	1,1–990	Pb	1,7–300	4,7–200

An X-rays spectrum from PIXE analysis of kaoline sample is shown in Fig.1. It is a typical spectrum but with an unexpected content of elements such as Au /46,9 ppm/ and Ga /14,6 ppm/.

This is a good illustration of the findings that can be offered to the geologist. It answers the question why the PIXE analyses are interesting from geological point of view. The PIXE analysis gives a clear picture of macro- and micro-elements present in the sample with many of them not easily detected by other methods. Indeed our PIXE data obtained for elements Nb, Sr, Y, Zr, Pb, Br gave the first geochemical information on their abundance in Lower Silesian serpentinities and thus contribute to our knowledge of geochemistry of ultrabasic rocks.

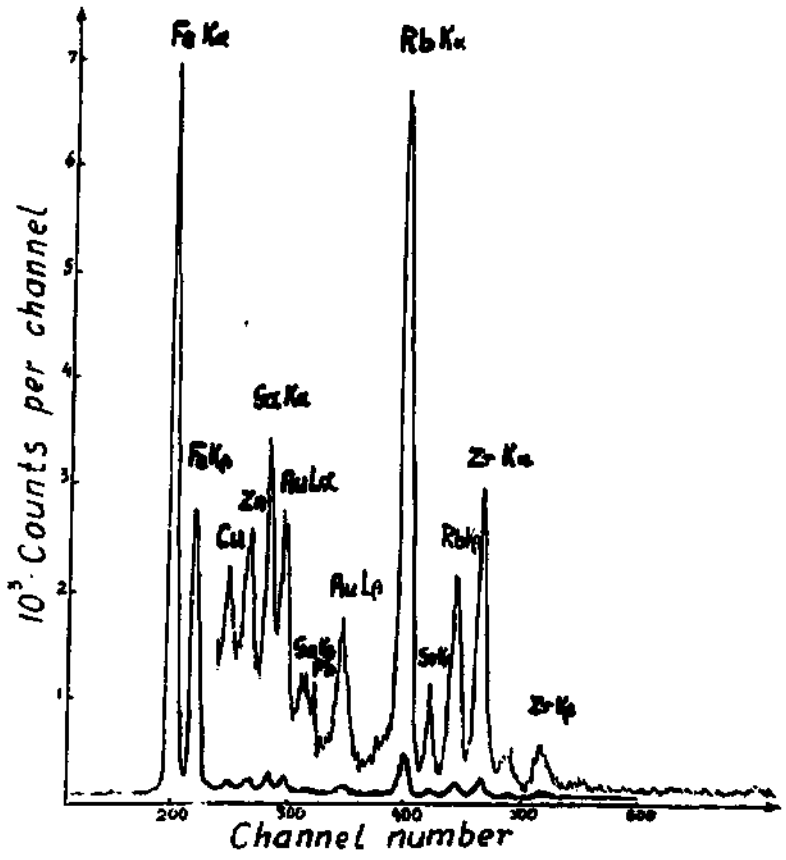

Fig.1. X-ray /PIXE/ spectrum of kaoline sample.

The advantage that no chemical pretreatment is needed increases the versatility of PIXE results as compared with other methods.
Of course we don't limit the studies to PIXE analysis; we only stress how useful this technique can be when included to a complete set of geochemical methods. Valuable conclusions can also be drawn from the determined inhomogeneity of the distribution of individual elements in the investigated geological material.
At the 3rd Conf. on PIXE, Heidelberg 1983 we presented a simple method for the determination of sample inhomogeneity [7].
The idea is the following: According to the Gaussian law of error propagation the resultant standard deviation σ_s can be regarded as composed of two contributions from different independent error sources according to the formula

$$\sigma_s = \left(\sigma_a^2 + \sigma_i^2\right)^{1/2}$$

In order to study the inhomogeneity problem we can consider the sample inhomogeneity to be one of the independent error sources contributing to σ_s, characterised by σ_i, whereas σ_a characterises the total contribution from all other error sources active in the analysis. The quantity σ_s can be determined from a series of independent measurements of the elemental concentration carried out with different targets made of the same sample, whereas σ_a can be determined from a series of independent measurements of the same concentration carried out with the same target of the sample. In this way an estimate of σ_i has been obtained from two such series of measurements for serpentinite sample from Grochowa /see Table II/.

TABLE II. Inhomogeneity of the distribution of 7 elements in serpentinite from Grochowa.

Element	Fe	Ni	Zn	Br	Rb	Sr	Pb
σ_i %	0	2-3	13-14	0	15	6	4

Definitely higher inhomogeneity of the Zn and Rb distribution is probably connected with the fact that these elements are components of minerals of higher hardness.

In the INP the method of light elements analysis by /p,pγ/ reaction has been developed as a tool complementary to PIXE. The so-called PIGE method was successfully tested and applied in some biological and medical research problems; in particular the fluorine contents in botanic samples could be estimated even on 2-3 ppm level. The sensitivities /detection limits/ for geological matrices were found to be worse because of higher background levels. Nevertheless the estimations of F, Li and B by PIGE with limit of detection on the level of ca 30 ppm proved to be better than in many others methods.

Up till now a large divergence of results published for fluorine concentrations in serpentinities rocks was observed. From our PIGE analysis the mean value for studied serpentinities was 204± 18 ppm. The amphibol rock from Grochowa contains 150 ppm of fluorine and the rodiginite rocks from Jordanów clearly more - 500 ppm. The obtained F concentrations in kaolins are from 130 ppm to 3000 ppm; in 4 samples the traces of B and Li elements were found on the level of the detection limit /20-30 ppm/.

We think that this outline gives some idea of how useful the PIXE method can be for geological applications, especially when supplemented by PIGE measurements.

REFERENCES:

1. L.E.Carlsson and K.R.Anselsson, Nucl.and Meth. 181, 531 /1981/.
2. Proceedings of 4th Meeting on Nuclear Analytical Methods, Dresden, May 4-6, 1987.
3. S.Szymczyk, J.Kajfosz, A.Mrynkiewicz and J.Curzydło, Nucl. Instr. and Meth. 181, 517 /1981/.
4. W.Przybyłowicz, S.Szymczyk, J.Kajfosz, Proc.of 7th Internat.Conf."ION BEAM ANALYSIS", Berlin, 1985; Nucl.Instr. and Meth.in Phys. Res, 16B/1986/
5. J.Kajfosz, S.Szymczyk, W.Przybyłowicz, Proc.of the Polish Symposium "DEVELOPMENT AND APPLICATION OF ISOTOPIC METHODS IN ENGINEERING AND TECHNOLOGY", Sept.1985, Zakopane; RAPORT INT 196/1,IFJ-AGH Kraków 1986,p.27.
6. W.Przybyłowicz, J.Kajfosz, S.Szymczyk, Mineralogia Polonica,17,No2/1986/.
7. J.Kajfosz, S.Szymczyk and G.Kornaś, Proc. of the 3rd Int.Conf.on PIXE, Heidelberg, 1983; Nucl.Instr. and Meth.in Physics Research B3,147/ 1984/.

ZX SPECTRUM - an Intelligent Terminal for a Mössbauer 2331 Spectrometer in a CAMAC System.

J. Holeczek; E. Popiel
Institute of Physics, Silesian University Katowice.

The automatic, multi-input Mossbauer spectrometer -type 2331, operating in the CAMAC system, is designed principally for working in conjunction with commercially available minicomputers SM-3,SM-4 Mera etc. This spectrometer can work in system of constant acceleration or constant velocity, making it possible to conduct four simultaneous Mossbauer experiments on two electrodynamic vibrators (G2) used on both sides. After an experiment lasting many hours or many days, ensuring adequate statistics, the appropriate Mossbauer spectra are recorded in the form of files in the memory of the minicomputer operating in conjunction with the spectrometer. After completing the experiment these files can be processed numerically on this same minicomputer or transferred to another computer for processing.

The operational system for controlling the experiment that is supplied together with the spectrometer has, however, one very serious drawback, during the time of experiment the operational system of minicomputer is suspended, in this way making it impossible for other users to work with the minicomputer during the experiment (this is particular importance when using in this set the SM-4 minicomputer with a broad configuration).

Hence it became necessary to develop the set described below since during prolonged experiments no other person could make use of the large SM-4 configuration, and conversely, during calculations it was impossible to perform Mossbauer measurements.

Modification to the original set was aimed at providing for the microcomputer ZX SPECTRUM to take over the performing of all the possible tasks which were envisaged for the SM-4 minicomputer in the original set (Fig.1). For this purpose an interface was designed by means of which the ZX SPECTRUM communicates with the Mossbauer spectrometer. In such set this communication is achieved via a standard 6606/1 Multiscaler Adapter , but the ZX SPECTRUM has no communication with the main line of the CAMAC system.

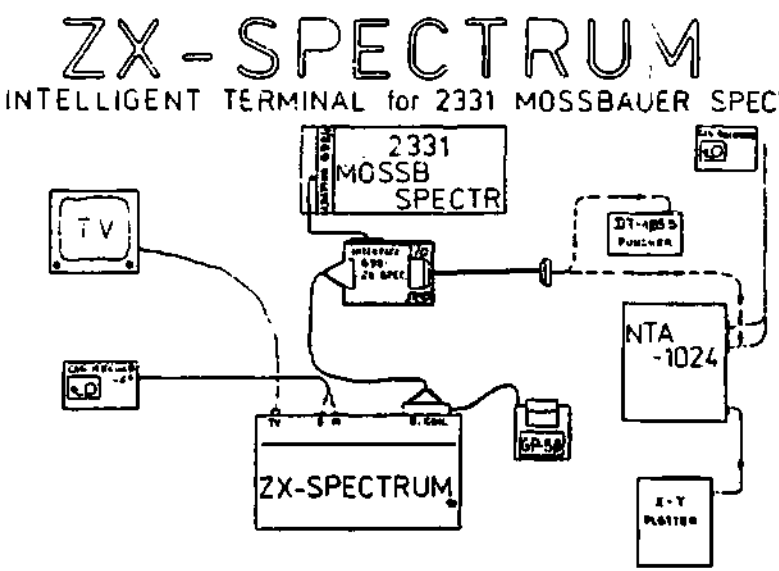

Fig. 1

Block diagram of ZX SPECTRUM -Mossbauer spectrometer data aquisition system. All connections for transmission of data from/to memory of microcomputer to/from different peripherals are given on this diagram.

Apart from the systems ensuring communication between the ZX SPECTRUM and the spectrometer the interface is additionally equipped with an 8-bit, parallel IN/OUT port for transmission with acknowledgement.

When modified in this way the Mossbauer spectrometer set, similarly as the set with a minicomputer, has the option of simultaneous performance of a maximum of four Mossbauer experiments in four paths (A1, A2, B1, B2) each with 256 or 512 channels. The capacity of each channel is $2^{32}-1$ and the first channel in paths A1 and B1 is used to count the number of cycles of the vibrators during measurement.

When the 669/1 Waveform Generator with four different working frequencies is used, then selecting the two highest frequencies and number of channels in the path as 512, it is possible to carry out simultaneously only two experiments, which is governed by the time of duration of one work cycle of the microprocessor in the ZX SPECTRUM. For other combinations of vibrator frequency and number of channels,four Mossbauer experiments can be performed simultaneously.

The programme controlling the ZX SPECTRUM operation during the experiment was written in assembler and partly in ZX Basic. Due to this programme, during the course of the experiment,after the spe-

cific number of cycles of the vibrator, as selected by the operator, data collection is discontinued and in a short time the collected spectra are displayed graphically on the TV-monitor, after which data collection is restarted. The spectra obtained in this way on the TV-monitor persist until the new display cycle. Thanks to this programme, after the end of experiment the spectra stored in ZX SPECTRUM memory can to be transferred to a standard, peripheral equipment item, i.e. to a tape recorder (in the form of a file) or on a printer plus TV-monitor (in graphical form). In Fig.2a,b the copies of the pictures from TV-monitor, obtained on small printer GP-50, after two different experiments are presented

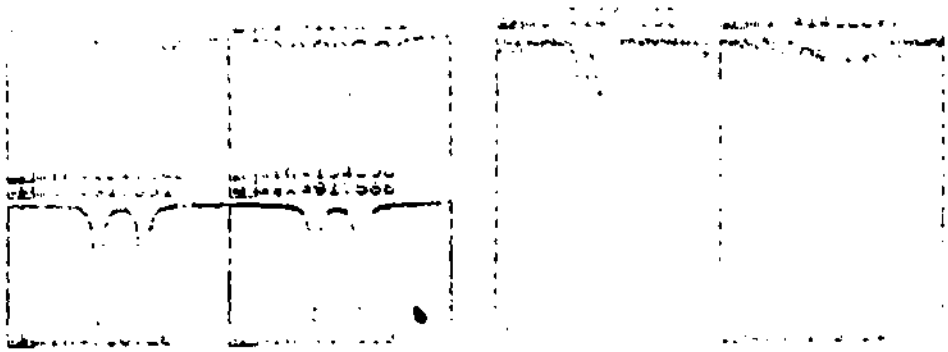

Fig. 2a

Fig. 2b

Copies of the TV-monitor screen after two Mossbauer experiments.
a.-two sources, two vibrators with different velocities
two different absorbers.
b.-one source, one vibrator and one absorber.

Due to this additional 8-bit IN/OUT port, spectra stored in the memory can be transferred to additional output equipment, e.g. a paper tape perforator. There is also the option of two-way communication with the Hungarian MTA-1084 analyzer, making it possible to display the spectra in graphical form on its XY-plotter and other analyzer's peripherial equipments.

In Fig.3 the picture,obtained by XY-plotter for the spectra transferred from ZX SPECTRUM to MTA-1084 analyzer, is presented. When using suitable software the additional IN/OUT port may also be used as a "Centronics" type connection.

The Mossbauer spectrometer with this ZX SPECTRUM microcomputer has been in use for more than six month and to date only one drawback has been observed. As the ZX Power Supply is highly sensitive to network voltage fluctuations it can happen that microcomputer operation is suspended and thus the spectra stored in the

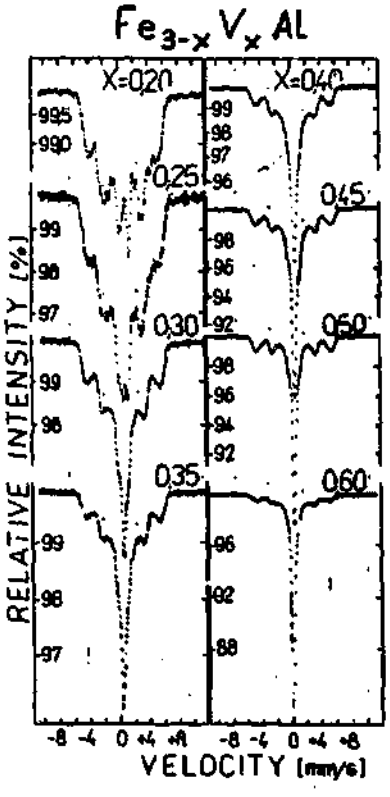

memory up to the moment of interruption are lost. This represents, however, only a small percentage of experiments, performed in our laboratory by last seven months.

Fig. 3

The picture of a few spectra, obtained with ZX SPECTRUM-ISSI Mossbauer spectrometer set and transferred by IN/OUT port to HP4-1614 analyzer. This picture was obtained on XY plotter of this analyzer in one "drawing run".

CLOSING REMARKS

given by Gunter Schatz

- physics — see next page
- participants — see list of participants
- organizers — see organizing committee
- complaints — see below

longer duration of school, so we could have longer fun!

PHYSICS

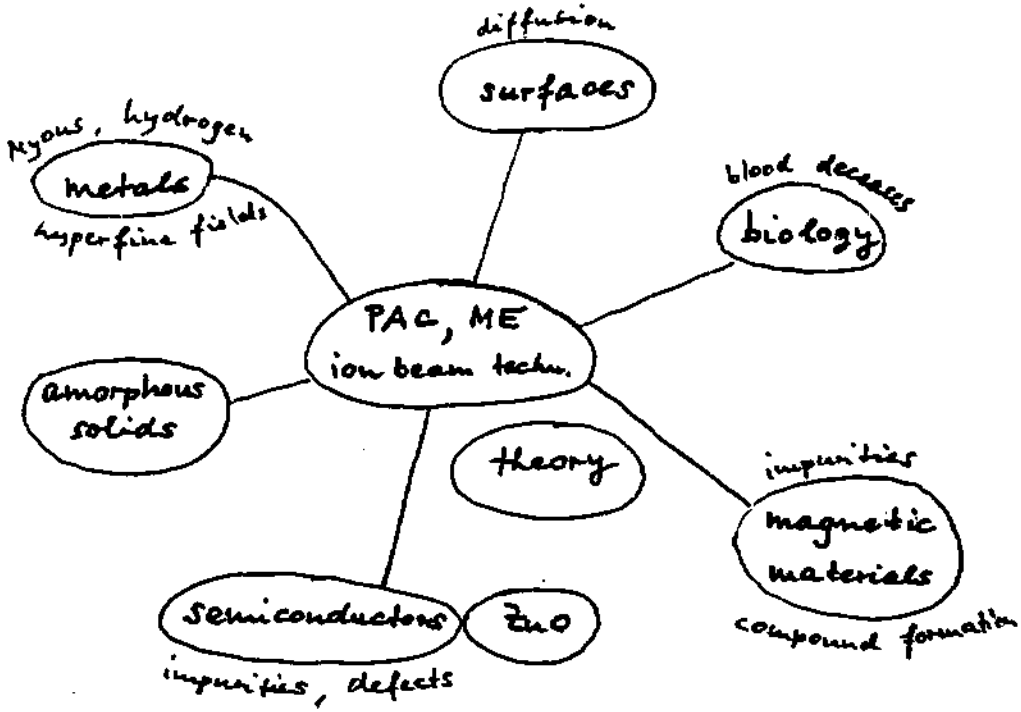
diffusion
surfaces
Nyons, hydrogen
metals
hyperfine fields
blood diseases
biology
PAC, ME
ion beam techn.
amorphous solids
theory
impurities
magnetic materials
compound formation
semiconductors
ZnO
impurities, defects

drawn by Ehud Dafni

LIST OF PARTICIPANTS

1.	M. Abd-Elmeguid	Bochum
2.	E. Bauminger	Jerusalem
3.	L. Bauminger	Jerusalem
4.	H. Bińczycka	Cracow
5.	B. Bogacz	Cracow
6.	M. Budzyński	Lublin
7.	J. Capała	Cracow
8.	N.H. Chau	Cracow
9.	J. Chojcan	Wrocław
10.	M. Cholewa	Cracow
11.	D. Cleff	Münster
12.	F. Constantin	Bucharest
13.	J. Czerbniak	Łódź
14.	G. Czjzek	Karlsruhe
15.	E. Dafni	Rehovot
16.	E. Danielsen	Aarhus
17.	L. De Doncker	Leuven
18.	J. Drużek	Cracow
19.	E. Dutkiewicz	Cracow
20.	P. Fedczyszyn	Wrocław
21.	H. Figiel	Cracow
22.	M. Finger	Dubna
23.	J. Frąckowiak	Katowice
24.	E. Görlich	Cracow
25.	J. Grębosz	Cracow
26.	A. Gustavsson-Seidel	Uppsala
27.	E. Gędłek	Cracow
28.	H. Haas	Berlin W.
29.	A. Habrowska	Katowice
30.	R. Hajduk	Cracow
31.	F. Hardeman	Leuven
32.	S. Harris	Uppsala
33.	J. Hietaniemi	Helsinki

34.	A. Hrynkiewicz	Cracow
35.	Z. Inglot	Cracow
36.	E. Japa	Cracow
37.	K. Jones	Brookhaven
38.	J. Kajfosz	Cracow
39.	Cz. Kapusta	Cracow
40.	G. Kemerink	Groningen
41.	W. Keune	Duisburg
42.	R. Kmieć	Cracow
43.	J. Komraus	Katowice
44.	J. Kowalski	Cracow
45.	J. Kraczka	Cracow
46.	K. Krop	Cracow
47.	K. Królas	Cracow
48.	D. Kulgawczuk	Cracow
49.	M. Lach	Cracow
50.	G. Langouche	Leuven
51.	J. Lekki	Cracow
52.	K.P. Lieb	Göttingen
53.	U. Lieb	Göttingen
54.	L. Liszkay	Budapest
55.	H. Lizurej	Cracow
56.	K. Łątka	Cracow
57.	M. Malki	Strasbourg
58.	G. Marest	Lyon
59.	M. Marszałek	Cracow
60.	A. Mayer	Uppsala
61.	H. Mehner	Dresden
62.	B. Mikołajczak	Lublin
63.	S. Nagel	Marburg
64.	M. Niewiara	Cracow
65.	A. Oziernoj	Alma Ata
66.	T. Panek	Katowice
67.	A. Polaczek	Warsaw
68.	E. Popiel	Katowice
69.	W. Potzel	München
70.	J. Przewoźnik	Cracow

71.	D. Rajko	Moscow
72.	H. Reuther	Dresden
73.	M. Rots	Leuven
74.	M. Rybicka	Cracow
75.	J.P. Sanchez	Strasbourg
76.	G. Schatz	Konstanz
77.	M. Sondergaard	Aarhus
78.	Z. Stachura	Cracow
79.	C. Stan-Sion	Bucharest
80.	J. Stanek	Cracow
81.	M. Subotowicz	Lublin
82.	M. Sudnik	Cracow
83.	J. Szlanta	Radom
84.	M. Szuszkiewicz	Wroclaw
85.	K. Szymański	Białystok
86.	S. Szymczyk	Cracow
87.	L. Trache	Bucharest
88.	K. Tomala	Cracow
89.	M. Tuszyński	Katowice
90.	S. Unterricker	Freiberg
91.	J. Urban	Cracow
92.	R. Vianden	Bonn
93.	R. Wasiewicz	Lublin
94.	A. Weidinger	Konstanz
95.	A. Woch	Cracow
96.	B. Wodniecka	Cracow
97.	P. Wodniecki	Cracow
98.	T. Zaleski	Cracow
99.	W. Zarek	Katowice
100.	W. Zych	Warsaw
101.	J. Żukrowski	Cracow
102.	J. Żurawicz	Lublin